Deciphering the γ-ray Sky

Study of the γ-Cygni SNR using a novel likelihood analysis technique for the MAGIC telescopes

Marcel C. Strzys

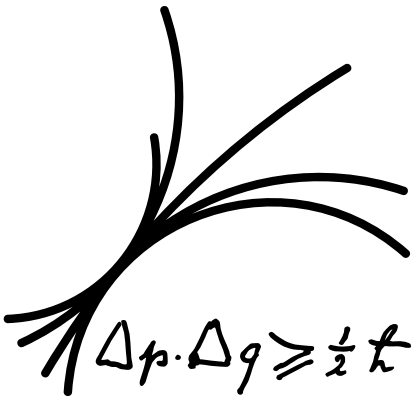

München 2019

Deciphering the γ-ray Sky

Study of the γ-Cygni SNR using a novel likelihood analysis technique for the MAGIC telescopes

Marcel C. Strzys

Dissertation
an der Fakultät für Physik
der Ludwig–Maximilians–Universität
München

vorgelegt von
Marcel C. Strzys
aus Iserlohn

München, den 16. Dezember 2019

Dissertation

an der Fakulät für Physik
der Ludwig-Maximilians-Universität München
vorgelegt von Marcel Constantin Strzys
am 16. Dezember 2019.

Erstgutachter: PD Dr. Georg G. Raffelt
Zweitgutachter: Prof. Dr. Masahiro Teshima
Vorsitzende der Prüfungskommission: Prof. Dr. Katia Parodi
Weiterer Prüfer: Prof. Dr. Til Birnstiel

Tag der mündlichen Prüfung: 30. Januar 2020

Zusammenfassung

Diese Dissertation befasst sich mit der Entwicklung einer Likelihood basierten Analyse für Daten von abbildenden Luft Cherenkov Teleskopen (IACTs) und deren Anwendung auf Beobachtungen des γ-Cygni Supernova Überrestes mit den MAGIC Teleskopen, einem System von zwei IACTs. Nach heutigem Wissensstand wird der galaktische Anteil der kosmischen Strahlung (CR), relativistischer Teilchen, welche hochenergetische Gammastrahlung erzeugen, hauptsächlich in den Schockwellen der Überreste von Supernovae (SNR) beschleunigt.

Diese Objekte sind ausgedehnt genug, sodass sie sich auch mit Gammastrahlen Teleskopen auflösen lassen. Dies ermöglicht einerseits eine genauere Untersuchung der verschiedenen Beschleunigungsregionen innerhalb des Objekts, stellt andererseits jedoch eine Herausforderung für die aktuellen Analysemethoden von IACTs dar. IACTs detektieren das Cherenkov Licht von Luftschauern, Teilchenkaskaden, die aus der Wechselwirkung von Gammastrahlung mit Luftmolekülen resultieren. Aktuell wird die Intensität einer Quelle aus den Daten von IACTs mittels der Aperture-Photometrie ermittelt. Dazu wird die Anzahl der detektierten Gammastrahlen-Ereignisse aus einem Gebiet um die Quelle mit der Anzahl an Ereignissen aus einem gleichgroßen Kontrollbereich ohne Quelle ermittelt. Überlagern sich jedoch Emissionsregionen, so lässt sich nicht bestimmen, zu welcher Region ein Ereignis zählt. Sehr ausgedehnte Quellen oder Objekte mit komplexer Morphologie stellen zudem ein Problem hinsichtlich der Wahl der Quellregion dar.

Durch eine räumliche Likelihood Analyse auf der Basis von Himmelskarten von IACTs lassen sich die Schwierigkeiten vermeiden. Dabei wird eine benutzerdefinierte Morphologie mit der Instrumentenantwort (IRF) gefaltet und dieses "realistische" Quellmodel mittels eines Poisson-Likelihood Fits an die Messdaten angepasst. Bei satellitengestützten Gamma-Teleskopen wie dem *Fermi* Large Area Telescope (LAT), wird diese Methode bereits angewandt. Die Schwierigkeit für IACTs ist die Bestimmung der IRF. Da die Atmosphäre ein Bestandteil des IACTs ist, kann die IRF nicht vorab im Labor ermittelt werden, sondern muss mit Hilfe von Monte-Carlo Simulationen für jede Beobachtung individuell bestimmt werden. Diese Arbeit präsentiert das Software Paket SkyPrism, das eine solche Analyse inklusive der Bestimmung der IRFs, für die MAGIC Teleskope durchführt.

Mit Hilfe von SkyPrism konnten MAGIC Beobachtungsdaten von dem ca. 7×10^3 Jahren alten γ-Cygni SNR analysiert werden. Während des Beschleunigungsvorgangs in

SNR Schockwellen streut die CR an magnetischen Turbulenzen vor und hinter dem Schock, wodurch der Grad der Turbulenzen ein wichtiger Bestandteil des Beschleunigungsvorgangs wird. Aus den schnellen Schockwellen von jüngeren SNR ($\lesssim 3 \times 10^3$ Jahren) entkommt nur ein kleiner Anteil der CR, während bei älteren SNR ($\gtrsim 1 \times 10^4$ Jahren) bereits nahezu die gesamte CR der Schockwelle entkommen ist und keine Beschleunigung mehr stattfindet. Die Beobachtungen mit den MAGIC Teleskopen (85 Stunden Beobachtungszeit) und dem *Fermi*-LAT (9 Jahre Daten) über einen Energiebereich von 5 GeV bis 5 TeV ermöglichten zum ersten Mal eine Untersuchung, wie die CR der Schockwelle eines SNR ins interstellare Medium entkommt. Mittels eines theoretischen Models für die Schockbeschleunigung konnte ermittelt werden, dass die maximale Energie, zu der die CR beschleunigt und im Schockbereich gehalten werden kann, schneller mit der Lebensdauer des SNR abnimmt als erwartet und der Grad an Turbulenzen über die Lebensdauer des SNR nicht konstant sein kann.

Abstract

This thesis presents a novel spatial likelihood analysis for Imaging Atmospheric Cherenkov Telescopes (IACTs) and its use to analyse observations of the γ-Cygni supernova remnant (SNR) with the MAGIC telescopes, a system of two IACTs. SNRs are the prime candidate source for the origin of the galactic component of cosmic rays (CRs).

These objects are sufficiently extended to be resolved with γ-ray telescopes. This allows the determination of different acceleration regions of a source, but poses issues for the current analysis approach for IACT data. IACTs detect the Cherenkov light generated in air showers, which are cascades of energetic particle that result from the interaction of γ-rays with the molecules in the atmosphere. Currently, the emission from a source is determined using the aperture photometry approach, in which the number of γ-ray events from the source region is compared against a source-free background control region. In the case of superimposed emission regions, an event count cannot be attributed to one emission region. Furthermore, extended objects or objects of complex morphology make the definition of the source region a difficult task.

These issues can be overcome by a spatial likelihood analysis of the skymaps of IACTs. In this approach, a user-defined source template is convolved with the instrument response functions (IRFs) and the "realistic" model fitted to the event count maps via a Poissonian likelihood fit. The data analyses of space-based γ-ray telescopes, such as the *Fermi* Large Area Telescope (LAT), are based on this technique. For IACTs the determination of the IRFs, however, is a challenging task: because the atmosphere is part of the detector, the IRFs cannot be measured in the laboratory but need to be computed from Monte-Carlo events for each observation individually. This thesis presents SkyPrism, a software package performing such an analysis on MAGIC data including the accurate determination of the IRFs.

Using SkyPrism it was possible to analyse observations of the $\sim 7 \times 10^3$ yr old γ-Cygni SNR taken with MAGIC between 2015 and 2017. CRs are accelerated and confined in the shock region by magnetic turbulences ahead and behind the shock, making the level of turbulence an important ingredient of the acceleration process. Only a small high energetic fraction of CRs may escape the fast shocks of young SNRs ($\lesssim 3 \times 10^3$ yr), whereas in the case of old SNRs ($\gtrsim 1 \times 10^4$ yr) almost all CRs have already escaped. I studied the escape of CRs from the shock into the interstellar medium

using 85 h of MAGIC data and 9 yr *Fermi*-LAT data covering the energy range from 5 GeV to 5 TeV. Using the theoretical model of the diffusive shock acceleration, I determined that the maximum energy of the CRs confined in the shock region decreases faster with the lifetime of the SNR than expected and that the level of turbulence is not constant over the lifetime of the SNR.

Megara:"Non est ad astra mollis e terris via."

— Seneca

Contents

List of Figures

List of Tables

List of acronyms

ADC	Analogue to Digital Converters
AGN	Active Galactic Nucleus
ASCA	Advanced Satellite for Cosmology and Astrophysics
a.s.l.	above sea level
Az	Azimuth
Chandra	Chandra X-ray Observatory
CGPS	Canadian Galactic Plane Survey
CMB	Cosmic Microwave Background
CO	Carbon Monoxide
CoG	Centre of Gravity
CR	Cosmic Ray
CTA	Cherenkov Telescope Array
DAQ	Data Acquisition System
DC	Direct Current
Dec	Declination
DSA	Diffusive Shock Acceleration
DT	Discriminator Threshold
Fermi	*Fermi* Gamma-ray Space Telescope
EGRET	Energetic Gamma-Ray Experiment Telescope
FADC	Flash Analogue to Digital Converters
FoV	Field of View
FSSC	*Fermi* Science Support Center
HAWC	High-Altitude Water Cherenkov Gamma-Ray Observatory
H.E.S.S.	High Energy Stereoscopic System
HPD	Hybrid Photo Detector
HV	High Voltage
IACT	Imaging Atmospheric (or Air) Cherenkov telescope
IC	Inverse Compton (effect/scattering)
INTEGRAL	International Gamma-Ray Astrophysics Laboratory
IR	Infrared
IRF	Instrument Response Function
ISM	Interstellar Medium
LAT	Large Area Telescope

LIDAR	Light Detection and Ranging
LUT	Lookup Table
MAGIC (telescopes)	Major Atmospheric Gamma Imaging Cherenkov (telescopes)
MARS	MAGIC Analysis and Reconstruction Software
MC	Monte Carlo
NN	Next Neighbour
NSB	Night Sky Background
PMT	Photomultiplier Tube
PSF	Point Spread Function
PSPC	Position Sensitive Proportional Counters
PSR	Pulsar
PWN	Pulsar Wind Nebula
RA	Right Ascension
RF	Random Forest
ROC	Receiver Operating Characteristic
RoI	Region of Interest
ROSAT	Roentgen Satellite
SED	Spectral Energy Distribution
SN	Supernova
SNR	Supernova Remnant
ST	Sedov-Taylor (phase)
TS	Test Statistic
VERITAS	Very Energetic Radiation Imaging Telescope Array System
XMM-Newton	X-ray Multi-Mirror Mission Newton
Zd	Zenith distance

Chapter 1.

Introduction

Since early times humans showed a natural desire to understand the enigmatic nature of celestial objects, but until less than a century ago their view was limited to the optical light alone. Technological advances in the 20$^{\text{th}}$ century opened observational windows invisible to the human eye. Today we can observe astrophysical objects over the whole electromagnetic spectrum. Each wavelength band traces different physical processes and provides unique information about physical properties of the emitting source.

The last observational window opened was the very high energy end of the electromagnetic spectrum, the γ-ray band, with photon energies $> 100\,\text{keV}$. In contrast to lower-energy parts of the electromagnetic spectrum, γ-rays cannot be produced by stable astrophysical sources via thermal emission. To produce γ-rays of $> 1\,\text{MeV}$ via thermal emission the temperature of the gas needs to be higher than $10^{10}\,\text{K}$, which cannot be reached by stable objects in the universe. Instead high energy γ-rays are mainly produced via the interactions of relativistic particles, linking γ-ray astronomy to a major discovery of the early 20th century, the discovery of cosmic rays (CRs).

CRs were discovered in 1912 by the Austrian physicist Victor Hess. Using balloon flights he showed that the ionising radiation increases with altitude and therefore must have its origin in outer space (Hess, V. F., 1912). The charged, relativistic particles hitting the atmosphere are to 86% protons, 11% helium, 1% heavier nuclei, and 2% electrons.[i] The total energy density of CRs in the interstellar space is $\sim 1\,\text{eV}\,\text{cm}^{-3}$, which is comparable to the energy density of starlight, the cosmic microwave background, and the Galactic magnetic field (Perkins, D. H., 2009) making them an important ingredient of the universe. Figure 1.1 shows the energy spectrum of all components of CRs combined, the so-called all-particle spectrum. It is multiplied by $E^{2.6}$ to emphasise the features of the steep, broken power-law spectrum: the two major breaks at $\sim 3 \times 10^{15}\,\text{eV}$, called the knee, and at $\sim 10^{18.5}\,\text{eV}$, called the ankle.

Since their discovery the origin of CRs is a key scientific question. Particles of energies above the ankle are assumed to be of extragalactic origin as their Larmor radius

[i] Based on this mixture the term CR usually refers to hadronic particles, whereas electrons are explicitly called CR electrons.

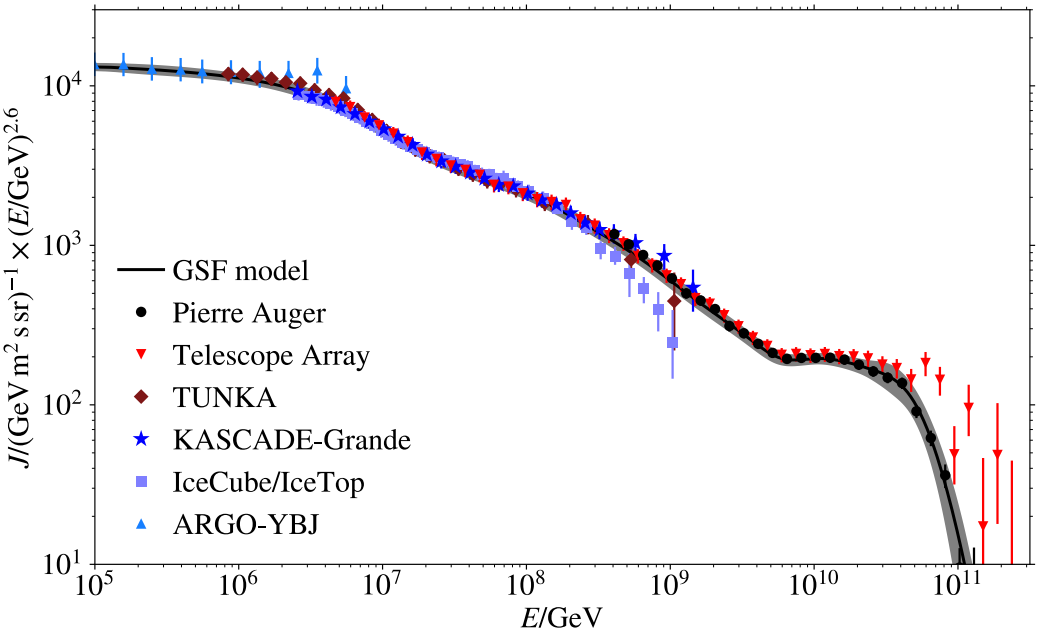

Figure 1.1.: All-particle spectrum of CRs multiplied by $E^{2.6}$. Figure from Anchordoqui (2019).

exceeds the thickness of the Galactic disk (∼300 pc) for the average Galactic magnetic field strength (∼6 µG, Beck, 2009). Possible sources are active galactic nuclei, starburst galaxies, and gamma ray bursts. CRs of energies below the knee are assumed to originate from sources within our Galaxy. It is supported by the softening of the spectrum at the knee and by a change of the chemical composition of CRs towards heavier elements at higher energies (Hörandel, J. R., 2006; De Rújula, A., 2019). Both features can be understood as a superposition of cut-offs in the spectra of different elements, where the cut-off is determined by the maximum energy of the source and the rigidity of the corresponding element e.g. $E_{\mathrm{Fe,max}} = 26\,E_{\mathrm{p,max}}$. Nonetheless, it is important to note that while there is scientific agreement about the position of the knee and a transition in composition towards heavier elements, the region between the knee and ankle and is not well understood. The transition between the Galactic and extragalactic component may either happen at the so-called second knee at $E \sim 5 \times 10^{17}$ eV or at the ankle.(see Kachelrieß & Semikoz, 2019, for a review).

Measuring CRs directly does not allow identifying their origin; due to their charge those particles are deflected by random magnetic fields in the Galaxy impeding to trace them back (see figure 1.2). Photons instead point back at their origin. Since γ-rays result from the interaction of the CRs with ambient magnetic fields, radiation fields, or matter, they are an important tool for studying the extreme environments accelerating particles to very high energies. The same applies to neutrinos, though their interaction cross section is extremely small allowing them to propagate nearly unabsorbed, but at the same time making it challenging to detect them.

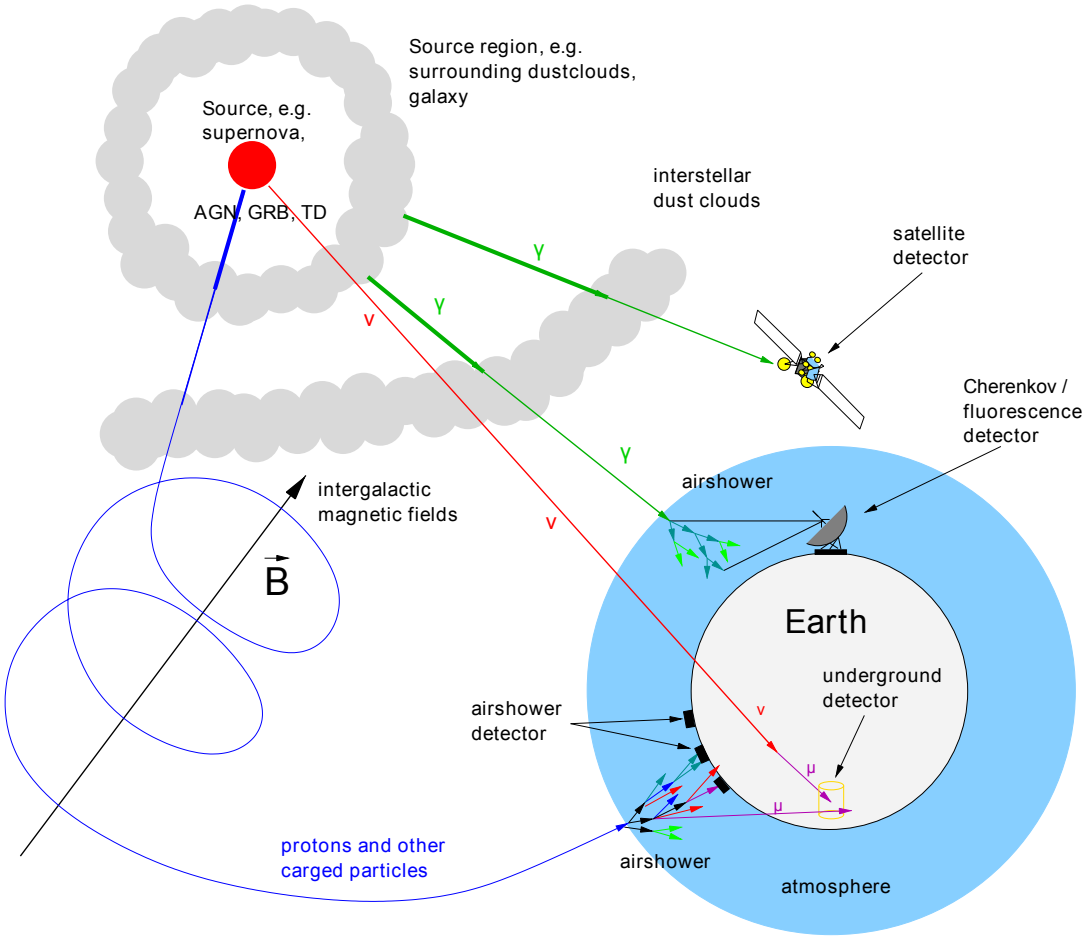

Figure 1.2.: A sketch summarising the field of astroparticle physics. Figure from Wagner (2004).

γ-rays can be detected either with space-based detectors or ground-based telescopes. Whereas satellite experiments have a larger field of view (FoV) and a better suppression of the CRs background penetrating the detector and mimicking γ-ray events, ground-based telescope provide a larger effective area and thus operate at higher energies ($> 50\,\mathrm{GeV}$), where the photon flux decreases. Ground based γ-ray telescopes are a rather young discipline effectively starting in 1989 with the detection of the Crab Nebula at TeV energies by the Imaging Air Cherenkov Telescope (IACT) Whipple (Weekes et al., 1989). At night-time IACTs observe astrophysical sources by detecting the optical light flashes from extended atmospheric showers (EASs), which result from γ-rays interacting with the atmosphere. Space- and ground-based γ-ray astrophysics experienced a boost in the recent years with the launch of the *Fermi* Gamma-ray Space Telescope in 2008 and with the second generation of IACTs, namely the High Energy Stereoscopic System (H.E.S.S.), the Major Atmospheric Gamma-Ray Imaging Cherenkov Telescopes (MAGIC), and the Very Energetic Radiation Imaging Telescope Array System (VERITAS).

This work is based on observations with the MAGIC telescopes. MAGIC is a system of two 17 m diameter modern IACTs. It is located at the Observatorio del Roque de los Muchachos on the Canary island La Palma, Spain, and operates in the energy range from $\sim 30\,\mathrm{GeV}$ to $> 100\,\mathrm{TeV}$. With the progressing improvement of their sensitivity, IACTs not only detect more objects but also resolve objects to larger details. This poses issues to the standard analysis techniques used by MAGIC and other IACTs today. It is based on comparing the detected photon counts from a source region to background control regions, which is free of sources. This technique proved to be successful as long as the sources are point like or rather small. It faces issues when one deals with extended, complex morphologies or several overlapping emission regions what mainly applies to Galactic sources.

This thesis presents a spatial likelihood analysis for MAGIC data, called SkyPrism, similar to the one used for space-based γ-ray missions such as the *Fermi* Large Area Telescope (LAT) overcoming the aforementioned limitation. By applying the known instrument response to an assumed source model, one can obtain an image of the model as it would be seen by the telescope. This model, together with the estimated background map, is fitted to the measured sky image to estimate the most likely flux of the model sources in the observed sky region. The application of this technique to MAGIC data however is more challenging as the atmosphere becomes part of the detector, the instrument is not background free, and the MAGIC telescope setup is not radially symmetry. This work shows how SkyPrism successfully implements the likelihood approach.

Among the Galactic sources that can currently be resolved with the angular resolution of IACTs ($\sim 0.1^\circ$) are the remnants of supernova explosions. They are the most promising origin for the Galactic cosmic ray component since the theoretical description of the acceleration process of CRs predicts the correct spectral slope to account for the CR spectrum below the knee. The expanding shock waves accelerate particles via diffusive shock acceleration (DSA), where CRs scatter on turbulences up- and downstream of the shock and gain energy when crossing the shock. Whereas the process is well studied, some issues remain, particularly, how low energetic seed particles are injected into the shock region to be accelerated and how the CRs generate scattering centres upstream. The latter question is closely connected to the escape of CRs from the shock, a process that can be studied by observing γ-rays produced in the interaction of CRs with the interstellar medium (ISM) surrounding the SNR.

For younger SNRs ($< 3\,\mathrm{kyr}$), the amount of CRs escaping is small, therefore they are not expected to show clear signatures of CR-ISM interaction. In the adiabatic phase, the so-called "Sedov-Taylor phase", the shock decelerates and large fractions of particles are released into the ISM. The interaction of escaping CRs with dense molecular clouds was observed for a number of such middle-aged SNR (W28, IC443, W44). However, these SNRs are so matured ($\sim 10\,\mathrm{kyr}$) that the shock already engulfs

molecular clouds and even low energetic CRs already escaped the accelerator, so the escape process cannot be studied in isolation any more.

The γ-Cygni SNR in the heart of the Cygnus region is a prime example for a younger "Sedov-Taylor phase" SNR ($\sim$7 kyr) and for studying a possible escape of CRs. At GeV energies observed by *Fermi* Large Area Telescope observed emission from the entire shell, whereas at TeV energies VERITAS reported concentrated emission from one part of the shell. This discrepancy suggests an ongoing, energy dependent process. This thesis investigates the discrepancy in the GeV to TeV regime in greater detail using deep observations with the MAGIC telescopes and combining them with a re-analysis of *Fermi*-LAT data. By using the aforementioned SkyPrism package to analyse the MAGIC data, this work analyses MAGIC and *Fermi*-LAT data in a consistent way.

This thesis is structured as follows:

Chapter 2 summarises the physics of SNR, how they accelerate CRs, and γ-rays emission from SNRs.

Chapter 3 gives an overview about γ-ray astronomy with a focus on *Fermi*-LAT and the MAGIC telescopes. As the analysis technique in chapter 4 will build up on these information, the technical details and analysis chain of the MAGIC telescopes are presented in greater detail.

Chapter 4 describes the spatial likelihood analysis used for *Fermi*-LAT and its statistical foundations. Based on this the main contribution to the MAGIC data analysis of this work a novel likelihood analysis package for the MAGIC telescopes, SkyPrism, is explained and it is validated against the standard analysis.

Chapter 5 presents the major scientific result of this thesis, the studies of the γ-Cygni SNR with the MAGIC telescopes and the *Fermi*-LAT including a theoretical model explaining the observations in the framework of DSA.

Chapter 6 concludes the thesis with a summary of the most important findings and an outlook how the methods and analysis results can further be improved in the future.

Major parts of this thesis are based on the following publication:

1. Vovk, I., **Strzys, M.**, and Fruck, C. "A spatial likelihood analysis for MAGIC telescope data", 2018, Astronomy and Astrophysics, 619, A7

2. **Strzys, M.**, Morlino, G., Vovk, I., Masuda, S., Celli S., and the MAGIC and *Fermi*-LAT Collaboration[ii] "Study of the GeV to TeV morphology of the γ-Cygni SNR (G78.2+2.1) with MAGIC and *Fermi*-LAT", currently in collaboration internal review

[ii] In the final publication the list of the authors will be in alphabetical order, but main authors will be listed as corresponding authors.

Furthermore, during my PhD I was involved in the study of

1. Fruck, C., Vovk, I., Iwamura, Y., **Strzys, M.** and the MAGIC Collaboration[ii] "MAGIC observations of the diffuse γ-ray emission in the vicinity of the Galactic Centre", submitted to Astronomy & Astrophysics,

which is not a part of this thesis.

Bibliography

Anchordoqui, L. A. 2019, Physics Reports, 801, 1

Beck, R. 2009, Astrophysics and Space Sciences Transactions, 5, 43

De Rújula, A. 2019, Physics Letters B, 790, 444

Hess, V. F. 1912, Physikalische Zeitschrift, 13, 1084–1091

Hörandel, J. R. 2006, Journal of Physics Conference Series, 47, 41

Kachelrieß, M., & Semikoz, D. V. 2019, Progress in Particle and Nuclear Physics, 109, 103710

Perkins, D. H. 2009, Particle astrophysics, 2nd edn., Oxford master series in particle physics, astrophysics, and cosmology (Oxford, UK: Oxford University Press)

Wagner, W. 2004, PhD thesis, Universität Dortmund (now TU Dortmund), Dortmund, Germany

Weekes, T. C. et al. 1989, The Astrophysical Journal, 342, 379

Chapter 2.

Supernova remnants, cosmic ray and gamma rays

Since their discovery, the origin of CRs remains a key scientific question. As mentioned in the introduction, CRs of energies above the ankle are believed to be of extragalactic origin. This assumption is based on the so-called Hillas criterion (Hillas, 1984): requiring that the size of the acceleration region is larger than twice the Larmor radius

$$R_{\mathrm{L}} = \frac{\gamma\, m\, v_{\perp}}{Z\, B} \approx 1.08\,\mathrm{pc}\frac{E}{10^{15}\,\mathrm{eV}}\frac{\mu\mathrm{G}}{Z\, B}\,, \tag{2.1}$$

for a particle with mass m, charge Z, velocity $v_{\perp}$, Lorentz factor γ, and energy E, and accounting for the characteristic velocity of the scattering centres $\beta\, c$, the resulting condition is:

$$L > 2\frac{R_{\mathrm{L}}}{\beta} \quad \Leftrightarrow \quad B\, L > 2\frac{E}{Z\beta} \quad \Rightarrow \quad B_{\mu\mathrm{G}} L_{\mathrm{pc}} > 2\frac{E_{\mathrm{PeV}}}{Z\beta}\,. \tag{2.2}$$

It gives an estimate of the size L and the magnetic field strength B of an astrophysical object necessary to confine particles of charge Z up to an energy E. Figure 2.1 shows the magnetic field strength vs. size for several astrophysical sources and compares it against the Hillas criterion for protons of energies at about the knee (green line) and the high energy end of the CR spectrum (blue line).

On the other hand, it is assumed that CR below the knee originate from within our Galaxy (see Ginzburg V. L., 1974). For example, depending on the exact structure of the Galactic magnetic field, CR with energies below $E < 10^6$ GeV may not be able to enter the Milky Way. A final clear evidence is the detection of a smaller CR density in the Small Magellanic cloud compared to the Galactic one, a finding that contradicts a homogeneous CR density (Abdo et al., 2010). Among the Galactic sources fulfilling the Hillas criterion for protons up to the knee, but not beyond, are the remnants of supernova explosions (SNRs). This results in a cut-off in the CR spectrum from SNRs agreeing with the compositional change mentioned in the introduction.

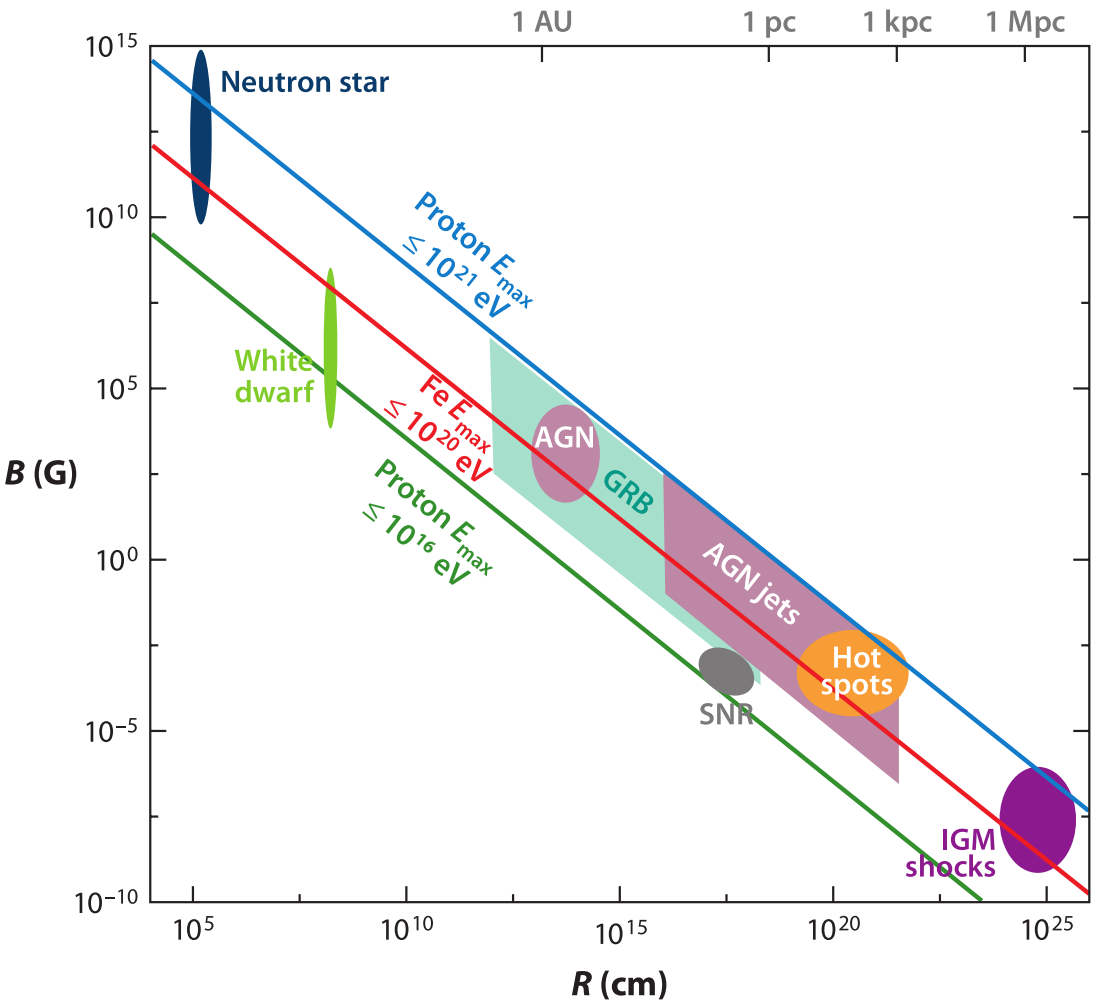

Figure 2.1.: Hillas plot comparing the magnetic field and extension of various source types against the limits needed to accelerate cosmic rays up to a certain energy. Modified plot from Kotera & Olinto (2011).

2.1. The supernova remnant paradigm

As shown in figure 1.1 the spectrum of CRs up to the knee can be described by a pure power-law with spectral index of 2.7. The smoothness suggests that the spectrum is dominated by a single source population emitting CRs with a universal power-law spectrum. One of the prime candidates for the origin of Galactic CRs are SNRs since — in addition to the Hillas criterion — SNRs fulfil several requirements that account for the CR component below the knee. This connection between CRs and SNRs is the so-called SNR paradigm. Without intending to be exhaustive the following list discusses the most important conditions and how SNRs fulfil them:

Energy balance Baade & Zwicky (1934) put forward supernova (SN) explosions as a candidate for the origin of CRs based on an energetic argument. Even though they

assumed an extragalactic origin, the argument can be applied to Galactic SNe. Assuming a rate of Galactic SNe of $R_{\mathrm{SN}} = 1\text{–}3/100\,\mathrm{yr}$, an energy output of $10^{51}\,\mathrm{erg/SN}$, and that 3 % to 30 % of the energy is transferred to CRs, SNRs can account for the energy density of CRs in our Galaxy ($1\,\mathrm{GeV\,cm^{-3}}$). Measurements of the Galactic SN rate support the required rate (Tammann et al., 1994; Diehl et al., 2006).

Spectral index of the CR spectrum So-called nuclear clocks and the ratio of primary CRs[i] to secondary CRs [ii] allow estimating the average amount of matter CRs traversed before reaching Earth. An estimated average grammage of $\lambda \sim 10\,\mathrm{g\,cm^{-2}}$ is large compared to the interstellar density ($\mathrm{nH} \sim 1\,\mathrm{cm^{-3}} = 1.6 \times 10^{-24}\,\mathrm{g\,cm^{-3}}$) suggesting that CRs diffuse for $\tau_{\mathrm{gal}} \sim 10^7\,\mathrm{yr}$ before escaping the Galaxy.[iii] The primary to secondary ratios are energy dependent scaling as $\tau_{\mathrm{gal}} \propto E^{-\delta}$. Thus the diffusion leads to a softening of the CR spectrum and CRs need to be injected with a power-law index of $\alpha = -2.7 + \delta$ with $0.3 < \delta < 0.6$ (see e.g. Strong et al., 2007; Kachelrieß & Semikoz, 2019). The lower limit of 0.3 is predicted if the magnetic turbulences scattering the CR follow a Kolmogorov spectrum, whereas the upper limit is constrained by the level of anisotropy of the Galactic CR flux (Blasi & Amato, 2012b). As it will be shown in the section 2.3.2, the theory of CRs acceleration at the shock fronts of SNRs predicts a power-law spectrum with an index of ~ 2. Thus, considering small deviations (Blasi & Amato, 2012a), the spectrum is in agreement with the CR spectrum.

CR composition In addition to the escape time of CRs from the Galaxy, the element composition of CR provides information about the environment of their production and acceleration sites. Comparisons of the ratios between different elements or with the local element abundance in the solar system suggest that the medium around the acceleration sites needs to be enriched with ejecta material from supernova explosions. The mixture is in good agreement with ratio of ISM swept-up by a SNR in the Sedov-Taylor phase (see 2.2.1) and the ejecta from core-collapse SNe. However, it is not entirely clear whether the ejecta material is produced in the same SN accelerating it. (see Lingenfelter, 2019, for a detailed discussion).

While other Galactic objects such as pulsars (PSRs) (Bednarek & Bartosik, 2004), pulsar wind nebulae (PWNe) (Gallant, 2018), or binary systems (Dubus, 2013) accelerate charged particles to high energies and may contribute to the CR spectrum, the evidence that the bulk of the Galactic CR come from SNR is far more compelling so far.

[i] Composition of CRs as emitted by astrophysical sources

[ii] Elements of low abundance in the solar system such as B and Li only produced via the spallation of primaries

[iii] The relation is $\tau_{\mathrm{gal}} \sim \lambda/(m_{\mathrm{p}}\, n_{\mathrm{H}}\, c_0)$)

2.2. Supernova remnants

A SNR is a complex system following the SN of a massive star. It consists of the blast wave of the explosion, the ejecta material, swept-up interstellar material, and possibly a collapsed compact object, a neutron star or black hole. Hence, SNRs cannot be classified according to the supernova type they resulted from (e.g. core collapse or thermonuclear/Type Ia). Instead SNRs are mainly classified based on the morphology in the radio or X-ray band. The Green's catalogue contains 294 SNRs in our Galaxy, most detected in the radio band (Green, 2014). The morphology and brightness of an SNR provide important information about its nature and overall hydrodynamical evolution. Depending on the emission characteristics in different wavebands, SNRs have traditionally been classified into the following categories:

Shell-type SNRs of the shell-type display a limb-bright radio shell sometimes coinciding with the X-ray emission. The emission originates from electrons in the SNR shock emitting synchrotron emission. The X-ray emission can be non-thermal synchrotron emission as well or be emitted by compressed swept-up gas. The majority of SNRs are of this type.

Filled-centre type Filled-centre SNRs or plerions (from the greek word for full, Weiler & Panagia, 1978) show bright non-thermal emission increasing towards a central engine. As a result of a core-collapse SN, a fast spinning neutron star may form. The strong, spinning magnetic fields create a wind of relativistic electrons/positrons terminating in a shock. The accelerated particles produce a nebula of strong synchrotron emission. Hence, those objects are also called pulsar wind nebulae (PWNe) with the Crab Nebula as prominent example. PWNe can exist inside SNRs, but can also move out of the SNR system or still emit beyond the lifetime of the SNR.

Composite type SNRs of the composite type are shell and centre-bright in non-thermal radio and X-rays. These objects consist of a PWNe inside a still bright SNR shell. These objects are usually rather young objects

Mixed-morphology type In contrast to the other types, the radio and X-ray morphology of this class do not spatially coincide. Such SNRs exhibit a shell-type morphology in the radio band and an X-ray-bright centre (Rho & Petre, 1998). Unlike composite SNRs, the X-ray emission is of thermal origin from shock heated gas and thus these SNRs are also called thermal-composites. Such object are usually older SNRs ($> 10^4$ yr) interacting with dense interstellar material.

2.2.1. Evolution of SNR

Independently of the SN type and the later morphology, the supersonic ejecta of a SN interact with the surrounding medium creating a blast wave with a kinetic energy of $\sim 10^{51}$ erg. As the shock wave of the SNR is expanding, it will sweep up an increasing part of the surrounding medium. This interaction modifies the dynamics of the shock wave and the SNR will undergo different evolutionary stages. The evolution is usually divided into four phases (Woltjer, 1972) displayed in figure 2.2: the free expansion phase, the Sedov-Taylor (ST) phase, the snowplough phase, and finally the merging stage with the ISM.

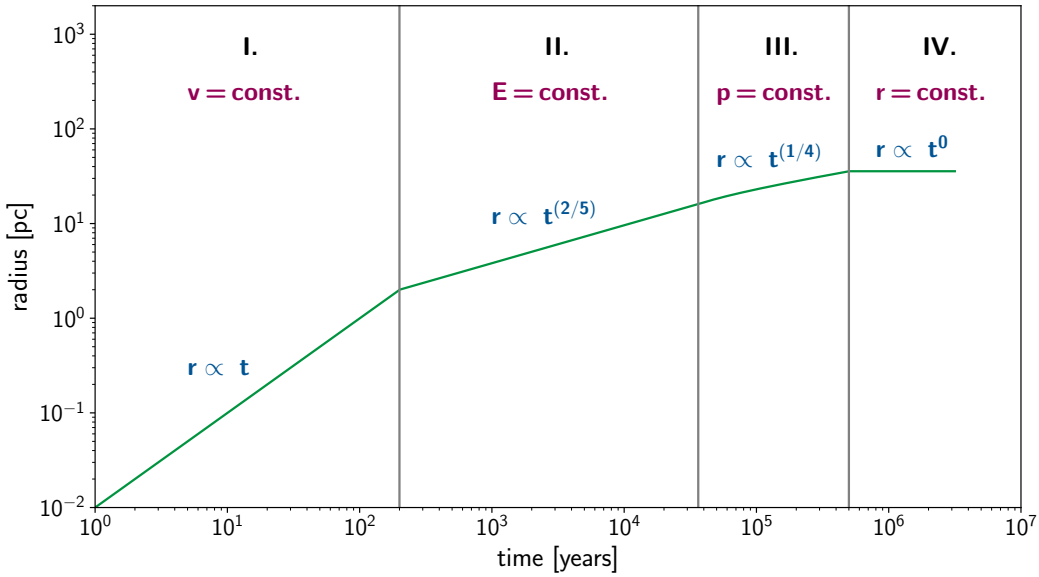

Figure 2.2.: Radius of a supernova remnant plotted against the age for the different evolutionary stages: free expansion (I), Sedov Taylor (II), radiative (III), and dissolving (IV).

I. Free expansion phase In the first phase, the forward shock expands freely at an approximately constant velocity u_0 and sweeps up interstellar material. The mass of the swept-up material is negligible compared to the ejecta and so are the speed losses. The shocked gas is heated up to temperatures, at which the plasma emits thermal X-rays. The radius R of the SNR grows linearly with time:

$$R(t) = u_0 t = \sqrt{E_{\mathrm{SN}}/M_{\mathrm{ej}}}\, t\,, \tag{2.3}$$

where E_{SN} is the kinetic energy and M_{ej} the ejecta mass. The outwards moving shock front accumulates compressed interstellar medium and a so-called contact discontinuity between the ejected stellar material and the shocked ISM forms. Behind the contact

discontinuity a reverse shock forms, which is moving outwards due to the kinetic energy of the ejecta.

II. Sedov-Taylor phase When a major part of the ejecta energy has been transferred to the swept-up material the SNR enters the ST phase. This happens when the swept-up mass is compatible to the ejecta mass:

$$M_{\mathrm{ej}} = \rho_0 \frac{4}{3} \pi R_{\mathrm{Sedov}}^3 \Leftrightarrow R_{\mathrm{Sedov}} = \left(\frac{3}{4} \frac{M_{\mathrm{ej}}}{\pi \rho_0} \right)^{1/3} \approx 2.1\,\mathrm{pc} \left(\frac{M_{\mathrm{ej}}}{M_\odot} \right)^{1/3} \left(\frac{n_1}{\mathrm{cm}^{-3}} \right)^{-1/3} \tag{2.4}$$

corresponding to an age of the system of

$$t_{\mathrm{Sedov}} = \frac{R_{\mathrm{Sedov}}}{u_0} \approx 210\,\mathrm{yr} \left(\frac{E_{\mathrm{SN}}}{10^{51}\,\mathrm{erg}} \right)^{-1/2} \left(\frac{M_{\mathrm{ej}}}{M_\odot} \right)^{5/6} \left(\frac{n_1}{\mathrm{cm}^{-3}} \right)^{-1/3} \tag{2.5}$$

(numerical values from Helder et al., 2012). As long as radiative cooling is negligible, the total energy of the explosion is conserved and the shock wave will expand with time as

$$\begin{aligned} R_{\mathrm{S}}(t) &= \left(\xi_0 \frac{E_{\mathrm{SN}}}{\rho_0} \right)^{1/5} t^{2/5} \\ u_s(t) &= \frac{\mathrm{d}R_{\mathrm{S}}}{\mathrm{d}t} = \frac{2}{5} \left(\xi_0 \frac{E_{\mathrm{SN}}}{\rho_0} \right)^{1/5} t^{-3/5}, \end{aligned} \tag{2.6}$$

where $\xi_0 = 2.026$ for a monoatomic gas with specific heat $\gamma = 5/3$ (Ostriker & McKee, 1988). Due to its energy conserving characteristic, this phase is also called the adiabatic phase. At $\sim t_{\mathrm{Sedov}}$ the deceleration of the ejecta will change the direction of the reverse shock, which starts to travel inwards and heats the ejected stellar material to high temperatures.[iv] For a model describing the transition between the free-expansion and ST phase in a more consistent way and also considering the reverse shock in greater detail please see Truelove & McKee (1999).

III. Snowplough or radiative phase When the temperature of the shocked gas drops below $\approx 10 \times 10^6$ K the electron and ions will recombine and cool the gas via optical line emission. According to Draine & McKee (1993) this happens when the shock speed drops below

$$u_s \lesssim 180\,\mathrm{km\,s^{-1}} \left(\rho_0^2 \frac{E_{\mathrm{SN}}}{10^{51}\,\mathrm{erg}} \right)^{1/14}. \tag{2.7}$$

Sometimes the phase is further divided into a pressure driven snowplough ($R_S \propto t^{2/7}$) and a momentum-conserving snowplough phase ($R_S \propto t^{1/4}$).

[iv] In the following this work will only consider particle acceleration in the forward shock, though the reverse shock can accelerate them as well.

IV. Dissolving In the final phase the speed of the shock becomes sub-sonic and its velocity becomes comparable to the turbulent velocity of the ISM. The SNR merges with its surrounding.

While the stages provide a useful framework for understanding the changes the shock wave undergoes over time, they are rather generic. As shown by the variety of SNR types, the evolution might differ for an individual remnant depending on the magnetic-field, the initial ejecta distribution, and the density profile of the surrounding medium to name but a few. Particularly, the progenitor can shape the initial density and velocity structure of the circumstellar medium (see Truelove & McKee (1999) or for more sophisticated considerations Dwarkadas (2005)). In case of an inhomogeneous surrounding medium, different parts of a SNR shock may even be in different evolutionary phases. Moreover, the hydrodynamics of the shock might be altered by efficient CR acceleration carrying away a significant fraction ($\sim$10%) of the SN energy and modifying the shock structure.

2.3. Cosmic-ray acceleration

To account for the cosmic-ray spectrum measured at Earth, a tentative source needs to provide an acceleration mechanism resulting in a relatively smooth power-law spectrum. Fermi (1949) put forward the idea that CRs scatter randomly on magnetic clouds in the ISM as displayed in Figure 2.3(a). If the particles have a higher velocity than the clouds and head-on collision occur more frequently, the particles gain energy via stochastic scattering leading to a power-law in momentum. However, the fractional energy gain is

$$\left\langle \frac{\Delta E}{E} \right\rangle = \frac{8}{3} \left(\frac{u}{c} \right)^2 \tag{2.8}$$

and only depends on the cloud's speed u in second order. The small gain ($u/c \sim 10^{-4}$) in combination with a large mean free path of particles in the ISM (0.1 pc) makes the acceleration process slow (Longair, 2011). Additionally, this process does not define the exact slope of the power-law spectrum.

2.3.1. Diffusive shock acceleration

Diffusive shock acceleration (DSA) has been proposed by several authors (Axford et al., 1977; Krymskii, 1977; Bell, 1978b; Blandford & Ostriker, 1978) as an efficient mechanism for the acceleration of CRs around shock waves. For a current review see Blasi (2013).

As the density of the ISM is low (1cm^{-3}) and the mean free path is in the order of pc, the shock waves need to be collisonless to efficiently accelerate particles. In

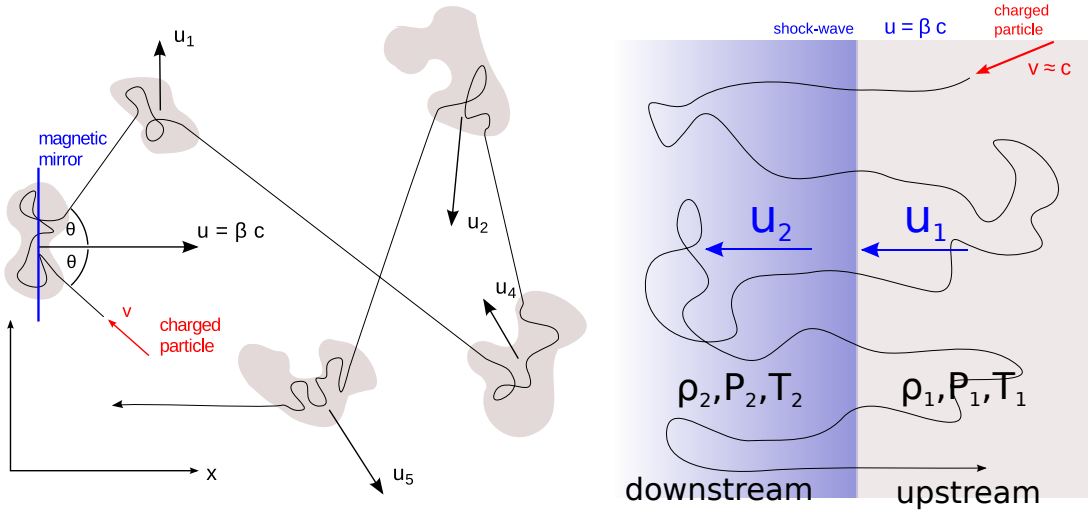

(a) (b)

Figure 2.3.: (a) Sketch displaying the random walk of a particle between magnetic clouds (2nd order Fermi acceleration). **(b)** Scattering of a particle on both sides of a shock (DSA/1st order Fermi acceleration.) Figure adopted from Fruck (2015).

such a shock structure the particles do not interact with each other via Coulomb collisions, but with plasma waves. Still the contact discontinuity of the shock propagating through the ISM obeys the Rankine-Hugoniot conditions (Macquorn Rankine, 1870; Hugoniot, 1887). They describe the conservation of

matter: $p_1 u_1 = p_2 u_2$

momentum: $p_1 + \rho_1 u_1^2 = p_2 + \rho_2 u_2^2$

energy: $\frac{\gamma}{\gamma-1}\frac{p_1}{\rho_1} + \frac{u_1^2}{2} = \frac{\gamma}{\gamma-1}\frac{p_2}{\rho_2} + \frac{u_2^2}{2}$

across the shock. The parameter u is the velocity, ρ the density, and γ the ratio of specific heats. The index 1 indicates the parameters for the upstream (region ahead of the shock) and the index 2 the ones for the downstream (post-shock region) in the frame of the shock. Based on these relations and using the definition of the Mach number $M^2 \equiv (u_1/u_{\text{sound}})^2 = u_1^2 \rho_1 / \gamma\, p_1$, the compression ratio r_{comp} can be defined as

$$r_{\text{comp}} = \frac{\rho_2}{\rho_1} = \frac{(\gamma+1)\, M^2}{(\gamma-1)\, M^2 + 2}\,. \tag{2.9}$$

For strong shocks ($M \gg 1$) passing through a medium consisting of an ideal monoatomic gas (specific heat $\gamma = 5/3$), the compression factor $r = 4$. Based on the jump-conditions, a relation between the post shock temperature T_2 and the shock speed can be derived

$$k_{\text{B}}\, T_2 = \frac{3}{16}\, \mu_2\, m_{\text{p}}\, u_1^2\,. \tag{2.10}$$

For a fully ionised gas of cosmic composition the mean mass per particle $\mu \simeq 0.6$ and for neutral gas of cosmic composition $\mu = 1.4$ (Reynolds, 2008). By using the conservation of matter and the definition of the compression ratio, one can further obtain a connection between the speed of the shock ($u_s = |u_1|$) and the speed of the post-shock bulk velocity $u_{\rm bulk}$:

$$u_{\rm bulk} = \left(1 - \frac{1}{r}\right) u_{\rm s}\,. \tag{2.11}$$

Note, that $u_{\rm bulk}$ is defined in the reference frame where the observer is at rest, whereas u_2 is defined in the reference frame of the shock.

A particle of velocity $v \gg u_{\rm s}$ close to the speed of light c entering the shock from upstream can cross the shock almost freely. It will scatter elastically on magnetic field turbulences on the downstream side. After several scatters, the particle may have changed its direction returning to the upstream. Assuming an efficient scattering on either side of the shock, the velocity distributions of the particles is isotropic in the rest frames of either side. Averaging over all scattering angles, with each round trip through the shock the particle will obtain an average energy gain of

$$\left\langle \frac{\Delta E}{E} \right\rangle = \frac{4}{3}\left(\frac{u_1 - u_2}{c}\right) = \frac{4}{3}\left(\frac{r-1}{r}\right)\frac{u_{\rm s}}{c} \tag{2.12}$$

2.3.2. Particle spectrum from diffusive shock acceleration

The spectrum of particles resulting from DSA can either be obtained with the so-called microscopic approach following Bell (1978b) or by solving the CR transport equation following Axford et al. (1977); Krymskii (1977); Blandford & Ostriker (1978). In its most general form the transport equation consists of the following terms describing the propagation of a particle distribution function f in space (Strong et al., 2007):

$$\begin{aligned} \frac{\partial f(\vec{r},p,t)}{\partial t} - \underbrace{\nabla\left(D_{xx}\,\nabla f\right)}_{①} + \underbrace{\nabla\,\vec{u} f - \frac{\partial}{\partial p}\frac{\nabla\,\vec{u}}{3} p\, f}_{②} - \underbrace{\frac{\partial}{\partial p} p^2 D_{pp} \frac{\partial}{\partial p}\frac{f}{p^2}}_{③} \\ + \underbrace{\frac{\partial}{\partial p}\left[\left(\frac{\mathrm{d}p}{\mathrm{d}t}\right)_{i,\rm ion} f_i\right]}_{④} + \underbrace{\frac{f_i}{\tau_{\rm f}}}_{⑤} + \underbrace{\frac{f_i}{\tau_{\rm r}}}_{⑥} = \underbrace{q(\vec{r},p,t)}_{⑦}\,, \end{aligned} \tag{2.13}$$

① : spatial diffusion, ② : convection (second term are adiabatic momentum losses), ③: stochastic acceleration, ④ : ionisation momentum losses, ⑤ : fragmentation (lifetime $\tau_{\rm f}$), ⑥ : radioactive decay (lifetime $\tau_{\rm r}$), ⑦ : source.

where $f(\vec{r},p,t)$ is the particle density of momentum p at position $\vec{r}$ and time t. D_{xx} is the spatial diffusion coefficient, u the convection velocity, and D_{pp} the diffusion coefficient in momentum space. It can describe the global propagation of CRs in the Galaxy as well as the local propagation at the acceleration side. Since the terms 3 to 6

are irrelevant for the shock acceleration process, they can be set to 0. For a stationary parallel shock (shock normal parallel to magnetic field orientation) the time derivative is 0 as well and in 1D the transport equation gets the form:

$$u\frac{\partial f}{\partial x} - \frac{\partial}{\partial x}D\frac{\partial f}{\partial x} = \frac{1}{3}\frac{\partial u}{\partial x}p\frac{\partial f}{\partial p} + Q \tag{2.14}$$

The equation can be solved for f at the shock position by integrating it over the shock region:

$$f_0(p) \propto K\left(\frac{p}{p_{\mathrm{inj}}}\right)^{-\alpha}, \quad \text{with}\, \alpha = \frac{3r}{r-1}\,, \tag{2.15}$$

where K is specified by the injection term e.g. $K = \alpha(\eta\, n_1)/(4\pi\, p_{\mathrm{inj}}^2)$ for an injection at the shock surface with a discrete injection moment p_{inj} (Blasi, 2013). For strong shocks ($r = 4$) the distribution follows a power-law in momentum with index -4 corresponding to a power-law particle spectrum in energy with index -2 (relation: $N(E)\,\mathrm{d}E = 4\pi\, p^2 f(p)\,\mathrm{d}p$). Solving equation 2.14 for the region upstream, at a distance x from the shock the particle distribution is:

$$f(x,p) = f(0,p)\exp^{-\frac{|x|u_1}{D}}\,, \tag{2.16}$$

whereas downstream the spatial distribution of particles is a constant. This approach is the so-called test particle limit, in which the backreaction of the particles onto the shock is ignored and the injection term is only an arbitrary normalisation term. Still the simplified picture shows that the DSA can generate a CR population following a power-law with index -2 required to explain the spectrum of CRs.

The CRs scatter on magnetic perturbations, so-called Alfvèn waves, with a wave length comparable to the Larmour radius and the diffusion coefficient for a weakly turbulent medium ($\delta B \ll B$) can be written as:

$$D(p) = \frac{1}{3}v\lambda_{\mathrm{m}fp} = \frac{1}{3}\frac{R_{\mathrm{L}}v}{\mathcal{F}} \tag{2.17}$$

$$\text{with} \quad \mathcal{F} = \frac{kP(k)}{B_0^2/8\pi}\,. \tag{2.18}$$

$\lambda_{\mathrm{m}fp}$ is the mean free path of a particle with speed v and R_{L} the corresponding Larmor radius. The factor $\mathcal{F}$ is the energy density of Alfvèn waves per unit logarithmic bandwidth relative to the ambient magnetic energy density i.e. $\mathcal{F}\,\mathrm{d}(\log(p))$ is the energy density in waves resonating with CRs of a momentum between p and $(p + \mathrm{d}p)$ normalised to $U_{\mathrm{M}} = B^2/(8\pi)$. For $\mathcal{F}\sim 1$, D approaches the Bohm limit which is considered to be the smallest diffusion coefficient.

2.3.3. Acceleration time and maximum energy

The spectrum is insensitive to the scattering properties and only depends on the compression ratio. Hence, the test particle approach does not make any statement

about the energy of the particles. In contrast, the acceleration time scale τ_{acc} does depend on the scattering process. Assuming an isotropic particle distribution up- and downstream, the flux of particles crossing the shock surface Σ from downstream to upstream is $nc/4$ (particle density n). The number of particles crossing Σ upstream within one diffusion time equals the number of particles within one diffusion length upstream $l_1 = D_1/u_1$ (based on equation 2.16):

$$\frac{n\,c}{4}\Sigma\tau_{\mathrm{diff},1} = n\Sigma\frac{D_1}{u_1} \;\Leftrightarrow\; \tau_{\mathrm{diff},1} = \frac{4D_1}{c\;u_1}\,. \tag{2.19}$$

The same estimate is valid for the downstream and using $\tau_{\mathrm{cycle}} = \tau_{\mathrm{diff},1} + \tau_{\mathrm{diff},2}$ the acceleration time is:

$$\tau_{\mathrm{acc}} = \frac{\tau_{\mathrm{cycle}}}{\Delta\,E/E} = \frac{3}{u_1 - u_2}\left(\frac{D_1}{u_1} + \frac{D_2}{u_2}\right) \quad\Rightarrow\quad \tau_{\mathrm{acc}} = \kappa\frac{D_1}{u_1^2}\,. \tag{2.20}$$

The last step assumes Bohm diffusion and a strong shock ($r = 4$). The factor κ depends on the type of shock: $\kappa = 8$ for perpendicular shocks and $\kappa = 20$ for parallel shocks.[v] For a more accurate derivation of τ_{acc} see Drury (1983). Equation 2.20 shows that τ_{acc} mainly depends on the diffusion in the region with less scattering (larger D). Since the level of turbulence downstream is at least the level upstream compressed by the shock or might even be amplified by fluid instabilities (Giacalone & Jokipii, 2007), the region of concern is the upstream.

Since the acceleration time cannot exceed the lifetime of the SNR and τ_{acc} further depends on the shock speed, the energy of CR at the shock will be limited and reach a maximum energy. This maximum is supposed to be reached at the end of the free expansion and beginning of the ST phase. In the ST phase the shock speed $u_1 \propto t^{-3/5}$ (formula 2.6) and accordingly the diffusion length upstream grow faster than the SNR radius:

$$l_1 = D_1/u_1 \propto t^{3/5} \;>\; R_{\mathrm{S}} \propto t^{\frac{2}{5}}\,. \tag{2.21}$$

Equating l_1 with R_{S} and using that $D_1 \propto R_{\mathrm{L}} \propto E/B$ leads to a decay of the maximum energy with time:

$$E_{max} \propto R_{\mathrm{S}} u_1 B \propto t^{-1/5}\,. \tag{2.22}$$

CRs with an energy higher than $E_{max}(t)$ will escape the shock region and not participate in the acceleration process any more. Considering a quasi-linear theory and Bohm diffusion, Lagage & Cesarsky (1983) computed a maximum energy of

$$E_{max} \approx 10^{14}\,\mathrm{eV}\,Z\left(\frac{B}{\mu\mathrm{G}}\right)\,, \tag{2.23}$$

with Z being the element number. For an average Galactic magnetic field ($\sim$6 µG, Beck, 2009), E_{max} falls short of reaching the knee by one order of magnitude. Accordingly, stronger magnetic fields, i.e. a higher level of turbulence, are required.

[v] In perpendicular shocks the magnetic field vector is perpendicular to the normal vector of the shock. In parallel shock both vectors are aligned. The standard description of DSA is based on the parallel shocks.

2.3.4. Extensions of the diffusive shock acceleration

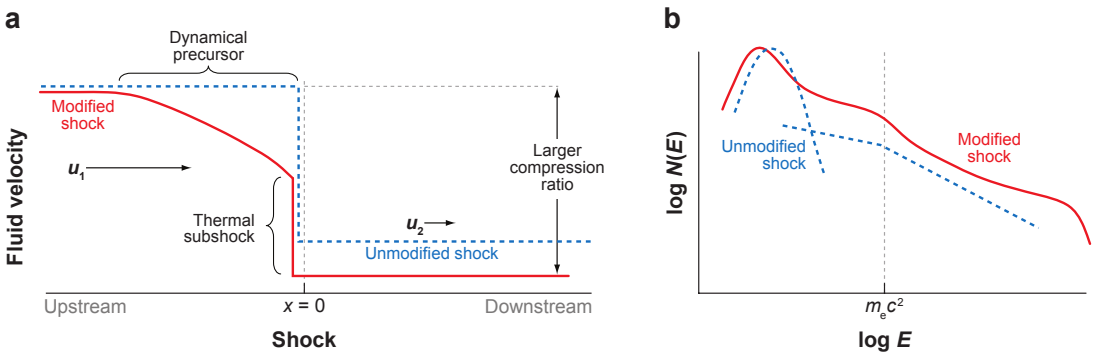

Figure 2.4.: (a) structure of the unmodified shock structure in the linear case and shock structure modified by CR pressure. **(b)** particle spectrum generated by linear diffusive shock acceleration and concave spectrum for the non-linear case. Figure from Reynolds (2008).

As suggested by formula 2.23, the simplified test particle description needs to be extended by considering effects resulting from the interplay of CRs, magnetic waves, and the hydrodynamics of the shock. As the different factors are mutually dependant, the complex interplay cannot be solved analytically but is studied using numerical, or MC based, semi-analytical approaches (see Caprioli et al., 2010, for a comparion). The following outlines the most important aspects of the non-linear diffusive shock acceleration (NLDSA); for a review see Blasi (2013):

Cosmic ray pressure If SNRs are efficient CR accelerators and a non-negligible fraction of energy ($\sim$10%) goes into CRs, CRs ahead of the shock will exert pressure onto the incoming gas upstream and slow it down. This creates an extended precursor ahead of the shock and a sub-shock between the upstream and downstream infinity (figure 2.4a). Since the diffusion coefficient is energy dependent, the CR pressure will depend on the position upstream increasing towards the shock. At the sub-shock, the compression factor $r_{sub} \lesssim 4$ due to its purely gaseous nature. The compression factor of the entire shock system can be $r_{tot} \sim 7$ (CR pressure changes the adiabatic index to $\gamma \sim 4/3$). Accordingly, the particle spectrum will become concave with a softer index (> 2) at lower energies and a harder one (> 2) towards the high energy tail (figure 2.4b). If the spectrum extends to infinity, the system would be destroyed by its own CR pressure. Thus in addition to the simple derivation in formula 2.22, NLDSA implies some kind CR escape mechanism, which makes the shock radiative even in the early stages of the SNR evolution and further increases r_{tot}.

Magnetic field amplification As suggested by formula 2.23 the magnetic field ahead of the shock needs to be amplified to reach knee energies. Another, observational signa-

ture are thin X-ray filaments detected closely behind the shocks of SNRs (Vink, 2012). The size of the synchrotron filament is too small too be explained by the adiabatic expansion behind the shock. Instead it either requires a rapid energy loss of electrons in strong magnetic fields or the disappearance of the magnetic field by damping mechanisms. In the former scenario, a magnetic field strength of 50 µG to 200 µG is needed (Reynolds, 2008). As mentioned before fluid instabilities could explain the filaments but would only amplify the magnetic field downstream and thus not solve the issue of the maximum energy.

If CRs stream faster than the Alfvén speed of the plasma, they excite Alfvén waves of wavelengths close to their gyroradius (Skilling, 1975; Bell, 1978a). This way small perturbations can be amplified by several orders of magnitude. Furthermore, the growth time τ_{growth} is sufficiently fast. However, the level of perturbation δB achievable by the so-called resonant streaming instability is limited to one of the pre-existing, large-scale magnetic field ($\mathcal{F} \lesssim 1$).

A second type of streaming instability is the non-resonant streaming, or Bell instability (Lucek & Bell, 2000; Bell & Lucek, 2001; Bell, 2004). It results from the Ampere force of the current of escaping CRs onto the plasma. For high Mach numbers ($M > 30$) the wave growth is faster than in the resonant case and the level can reach $\mathcal{F} \gg 1$, but the wavelengths are small compared to the Larmor radius. Thus to accelerate CRs, a mechanism transferring power from small to large scales is necessary. Additional nonlinear instabilities that may excite turbulence at larger scales are firehose and acoustic instabilities (Blasi, 2013; Bykov et al., 2013).

Magnetic field pressure Due to the amplification of the magnetic field upstream, the pressure from magnetic waves may become larger than the thermal pressure of the upstream plasma. In this case, the magnetic field reduces the plasma compressibility and thereby the compression factor. The reaction of the magnetic field onto the shock counters the effect of the CR pressure and leads in a less concave spectrum (Caprioli et al., 2009). Furthermore, the compression factor can also be reduced if the pre-shock plasma is heated at the cost of magnetic field strength via damping mechanisms.

Injection The test particle approach does not determine how particles are injected into the shock system. To be efficiently accelerated, particles need to cross the shock surface freely i.e. their Larmor radius needs to be larger than the shock thickness. It is assumed that enough particles in the exponential tail of the Maxwellian distribution (see figure 2.4b) of the thermal downstream gas can have sufficient momentum; a process called thermal injection. Whereas simulation showed that this mechanism may work for ions, the smaller mass of electrons and thereby smaller gyroradius impairs such a mechanism for electrons (for a discussion of problem of electron injection see Malkov & Drury, 2001). Even for ions the simulations suggest that the efficiency of

the ion injection strongly depends on the shock dynamics and the magnetic field orientation with respect to the shock (Völk et al., 2003).

The strength and interplay of these factors is a field of active research. However, simulations showed that — under certain conditions — SNRs might be able to accelerate protons to PeV energies (Bell et al., 2013; Schure & Bell, 2013). Moreover, the studies showed the importance of CR escape for the acceleration process. While the acceleration process is more or less understood, little is known about the escape process. Most of the studies consider the escape of particles upstream by introducing an escape boundary, at which CR of certain momentum can freely escape the SNR system (Drury, 2011). While this is sufficient to study the total CR spectrum released into the Galaxy and for studying effects close to the shock, it neglects a possible self-confinement of CR in the vicinity of the source. Once the CRs escape the shock, they are expected to confine themselves in the vicinity by continuing to generate magnetic waves (Malkov et al., 2013; Nava et al., 2016; D'Angelo et al., 2016). Hence, escaping CRs may provide important insights for the understanding the non-linearity of the CR acceleration process.

2.4. Generation of photons by cosmic rays

As explained in the introduction, CRs can hardly be studied by detecting them on Earth. Instead studying their origin requires tracers such as neutrinos and photons resulting from CRs interacting with the ISM around the emitting source. Since this thesis focusses on γ-ray with energies $E \gtrsim 1\,\mathrm{GeV}$ and their synchrotron counterpart at lower wavelength, this chapter will not discuss γ-rays emission from radioactive decays or particle annihilation.

The processes can be either due to the acceleration of charged particles or particle scattering processes. Figure 2.5 displays the main processes namely: synchrotron radiation, bremsstrahlung, Inverse Compton scattering (IC), and ion-ion collisions. Due to their lower mass electrons will mainly loose energy via the first three, while protons mainly loose energy via the latter.

2.4.1. Interaction of particles with magnetic fields

When charged relativistic particles encounter a magnetic field, they will be accelerated and thus emit electromagnetic radiation, so-called synchrotron radiation (see e.g. Longair, 2011; Funk, 2015). Magnetic fields in SNRs are typically much smaller than the critical limit of $4.4 \times 10^{13}\,\mathrm{G}$ and classical description of the process is valid (Aharonian, 2004). The spectrum of the emitted photons will rise towards higher energies

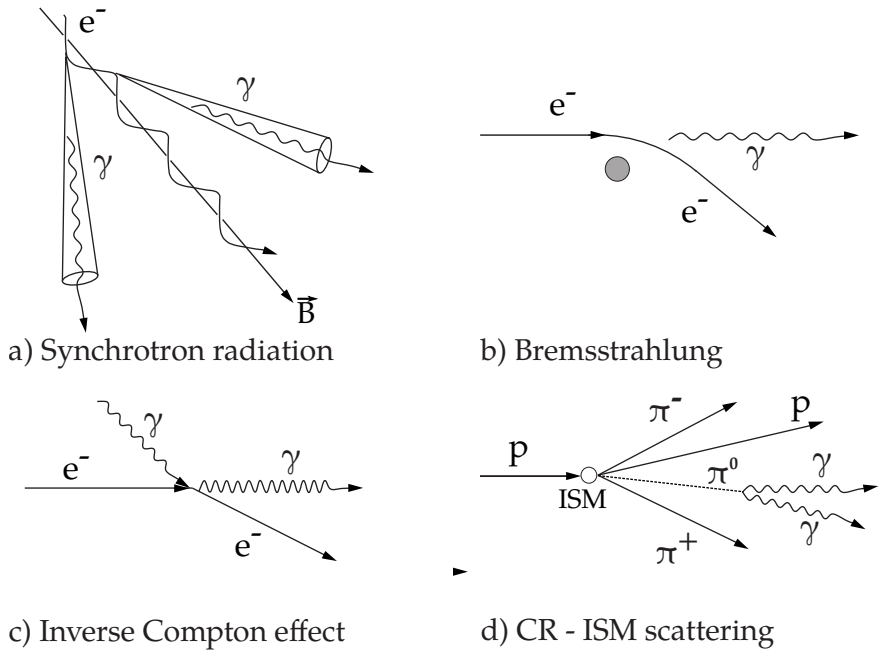

Figure 2.5.: Main non-thermal processes via which CR generate photons. Adopted Figure from Tonello (2005).

and peak at

$$E_{\mathrm{syn,\,peak}} = 0.19\,\mathrm{eV}\left(\frac{B_{\perp}}{\mathrm{nT}}\right)\left(\frac{E_{\mathrm{e}}}{\mathrm{TeV}}\right)^{2}, \tag{2.24}$$

which usually will be in the optical to X-ray band. Beyond a critical energy $E_{\mathrm{c}} = E_{\mathrm{syn,\,peak}}/0.29$ the synchrotron curve sharply falls off. Averaging over all pitch angles, the energy loss rate of the electrons due to synchrotron radiation is

$$\frac{\mathrm{d}E}{\mathrm{d}t} = \frac{4}{3}\sigma_{\mathrm{T}}\,\mathrm{c}\,U_{\mathrm{B}}\,\beta^{2}\,\gamma^{2}\,, \tag{2.25}$$

where σ_{T} is the Thompson cross-section ($8\pi\,r_{\mathrm{e}}^{2}/3 \sim 0.665\,\mathrm{b}$) and U_{B} the energy density of the magnetic field.

2.4.2. Interaction of particles with photon fields

In the presence of a photon field, relativistic electrons loose a fraction of their energy to the photons and up-scatter them to higher energies via the IC effect (see e.g. Longair, 2011; Funk, 2015). The background radiation field predominantly consists of cosmic microwave background (CMB) photons and additionally local infra-red and optical radiation.

The cross-section of this process depends on the product of the photon and electron

energy $\eta = \frac{E_e E_\gamma}{(m_e c^2)^2}$ or in the rest frame of the electron on $\epsilon = \frac{E_\gamma}{m_e c^2}$:

$$\sigma_{IC} = \begin{cases} \sigma_T(1-2\epsilon) \approx \sigma_T & \text{if } \epsilon << 1 \\ \frac{3}{8}\sigma_T \frac{1}{\epsilon}\left(\ln(2\epsilon) + \frac{1}{2}\right) & \text{if } \epsilon >> 1 \end{cases} . \tag{2.26}$$

If the photon's energy is small compared to the electron mass ($\epsilon \gg 1$) the scattering will be elastic and the cross-section approximates the Thompson cross-section. In this regime the average energy of the up-scattered photons is $\frac{4}{3}\eta\ E_e$ or

$$E_{\mathrm{IC,\,peak}} = 5 \times 10^9\,\mathrm{eV} \left(\frac{E_{ph}}{10^{-3}\,\mathrm{eV}}\right)\left(\frac{E_e}{\mathrm{TeV}}\right)^2 . \tag{2.27}$$

The energy loss rate of the relativistic electrons is given by

$$\frac{\mathrm{d}E}{\mathrm{d}t} = \frac{4}{3}\sigma_T\, c\, U_{rad}\, \beta^2\, \gamma^2 . \tag{2.28}$$

With growing photon energy, quantum mechanical effects needs to be considered and for $\eta \gg 1$ the cross-section approximates the lower formula in 2.26. In this so-called Klein-Nishina regime the IC scattering becomes less efficient and the energy transfer to the photon reduces to $\gamma\ m_e$. Accordingly, high energy photons are cooled less efficiently. For a typical CMB photon of 7×10^{-4} eV the Thomson limit is valid up to electron energies of tens of TeV and lower in the presence of strong IR/optical radiation fields.

2.4.3. Interaction of particles with matter

Bremsstrahlung

When electrons enter a medium of high density $\rho = m_p\, n_p$, they decelerate in the electric field of the nuclei and emit photons. The energy loss of an electron is proportional to its energy. The process depends on the target material, which characteristics are summarised in the so-called radiation length X_0. It is the mean distance over which the electron keeps 1/e of its energy:

$$-\frac{1}{\rho}\frac{\mathrm{d}E}{\mathrm{d}x} = \frac{E}{X_0} . \tag{2.29}$$

X_0 is usually given in the unit [g cm^{-2}], called interaction depth: e.g. $X_0(hydrogen) = 63.05\,\mathrm{g\,cm^{-2}}$ and $X_0(air) = 36.62\,\mathrm{g\,cm^{-2}}$ (Patrignani & Particle Data Group, 2016). Accordingly the loss rate can be written as:

$$\frac{\mathrm{d}E}{\mathrm{d}t} = \frac{c\,\rho}{X_0}E \tag{2.30}$$

Pion-decay

Due to their large mass, hadronic CRs produce γ-rays mainly via deep, inelastic scattering on protons of the ambient ISM. With roughly the same probability the main channels of this interaction are:

$$\begin{aligned} \mathrm{p} + \mathrm{p} &\rightarrow \mathrm{p} + \mathrm{p} + \pi^0 \\ \mathrm{p} + \mathrm{p} &\rightarrow \mathrm{p} + \mathrm{n} + \pi^+ \\ \mathrm{p} + \mathrm{p} &\rightarrow \mathrm{p} + \mathrm{p} + \pi^+ + \pi^- \end{aligned}$$

The kinematic threshold for the neutral pion production is 280 MeV. The charged pions primarily decay into neutrinos and muons, what makes neutrino events coinciding with γ-rays a strong indicator for hadronic CR accelerators. The muons further decay into electrons and positrons, which can contribute to the photon emission via the channels mentioned above (see figure 2.6). However, the γ-ray emissivity via the leptonic secondaries is two orders of magnitude lower compared to the hadronic emission. With 98.8 % probability π^0 mesons decay nearly instantaneously ($\tau_{\pi^0} = 8.4 \times 10^{-17}$ s) into 2 γ (Patrignani & Particle Data Group, 2016). For kinematics reasons the energy of the generated γ-rays is at least:

$$E_\gamma^* = \frac{m_\pi \mathrm{c}^2}{2} = 67.5\,\mathrm{MeV}\,. \tag{2.31}$$

Thus, the spectrum of the γ-rays will show a clear cut-off in the MeV range. At energies $E_{\mathrm{kin}} \gtrsim 1$ GeV the cross section for the pp interaction can be approximated as

$$\sigma_{\mathrm{pp}} \sim 30\,\mathrm{mb}\,[0.95 + 0.06 \ln{(E_{\mathrm{kin}}/\mathrm{GeV})}]\,, \tag{2.32}$$

(Aharonian, 2004). Due to the mild energy dependence, the cross section hardly affects the γ-ray spectrum. In general the spectrum of a mono-energetic CR population increases towards a peak at about

$$\langle E_\gamma \rangle \approx 0.1 \langle E_{\mathrm{p}} \rangle \tag{2.33}$$

and sharply falls off beyond (Kelner et al., 2006).

2.4.4. Cooling of relativistic particles

The loss rates of CRs (formulas (2.25) (2.28) (2.30)) can be translated into time periods over which the particle loose a significant fraction of their energy via a certain process, the so-called cooling times $\tau = \frac{E}{\mathrm{d}E/\mathrm{d}t}$. This also allows comparing the relative importance of the production processes depending on the environmental conditions (Aharonian, 2004):

$$\tau_{\mathrm{syn}} = 1.3 \times 10^{10}\,\mathrm{yr} \left(\frac{B}{\mu\mathrm{G}}\right)^{-2} \left(\frac{E}{\mathrm{GeV}}\right)^{-1} \mathrm{yr} \tag{2.34}$$

$$\tau_{\mathrm{IC}} = 3 \times 10^{8}\,\mathrm{yr} \left(\frac{U_{\mathrm{rad}}}{1\,\mathrm{eV\,cm^{-3}}}\right)^{-1} \left(\frac{E}{1\,\mathrm{GeV}}\right)^{-1} \tag{2.35}$$

$$\tau_{\mathrm{br}} = \frac{X_0}{c\, m_{\mathrm{p}}\, n_{\mathrm{p}}} \approx 4 \times 10^{7}\,\mathrm{yr} \left(\frac{n_{\mathrm{p}}}{\mathrm{cm^3}}\right)^{-1} \tag{2.36}$$

$$\tau_{\mathrm{pp}} = \frac{1}{n_{\mathrm{p}}\, \sigma_{\mathrm{pp}}\, c\, f} = 5.3 \times 10^{7}\,\mathrm{yr} \left(\frac{n_{\mathrm{p}}}{\mathrm{cm^3}}\right)^{-1} \tag{2.37}$$

The cooling time of the bremsstrahlung and pp-interaction are based on the mean free path of the particles. The factor $f \sim 0.5$ defines the average fraction lost via inelastic scattering (Aharonian, 2004).

Considering a particle energy of 1 TeV, an average interstellar medium ($n_{\mathrm{p}} = 1\,\mathrm{cm^{-3}}$, $B = 3\,\mu\mathrm{G}$), and the CMB photon field ($U_{\mathrm{rad}} = 0.25\,\mathrm{eV\,cm^{-3}}$), the cooling time for protons via pp-interaction is an order of magnitude longer than for any of the other processes predominantly affecting electrons. For dense molecular clouds with densities of $n > 10^4\,\mathrm{cm^{-3}}$ the situation is reversed.

2.4.5. Model spectra

Based on the shapes of the emission spectra of a single particle, one can estimate the spectral shape of the emission generated by a CR population of certain spectrum. For simplicity the assumed spectrum of the parent CR population is a power-law spectrum. Figure 2.6 shows the spectra of γ-rays generated by a CR populations following a power-law spectrum with spectral index $\alpha_{\mathrm{inj}} = 2$.

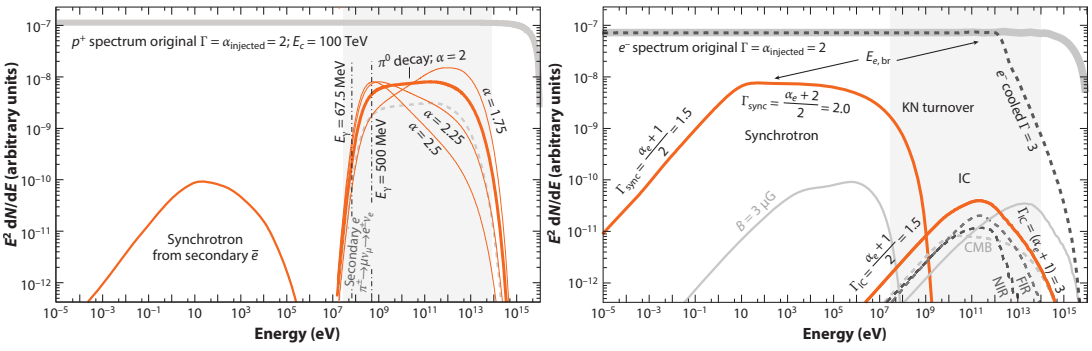

Figure 2.6.: Spectral energy distribution of γ-rays produced by hadronic (left) and leptonic (right) cosmic rays of and injected power-law spectrum with spectral index $\alpha_{\mathrm{inj}} = 2$. Images from Funk (2015).

For the synchrotron emission by electrons it can be assumed that a mono-energetic particle emits only photons at the peak energy of the synchrotron curve (equation

2.24). In this case the photon spectrum of the entire electron population will follow a power-law with index $\alpha = (\alpha_{\rm inj} + 1)/2$. Due to the similarity with the synchrotron process, the spectrum of IC photons is also a power-law with index $\alpha = (\alpha_{\rm inj} + 1)/2$ as long as the Thomson cross-section applies. In the Klein-Nishina regime the spectrum steepens to an index of $\alpha = (\alpha_{\rm inj} + 1)$.

The energy of an γ-ray generated via bremsstrahlung is of the same order as the energy of the incident electron. Thus, the spectral power-law index of the total bremsstrahlung spectrum is the same as the one of the electron population: $\alpha \sim \alpha_{\rm inj}$.

The cross section for the π^0 production only mildly depends on energy of the cosmic-ray. Accordingly, the slope of the generated γ-ray spectrum roughly reflects the one of the proton spectrum: $\alpha \sim \alpha_{\rm inj}$.

From figure 2.6 one can see that e.g. a softer spectrum of protons and a harder spectrum of electrons may results in a very similar spectral slope towards the higher energies. Furthermore, the spectral slope of the photon spectrum from bremsstrahlung and pion decay have the same dependence on the incident particle spectrum. Hence, it is challenging to distinguish between a leptonic or hadronic origin by only observing a small part of the photon spectrum. It takes either regions of extreme conditions (strong B-field or high density) or a multi-wavelength coverage to identify the parent particle population of the photons. Important to note, that even if the emission of a source is dominated by either leptons or hadrons, it does not rule out the acceleration of the other particle type.

Table 2.1.: Summary of the interaction processes of CRs generating γ-ray emission. Table according to De Naurois (2012).

Process	Energy Losses	Particle Energy	Radiated Spectrum
Synchrotron	$\frac{\mathrm{d}E}{\mathrm{d}t} \propto E^2$	$E_\gamma \approx \frac{3eB}{4\pi\, m_e^3 c^4} E_e^2$	$I(E_\gamma) \propto E_\gamma^{-(1+\alpha_{inj})/2}$ up to $\frac{3eB}{4\pi\, m_e^3 c^4} E_{\rm C}^2$
Inverse Compton (Thompson)	$\frac{\mathrm{d}E}{\mathrm{d}t} \propto E^2$	$E_\gamma \approx \frac{E_e^2 E_0}{m_e^2 c^4}$	$I(E_\gamma) \propto E_\gamma^{-(1+\alpha_{inj})/2}$ up to $\gamma_{\rm C}^2 E_0$
Inverse Compton (Klein-Nishina)	$\frac{\mathrm{d}E}{\mathrm{d}t} \propto E^2$	$E_\gamma \approx \frac{E_e^2 E_0}{m_e^2 c^4}$	$I(E_\gamma) \propto E_\gamma^{-(1+\alpha_{inj})}$ up to $\gamma_C m e_e c^2$
Bremsstrahlung	$\frac{\mathrm{d}E}{\mathrm{d}t} \propto E$	$E_\gamma \approx \frac{E_0}{2}$	$I(E_\gamma) \propto E_\gamma^{-\alpha_{inj}}$
Hadronic Interaction	$\frac{\mathrm{d}E}{\mathrm{d}t} \propto E$	$E_\gamma \approx \frac{E_0}{10}$	$I(E_\gamma) \propto E_\gamma^{-\alpha_{inj}}$ above 67.5 MeV

Table 2.1 gives an overview of the processes discussed above. It summarises the

most important dependencies of the energy losses, characteristic photon energies, and photon spectra produced by the different processes.

2.5. Gamma-ray emission from SNRs

Due to the connection between CRs and γ-ray emission, γ-ray observations provide an important tool to test the CR acceleration at the SNR sites at the highest energies. Moreover, while observations of the synchrotron emission at radio and X-ray energies can test the presence of electrons, they cannot prove the presence of hadronic acceleration. Instead hadrons can only be observed when interacting with ISM.

The SNRs detected in γ-rays up to TeV energies can be roughly divided into three classes: young, intermediate, and middle-aged SNRs. Figure 2.7 shows the spectra of several γ-ray bright SNRs.

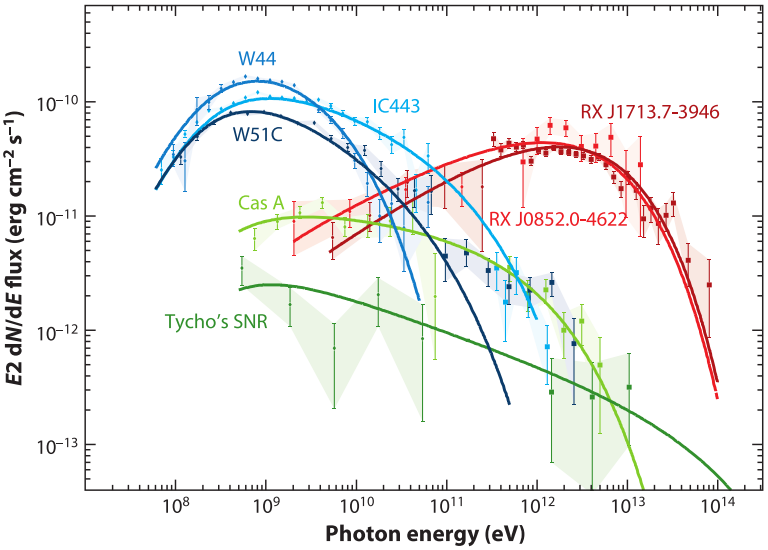

Figure 2.7.: Spectra of several supernova remnants from different populations: young SNRs (green; $< 10^3$ yr), intermediate SNRs (red; $\sim 2 \times 10^3$ yr), and middle-aged SNR know to interact with molecular clouds (blue; $\sim 10^4$ yr). Image from Funk (2015).

Young SNRs , also called historic[vi] SNRs, are usually younger than 10^3 yr. They are supposed to be in the free-expansion or early ST phase and thus to reach the highest energies. Accordingly, their spectra (green, in figure 2.7) are rather hard and can best be described with hadronic emission models (Morlino & Caprioli, 2012; Ahnen et al., 2017). However, since their shocks have not swept up much material their luminosity in γ-rays is rather low. The young SNRs detected so far fall short of accelerating CRs up to PeV at their current stage.

Intermediate SNRs have an age of 1×10^3 yr to 3×10^3 yr. They usually show a bright shell in γ-rays coinciding with X-ray emission. It is unclear whether their emission (red spectra) is dominated by leptons or hadrons. The most prominent

[vi] Meaning that the SN explosion was observed by humans and thus the age is known precisely.

example of this class is RX J1713.7-3946. The lack of thermal X-ray emission in this source suggests a low gas density. Still target material in form of clumps can explain the X-ray and γ-ray emission within a hadronic scenario. Moreover, leptonic scenarios would require an unexpectedly high IR density. (see Funk, 2017, and references therein)

Middle-aged SNRs with ages $t_{\mathrm{SNR}} \gtrsim 10^4$ yr are so evolved that the shock has already encountered a large amount of the ISM and might even have engulfed high-density molecular clouds (MCs, up to $10^3\,\mathrm{cm}^{-3}$). (see Slane et al., 2015, for a review) Due to the large amount of target material, these SNRs are bright at GeV energies and show the remarkable low-energy cut-off confirming a hadronic origin of the emission (Ackermann et al., 2013; Jogler & Funk, 2016). The pion bump detected by *Fermi*-LAT clearly proves the presence of protons in SNRs, but the steep spectra suggest that the acceleration ceased.

Whether these classes suggest an intrinsic trend in the evolution of SNRs or rather connected to environmental effects in each source, is not conclusive yet. Despite the progress in the observation of SNRs in γ-rays, the proof that SNRs are the source of Galactic CR is missing. An unambiguous signature would be unattenuated γ-ray emission extending up to the multi-TeVs possibly accompanied by neutrino emission (Gabici & Aharonian, 2007). Given that SNRs may only accelerate CRs during a short period of their lifetime and that they are rather dim in γ-rays at that stage, the non-detection of a SNR-PeVatron does not yet rule out their possibility of reaching PeV energies (Cristofari et al., 2018). Moreover, the spectra of the individual SNR show rather steep spectra compared to the concave spectra resulting from NLDSA. However, solutions based on the speed of the scattering centres around the shock or the shock geometry have been proposed (see Blasi, 2013, and references therein).

Caprioli (2011) discusses the caveats when confronting NLDSA models with data. The author emphasises the importance of understanding the escape from CR from the accelerator and the time dependence of the maximum energy of CRs at the shock. Particularly, when drawing conclusions from SNRs illuminating MCs, which are attractive observational targets for γ-ray telescopes since the emission is less ambiguous and they allow studying the high-energy run-away CRs even for older SNRs (see e.g. Gabici, 2013, for a review).

A famous example of a SNR illuminating MCs is the middle-aged SNR W28 ($\sim 3 \times 10^4$ yr). Due to the old age of the SNR, all particles already escaped the shock. Hence, studies of the CR propagation in the vicinity of the shell require assumptions about the CR escape process to draw conclusion (Gabici et al., 2010; Hanabata et al., 2014). Interestingly, those studies found that the diffusion coefficient of CR running away from the shell and hitting molecular clouds in the vicinity is smaller than the average galactic one. This suggest that run-away CRs generate their own scattering centres. Other

middle-aged SNR such as IC443, W44, or W51c show maser emission behind the shock pointing at an direct interaction between the shock and the MC (Hewitt et al., 2009). Hence, their evolution is already significantly influenced by the surrounding environment. Either due to the age or the interaction with molecular clouds, most of the CR already escaped the shock of these SNRs and the escape process cannot be studied in isolation any more.

H.E.S.S. Collaboration et al. (2018) reported γ-rays beyond the X-ray emitting shell of the SNR RX J 1713.7-3946, which might either be the signature of the CR precursor consisting of CR diffusing ahead of the shock, but still confined in the shock system or the signature of CR escape. As described above, it could provide interesting insights into the CR escape process. However, the angular resolution of the γ-ray telescope was insufficient to distinguish between both scenarios.

Bibliography

Abdo, A. A. et al. 2010, Astronomy and Astrophysics, 523, A46, 1008.2127

Ackermann, M. et al. 2013, Science, 339, 807

Aharonian, F. A. 2004, Very high energy cosmic gamma radiation : a crucial window on the extreme Universe (World Scientific Publishing Co. Pte. Ltd.)

Ahnen, M. L. et al. 2017, Monthly Notices of the Royal Astronomical Society, 472, 2956

Axford, W. I., Leer, E., & Skadron, G. 1977, in Proc. of the 15th International Cosmic Ray Conference, Plovdiv, Bulgaria, Vol. 11, 132–137

Baade, W., & Zwicky, F. 1934, Proceedings of the National Academy of Science, 20, 259

Beck, R. 2009, Astrophysics and Space Sciences Transactions, 5, 43

Bednarek, W., & Bartosik, M. 2004, Astronomy and Astrophysics, 423, 405

Bell, A. R. 1978a, Monthly Notices of the Royal Astronomical Society, 182, 147

——. 1978b, Monthly Notices of the Royal Astronomical Society, 182, 443

Bell, A. R. 2004, Monthly Notices of the Royal Astronomical Society, 353, 550

Bell, A. R., & Lucek, S. G. 2001, Monthly Notices of the Royal Astronomical Society, 321, 433

Bell, A. R., Schure, K. M., Reville, B., & Giacinti, G. 2013, Monthly Notices of the Royal Astronomical Society, 431, 415

Blandford, R. D., & Ostriker, J. P. 1978, The Astrophysical Journal, 221, L29

Blasi, P. 2013, Astronomy and Astrophysics Review, 21, 70

Blasi, P., & Amato, E. 2012a, Journal of Cosmology and Astroparticle Physics, 2012, 010

——. 2012b, Journal of Cosmology and Astroparticle Physics, 2012, 011

Bykov, A. M., Brandenburg, A., Malkov, M. A., & Osipov, S. M. 2013, Space Science Reviews, 178, 201

Caprioli, D. 2011, Journal of Cosmology and Astroparticle Physics, 2011, 026

Caprioli, D., Blasi, P., Amato, E., & Vietri, M. 2009, Monthly Notices of the Royal Astronomical Society, 395, 895

Caprioli, D., Kang, H., Vladimirov, A. E., & Jones, T. W. 2010, Monthly Notices of the Royal Astronomical Society, 407, 1773

Cristofari, P., Gabici, S., Terrier, R., & Humensky, T. B. 2018, Monthly Notices of the Royal Astronomical Society, 479, 3415

D'Angelo, M., Blasi, P., & Amato, E. 2016, Physical Review D, 94, 083003

De Naurois, M. 2012, Habilitation à diriger des recherches, Université Pierre et Marie Curie - Paris VI

Diehl, R. et al. 2006, Nature, 439, 45

Draine, B. T., & McKee, C. F. 1993, Annual Review of Astronomy and Astrophysics, 31, 373

Drury, L. O. 1983, Reports on Progress in Physics, 46, 973

Drury, L. O. 2011, Monthly Notices of the Royal Astronomical Society, 415, 1807

Dubus, G. 2013, The Astronomy and Astrophysics Review, 21, 64

Dwarkadas, V. V. 2005, The Astrophysical Journal, 630, 892

Fermi, E. 1949, Physical Review, 75, 1169

Fruck, C. 2015, PhD thesis, TU München, Munich, Germany

Funk, S. 2015, Annual Review of Nuclear and Particle Science, 65, 245

——. 2017, High-Energy Gamma Rays from Supernova Remnants (Cham: Springer International Publishing), 1737–1750

Gabici, S. 2013, in Cosmic Rays in Star-Forming Environments, ed. D. F. Torres & O. Reimer, Vol. 34, 221

Gabici, S., & Aharonian, F. A. 2007, The Astrophysical Journal, 665, L131

Gabici, S., Casanova, S., Aharonian, F. A., & Rowell, G. 2010, in SF2A-2010: Proceedings of the Annual meeting of the French Society of Astronomy and Astrophysics, ed. S. Boissier, M. Heydari-Malayeri, R. Samadi, & D. Valls-Gabaud, 313

Gallant, Y. A. 2018, Nuclear and Particle Physics Proceedings, 297-299, 106

Giacalone, J., & Jokipii, J. R. 2007, The Astrophysical Journal, 663, L41

Ginzburg V. L. 1974, Philosophical Transactions of the Royal Society of London. Series A, Mathematical and Physical Sciences, 277, 463

Green, D. A. 2014, Bulletin of the Astronomical Society of India, 42, 47

Hanabata, Y. et al. 2014, The Astrophysical Journal, 786, 145

Helder, E. A., Vink, J., Bykov, A. M., Ohira, Y., Raymond, J. C., & Terrier, R. 2012, Space Science Reviews, 173, 369

H.E.S.S. Collaboration et al. 2018, Astronomy and Astrophysics, 612, A6

Hewitt, J. W., Yusef-Zadeh, F., & Wardle, M. 2009, The Astrophysical Journal, 706, L270

Hillas, A. M. 1984, Annual Review of Astronomy and Astrophysics, 22, 425

Hugoniot, H. 1887, Journal de l'École Polytechnique, 58, 1

Jogler, T., & Funk, S. 2016, The Astrophysical Journal, 816, 100

Kachelrieß, M., & Semikoz, D. V. 2019, Progress in Particle and Nuclear Physics, 109, 103710

Kelner, S. R., Aharonian, F. A., & Bugayov, V. V. 2006, Physical Review D, 74, 034018

Kotera, K., & Olinto, A. V. 2011, Annual Review of Astronomy and Astrophysics, 49, 119

Krymskii, G. F. 1977, Akademiia Nauk SSSR Doklady, 234, 1306

Lagage, P. O., & Cesarsky, C. J. 1983, Astronomy and Astrophysics, 125, 249

Lingenfelter, R. E. 2019, The Astrophysical Journal Supplement Series, 245, 30

Longair, M. S. 2011, High Energy Astrophysics, 3rd edn. (Cambridge University Press)

Lucek, S. G., & Bell, A. R. 2000, Monthly Notices of the Royal Astronomical Society, 314, 65

Macquorn Rankine, W. J. 1870, Philosophical Transactions of the Royal Society of London Series I, 160, 277

Malkov, M. A., Diamond, P. H., Sagdeev, R. Z., Aharonian, F. A., & Moskalenko, I. V. 2013, The Astrophysical Journal, 768, 73

Malkov, M. A., & Drury, L. O. 2001, Reports on Progress in Physics, 64, 429

Morlino, G., & Caprioli, D. 2012, Astronomy and Astrophysics, 538, A81

Nava, L., Gabici, S., Marcowith, A., Morlino, G., & Ptuskin, V. S. 2016, Monthly Notices of the Royal Astronomical Society, 461, 3552

Ostriker, J. P., & McKee, C. F. 1988, Reviews of Modern Physics, 60, 1

Patrignani, C., & Particle Data Group. 2016, Chinese Physics C, 40, 100001

Reynolds, S. P. 2008, Annual Review of Astronomy and Astrophysics, 46, 89

Rho, J., & Petre, R. 1998, The Astrophysical Journal Letters, 503, L167

Schure, K. M., & Bell, A. R. 2013, Monthly Notices of the Royal Astronomical Society, 435, 1174

Skilling, J. 1975, Monthly Notices of the Royal Astronomical Society, 173, 245

Slane, P., Bykov, A., Ellison, D. C., Dubner, G., & Castro, D. 2015, Space Science Reviews, 188, 187

Strong, A. W., Moskalenko, I. V., & Ptuskin, V. S. 2007, Annual Review of Nuclear and Particle Science, 57, 285

Tammann, G. A., Loeffler, W., & Schroeder, A. 1994, The Astrophysical Journal Supplement Series, 92, 487

Tonello, N. 2005, PhD thesis, TU München, Munich, Germany

Truelove, J. K., & McKee, C. F. 1999, The Astrophysical Journal Supplement Series, 120, 299

Vink, J. 2012, The Astronomy and Astrophysics Review, 20, 49, 1112.0576

Völk, H. J., Berezhko, E. G., & Ksenofontov, L. T. 2003, Astronomy and Astrophysics, 409, 563, astro-ph/0306016

Weiler, K. W., & Panagia, N. 1978, Astronomy and Astrophysics, 70, 419

Woltjer, L. 1972, Annual Review of Astronomy and Astrophysics, 10, 129

Chapter 3.

Gamma-ray astronomy

3.1. Opaqueness of the atmosphere

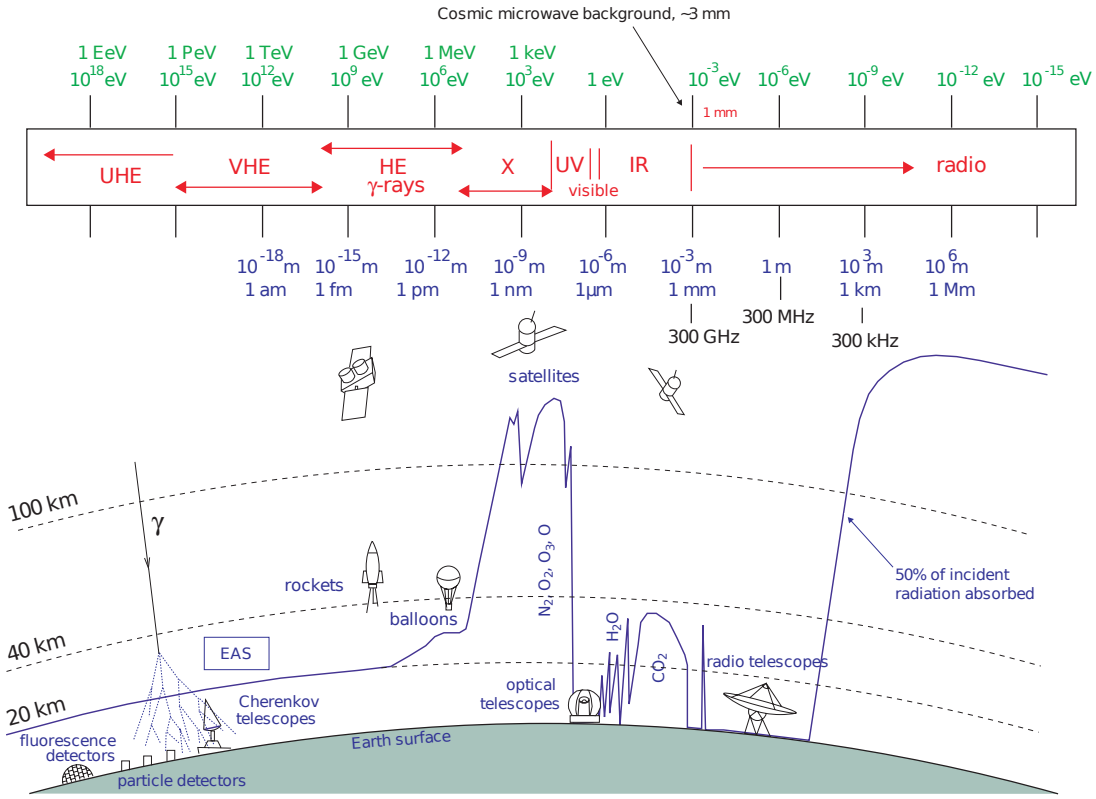

Figure 3.1.: Atmospheric transmission for photons of different wavelengths. Figure from Wagner (2006).

The transparency of the Earth's atmosphere changes over the electromagnetic spectrum as depicted in figure 3.1. The optical (ca. 1.5 eV to 3.43 eV) and radio band (ca. 6.20×10^{-8} eV to 1.24×10^{-3} eV) are the only ones that allow absorption-free observations from the ground, sometimes called observational windows. All other bands require space-based detectors to avoid the significant absorption of the atmosphere. In most bands the opaqueness is due to molecular or atomic absorption lines. At gamma-

ray energies (>200 keV) the direct detection is impaired by interactions of the γ-rays with nuclei in the upper atmosphere. The particle interaction initiates a cascade of secondary particles, a so-called extensive air shower (EAS). As γ-rays cannot traverse the atmosphere, one can only detect them from space or indirectly by their cascades.

3.2. Electromagnetic cascades

Photons interact with matter via three major mechanisms: the photo-electric effect, the Compton-effect and the pair production process. As the cross-section of the processes are energy dependent, each process dominates in a different energy range. At the highest energies ($E_\gamma \gtrsim 20\,\mathrm{MeV}$) the pair production process is dominant over the others (at least one order of magnitude larger cross-section). A γ-ray interacting with the Coulomb field of a nucleus of the target material produces an electron-positron pair. These secondaries, if energetic enough, in turn generate γ-rays via bremsstrahlung. This cycle undergoes as many iterations until the initial energy is distributed over so many particles that each is not energetic enough to further create secondaries. The electromagnetic cascade diminishes out since the secondary charged particles suffer ionisation losses and the γ-rays get absorbed via the Compton process.

The medium dependent parameter of the bremsstrahlung losses of an electron can be comprised in one characteristic distance scale, the radiation length X_0, which is the distance over which the electron keeps $1/e$ of its energy (see equation 2.29). In addition, electrons lose energy via ionisation scaling logarithmically with energy. As the bremsstrahlung losses scale linearly with energy, one can define a critical energy E_c, at which the ionisation losses over one radiation length equal the bremsstrahlung losses. Like the radiation length, this value is characteristic of the target medium and defines the energy per particle, at which the radiation losses prevent the particle cascade from growing. The point where the cascade reaches the maximal size (the largest number of secondaries) is called the shower maximum.

To produce an electron-positron pair, a photon needs to exceed an energy of $E_\gamma > 2\,m_e\,{c_0}^2 \approx 1.022\,\mathrm{MeV}$. The cross-section of this process increases with energy until it saturates above $\approx 1\,\mathrm{GeV}$ and the mean free path becomes $X_p \approx 9/7\,X_0$. Additional processes in electromagnetic cascades such as the photo production of mesons ($\approx 1.5\,\mathrm{mb}$) and the pair production of muons ($\approx 12\,\mu\mathrm{b}$) can be neglected compared to electron-positron pair production ($\approx 520\,\mathrm{mb}$).

Due to the similar cross-section and the quantum mechanical nature of the bremsstrahlung and electron pair production process, a simple model of an electromagnetic cascade, the so-called Heitler model (Heitler, 1936), can be constructed. It assumes that

- $X_p = X_0$

- after a splitting length of $d = X_0 \ln(2)$ an electron/positron generates a γ-ray via bremsstrahlung and a γ-ray produces an electron-positron pair
- the energy of the original particle of each process is shared equally among the particles of the final state
- the cascade reaches the maximum, when the energy per particle equals E_c

Even though the model overestimates the number of electrons/positrons and underestimates the depth of the shower maximum (Matthews, 2005; Hörandel, 2007), it correctly explains the two major characteristics of electromagnetic cascades:

- the number of secondaries in the cascade is proportional to the energy of the primary particle E_0
- the depth of the shower maximum $X_{max} \propto \ln(E_0/E_c)$

Electromagnetic cascades will undergo the same processes regardless if they are initiated by γ-rays or electrons/positrons. As the electron/positron initiated cascade begins with bremsstrahlung interaction, it starts at a higher altitude compared to the first γ-ray interaction and reaches its shower maximum at smaller depths. The differences was experimentally found to be $\approx$ 1 radiation length.

Because of the high energy of the primary, the direction of the secondaries is usually strongly beamed into the forward direction, so that the showers are longitudinally elongated but have little lateral spread. The transversal extension of electromagnetic cascades mainly results from multiple Coloumb scattering of electrons on atmospheric nuclei.

Hadronic primaries can initiate cascades as well adding to the background from electrons. As satellite experiments can effectively veto the background from charged particles, the hadronic air showers will be discussed for ground-based telescopes in section 3.4.1, where they become an important background component.

3.3. Space-based γ-ray astronomy and the *Fermi*-LAT

At lower γ-ray energies the number of photons is usually high enough that a small-sized detector ($\approx$ m^2) can collect a sufficient number of photon counts, so the detector can be carried on board of a satellite. The detector is usually a pair-conversion telescope, where the particle cascade develops inside the target material of the detector. In contrast to ground-based telescopes, the space-based γ-ray approach allows an accurate calibration of the detector before launch into space and the possibility to discriminate background of charged cosmic rays by a veto system. Such detectors are thus nearly background free. In addition they combine a decent angular and energy resolution with a large field of view (FoV).

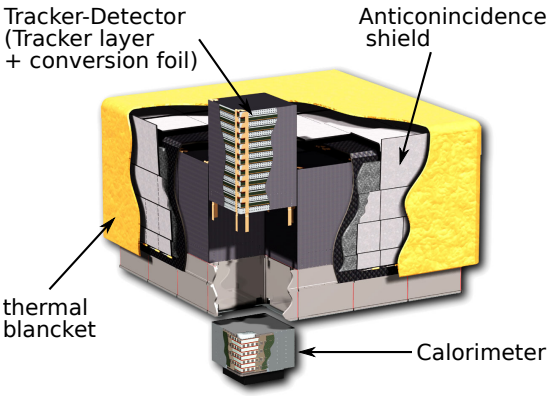

Figure 3.2.: Schematic drawing of the LAT and its components onboard the *Fermi* satellite. Adapted image from the Fermi Gamma-ray Space Telescope webpage at SLAC: `http://fgst.slac.stanford.edu/WhatIsLAT.asp` (Accessed: 2018-08-10).

In the recent years the Large Area Telescope (LAT) has successfully applied this approach. It is the main scientific instrument on board the *Fermi* satellite (Atwood et al., 2009). The satellite was launched into a low-altitude orbit in June 2008 and is still in full operation today. Alongside the LAT, *Fermi* carries the Gamma-ray Burst Monitor (GBM) designed to search for gamma-ray bursts in a wide field of view of 9.5 sr and a broad energy range from several keV to MeV (Meegan et al., 2009).

The *Fermi*-LAT observes the γ-ray sky at higher energies in the rage from 20 MeV to 500 MeV using the pair-conversion technique. A schematics of the detector layout is shown in figure 3.2. It consists of three components: the anti-coincidence scintillator detector (Moiseev et al., 2007), the converter-tracker system (Atwood et al., 2007), and the calorimeter (Johnson et al., 2001).

The outermost system directly beneath a thermal blanket, providing insulation and protection against space debris, is the anti-coincidence shield. It is a veto system against the charged cosmic ray background and consists of 89 segmented plastic scintillator tiles covering the top and four sides of the LAT. The gaps between the tiles are covered by 8 plastic ribbons. It can identify CR entering the detector with an efficiency of 0.9997. The segments and thereby spatial information allows distinguishing cosmic-ray primaries entering from secondaries leaving the detector.

The converter-tracker system (1.7 m $\times$ 1.7 m) is arranged in 4 $\times$ 4 so-called towers carrying a stack of 19 trays of 0.72 m length. Between the 19 trays 18 paired silicon strip detector layers are situated, of which the first 16 layers are covered with a conversion foil of high Z-material (tungsten). The conversion plates provide the target material for the primary γ-ray to convert into an electron-positron pair. The silicon tracker records the passage of the charged secondaries, from which the arrival direction of the initial γ-ray can be reconstructed. The first 12 tracker layers are covered with a thinner conversion foil (0.03 radiation lengths) to reduce the chance for multiple Coulomb scattering, while the last 4 layers have a thicker layer (0.18 X_0) providing a larger effective area. Accordingly events are classified as 'front' or 'back' events.

At the bottom of the LAT underneath the converter-tracker system, each tower carries a calorimeter module consisting of 8 layers of 12 CsI(Tl) crystals. Since it is

a hodoscopic system, it measures the energy deposit of the electromagnetic shower and images the cascade in 3D. The energy deposition and the spatial shower profile allows the estimation of the primary photon energy, a further discrimination of cosmic ray induced showers, and an estimation of the energy leakage. The calorimeter layers correspond to 8.6 radiation lengths summing up to 10.1 X_0 for the whole LAT detector. Hence, the calorimeter can contain showers up to TeV energies.

The Data Acquisition System (DAQ) collects the data, applies the trigger criteria and performs the pre-processing of the data. The minimal deadtime of the readout per event is 26.50 µs.

3.3.1. The *Fermi*-LAT performance

The *Fermi*-LAT has a wide FoV of > 2.4 sr, however, the performance of the instrument depends on the direction and energy of the incoming event. The instrument performance is characterised by the instrument response functions (IRFs), which describe how the instrument influences the measurement. It can be factorised into three items:

Effective area The effective area $\mathcal{A}_{\text{eff}}$ of a telescope corresponds to the size of an ideal detector (with a 100% detection efficiency) recording the same number of events as the real instrument. Accordingly, it is the product of the nominal detector size and the detector efficiency. It depends on the energy E and the incident direction p of an event.

Point spread function The PSF $\mathcal{P}$ is the probability density function to reconstruct an event of energy E, incident direction p, and event class s at the arrival direction p'. It describes the spread or blurring of a point source due to the imaging system.

Energy dispersion The energy dispersion $\mathcal{D}$ is the probability density function to reconstruct an energy E' for an event of energy E and incident direction p. It causes a migration of events between the energy bins in a spectrum.

The IRFs are determined by the technical design of the detector, by the event reconstruction algorithm, and the event quality selection. While the hardware is fixed, improvements of the event reconstruction are classified in data releases, so-called "Passes" . After the releases of each update of the analysis, the *Fermi*-LAT collaboration reprocessed all data accordingly. All LAT data in this thesis use the latest, so-called Pass8 data version (Atwood et al., 2012), which is the first major revision of the reconstruction since launch and supposed to bring the *Fermi*-LAT close to its full scientific potential.

Except for the selection of the release version, the event reconstruction cannot be influenced during the analysis process. However, the events are grouped in event

classes and event types[i]. The event class defines the strictness of the selection criteria for an event to be classified as a γ-ray. For transient events usually a higher background from cosmic rays is tolerated, while studies of the diffuse emission usually use tighter criteria. As the number of background events differ, each event class comes with their own IRFs and simulation of the galactic and extragalactic γ-ray background. To balance the event statistics and cleanness of the data sample this thesis will use the "SOURCE" class as recommended for galactic sources by the *Fermi*-LAT Collaboration.

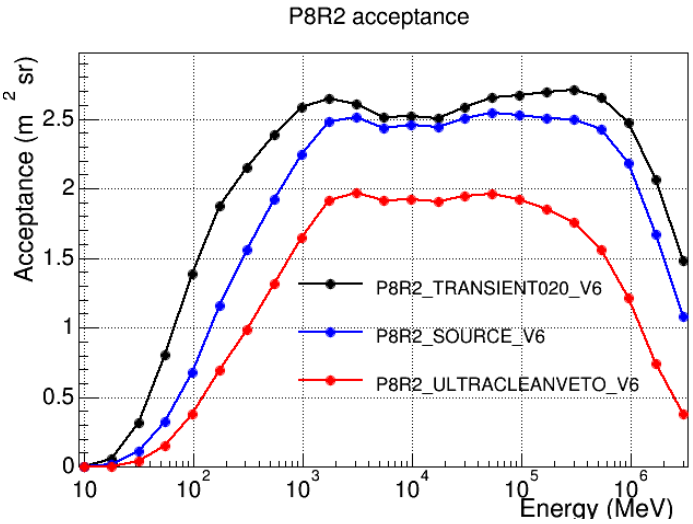

Figure 3.3.: Acceptances of the *Fermi*-LAT depending on the event classes and the energy. Images from (Wood et al., 2016)

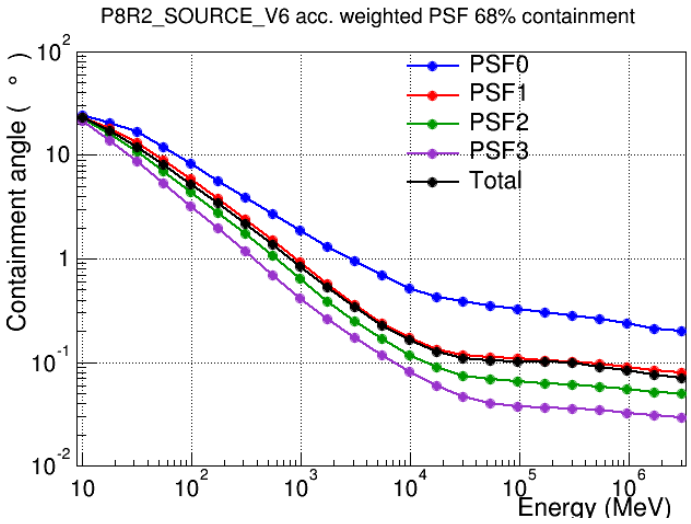

Figure 3.4.: Point spread function of the *Fermi*-LAT event type PSF classes shown by its 68 % containment radius depending on the energy. Images from (Wood et al., 2016).

The event types group events based on the accuracy of the reconstruction and thus are a subdivision of an event class. The quality is mainly governed by the place of the first interaction of an incident event in the detector. The lower conversion layers are thicker, which increases the chances for multiple scattering of the first electron/positron before their track gets recorded, worsening the reconstruction of the

[i] https://fermi.gsfc.nasa.gov/ssc/data/analysis/documentation/Cicerone/Cicerone_Data/LAT_DP.html

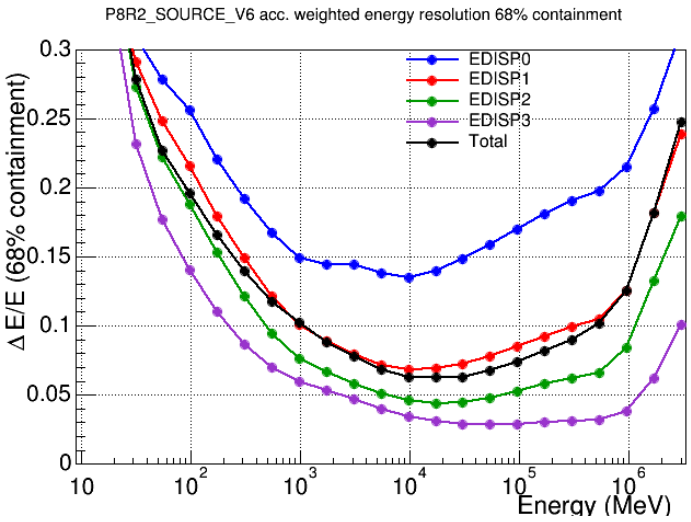

Figure 3.5.: Energy resolution of the *Fermi*-LAT event type energy dispersion classes shown depending on the energy. Images from (Wood et al., 2016).

incident direction of the γ-ray. These events are so-called back (conversion) events in contrast to the front events that interacted in one of the upper, thinner conversion layers. The concept of event classes in Pass 8 got expanded from the front/back event classes to PSF and energy-precision classes, where the events are grouped in quantiles with group 3 containing the most precisely reconstructed events to 0 for the lowest quality quantile. The event-type classes further define the IRFs of the corresponding category to be used in the analysis. Figure 3.4 shows the extent of the 68 % containment radius of the PSF versus the energy for the different event classes as well as the PSF when all PSF are joined in a single analysis. However, for this work the four subclasses of the PSF $\mathcal{P}$ are used separately, but later are used together in a combined likelihood analysis. This way the analysis considers the better reconstruction in the higher quality classes and at the same time avoids a loss of events.

3.3.2. Systematic uncertainties

The uncertainty in the accuracy of the diffuse background and the knowledge of the IRFs can introduce systematic discrepancies between the data and the model based prediction. The uncertainties can be quantified by comparing Monte-Carlo simulations against data, performing calibration measurements on bright sources, or deriving them from the data via nuisance parameters. As calibration sources the *Fermi*-LAT Collaboration used sources such as Vela, AGNs, and the Earth limb.

Figure 3.6 displays the systematic uncertainty of the effective area and PSF plotted against the energy in terms of the minimum and maximum deviation of $\mathcal{P}$ and $\mathcal{A}_{\text{eff}}$ from the nominal value. It shows that the that systematics effects get stronger towards the lower and upper energy thresholds of the *Fermi*-LAT detector. Including data outside the shown ranges ($< 30\,\text{MeV}$ and $> 1\,\text{TeV}$) is discouraged by the *Fermi*-LAT Collaboration. The deviation further depends on the event selection criteria. When using the energy dispersion and different event types in a joint likelihood

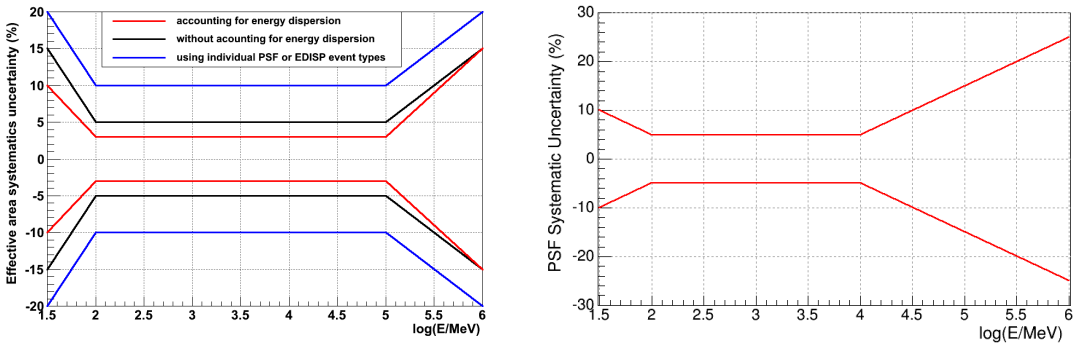

(a) (b)

Figure 3.6.: (a) Systematics of the *Fermi*-LAT for different analysis class and event type considerations. (b) Point spread function of the *Fermi*-LAT event type PSF classes shown by its 68 % containment radius depending on the energy. Both images are from Wood et al. (2016).

analysis the systematic uncertainties can be reduced as indicated by the red and black line in figure 3.6 (a). The systematic uncertainty of the energy dispersion plays a minor role at energies above $E > 1\,\mathrm{GeV}$ compared to ones of $\mathcal{P}$ and $\mathcal{A}_{\mathrm{eff}}$ and was estimated to be $< 5\%$.

In contrast to the uncertainties resulting from the IRFs, the effect of the interstellar emission model (IEM) cannot be generally quantified but can only be assessed by analysing a data set using different IEMs. In chapter 5 the same models as in Acero et al. (2016) are going to be used, but for the P8R2 data release instead of P7V6. The models are based on physical simulations adjusted to the *Fermi*-LAT data and differ in the parameter set used for the simulations such as CR source distribution, the height of the CR propagation halo, and the HI spin temperature.

3.4. Imaging Air Cherenkov telescopes

Most galactic sources have differential power law indices between 2 and 3 and extra-galactic sources have even softer spectra due to the absorption by the extragalactic background light. Hence, towards higher energies the flux of cosmic rays and thereby the number of photons decreases rapidly. To still detect a sufficient number of events the detector area needs to increase accordingly. In addition the shower length increases as shown section 3.2 and larger detector depth is required to still confine the shower inside the detector. Hence, satellite experiments like the *Fermi*-LAT cannot observe energies beyond $\gtrsim 100\,\mathrm{GeV}$ effectively. Since the possible payload of space missions is limited, showers need to be observed from ground and the atmosphere becomes part of the detector. From a particle physics point of view, the air is becoming the

calorimeter volume.

3.4.1. Air showers

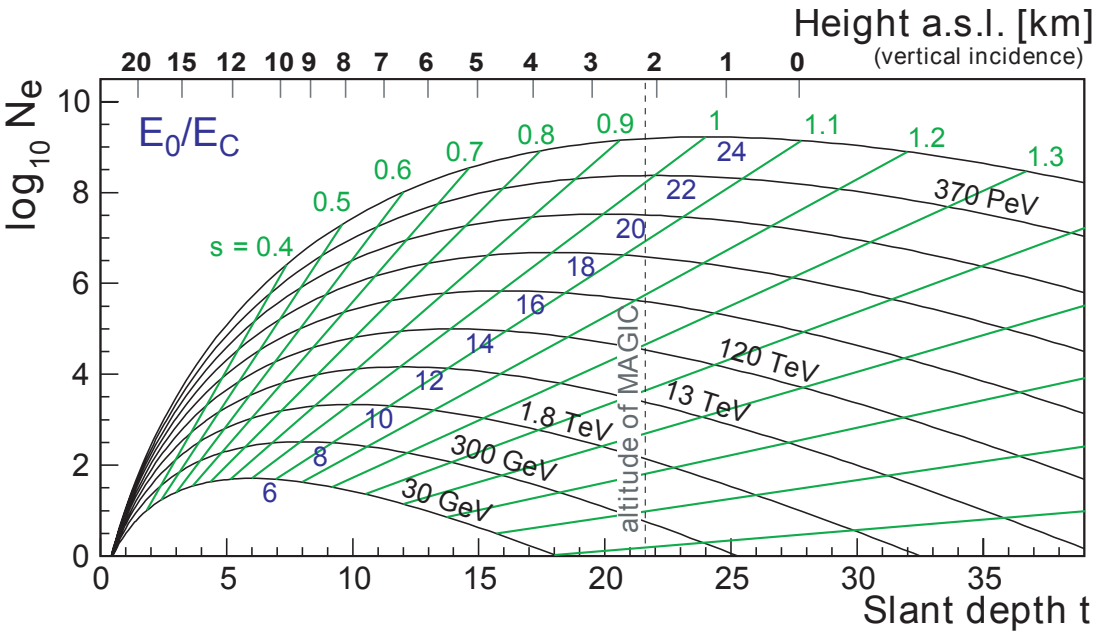

Figure 3.7.: Longitudinal development of electromagnetic air showers of different primary energies. The size of the shower is plotted against the radiations lengths in air (here t). The vertical line indicates the altitude of the MAGIC telescopes. Image from Wagner (2006).

A particle cascade initiated in the upper layers of the atmosphere is called an air shower. The radiation length of air is $X_0 \approx 36.62\,\mathrm{g\,cm^{-2}}$ (Patrignani & Particle Data Group, 2016). Accordingly, γ-rays have their first interaction with an atmospheric nucleus at about $47\,\mathrm{g\,cm^{-2}}$ corresponding to an altitude of 20 km to 30 km. The critical energy in air is $E_c^{air} \approx 83\,\mathrm{MeV}$. Figure 3.7 shows the development of showers depending on the primary's energy. Showers from Zenith in the energy range $0.1 - 10\,\mathrm{TeV}$ usually reach their maximum at $\approx 8\,\mathrm{km}$. When a shower enters the atmosphere at a Zenith angle $\theta > 0°$, the total depth of the atmosphere increases. Accordingly the shower develops and reaches the shower maximum farther away from the observer. Assuming a flat atmosphere in first order approximation the distance is expected to scale with $\sim \cos^{-1}(\theta)$.

In addition to γ-rays, air showers can be initiated by charged cosmic rays as displayed in figure 3.8. The primaries can either be electrons or positrons that, like γ-ray, introduce pure electromagnetic cascades or hadronic particles, mainly protons. Additionally to an electromagnetic component, hadronic air showers have a muonic and hadronic component. The electromagnetic component results from the production of π^0, while $\pi^\pm$ lead to the muonic component. The hadronic component usually

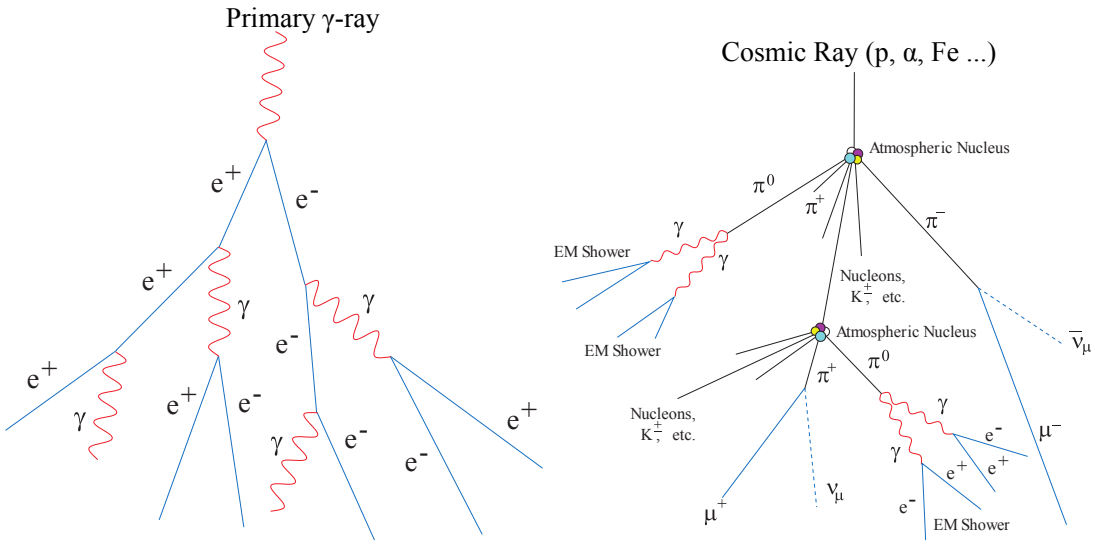

Figure 3.8.: Sketch of an electromagnetic (left) and hadronic (right) air shower. Figure from Wagner (2006).

produces protons and kaons (which via decay can add to the muon component). As just 10 % of the primary energy goes into protons and kaons, pions constitute the largest component by far. The energy share among the three pion types is about equal. Whereas neutral pions decay nearly instantaneously into 2 γ, charged pions have a larger lifetime ($\tau_{\pi^{-,+}} = 2.6 \times 10^{-8}$ s; Patrignani & Particle Data Group, 2016) allowing them to reach ground if their energy exceeds 3 GeV.

The large traverse momentum of hadronic interactions can spread the lateral size of the air shower considerably and make it less symmetric with respect to the shower axis (see Grieder, 2010, and references therein).

3.4.2. Cherenkov light in air showers

As shown in figure 3.7, a primary particle needs be of energy $E_0 \gtrsim$ TeV that a sufficient number of secondaries can pass the 22 radiation lengths to reach ground at 2200 m altitude. Nonetheless, also air shower of lower energy can be detected from ground via the Cherenkov radiation generated by the charged secondaries.

Cherenkov effect

In dielectric media, the charge of the particle induces a dipole field in the vicinity. As the charge of relativistic speed $\beta = v/c$ passes, the dipole field relaxes by emitting electromagnetic radiation. As long as the particle's speed is lower than the local phase velocity of electromagnetic waves, defined by the refractive index of the medium n, the emission interferes destructively along the particle's track. If the speed, however, exceeds this boundary, the emitted waves can interfere coherently, generating so-called

Cherenkov light named after the Russian physicist, who discovered the effect in 1934. Due to the kinetic condition, one can define an energy threshold a charged particle of rest mass m_0 needs to exceed:

$$\beta c \geq \frac{c}{n} \quad \Rightarrow \quad E_{th} = \frac{m_0 c^2}{\sqrt{1 - n^{-2}}} \,. \tag{3.1}$$

According to the Huygens-Fresnel principle, the waves interfere constructively only along a cone with opening angle θ_C, the Cherenkov angle. Like the threshold, it is determined by the refractive index of the medium and the energy of the charged particle

$$\cos(\theta_C) = \frac{1}{n\beta} \,. \tag{3.2}$$

From the Frank-Tamm formula, which determines the energy and spectrum radiated by a particle per unit length, the number of photons generated by a relativistic particle can be inferred (e.g. see Grieder, 2010):

$$\frac{\mathrm{d}N}{\mathrm{d}x} = 2\pi\alpha \, Z^2 \int\limits_{\lambda(n>1/\beta)} \left(1 - \frac{1}{\beta^2 n(\lambda)^2}\right) \frac{\mathrm{d}\lambda}{\lambda^2} \,. \tag{3.3}$$

The energy loss of the relativistic particles via Cherenkov radiation is negligible and thus the effect does not affect the particle cascade. Nonetheless, it is an important tool in particle and astroparticle physics.

The development of the shower light

Due to the hydrostatic pressure, the density of the atmosphere and thereby the refractive index increases towards lower altitude. Assuming an isothermal atmosphere the density profile can be approximated by the simple barometric formula. As the refractive index $n - 1$ is proportional to the density, it can be described with an exponential function as well:

$$n - 1 = \eta_0 \exp\left(-h/h_0\right) \,, \tag{3.4}$$

where h is the height above sea level (a.s.l.), h_0 the characteristic scale height, and η_0 a constant scaling factor. For example Aharonian et al. (2008) specifies the constants with $h_0 \approx 7.25\,\mathrm{km}$ and $\eta_0 = 2.9 \times 10^{-4}$. Figure 3.9 shows that the atmospheric profile used in the MAGIC telescope simulation approximately follows an exponential, both in terms of density and refractive index.

The cone of Cherenkov light of the particles will mainly illuminate a ring on the ground, which radius R_C depends on the emission height of the light h, the observational height h_{obs} a.s.l. and the Cherenkov angle:

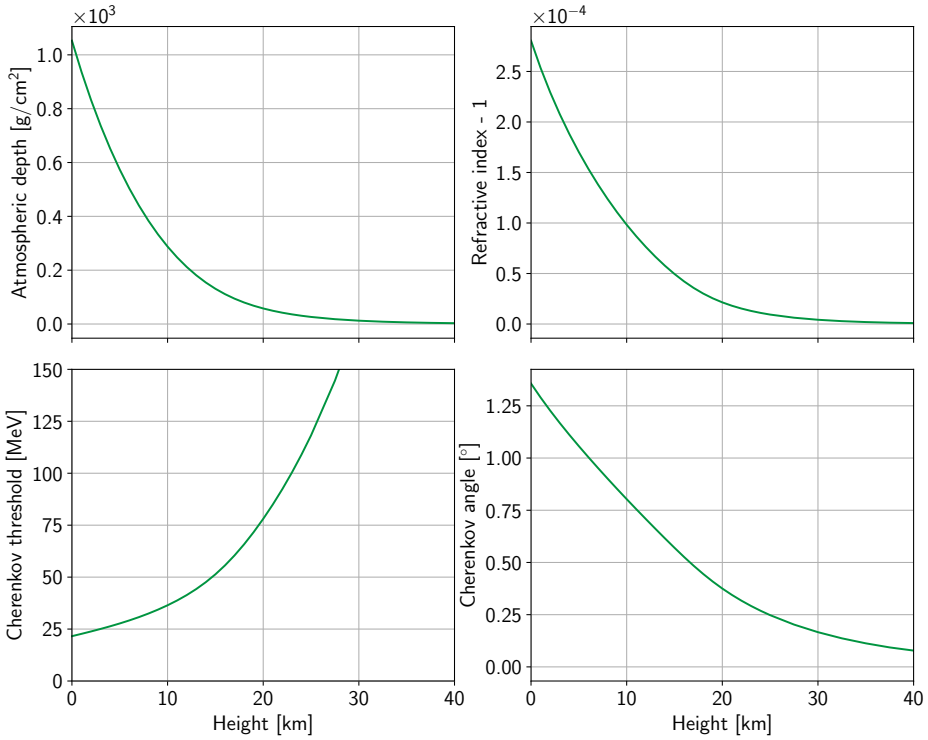

Figure 3.9.: Depth of the atmosphere and its effects on the characteristics of the Cherenkov light production in the atmosphere. The graphs are based on the atmospheric profile used in the MAGIC Monte-Carlo simulation.

$$R_C = \tan(\theta_C)\,(h - h_{obs})\ . \tag{3.5}$$

As a result of the changing index n, the superposition of the rings from different altitudes will mainly illuminate a circle with 80 m to 130 m radius around the impact point of the shower axis on the ground. This circle is called the light pool. The illumination inside is rather homogeneous, while the edge of the ring is illuminated strongest, called the hump. Due to the lateral spread of the shower caused by multiple Coulomb scattering, light of the shower can also be observed beyond the hump, but the lateral light distribution exponentially falls off with distance. While γ-ray showers follow the above description, the sub-cascades and large transverse momentum in hadronic showers result in a less regular footprint with several sub-lightpools and light found comparably far away from the shower core.

Just as the number of particles, the light in air showers is proportional to the energy of the primary. Figure 3.10 shows that the relation is nearly linear for electromagnetic cascades. For hadronic showers this relation is only valid towards higher energies and they are less efficient in generating Cherenkov photons. As the particles in the shower

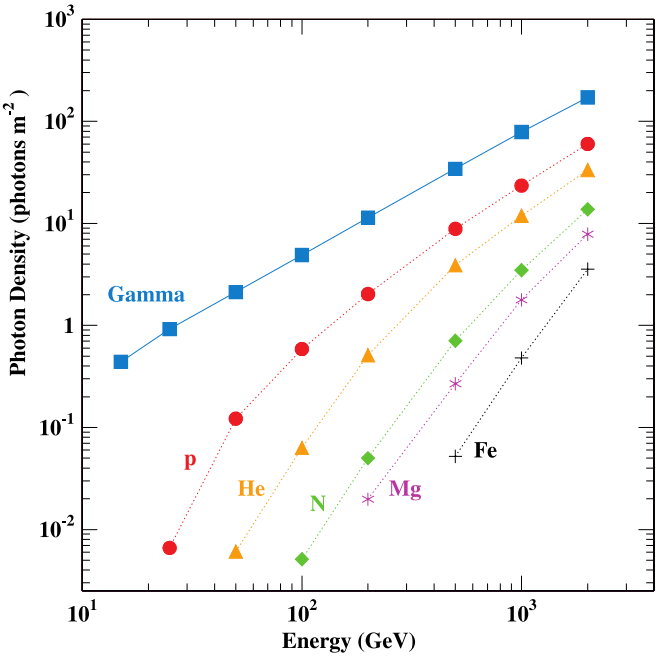

Figure 3.10.: Mean density of Cherenkov photons inside 125 m from the shower core versus the energy for different primary types. Figure adapted from Oser et al. (2001).

are relativistic, the duration of the Cherenkov flashes is in the order of 4 ns to 10 ns. In hadronic showers the numerous sub-cascades cause a wider time spread of 10 ns to 15 ns. Hence, the differences between γ-ray and hadronic showers are reflected by the Cherenkov light they emit.

Independently of the primary the shape of the light pool and the light density is affected by the Zenith angle θ of the shower axis. The light pool still has a roundish shape in the plane perpendicular to the shower axis, but the projected footprint on the ground is stretched out over a larger area. Thus, the light density of showers at larger Zenith distances (Zd) is reduced, but showers can be detected farther away from the impact point at the same time. Fruck (2015) computed that the geometrical change of the light density and the covered area scales as $\sim \cos^{3.5-4}(\theta)$.

Absorption in the atmosphere

According to formula 3.3 most of the Cherenkov photons are emitted in the UV and optical wavelength range with an λ^{-2} dependency. As mentioned at the beginning of this chapter, the atmosphere is far from being ideally transparent (even in the observational windows) and not equally transparent at all wavelengths. For Cherenkov light there are three important processes reducing the yield and modify the detectable spectrum on the ground.

Rayleigh scattering describes the scattering of photons on polarisable particles, smaller than the wavelength of the photon. At an altitude between 3 km to 15 km and, under good atmospheric conditions, it is the dominant process reducing the Cherenkov photon intensity. The cross section is proportional to λ^{-4}, conse-

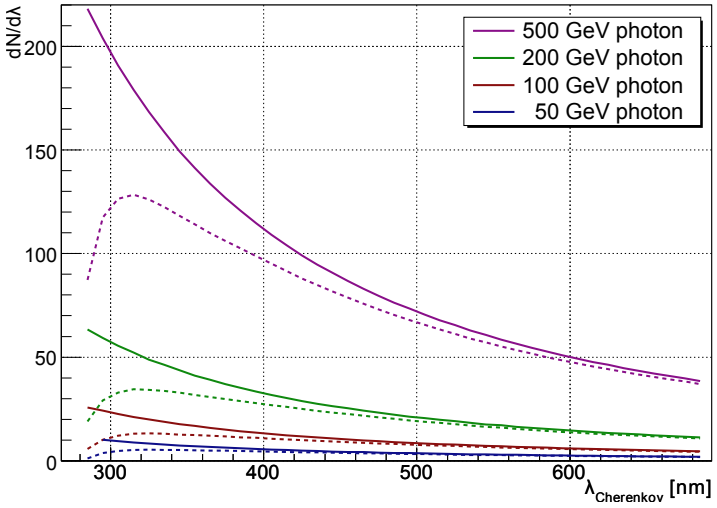

Figure 3.11.: Modification of the Cherenkov spectrum emitted at 10 km due to absorption processes in the atmosphere for γ-ray showers of different primary energies (solid lines: emitted spectrum, dashed lines: transmitted spectrum). Figure from Wagner (2006).

quently it mainly reduces photons with small wavelengths.

Mie scattering is caused by atmospheric aerosols of sizes comparable to the wavelength of light (for example dust, humidity, clouds). The concentration of aerosols and thus the scattering is significantly reduced above 2 km height and moreover time variable and site dependent. The wavelength dependency of the Mie scattering lies between λ^{-1} and $\lambda^{-1.5}$.

Ozone can be found in the atmosphere above 10 km. It strongly absorbs photons in the UV range ($\lambda < 300\,\text{nm}$) via $O_3 + \gamma \rightarrow O_2 + O$.

Figure 3.11 shows how absorption modifies the Cherenkov spectrum. One can clearly identify the sharp cut-off towards UV wavelengths, the stronger absorptions in the blueish range, and the rather moderate changes towards higher wavelengths.

3.4.3. The Imaging Air Cherenkov Telescope technique

Following a suggestion by Blackett (1948) that Cherenkov light might contribute to the light of the night sky, Galbraith & Jelley (1953) demonstrated that indeed the Cherenkov light reaching the observational level can be detected against the general night sky illumination. The **I**maging **A**ir **C**herenkov **T**elescopes (IACTs) used today are large optical telescopes projecting the light into the camera plane using parabolic or spherical mirrors. The mirror system projects rays arriving at the same angle onto the same point in the plane and thus basically converts incident angles to distance from the camera centre as displayed in figure 3.12. Light arriving from the same direction as the telescope pointing direction is projected into the camera centre.

As the Cherenkov angle changes along the track, the light from different parts of the shower are reflected at different position in the camera plane (red and green point in figure 3.12) and an image of the shower is constructed. Further the projection of the

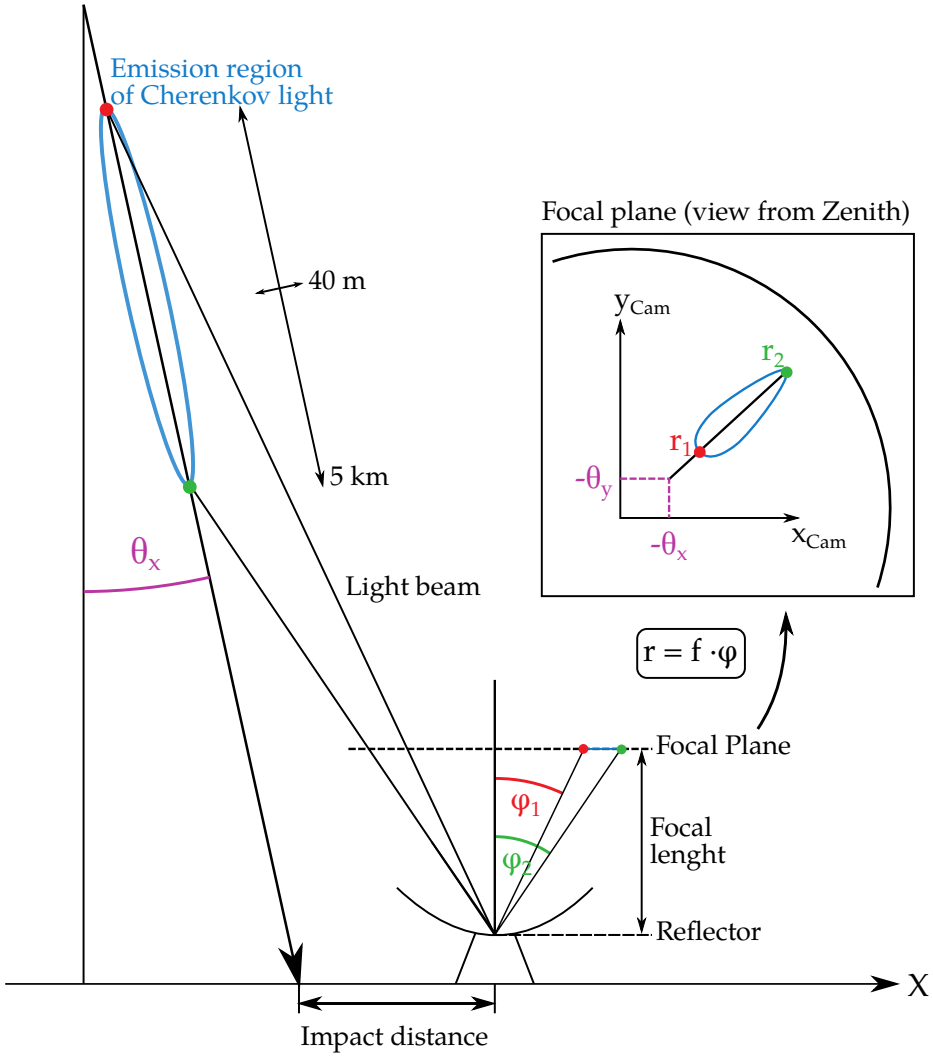

Figure 3.12.: Working principle of an Cherenkov telescope, which maps the shower into the focal plane. The telescopes converts incident angles into distance from the camera centre as shown by the inlay.

shower axis reflects the angular orientation of the shower axis to the telescope pointing position. The axis is a straight line connecting the impact point on the ground with the arrival direction (purple angles in figure 3.12).

As no Cherenkov light is collected from the impact (except the shower directly hits one telescope) or the arrival direction, both parameters can hardly be inferred from a single telescope image, which just determines the orientation of the shower axis in a plane. Reconstruction methods based on apriori knowledge of the shower characteristics may allow the estimation of both parameter, still the underdeterminition can more accurately be solved by operating several Cherenkov telescopes in stereo mode. This way the shower is viewed under different positions and angles. Each reconstructed shower axis defines a plane which includes the shower axis, so the crossing of the two

planes determines the shower axis as displayed in figure 3.13. In practise the crossing of the two reconstructed images in the ground coordinates system determines the impact point ((X_0, Y_0) in fig. 3.13) (Kohnle et al., 1996). The projection of both images into a common camera coordinate system allows finding the arrival direction of the shower with respect to the orientation of this camera system ($(-\theta_{x0}, -\theta_{y0})$ in fig. 3.13)(Kohnle et al., 1996).

3.5. The MAGIC telescopes

The **M**ajor **A**tmospheric **G**amma-ray **I**maging **C**herenkov (MAGIC) telescopes are a streoscopic system of two 17 m diameter telescopes. They are situated at the Observatorio de Roque de los Muchachos at 2200 m altitude above sea level on the Canary Island of La Palma (28°45′42″ N; 17°53′25″ W). The first MAGIC telescope, MAGIC I, was built in 2004 and was operated as a single telescope until the construction of MAGIC II in 2008. Since then they operate in stereo-mode covering the energy range from tens of GeV ($\sim$ 30 GeV) up to hundreds of TeV. In 2011/12 the telescopes underwent a major revision consisting of an upgrade of the MAGIC I camera and the full electronics to further improve their performance and unify the components of both telescopes. The main characteristics of the MAGIC telescopes, in comparison to other IACTs, is their low energy threshold and their fast rotation speed ($\sim$ 25 s for 180° rotation) needed to catch the signal of rapid transient events such as GRBs.

3.5.1. Structure and reflector system

To achieve a low energy threshold and at the same time a fast rotation speed, the MAGIC telescopes have a large $D = 17$ m diameter mirror support frame made of light-weight carbon-fibre tubes (total weight < 70 t). The frame is mounted on a steal understructure on-top of a circular rail system; accordingly the telescopes have an Alt/Az mount with a positioning accuracy of $< 0.^{\circ}02$ (Bretz et al., 2009). An aluminium arch holds the camera in the focal plane. The focal length to diameter ratio is $F/D = 1.03$.

The support frame carries spherical mirror facets forming an approximatively parabolic reflector of $\sim 240\,\mathrm{m}^2$. The mirrors are either spherical aluminium or glass mirrors of different radii (Doro et al., 2008). At wavelengths between $290 - 650$ nm these mirrors reflect most of their light ($> 80\%$) onto a spot of 2 cm diameter, which is about the size of a camera pixel (diameter of the PMT ~ 2.54 cm and ~ 3 cm including the Winston cone; Bastieri et al., 2005, 2008). The parabolic structure conserves the time structure of the Cherenkov flash at the focal plane (time spread < 1 ns) allowing for the use of the arrival time of each pixel in the subsequent analysis. This comes at the cost of a worse off-axis performance due to an increased coma aberration compared to the traditional Davies-Cotton design.

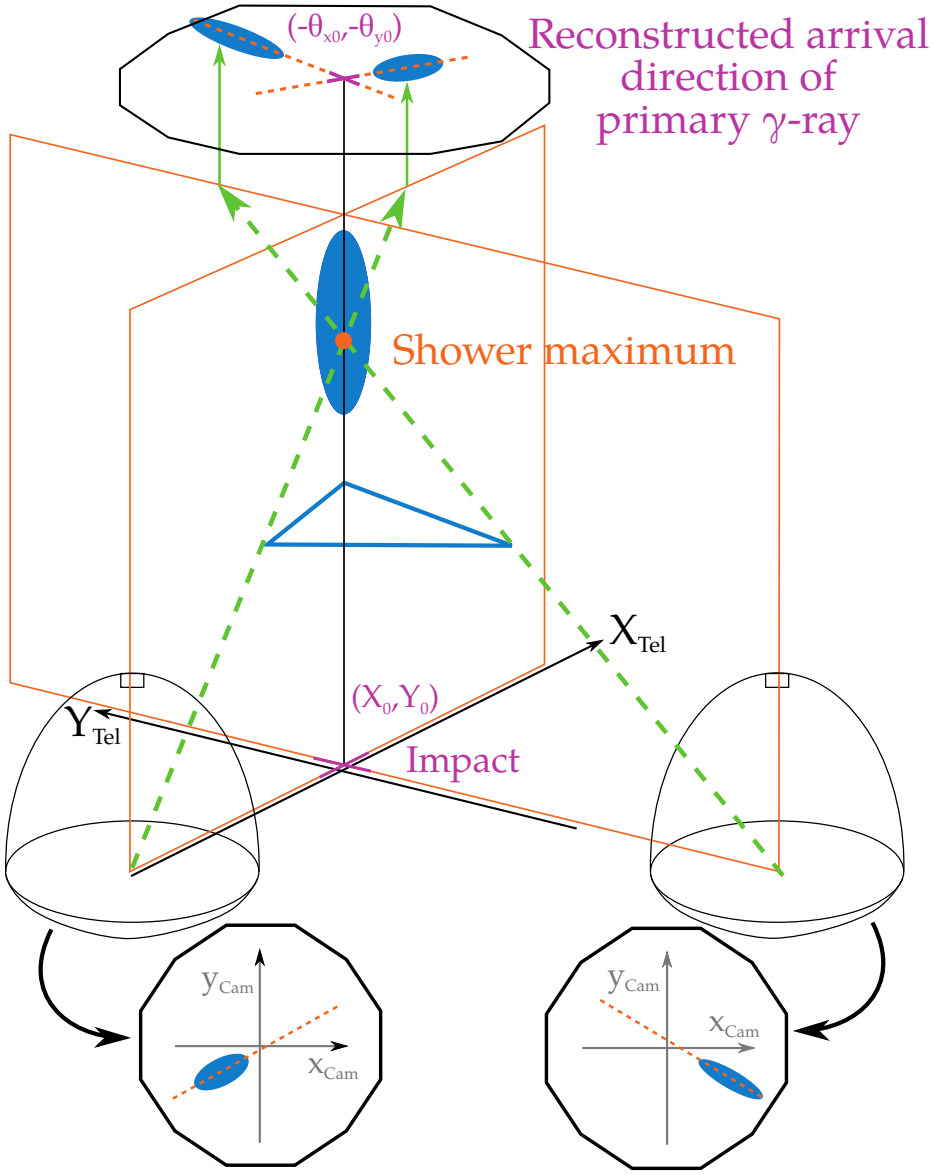

Figure 3.13.: Stereo reconstruction of the shower axis by two Cherenkov telescopes. The shower axis of each telescope defines one of the planes, which cross at the shower axis. Using the crossing of the shower axes in the telescope/ground coordinate system, one can determine the impact point. Projecting both images in a common camera system, the crossing defines the arrival direction with respect to this system. The blue triangle is used in MARS to estimate the height of the shower maximum (see section 3.5.5).

Due to the light-weight design, the carbon-fibre structure deforms under its own weight. As the load depends on the telescopes orientation, the mirror alignment needs to be adjusted during observations to preserve the parabolic shape and to minimise the point spread function. The orientation of the mirrors is controlled by an Active

Mirror Control (AMC; Biland et al., 2008): each mirror panel is attached to the support frame at three points, of which one is fixed and the other two are movable actuators with a precision of $< 20\,\mu m$ corresponding to less than 1 mm shift in the camera plane. The AMC keeps the optical spread of a points source at $\sim$8 mm to 10 mm (39 % containment), which agrees with the theoretical minimum of the PSF of a single mirror. Since, the bending of the reflector further affects the positioning accuracy of the camera, MAGIC monitors the pointing with a CCD camera (called the Starguider camera) comparing the camera position against the position of stars. The correction is applied to the recorded events offline in the MARS analysis.

3.5.2. Camera

Since the upgrade of the MAGIC I camera in 2012, both telescopes are equipped with a 1039 pixel photomultiplier-tube (PMT) camera (see Aleksić et al. (2016a) and references therein). The PMT type is Hamamatsu R10408 with a diameter of 2.54 cm and a FoV of $0.^{\circ}1$. It has a peak quantum efficiency of 32 %. In front of each PMT is a hexagonal Winston cone that concentrates the light onto the PMT and avoid gaps between the roundish detectors. The front of the camera is protected by an acrylic glass cover. The FoV of the full camera is $3.^{\circ}5$. To simplify the maintenance the PMTs are arranged in clusters of 7 as shown in figure 3.14.

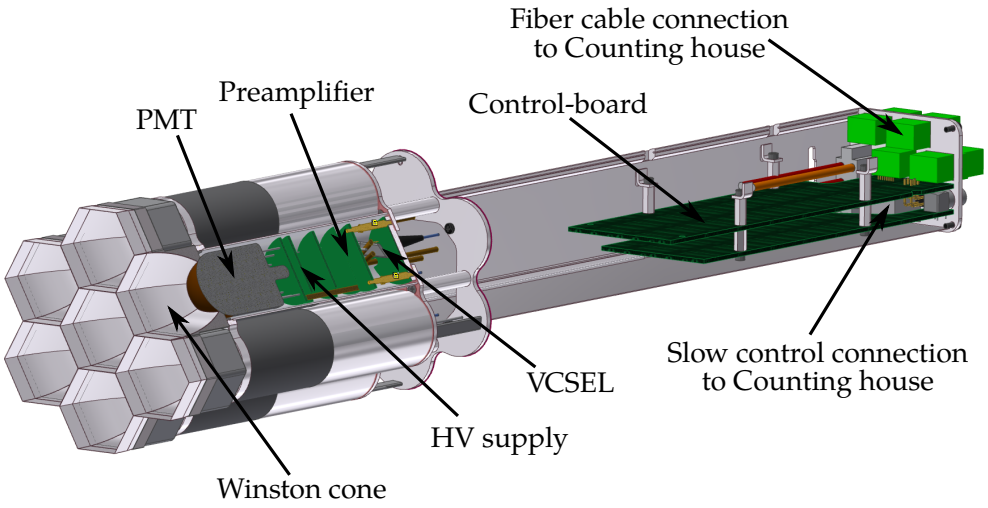

Figure 3.14.: Schematic of a PMT cluster as used in the MAGIC cameras and its components. By courtesy of Alexander Hahn and the MPI electronics department.

Each cluster contains a control processor, which sets the high voltage of the PMTs and records their direct current (DC, current at the PMT anode). Besides, it is equipped with a pulse generation board, which can generated test pulses at the base of the PMT and allow testing the electronic chain from the base to the trigger system.

The PMT high voltage (HV) is generated by a Cockcroft-Walten DC-DC converter and are operated at low gain ($(3-4) \times 10^4$). The low gain decreases the charge hitting the PMT anode and thereby reduces the ageing of the PMT. Due to limitations in the production process, each PMT has a different gain when operated at the same HV, which is compensated by a so-called flatfielding procedure (see Aleksić et al. (2016a)). The signals are amplified by $\sim$ 25dB, converted to optical signals by a vertical cavity surface emitting lasers (VCSELs), and transmitted via optical fibers to the counting house, where the read out electronics is located. The time spread due to the different HVs or the optical cables, which would otherwise spread the short Cherenkov flashes, is compensated by programmable delay lines.

3.5.3. Trigger and read-out electronics

The trigger system discriminates between air showers and spurious events from night sky background (NSB), so that just the former are recorded. The NSB consists of light from stars, the Moon, and other natural or human light sources and poses a background to the detection of Cherenkov flashes. The trigger region comprises of the inner 547 pixels of the camera highlighted in figure 3.15 and has a radius of 1.°17 vs. 1.°75 of the entire FoV. The trigger logic consists of three steps (Aleksić et al., 2016a):

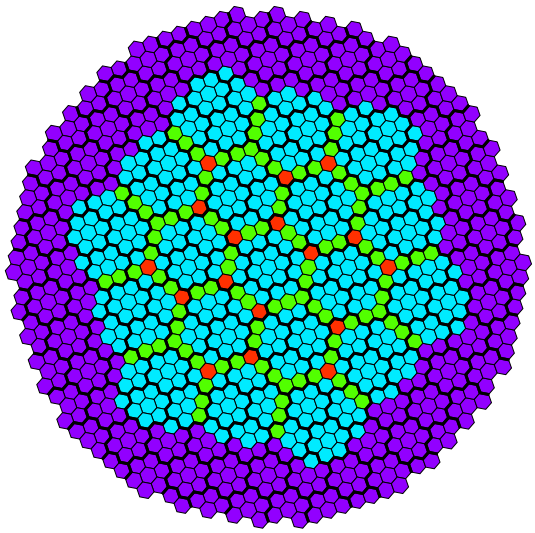

Figure 3.15.: Trigger Area of the MAGIC camera. The thick black lines separate the PMT clusters. The cyan area indicate the macro-cells belonging to the L1 trigger area. PMTs coloured in green belong to two overlapping macro-cells; red indicates an overlapp of tree macro-cells. Figure from Aleksić et al. (2016a).

Level 0 is the first level and a simple amplitude discriminator that any pixel needs to pass. The discriminator threshold (DT) is calibrated for each pixel to have the same sensitivity to a light signal across the camera. However, the presence of bright stars may spoil the flat response, so the DTs are further adjusted online by a control of the individual pixel rates (IPRC), which keeps the rate in a certain range by modifying the DT (Aleksić et al., 2016a).

Level 1 checks the 19 macrocells (each containign 39 pixels; see figure for tempo-

rally coinciding L0 signals in a certain number of neighbouring pixels. The next-neighbour pattern could range between 2 and 5, but usually MAGIC uses 3NN logic. The level 2 trigger was a system working on top of the L1 trigger in MAGIC 1, but is not used any more.

Level 3 is the stereo trigger. It issues a trigger signal if it receives a signal from both L1 triggers within 200 ns. Each L1 signal is stretched to 100 ns and delayed depending on the pointing direction of the telescopes. The former shall ensure a high L3 efficiency and the latter considers the arrival time difference of the shower light between the two telescope positions. If an event passes all trigger level, the L3 trigger sends a signal to the read-out electronic of each telescope.

MAGIC operates two additional trigger systems the Sum-Trigger (García et al., 2013) and the Topological (Topo) trigger (López-Coto et al., 2016), which are not going to be explain further in this work as all of the data used were taken with the trigger system outlined above.

The upgrade of the read-out electronics was the second major part of the upgrade of both MAGIC telescopes in 2012 (Aleksić et al., 2016a), which now share the same electronic set-up. The signal arrives at the counting house as an analogue, optical signal, which needs to be digitised so it can be written to disk. The readout electronics consists of two parts: the receiver and the digitisation system. The former converts the optical signal back to an electrical one, applies the L0 trigger, and transfers the signal to the digitisation system. The latter is based on a Domino Ring Sampler 4 (DRS4) chip, which consists of a switched capacitor array with 1024 cells; it basically is an analogue memory. The switches are synchronised with an external clock and the sampling rate can range between 700 MHz and 5 GHz. The data in this thesis were taken with 1.64 GHz. If the system receives a trigger, the propagation of the charges is terminated and 50 capacitors around the expect signal arriving time are read out sequentially by analogue to digital converters (ADC) leading to a dead time of $\sim 27\,\mu s$. It is negligible compared to the data acquisition rate of 250 Hz (Aleksić et al., 2016a). The length of the read-out capacitor chain and the sampling speed define the recorded duration of the shower signal, which is $1.64\,\text{GHz} \cdot 50 = 30.5\,\text{ns}$. In the analysis description the 50 sequential read-out signals will be referred to as time slices.

At the beginning of each night a pedestal calibration run is taken to estimate the offset in the mean ADC count value of the capacitors in each chip. The single capacitor baseline varies up to $\sim$ 15 % between the cells. The baseline measured during the calibration run is subtracted from each capacitor. The DAQ software further corrects the time spread on the delay of the recorded signal pulses between the ring buffer positions. This correction is based on the usual calibration runs described below.

3.5.4. Additional subsystems of the telescopes

This subsection introduces additional subsystems that are not directly involved in the data taking but play an important role in the analysis of MAGIC data.

Calibration system To perform the flat fielding of the PMT gains, to calibrate the analogue arrival times in the DRS4 channels, and to later convert the recorded signal to a physical unit, the camera can be uniformly illuminated with light pulses from a laser system. The calibration box housing this system is located in the centre of the telescope's dish (for technical details see Aleksić et al. (2016a) and references therein). The laser was tested to be stable within 1% over the time-scales of 10 min, the duration that is used for the initial event calibration. A calibration run with 2000 calibration pulses is taken at 300 Hz at the beginning of each observational run and the further constantly monitored by firing pulse at a rate of 25 Hz.

In addition to the calibration run, a pedestal run and interleaved pedestal events are taken. Pedestal events are recorded events without applying the trigger conditions. In the following they will serve as a measurement of the base level of the camera illumination due to background light coming from the Moon or stars.

LIDAR As explained in section 3.4.2 varying atmospheric conditions change the absorption of Cherenkov light in the atmosphere. The main instrument in MAGIC to measure the transparency of the sky is a light detection and ranging (LIDAR) system (Fruck et al., 2013). It is located at the roof of the counting house and consist of a laser operating at 532 nm and a small optical telescope. The LIDAR shoots short laser flashes into the sky and the backscattered light is collected by a 60 cm mirror focusing the light onto a hybrid photo detector (HPD) at focal length of 150 cm. The HPD is placed behind a diaphragm and an interference filter with 3 nm bandwidth to reduce the background from NSB. Since the laser flashes can cause accidental triggers, the LIDAR pointing direction is slightly misaligned from the telescope one.

Clouds and aerosols will backscatter more light than expected from Rayleigh scattering only. Hence, using an atmospheric model for the backscattered light the transparency of the atmosphere at different heights can be estimated. The height is estimated by the arrival time of the photons. With the absorption profile the estimated energy of an air shower and the effective area can be corrected for the reduced light yield and lower detection efficiency respectively. However, this is only necessary if the transparency falls below a certain limit, what is not the case for the data in this thesis. For a detailed explanation on the LIDAR system and the corrections see Fruck (2015).

Pyrometer The second system for measuring the transparency of the sky is a *Heitronics KT19.82* pyrometer, which is attached to MAGIC 1 and always points in the same

direction. It monitors the temperature via infrared radiation inside a 2° FoV. The presence of water or dust changes the emissivity of the infrared radiation, which is otherwise just expected to drop with height, at the corresponding atmospheric layer. Additionally, clouds reflect the heat radiation from ground further increasing the measured temperature from the layer. The temperature is corrected for the Zd effect and using empirical formula can be converted to measurement of the cloudiness. It allows to infer the height of a cloud, but since it integrates the temperature, the pyrometer does not provide an absorption profile. It serves as a cross-check for the LIDAR or can be used to assess the data quality when LIDAR measurements are not available. Further details can be found in Will (2017).

3.5.5. The MAGIC data analysis chain

The **M**AGIC **A**nalysis and **R**econstruction **S**oftware (MARS) is a software package for the reduction of the MAGIC data and computation of the final analysis results (Zanin et al., 2013). It consists of a chain of consecutive executable programs and macros in C++ code. It heavily relies on the ROOT data analysis framework and uses the ROOT data format for storing the event information (Antcheva et al., 2009).

Signal calibration

The first step in the calibration of the digitised image is subtracting the baseline of ADC counts in each channel. Therefore the program fills a histogram combining the slices of all pedestal events. The mean of this histogram is used as the baseline for the corresponding channel. After subtracting the baseline the charge and mean arrival time of each pixel is extracted using a sliding window for finding the 5 consecutive time slices ($\widehat{=}\,3.0\,\mathrm{ns}$) within the total readout window with the highest charge (Albert et al., 2008a).

The extracted charge is still in ADC counts and needs to be converted to the actual number of photoelectrons (ph.e) that hit the cathode of the PMT, a quantity that is related to the light yield of the shower. The calibration process follows the excess noise factor or F-factor method (Mirzoyan & Lorenz, 1997). The eponymous F-factor describes the limited charge resolution of a PMT due to the dynode cascade. It can be determined from a single ph.e distribution and thus is measured in the laboratory.

Knowing the intrinsic F-factor and using calibration pulses, the conversion factor can be measured. A calibration pulse with mean N ph.e results in a wider measured signal distribution in FADC charge with mean $\langle\, Q \,\rangle$ and root mean square Q_{rms} than the expected variance of a Poisson statistics $\sqrt{N}$. The conversion factor C is

$$C = F^2 \frac{\langle\, Q \,\rangle}{Q_{\mathrm{rms}}}\,. \tag{3.6}$$

It is measured at the beginning of a data taking run, but can change over the time of a run. The interleaved calibration events constantly update the conversion factor, which is the averaged over all pixels. Still it means that the conversion factor applied to an event is based on the calibration and pedestal events taken over a few minutes before the event is recorded.

Quality selection

The level of the night sky background light and the transmission of the atmosphere significantly affect the performance. Also times of hardware failures should be prevented from entering the analysis.

To account for these effects in the subsequent analysis, the data are grouped in terms of transmission and sky brightness. The former is measured using the LIDAR shoots or if not available, the estimated transmission from the pyrometer can be used instead. The data quality tools in MARS can also use the number of stars in the FoV or the Zd corrected event rate as a measure for the transmission. Compared to the previous two they are, however, less reliable. Data with a transmission of $>$80-85 % can be analysed using the standard procedure. If the level drops below, the data can be corrected using the LIDAR profile down to a level of $\sim$65 % with respect to the optimal transmission.

The sky brightness is inferred from the DC level in the camera pixels (Ahnen et al., 2017). Based on the minimum NSB level at the region of interest, the data can be grouped in multiples of the base level. In the next step the cleaning levels can be adjusted for each group.

Image cleaning

During operation the camera is permanently exposed to a night sky background (NSB), so not only pixels illuminated by the shower contain signal counts, but all pixels. In addition the NSB the electronic noise adds up to the background signal. To compute the shower image parameters, the pixels containing only noise need to be removed from the reconstruction. To balance the removal of noisy pixels while preserving the shower light, MARS applies a so-called "sum-cleaning" consisting of two steps (Shayduk et al., 2005; Aleksić et al., 2011):

1. Determination of the brightest pixels of the showers, the so-called core pixels: the summed charge of groups of 2, 3, or 4 next neighbour (NN) combinations of pixels is compared against a given threshold Q_c. Additionally only groups, which signal arrives within a time window t_{core}, are considered. To prevent one pixel from dominating the signal of a group, the signal of each pixel is clipped at level Lvl_{clip} before the summation. Lvl_{clip}, Q_c and t_c depend on the NN combination in question.

2. Identifying the boundary of the shower image: for each pixel next to a core pixel the program tests whether the charge is above a second threshold $Q_b = 3.5$ phe and the arrival time is not more than 1.5 ns offset against the arrival time of adjacent core pixel.

The quality of the image cleaning can be controlled using pedestal events. The fraction of those noise-only events surviving the image cleaning provides an estimate for the number of noisy pixels remaining in images of triggered events. These noisy pixels form spurious islands in the event image that can spoil the parameter estimation and event classification. To not affect the analysis too much this fraction has to stay $< 20\%$ for stereo events. If the fraction rises above this limit e.g. due to observations during strong Moon light, the cleaning levels Q_c and Q_b need to be increase. To keep the same ratio for the NN combinations, Q_c is defined by a NN-multiplier applied to a common multiplicand Lvl_1. In the same way $\mathrm{Lvl}_{\mathrm{clip}}$ is obtained by multiplying the single pixel threshold (NN-multiplier $\times$ Lvl_1) with a clipping-multiplier.

Table 3.1.: Cleaning Levels.

Topology	Lvl_1 [phe]	NN-multiplier	clipping-multiplier	Q_c [phe]	t_c [ns]
2 NN	6	1.8	2.2	2×10.8	0.9
3 NN	6	1.3	1.05	3×7.8	0.7
4 NN	6	1.0	1.05	4×6.0	1.1

Table 3.1 lists the clipping multiplier, Lvl_1, the NN-multipliers, and the resulting Q_c for dark conditions; settings for different Moon conditions were studied in Ahnen et al. (2017). The arrival time offsets are not affected by higher NSB levels and thus are kept constant. The MAGIC Monte-Carlo events are always generated for dark conditions. For the Moon analysis the NSB noise in the data can be increased to match the noise level in the pedestal events in terms of the mean and root mean square of the pixel content distribution. The modified MC are cleaned in the same way as the Moon data.

Hillas parametrisation

To reduce computational needs and make the analysis more robust, after cleaning, the camera images are parametrised. The first approach for this data reduction was proposed by Hillas (1985) suggesting to fit an ellipse to the shower image. The most important image parameters used in MARS are the centre of gravity (CoG) and the minor (width) and major (length) axis of the ellipse, the amount of photon counts (size), the time gradient of the arrival times of the pixels along the major axes, and the leakage, which is the charge contained in the outermost pixel ring of the camera divided by the size. Another parameter used for discriminating hadronic events later on

is the number of islands, which is the number of separated regions of pixels surviving the image cleaning.

Stereo reconstruction

Events, which were successfully reconstructed in both telescopes ($\sim$ 80 % of the recorded events), are combined to reconstruct information about the position and orientation of the shower. As described in section 3.4.3 combining the images from both telescopes allows the reconstruction of the arrival direction and impact position.

By projecting the CoG of both shower images into the sky, one obtains the two dashed lines in figure 3.13. Those are supposed to cross together with the shower axis at the height of the shower maximum. In reality, however, the lines do not necessarily cross and instead the shower maximum is defined as the height, where the perimeter of the triangle formed by the three lines (blue triangle in figure 3.13) is smallest.

Using the shower maximum the MAGIC stereo reconstruction further computes physical parameters of the shower such as the Cherenkov radius R_C and Cherenkov density ρ_C based on a simplified shower model. The Cherenkov radius is the radius of the Cherenkov cone at ground level emitted by an electron of 86 MeV (E_c in air; see section 3.2 at the shower height maximum moving towards the impact point. The density is the light density emitted by the same assumed electron inside the Cherenkov ring along one metre distance. Both quantities are estimated in the plane perpendicular to the shower axis. Based on the reconstructed single-telescope and stereo parameters the MAGIC analysis chain can compute the characteristics of the primary particle such as the particle type, the energy, and the arrival direction.

Gamma/Hadron separation

As most of the recorded events are of hadronic origin (only $\sim 0.1\%$ are γ-rays, Aleksić et al., 2016b), the background needs to be suppressed to make faint signals detectable. The discrimination algorithm makes use of the image parameters, which reflect the differences in the shower development between the γ-ray signal and the hadronic background (see section 3.4). Traditionally cuts in the image parameter space were used, but machine learning algorithms were found to outperform simple parameter cuts as they can take into account correlations in the multi-dimensional parameter space. The MAGIC analysis uses a Random Forest (RF) (Albert et al., 2008b), a classifier that consists of multiple, uncorrelated decision trees (Breiman, 2001) and which was found to be the most effective classifier (Bock et al., 2004; Sharma et al., 2014). The trees are trained with a subset of Monte-Carlo (MC) simulated γ-ray events bootstrapped from a larger sample (called bagging) and real (background) data taken from a source-free region.

At the beginning all events (γ-rays and hadrons) are in one node. The events are

separated by splitting the root node into two nodes using a cut value in one parameter (sometimes called feature). The quality of each successor node is measured by the Gini-index

$$Q_{\text{Gini}} = \frac{4\,\sigma_{\text{binomial}}}{N} = 4\frac{N_\gamma}{N}\frac{N_\text{h}}{N}\,. \tag{3.7}$$

To judge the total quality of the split the indices are summed up:

$$Q_{\text{Gini,split}} = \frac{1}{2}\left(Q_{\text{Gini,node1}} + Q_{\text{Gini,node2}}\right)\,. \tag{3.8}$$

The feature used for the split is randomly selected, called random split selection. In MAGIC a set of three features is drawn and for each the cut value is optimised to minimise $Q_{\text{Gini,split}}$. The feature providing the lowest $Q_{\text{Gini,split}}$ is chosen for the split. The shower parameters used as features of the RF are: the size, width, length, the time gradient, and impact distance of each telescope, the shower height maximum, and the Zenith distance. The splitting of a node terminates if the events in the node fall below a limit (in MAGIC 5) or it just contains events of one kind. When applying the tree to data, it will assign a value to each event called hadronness ($h \in [0,1]$) depending in which final node the event is classified: 0 for a pure γ-ray node, 1 for a pure hadron node, and for mixed nodes the average of the node.

The method gets its power from using multiple threes together. The single results are combined by taking the arithmetic mean. A single tree has a precision (root mean square) of the hadronness estimate of about 0.2, but combining a sufficient number of threes the rms can be reduced to 0.1 (Albert et al., 2008b). The standard MAGIC analysis uses 100 threes, and so does the RF used for the results in this thesis. Figure 3.16 shows an example of the hadronness distribution of background data and MC events as estimated by the RF classifier. After the classification the two event classes can be separated by a cut in the hadronness parameter. The right plot of figure 3.16 displays the receiver operating characteristic (ROC) curve, which allows to evaluate the performance of the classifier by true positive rate (γ-ray efficiency) as a function of the false positive rate (background rejection efficiency).

Even though the classifier is able to reject 90% of the background events while keeping 90% of the signal, the recorded data are still dominated by an irreducible fraction of γ-like hadronic events (Maier & Knapp, 2007; Sobczyńska, 2009, 2015; Sitarek et al., 2018) and electron-induced showers, which like γ-ray showers are purely electromagnetic. Albert et al. (2008b) showed that the background discrimination performs better at higher energies ($\sim$TeV). When applying the RF classifier to real γ-ray events the hadronness distribution is slightly wider than for MC. Too tight hadronness cuts (< 0.2) may thus not just lead to a better background separation but also to a loss of γ-ray events due to the data/MC mismatch.

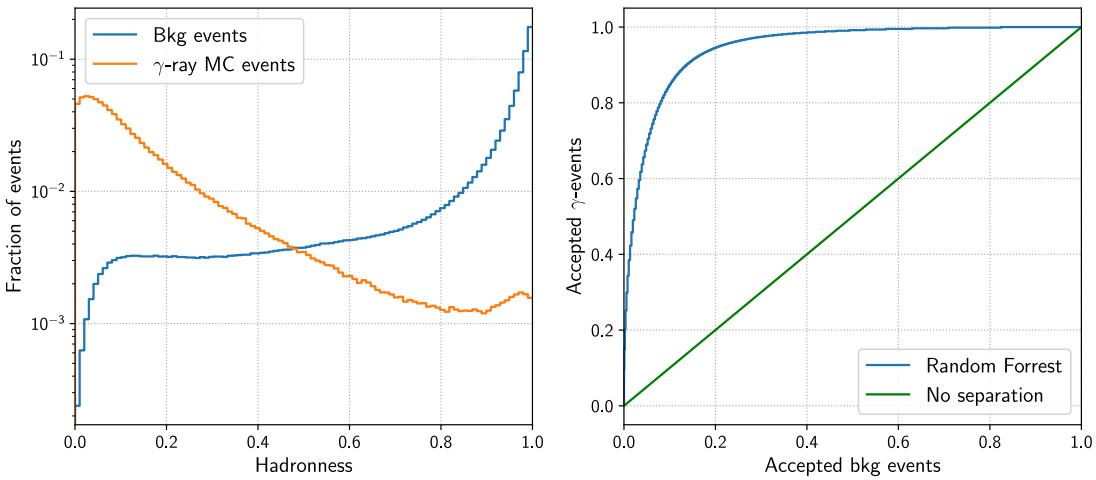

Figure 3.16.: Left: hadronness distribution of *gamma*-ray MC events and background data after a RF classification. **Right:** ROC curve corresponding to the left hadronness distribution showing the fraction of γ-ray events kept against the fraction of rejected hadrons and the improvement over random guessing (green curve).

Energy reconstruction

The energy estimation of an event in the MAGIC analysis chain is based on a lookup table (LUT). The table is generated for each telescope separately and consists of bins of $\sqrt{\log(size)}$ and impact over the Cherenkov radius $impact/R_C$. The bins are filled with the mean and root mean square of the distribution of the true event energy times the Cherenkov density over size $E_{\text{true}} \cdot \rho_C / size$. Including the factor $\rho_C / size$ brings the bin content closer to unity reducing variations and automatically considers the zenith dependence (Aleksić et al., 2012). $E_{\text{true}} \cdot \rho_C / size$ is further corrected using empirical corrects for the zenith distance, the leakage, and the angle between the shower axis and the geomagnetic field.

Using the prepared table the estimated energy of a recorded event and its uncertainty are obtained for each telescope from the image parameters. The stereo reconstructed energy is the average of the single telescope estimates weighted with their inverse uncertainty.

Alternatively the MAGIC analysis also contains an energy reconstruction based on a RF. It works similarly to the γ/hadron RF, but instead of minimising the Gini index it aims for a minimal variance of the γ-MC event energies in the nodes. Since this energy RF is a recent development, the energy estimations used in this thesis are based on the LUTs.

Disp stereo reconstruction

The precision of the direction reconstruction from the crossing point of the images' main axes can be improved by taking into account the shape and timing information.

This method was developed to reconstruct the arrival direction with a single IACT (Lessard et al., 2001). The DISP is defined as the distance between the image centre of the Hillas ellipse and the arrival direction of the shower, which is supposed to lie on the line through the major axis of the ellipse. Hence, there exist two possible solutions on either side of the ellipse as sketched in in figure 3.17 by the pairs 1A/1B and 2A/2B.The DISP parameter for each telescope is computed using a RF regression, where the RF is trained to minimise the variance $\sigma^2(p_{\text{est}})$ in the successor nodes similar to the novel energy RF:

$$\sigma^2(p_{\text{est}}) = \frac{N_1\sigma_1^2(p_{\text{est}}) + N_2\sigma_2^2(p_{\text{est}})}{N_1 N_2} \tag{3.9}$$

The features are the size, the impact, time gradient, zenith distance, height of the shower maximum, width and length.

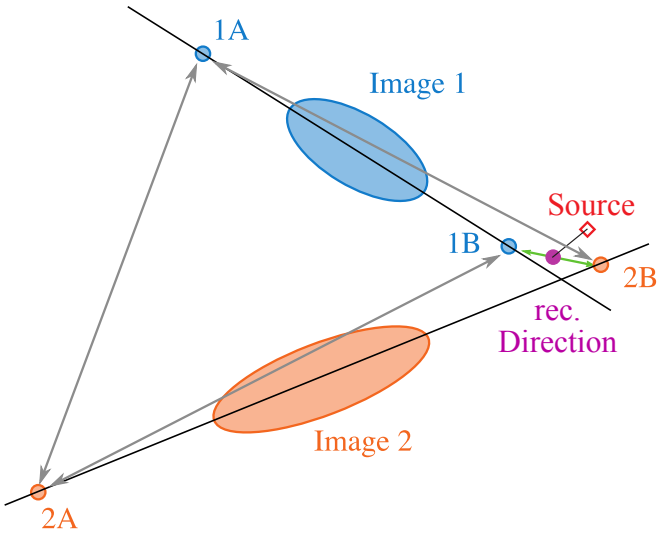

Figure 3.17.: Principle of the Stereo Disp method for the reconstruction of the arrival direction. The dashed line represent the shower axes of the images. The Disp RF estimates 2 possible arrival directions per telescope (1A/B and 2A/B). The two points with the closest distances are averaged weighted with the number of their pixels (purple point). The true source positions is marked with a red diamond. Figure adapted from Aleksić et al. (2016b).

The crossing point of the major axes, the asymmetry along the shower axis, or the time gradient may solve this ambiguity, called the head-tail discrimination (the latter two can be used for single telescopes). However, comparing the distances between the 4 reconstructed arrival directions (2 per telescope) proved to be the more robust procedure, particularly for small shower images at low energies. The two positions with the smallest distance are averaged weighted with the number of pixels of the corresponding image (purple point in figure 3.17). If the distances between all posi-

tions exceed a minimum value (0.22 ° in MAGIC), the event is discarded what affects between 10 % (at low energies) and 1 % (at high energies) (Aleksić et al., 2016b).

3.5.6. Performance of MAGIC

The performance of the MAGIC telescopes can be describe by the same instrument responses as the *Fermi*-LAT : the effective area $\mathcal{A}_{\text{eff}}$, the PSF $\mathcal{P}$, and the energy dispersion $\mathcal{D}$. Since the atmosphere is an integral part of IACTs, the telescopes, unlike satellite detector, cannot be calibrated in a laboratory. The only way to determine the instrument response is via Monte-Carlo (MC) event simulations. In MAGIC air showers and their Cherenkov light is simulated with the CORSIKA package (Heck et al., 1998). For the MC events used in this work the CORSIKA versions 6500 and 6990 were used. The telescope system is simulated with collaboration-owned programs, called reflector (simulating the optical system) and camera (light detector, noise, and readout electronics). After camera the simulated events undergo the same analysis chain as regular data. Using those MCs together with data, one can determine the accuracy of the IACT system.

Angular resolution

Like all imaging system, IACTs have a finite angular resolution described by the PSF. As in the case of the *Fermi*-LAT , the PSF is a probability density function $\mathcal{P}^{ij}_{\alpha\beta}$ for reconstructing a detected event in the bin $\alpha\beta$ instead of ij corresponding to its original arrival direction. It determines the minimum extension of a point-like source, placed at infinity, in the final reconstructed image.

Figure 3.18 shows the θ^2 distribution of the excess events from Crab Nebula observations. θ^2 is the square angular distance between the reconstructed arrival direction of an event and the assumed source position (the squaring counters the area increase with radius). Even though H.E.S.S. recently measured the extension of the Crab Nebula (H. E. S. S. Collaboration et al., 2019), the extension is still small compared to the MAGIC PSF and for short observation it can be considered point-like. A single 2D Gaussian falls short to account for the tails, but the shape of the data can be described by a 2D double Gaussian function (Aleksić et al., 2016b). Alternatively, Da Vela et al. (2018) found that a King function describes the PSF equally well as the 2D double Gaussian.

Events of higher energy have a larger size and spread over more pixels in the camera and consequently their arrival directions are better reconstructed. The resolution power with energy is displayed in figure 3.19 by the 68 % containment radius. It further shows that the MC PSF is smaller than the point source by $\sim 0.02^\circ$ (Aleksić et al., 2016b).

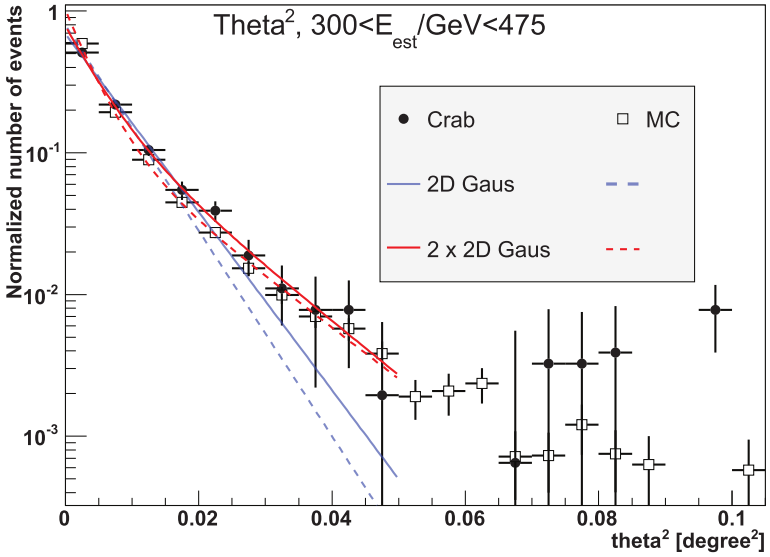

Figure 3.18.: θ^2 radial profile of excess event distribution from the Crab Nebula in the energy range between 300 and 475 GeV. The distribution is fitted with a 2D and a 2D double Gaussian projected into the θ^2 space. For comparison also the distribution of MC events and their corresponding Gaussian fits are shown. Figure adapted from Aleksić et al. (2016b).

Energy resolution

The energy reconstruction quality is evaluated from γ-ray MC events, for which the real energy E_{true} used for the simulation and the reconstructed energy E_{est} are know. By computing the relative difference

$$\delta E = (E_{\text{est}} - E_{\text{true}}) / E_{\text{true}} \tag{3.10}$$

for each event and fitting the δE distribution with a Gaussian, one can obtain the energy bias as the mean of the distribution and the energy resolution as its standard deviation. Figure 3.20 shows the energy resolution of the MAGIC telescopes from Aleksić et al. (2016b) using 5 bins per decade in E_{true}.

The energy bias is fluctuating around 0 % and the energy resolution around 18 % in the optimal energy range. Towards lower energies the bias increases rapidly due to the threshold, where just images, which are comparably large for its size, are recorded and thus mistaken for higher energetic events. At the highest energies events are not fully contained inside the camera any more. Furthermore, at the low and high energy edges the Gaussian approximation gets unreliable due to large tails of the δE-distribution. If one instead uses the RMS as an estimator, the resolution is between 20 % to 30 %. The reduced light yield at larger Zenith angles (blue graph in figure 3.20) results in a higher threshold, but less truncated images at higher energies.

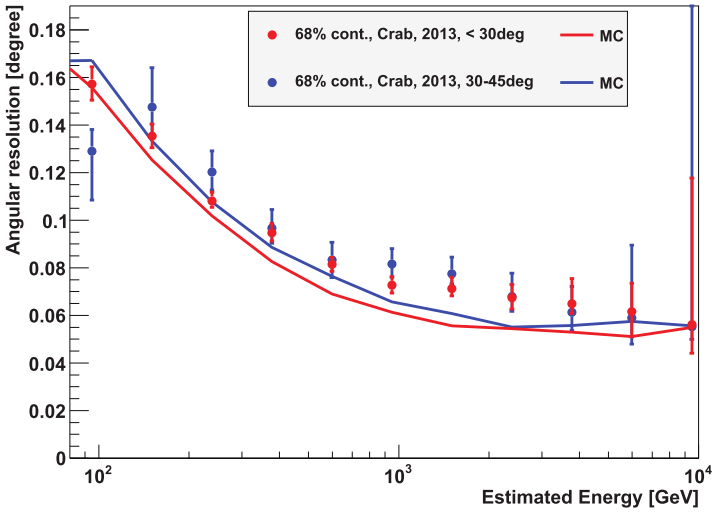

Figure 3.19.: Angular resolution of the MAGIC telescopes in terms of the 68 % containment radius as measured with Crab Nebula data and MC events for the low and medium Zenith range. Figure adapted from Aleksić et al. (2016b).

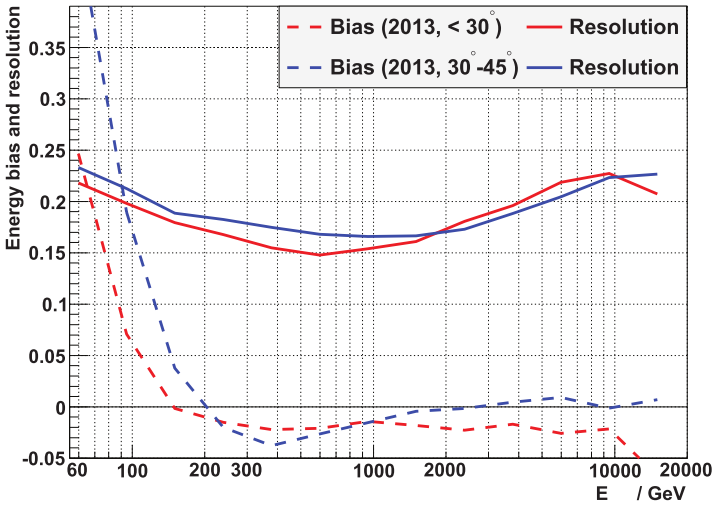

Figure 3.20.: Energy resolution (solid lines) and bias (dashed lines) of the MAGIC telescopes obtained from the MC simulations of γ-rays for low (red) and medium Zenith angles (blue). Figure adapted from Aleksić et al. (2016b).

Effective area

Well above the threshold the effective detector area of an IACT is determined by the physical size of the array and the size of the light pool, though large showers can be detected beyond the light pools. It is usually estimated with MC simulations, where the detection efficiency $\varepsilon_{\mathrm{Det}}$ is a ratio of the detected events to the simulated ones:

$$\mathcal{A}_{\mathrm{eff}}(E) = \frac{N_{\mathrm{det}}(E)}{N_{\mathrm{sim}}(E)} \times \pi r_{\mathrm{sim}}^2 = \varepsilon_{\mathrm{Det}}(E) \times \pi r_{\mathrm{sim}}^2 , \tag{3.11}$$

where N_{det} is the number of detected MC events, N_{sim} the number of originally simulated events, and r_{sim} is the maximum simulated distance between the impact point of the shower axis and the telescope (impact parameter), playing the role of an assumed physical detector size. The events inside an energy bin are weighted with an assumed spectral shape to slightly counter the energy dispersion.

Figure 3.21 shows the dependency of the effective area on the energy. The effective area sharply increases until $\mathcal{O}\left(10^2\,\mathrm{GeV}\right)$ and starts saturating above $\mathcal{O}\left(10^3\,\mathrm{GeV}\right)$. Aleksić et al. (2016b) explains the dip at $\sim 300\,\mathrm{GeV}$ with a change in the hadronness

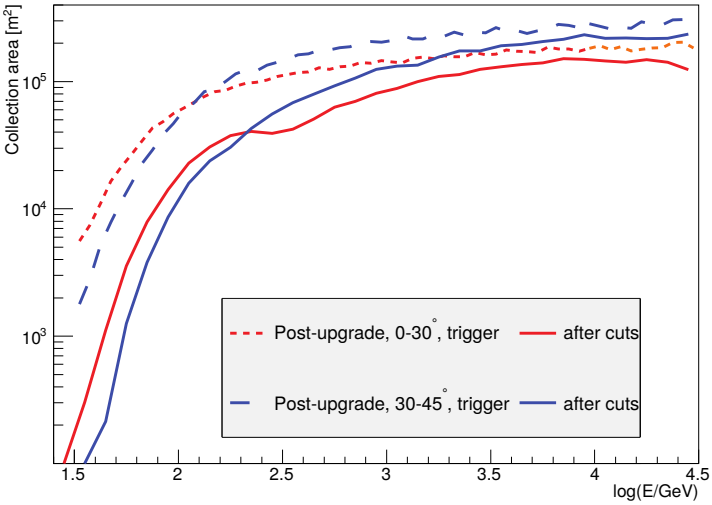

Figure 3.21.: Collection area of the MAGIC telescope for low (red) and medium (blue) zenith angle observations and the trigger (dashed) and high data level (solid). Figure adapted from Aleksić et al. (2016b).

cut. As described in section 3.4.2 at larger zenith angles the effective area is reduced at lower energies but saturates at a larger level.

Energy threshold

All instruments (figures 3.19, 3.20, 3.21) exhibit a rapid worsening below $\sim 10^2$ GeV. In this regime the telescopes gets sensitive to shower-to-shower fluctuations and only showers of comparably large size for their energy are recorded. Accordingly the recorded event rate does not follow the source spectrum, but decreases with lower energy. The turning point is considered the energy threshold of the instrument. Observations just below the threshold are possible, but the instrument responses change quickly in this regime and systematic uncertainties increase. The light reaching ground level depends on the depth and thereby on the Zenith distance Zd of the shower axis. Aleksić et al. (2016b) found the threshold to scale as

$$E_{\mathrm{th}} = 74 \cos\left(Zd\right)^{-2.3} \mathrm{GeV}\,. \tag{3.12}$$

Higher cleaning levels necessary for Moon observations decrease the recorded size and thereby increase the threshold. Ahnen et al. (2017) spotted that the threshold increases as

$$E_{\mathrm{th}}\left(I_{NSB}\right) = E_{\mathrm{th}}^{\mathrm{Dark}} \times \left(\frac{I_{NSB}}{I_{\mathrm{Dark}}}\right)^{0.4}, \tag{3.13}$$

with the NSB level I_{NSB} measured in terms of the DC level during the observations and under dark conditions I_{Dark}.

Sensitivity

The overall performance of the telescopes can be summarised by its capability to detect points sources at certain energy ranges. For Cherenkov telescopes the sensitivity is defined as the flux limit of a source that can be detected at $5\,\sigma$ confidence within

50 h of effective observation time. For simplicity the significance is given by the number of excess events N_{excess} over a background N_{bkg} as $N_{\text{excess}}/\sqrt{N_{\text{bkg}}}$. To make the estimation more realistic the MAGIC collaboration further requires $N_{\text{excess}} > 10$ and $N_{\text{excess}} > 0.05\, N_{\text{bkg}}$.

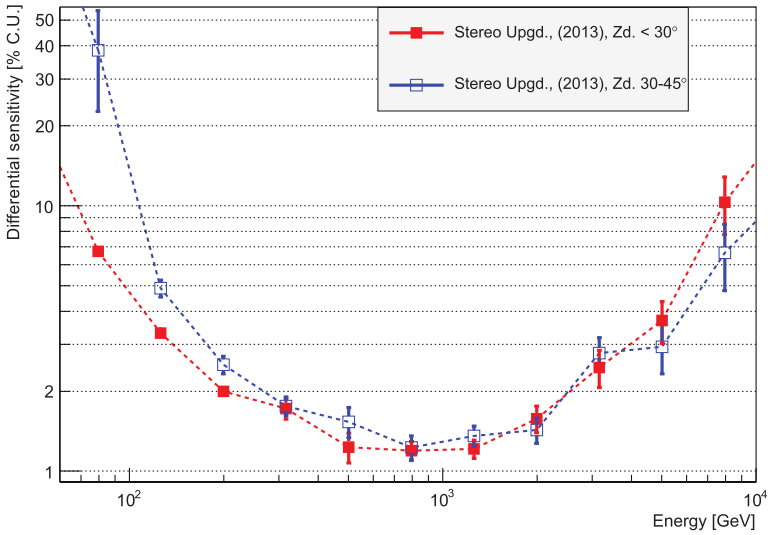

Figure 3.22.: Differential sensitivity in Crab units (C.U.) of the MAGIC telescopes in 5 energy bins per decade for different Zd ranges. The sensitivity is defined as the flux of a source resulting in a significant detection ($N_{\text{excess}}/\sqrt{N_{\text{bkg}}} = 5$) detection after 50 h of observation time. It is further required that the number of excess events $N_{\text{excess}} > 10$ and $N_{\text{excess}} > 0.05\, N_{\text{bkg}}$. Figure from Aleksić et al. (2016b).

Figure 3.22 displays the differential sensitivity in units of the Crab Nebula Flux at the corresponding energy. The curves show the sweet spot of the MAGIC telescopes at ~ 1 TeV, the degradation towards the detection threshold at lower energies, and limitation at larger energies. Longer observation times can improve the sensitivity at higher energies by increasing the event statistics, but not below the energy threshold at $E \lesssim 100$ GeV, where the sensitivity is limited by detector systematics. Furthermore the figure shows the curves for different Zd. Observations at larger Zd increase the energy threshold but also the effective area and thus the event statistics at higher energies.

3.5.7. Systematics uncertainties

Since IACTs can only be calibrated with limited precision and the atmospheric conditions not perfectly stable, the measurements are affected by systematic uncertainties. Since most of the sources observed with MAGIC are point sources, the MAGIC collaboration studied the sources of systematics uncertainties on the spectral reconstruction in (Aleksić et al., 2012) and updated them in Aleksić et al. (2016b). The sources of the systematic uncertainties are listed in table 3.2 and are sorted according to the param-

eter of a power-law function, which they affect: the absolute flux level, the energy scale, and the spectral slope. The studies are base on data-MC comparisons, muon

Table 3.2.: Values of the main sources of systematic uncertainties affecting the spectral reconstruction. They can affect the energy scale (ES), flux normalization (FN), and the spectral slope (SL). Table from Aleksić et al. (2012).

Systematic effect	Uncertainty	Affects
F-Factor	10 %	ES
atmospheric transmission	$\lesssim$10 %	ES
mirror reflectivity	8 %	ES
PMT electron collection efficiency	5 %	ES
light collection in a Wiston Cone	5 %	ES
PMT quantum efficiency	4 %	ES
signal extraction	3 %	ES
temperature dependence of gains	2 %	ES
charge flat-fielding	2-8 %	ES, FN
analysis and MC discrepancies	$\lesssim$10-15 %	FN
background subtraction	1-8 %	FN
broken channels/pixels	3 %	FN
mispointing	1-4 %	FN
NSB	1-4 %	FN
trigger	1 %	FN
unfolding of energy spectra	0.1 %	SL
non-linearity of readout	0.04 %	SL

calibrations, dedicated measurements of the telescope components, and comparisons of different analysis techniques and parameter settings (for details see Aleksić et al., 2012). Since the parameter are mostly independent they can be added in quadrature. For strong sources with a signal to background ratio of $\gtrsim$25% Aleksić et al. (2016b) found the total uncertainty to be $<$15% on the energy scale, 11%–18% on the flux normalisation, and $\pm$0.15 on the spectral index. For a softer source with a signal to background ratio of $\sim$5% the uncertainty of the flux normalisation increases to $\sim$20% and the uncertainty of the spectral slope to $\pm$0.25. The systematics uncertainties are smallest around the sweet sport of the performance at a few hundred GeV to TeV and increase towards the energy threshold ($<$ 100 GeV) and $>$ 1 TeV.

As morphological analyses usually based on two-dimensional, binned sky images, they are performed over a wide energy range to achieve a sufficient number of event counts per image bin. Hence, the systematic effects on the spectral reconstruction are less important. Instead the systematics arise from inaccuracies of the reconstructed PSF shape, Exposure shape, and distribution of background events over the FoV. To

study the effects on the final analyses results, the shape of the IRFs can be varied according to the statistical distributions defining them. The PSF can be enlarged by adding an random mispointing to the real or MC event used for determining the PSF. If the off-axis performance can be described by an analytical functions, alternative random models can be obtained by varying the parameters of this function (as e.g. described in section 4.4.1).

Bibliography

Acero, F. et al. 2016, The Astrophysical Journal Supplement Series, 224, 8

Aharonian, F., Buckley, J., Kifune, T., & Sinnis, G. 2008, Reports on Progress in Physics, 71, 096901

Ahnen, M. L. et al. 2017, Astroparticle Physics, 94, 29

Albert, J. et al. 2008a, Nuclear Instruments and Methods in Physics Research A, 594, 407

——. 2008b, Nuclear Instruments and Methods in Physics Research A, 588, 424

Aleksić, J. et al. 2011, The Astrophysical Journal, 742, 43

——. 2012, Astroparticle Physics, 35, 435

——. 2016a, Astroparticle Physics, 72, 61

——. 2016b, Astroparticle Physics, 72, 76

Antcheva, I. et al. 2009, Computer Physics Communications, 180, 2499

Atwood, W. et al. 2012, in 4th International Fermi Symposium Proceedings, Monterey, CA, USA, 8, arXiv:1303.3514

Atwood, W. B. et al. 2009, The Astrophysical Journal, 697, 1071

——. 2007, Astroparticle Physics, 28, 422

Bastieri, D. et al. 2005, in Proc. of the 29th International Cosmic Ray Conference, Pune, India, Vol. 5, 283

Bastieri, D. et al. 2008, in Proc. of the 30th International Cosmic Ray Conference, Mexico City, Mexico, Vol. 3, 1547–1550

Biland, A., Garczarczyk, M., Anderhub, H., Danielyan, V., Hakobyan, D., Lorenz, E., & Mirzoyan, R. 2008, in Proc. of the 30th International Cosmic Ray Conference, Mexico City, Mexico, Vol. 3, 1353–1356

Blackett, P. M. S. 1948, in The Emission Spectra of the Night Sky and Aurorae, 34

Bock, R. K. et al. 2004, Nuclear Instruments and Methods in Physics Research A, 516, 511

Breiman, L. 2001, Machine learning, 45, 5

Bretz, T., Dorner, D., Wagner, R. M., & Sawallisch, P. 2009, Astroparticle Physics, 31, 92

Da Vela, P., Stamerra, A., Neronov, A., Prandini, E., Konno, Y., & Sitarek, J. 2018, Astroparticle Physics, 98, 1

Doro, M. et al. 2008, Nuclear Instruments and Methods in Physics Research A, 595, 200

Fruck, C. 2015, PhD thesis, TU München, Munich, Germany

Fruck, C., Gaug, M., Zanin, R., Dorner, D., Garrido, D., Mirzoyan, R., Font, L., & for the MAGIC Collaboration. 2013, in Proc. of the 33st International Cosmic Ray Conference, Rio de Janeiro, Brasil, Vol. 5, 3143–3146

Galbraith, W., & Jelley, J. V. 1953, Nature, 171, 349

García, J. R. et al. 2013, in Proc. of the 33st International Cosmic Ray Conference, Rio de Janeiro, Brasil, Vol. 5, 3008–3011

Grieder, P. K. F. 2010, Extensive Air Showers (Springer, Berlin, Heidelberg)

H. E. S. S. Collaboration et al. 2019, Nature Astronomy, doi:10.1038/s41550

Heck, D., Knapp, J., Capdevielle, J. N., Schatz, G., & Thouw, T. 1998, CORSIKA: a Monte Carlo code to simulate extensive air showers., Tech. Rep. 6019, Forschungszentrum Karlsruhe GmbH

Heitler, W. 1936, The Quantum Theory of Radiation, 1st edn. (London, UK: Oxford University Press), reprinted 3rd edition (Dover Publication, 1986, New York)

Hillas, A. M. 1985, in Proc. of the 19th International Cosmic Ray Conference, La Jolla, CA, USA, Vol. 3, 445–448

Hörandel, J. R. 2007, Modern Physics Letters A, 22, 1533

Johnson, W. N., Grove, J. E., Phlips, B. F., Ampe, J., Singh, S., & Ponslet, E. 2001, IEEE Transactions on Nuclear Science, 48, 1182

Kohnle, A. et al. 1996, Astroparticle Physics, 5, 119

Lessard, R. W., Buckley, J. H., Connaughton, V., & Le Bohec, S. 2001, Astroparticle Physics, 15, 1

López-Coto, R., Mazin, D., Paoletti, R., Blanch Bigas, O., & Cortina, J. 2016, Journal of Instrumentation, 11, P04005

Maier, G., & Knapp, J. 2007, Astroparticle Physics, 28, 72

Matthews, J. 2005, Astroparticle Physics, 22, 387

Meegan, C. et al. 2009, The Astrophysical Journal, 702, 791

Mirzoyan, R., & Lorenz, E. 1997, in Proc. of the 25th International Cosmic Ray Conference, Durban, South Africa, ed. 7, 265

Moiseev, A. A., Hartman, R. C., Ormes, J. F., Thompson, D. J., Amato, M. J., Johnson, T. E., Segal, K. N., & Sheppard, D. A. 2007, Astroparticle Physics, 27, 339

Oser, S. et al. 2001, The Astrophysical Journal, 547, 949

Patrignani, C., & Particle Data Group. 2016, Chinese Physics C, 40, 100001

Sharma, M., Nayak, J., Krishna Koul, M., Bose, S., & Mitra, A. 2014, Research in Astronomy and Astrophysics, 14, 1491

Shayduk, M., Hengstebeck, T., Kalekin, O., Pavel, N., & Schweizer, T. 2005, in Proc. of the 29th International Cosmic Ray Conference, Pune, India, Vol. 5, 223

Sitarek, J., Sobczyńska, D., Szanecki, M., Adamczyk, K., Cumani, P., & Moralejo, A. 2018, Astroparticle Physics, 97, 1

Sobczyńska, D. 2009, Journal of Physics G Nuclear Physics, 36, 125201

——. 2015, Journal of Physics G Nuclear Physics, 42, 095201

Wagner, R. M. 2006, PhD thesis, Technische Universität München, Munich, Germany

Will, M. 2017, in AtmoHEAD 2016. Olomouc, Czech Republic, Vol. 144, 01002

Wood, M., Caputo, R., Rando, R., Charles, E., Digel, S., & Baldini, L. 2016, Fermi LAT Performance, `http://www.slac.stanford.edu/exp/glast/groups/canda/lat_Performance.htm`, Accessed: 2018-08-10

Zanin, R., Carmona, E., Sitarek, J., Colin, P., & Frantzen, K. 2013, in Proc. of the 33rd International Cosmic Ray Conference, Rio de Janeiro, Brasil, Vol. 4, 2937–2940

Chapter 4.

A novel spatial likelihood analysis technique for MAGIC

Note: partial results of this chapter, as well as appendix A, have been published in Vovk et al. (2018). I particularly contributed to the development of the programs generating the instrument response functions and the validation of the exposure and off-axis performance.

4.1. Data analysis in gamma-ray astronomy

As shown in the previous chapter, IACTs always measure astrophysical signals in the presence of an irreducible background; either coming from the background from isotropic cosmic rays (hadrons and electrons) or underlying diffuse, galactic and extra-galactic gamma-ray emission. Hence, statistical methods are required to establish the existence of a signal from a tentative source over possible background fluctuations and to extract the signal of the source.

After introducing the general statistical foundations, this chapter will explain the current analysis approach for IACT data and its limitations. It shows how these issues are overcome for γ-ray satellites and the analysis of Fermi Gamma-ray Space Telescope data is described. Finally I present a new analysis for IACT data based on the *Fermi*-LAT analysis and its application and validation using MAGIC telescope data.

4.1.1. The method of maximum likelihood

As shown in chapter 3, an IACT is an event counting experiment. Since the observation time, the detector size, and the energy range are finite and the events are usually binned (e.g. in time or arrival direction in the sky), each bin will contain a finite number of events n_{ij}. Since this work mainly deals with 2D skymaps, the bins will get the indices ij. The probability density P_{ij} for each bin to contain n_{ij} events given an

expected content of θ_{ij} follows a Poisson distribution:

$$P_{ij} = \frac{\theta_{ij}^{n_{ij}}\, e^{-\theta_{ij}}}{n_{ij}!} \tag{4.1}$$

In case of several bins, the probabilities can be combined into the likelihood function $\mathcal{L}$, but for computational convenience usually the logarithm of $\mathcal{L}$ is used.

$$\mathcal{L} = \prod_{ij} P_{ij} \tag{4.2}$$

$$\Rightarrow \ln(\mathcal{L}) = \sum_{ij} n_{ij} \ln(\theta_{ij}) - \sum_{ij} \theta_{ij} - \sum \ln(n_{ij}!) \tag{4.3}$$

The expected counts θ_{ij} are a function of a model f describing the signal and background emission, with the intensity of the signal and background being a set of free parameters ϑ of the model. By maximising the log-likelihood function by varying ϑ, one can find the parameter set that make f agreeing best with the observed data set X.

To make statements about the significance of a source and state confidence ranges for f, one needs to define a test statistics. According to the Neyman-Pearson lemma the test statistic giving the highest power at a given significance level is the likelihood ratio Λ (Neyman & Pearson, 1933). To construct the test statistics one varies ϑ in the whole parameter space Θ and compares the likelihood against the one for ϑ_0, where the sought component is fixed (parameter space Θ_0).

$$\Lambda(X) = \frac{\sup_{\vartheta\in\Theta_0} \mathcal{L}(f(\vartheta)|X)}{\sup_{\vartheta\in\Theta} \mathcal{L}(f(\vartheta)|X)} = \frac{\mathcal{L}(f(\hat{\vartheta}_0)|X)}{\mathcal{L}(f(\hat{\vartheta})|X)} \tag{4.4}$$

$$\Rightarrow \ln(\Lambda(X)) = \ln(\mathcal{L}(f_0)) - \ln(\mathcal{L}(f_1)) \tag{4.5}$$

If the null hypothesis f_0 is true, Wilks (1938) showed that the test statistics based on the likelihood ratio approximates a χ^2_k distribution (convergence in distribution) with k being the difference in the number of degrees of freedom between f_0 and f_1.

$$\begin{aligned} \Lambda &\xrightarrow{\mathrm{d}} \exp^{-\frac{1}{2}\chi_k}\left(1 + \mathcal{O}\left(1/\sqrt{n}\right)\right) \\ &\xRightarrow[n\to\infty]{\lim} -2\ln(\Lambda) \xrightarrow{\mathrm{d}} \chi^2_k \end{aligned} \tag{4.6}$$

This relates the likelihood ratio to a probability distribution, so in the limit of large event numbers one can easily define confidence intervals of a model. However, this procedure can only be used to test model f_0 against another f_1 as long as f_0 is nested within f_1, which means $\Theta_0 \subset \Theta$ and Θ_0 is in the interior of Θ, and $\mathcal{L}$ meets the regularity conditions from Protassov et al. (2002): $\mathcal{L}$ is 3 times differentiable with respect to θ, the derivatives are limited and the information/Hessian matrix is positive definite. Further, it shall be noted that the likelihood method and ratio cannot make any statements regarding the probability of the model itself. Besides, the conditions above limit the applicability regarding model selection. Models can instead be selected using dedicated methods such as the Akaike information criterion (Akaike, 1974).

4.2. The classical analysis approach for IACT data

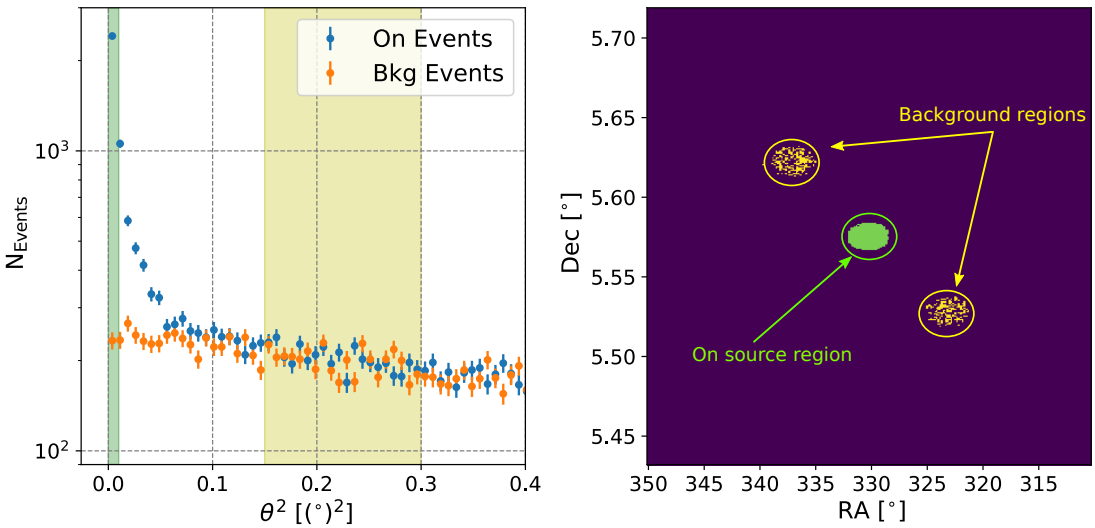

Figure 4.1.: *Left:* detection plot in γ-ray astronomy showing the count numbers depending on the distance square from the expected source position (blue) and with respect to a background position (orange). The background distribution is normalised to the source measurement in the source-free region (ochre). The significance of the signal to background is estimated in the green area. *Right:* position of the extraction regions for the signal (green) and the background (yellow) in the sky in equatorial coordinates.

The standard analysis approach of IACT data is based on a comparison of event counts from a source region with the counts from a control region without the source, called the Off region. This region is used as an estimate of the irreducible background level (see section 3.5.5) in the data. As the shape of the PSF of the MAGIC telescopes can be well approximated by a double 2D-Gaussian, the shape of point or just slightly extended sources will be roundish as well. Hence, in the standard approach the source and background regions are defined as circles around the corresponding positions source or background positions (green an yellow regions in figure 4.1 respectively). For each wobble usually one can define several Off regions. More off-source regions help in reducing the statistical fluctuations of the background estimate, but as they must not overlap one can just accommodate a certain number inside the MAGIC FoV; up to 7 Off-regions can theoretically be accommodated, but usually 3 are used.

As demonstrated in figure 4.1, the events from the On region (blue) and the average from the Off regions (orange) are binned in terms of θ^2. This way the geometrical factor is cancelled and the uniform Off distribution appears as flat. The distributions are normalised in a region far enough away from the source (ochre area) to overcome differences in the observation time. Finally one can compare the number of events in the region close to the source with the ones close to the off positions (green area).

4.2.1. Wobble mode

The Off data used to estimate background in the signal region need to be taken under the same conditions as the source data since any difference leads to a systematic miscalculation of the signal. The Off data sample needs to match the source data in terms of Zd, Az, camera position, and atmospheric conditions. Under stable conditions, this can be achieved by observing a skyfield without source that follows the same path along the sky as the sources. Such so-called On-Off observations are an established mode of observation for IACTs. However, given the stability requirement and the additional time needed for the Off observations, they are rarely used.

Instead for sources of limited extension ($< 1/2\,\mathrm{FoV}$), the established mode of observation is the so-called wobble mode (Fomin et al., 1994). The telescope points in an alternating way to coordinates at a fixed offset around the object as displayed in figure (left). In this way, On and Off date are taken simultaneously in either half of the camera. The alternation of the pointings cancels out possible inhomogeneities in the camera halves.

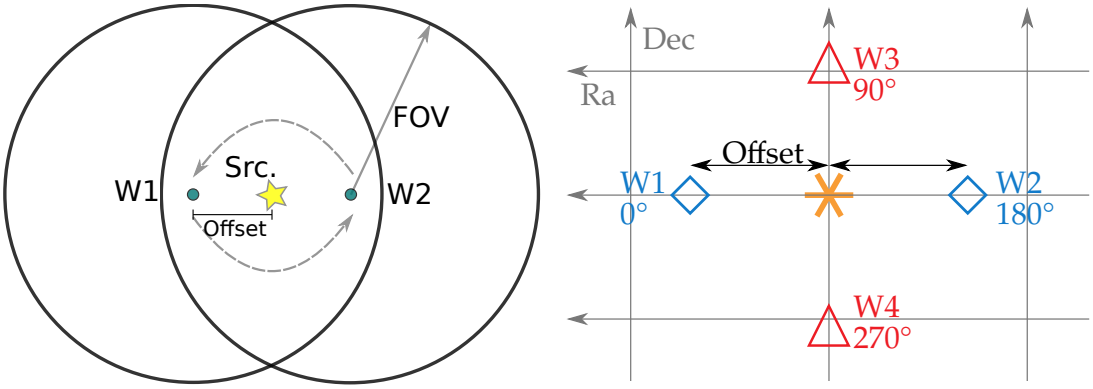

Figure 4.2.: Sketch showing the principle of Wobble mode observations.

The standard MAGIC observation uses two wobble pairs as depicted in figure 4.2 (right) : W 1 is combined with W 2 and W 3 with W 4. The pointings are defined by the offset between the camera centre and the target and the angle towards the positive right ascencion (RA) axis. The standard wobble offset is 0.4° and the wobble angles 0°/180° and 90°/270°. The angle and number of wobble positions can be adjusted according to the source morphology or to avoid bright stars.

4.2.2. Source detection

The corresponding statistical approach was developed by Li & Ma (1983) assuming the counts from the source region being $N_{\mathrm{on}} = N_{\mathrm{S}} + \alpha\, N_{\mathrm{off}}$ and the background region being N_{off}. The dimensionless scaling factor α comprises the observational differences between the On and Off measurement such as observation time and telescope orientation. Its estimation is usually a challenging task, but observational techniques like

the mentioned Wobble observation or the normalisation region are used to keep the influence under control.

Assuming the On and Off counts to obey the Poisson statistics 4.1 (On and Off region can be considered as a single bin) one can construct the likelihood ratio for the null-hypothesis, no source present, and the alternative hypothesis, source exists:

$$\Lambda = \left[\frac{\alpha}{1+\alpha}\left(\frac{N_{\mathrm{on}}-N_{\mathrm{off}}}{N_{\mathrm{on}}}\right)\right]^{N_{\mathrm{on}}}\left[\frac{1}{1+\alpha}\left(\frac{N_{\mathrm{on}}-N_{\mathrm{off}}}{N_{\mathrm{off}}}\right)\right]^{N_{\mathrm{off}}} \tag{4.7}$$

As the squared normal distribution follows a χ^2_1, the likelihood ratio can express the probability in terms of standard deviations of a standard normal distribution. Hence, the significance to reject the null hypothesis is:

$$S = \sqrt{2}\left\{N_{\mathrm{on}}\ \ln\left[\frac{1+\alpha}{\alpha}\ \left(\frac{N_{\mathrm{on}}}{N_{\mathrm{on}}-N_{\mathrm{off}}}\right)\right] + N_{\mathrm{off}}\ \ln\left[(1+\alpha)\left(\frac{N_{\mathrm{off}}}{N_{\mathrm{on}}-N_{\mathrm{off}}}\right)\right]\right\}^{1/2} \tag{4.8}$$

4.2.3. Flux estimation

If the existence of a source is established, its flux provides important insights into the physical mechanisms at work. The best estimate for the number of events from the source N_{S} is the number of excess counts N_{Excess}. The excess counts are obtained from the theta square histograms in each energy bin. By dividing N_{Excess} by the effective observation time t_{Eff} and the effective detector area $\mathcal{A}_{\mathrm{Eff}}$ one can compute the integral flux of the source in each energy bin:

$$F(E) = \frac{N_{\mathrm{Excess}}(E)}{t_{\mathrm{Eff}}\,\mathcal{A}_{\mathrm{Eff}}(E)}\,. \tag{4.9}$$

Since the arrival time of the events is Poisson distributed, the probability of detecting no event within the time t scales as $\exp^{-\lambda\, t}$, with λ being the average event rate. λ can be obtained by fitting the exponential to the distribution of the time difference between consecutive events. The effective observation time is finally defined by $t_{\mathrm{Eff}} = N_0/(1+\lambda\, d)$, where N_0 is the number of recorded events and d is the readout dead-time (Wittek, 2002). For MAGIC d is 27 µs.

The effective Area $\mathcal{A}_{\mathrm{Eff}}$ is subjected to the applied cuts in hadronness and size of the On region θ^2. Hence, it is estimated using Monte-Carlo events (MCs) selected according to the same criteria as for the data. Based on those MCs the effective area is computed following section 3.5.6 (precisely formula 3.11). The product of the t_{Eff} and $\mathcal{A}_{\mathrm{Eff}}$ is called the exposure. As $\mathcal{A}_{\mathrm{Eff}}$ depends on the pointing direction, the exposure is usually calculated in horizontal coordinate bins. The exposure of each bin can be summed up to obtain the total exposure.

If the Flux is calculated in several energy bins and a spectral shape is assumed according to which the events within a bin are weighted, the differential flux $\mathrm{d}F/\mathrm{d}E$

can be computed:

$$\frac{\mathrm{d}F}{\mathrm{d}E} = \frac{\mathrm{d}^3 N_{\mathrm{Excess}}(E)}{\mathrm{d}E\,\mathrm{d}t_{\mathrm{Eff}}\,\mathrm{d}\mathcal{A}_{\mathrm{Eff}}(E)}\,. \tag{4.10}$$

The weighting defines the central energy E_* of the bin and can be either chosen as the spectral weighted mean energy or e.g. according to Lafferty & Wyatt (1995). The differential energy spectrum is further weighted with E^2 to obtain the spectral energy distribution (SED). Its main feature is that it directly shows the energy output per logarithmic bandwidth.

If the source is not detected, an upper limit on the flux level can be placed instead. The methodology used in the MAGIC analysis is based on the likelihood of the source and background counts:

$$\begin{aligned}\mathcal{L}(g, b, \epsilon; N_{\mathrm{On}}, N_{\mathrm{Off}}) = \frac{(\epsilon g + b)^{N_{\mathrm{On}}}}{N_{\mathrm{On}}!}\exp^{-(\epsilon g + b)} \times \frac{(\tau b)^{N_{\mathrm{Off}}}}{N_{\mathrm{Off}}!}\exp^{-\tau b} \\ \times \frac{1}{\sigma_\epsilon\sqrt{2\pi}}\exp^{-\frac{1}{2}\left(\frac{\epsilon-\epsilon_0}{\sigma_\epsilon}\right)^2},\end{aligned} \tag{4.11}$$

where g and b are the predicted source and background counts and ϵ is a nuisance parameter covering the systematic uncertainties on the γ-ray efficiency. It is modelled with a Gaussian probability density function (pdf) with mean $\epsilon_0 = 1$ and standard deviation σ_ϵ. Using the "bounded" method from Rolke et al. (2005), the profile likelihood $\mathcal{L}_{\mathrm{p}}(g; N_{\mathrm{On}}, N_{\mathrm{Off}})$ is scanned to find the minimum g' and g_{up}, where $-2\log(\mathcal{L}_{\mathrm{p}})$ increases by an percentile α according to the Wilks theorem. If $g' > 0$, the upper limit is given by g_{up}. If $g' < 0$, the likelihood is scanned for the $-2\log(\mathcal{L}_{\mathrm{p}})$ increase not from g', but 0. The found upper limit in terms of counts can be converted into an upper limit on the flux level by substituting N_{Excess} with g_{up} in formula 4.10.

4.2.4. Spectrum deconvolution

Due to the limited energy resolution of the instrument and fluctuations in the measurement process the observed spectrum is different from the true spectrum of the source, but the true spectrum multiplied with the energy dispersion matrix $\mathcal{D}$:

$$\vec{g} = \mathcal{D}\cdot\vec{f}\,. \tag{4.12}$$

Even if $\mathcal{D}$ is not invertible, a solution for $\vec{f}$ can be found by minimising the least-squares estimate

$$\chi_0^2 = \left(\vec{g} - \mathcal{D}\cdot\vec{f}\right)^{\mathsf{T}} \boldsymbol{V}\left[\vec{g}\right]\left(\vec{g} - \mathcal{D}\cdot\vec{f}\right) \tag{4.13}$$

with $\boldsymbol{V}\left[\vec{g}\right]$ being the covariance matrix of $\vec{g}$. As $\mathcal{D}$ can contain large, non-diagonal entries, small fluctuations in $\vec{g}$ can easily lead to strong oscillations in the final spectrum. This effect can be remedied by adding a regularisation term Reg, whose strength can be controlled by a weight τ/w:

$$\chi^2 = \chi_0^2 + \frac{\tau}{2} Reg\left(\vec{f}\right) = \frac{w}{2}\chi_0^2 + Reg\left(\vec{f}\right) . \tag{4.14}$$

The regularisation imposes apriori restrictions on $\vec{f}$ resulting in a smoothing of the deconvolved spectrum. Hence, the reduction of the correlations of the components of $\vec{f}$ comes at the expense of a bias introduced in the estimate of the true spectrum. MARS contains different regularisation methods (see Albert et al. (2007) and references therein). Instead of deconvolving the measured spectrum, one can also find $\vec{f}$ by fitting an assumed spectral shape modified with the instrument response functions to the measured spectrum. This approach is called a forward folding. While no assumption about the smoothness of the spectrum is required, the approach requires knowledge about the shape of the true spectrum.

If the true spectrum S is know to some extent (e.g. due to previous measurements), the effect of the energy migration can also be corrected via $\mathcal{A}_{\mathrm{Eff}}$. By binning N_{det} in formula 3.11 based on the estimated energy E' of an MC event and N_{sim} according to the true energy E, $\mathcal{A}_{\mathrm{Eff}}$ accounts for the shift of events between the energy bins. This spill-over correction requires the shape to be known and even the parameters to be close to the real values:

$$\frac{\mathrm{d}F}{\mathrm{d}E} = \frac{N_{\mathrm{Excess}}\left(E_{\mathrm{min}} < E < E_{\mathrm{max}}\right) S\left(E_*\right)}{t_{\mathrm{Eff}} \int_0^\infty \mathrm{d}E \;\; S\left(E\right) \mathcal{A}_{\mathrm{Eff}}\left(E; E_{\mathrm{min}} < E' < E_{\mathrm{max}}\right)} , \tag{4.15}$$

where E_* is the central energy of the energy bin and the position, where the data point is placed (see above).

4.2.5. Limitations of the current approach

The classical analysis approach for IACTs as described is based on photon counting in certain regions in the FoV, sometimes referred to as "aperture photometry". With the advance of γ-ray astronomy however, telescopes are capable of detecting even fainter sources and resolve sub-structures of sources. This leads to cases where the current approach starts having issues such as the followings:

1. **Extended sources:** the flux is computed by equation (4.9) based on the excess counts in the source region and the effective area derived from Monte-Carlo events. However, the position of the photons and the MC events inside the source region is not considered and both quantities are averaged over the source region. As the effective area drops with distance to the camera centre, averaging the effective area is just correct and applicable if the source is sufficiently small and the acceptance is more or less constant over the source region. For large extended sources, this approach will lead to a systematic error in the flux

estimation. If the source morphology is not flat over the source region either, it can further increase this bias.

2. **Source shapes:** when detecting even fainter structures the found morphology of a source can get more complex deviating from a roundish shape. For extracting the full emission while keeping the signal-to-background ratio high, the apertures will become complex.

3. **Off-centred sources:** in case a source is found at a different than the expected position or another source is found inside the FoV, the On position (and accordingly the Off positions) may not have the same distance to each wobble position. It makes the computation of the α-factor very challenging and sometimes it is even impossible to define a normalisation region not containing emission, especially if there are several sources in the FoV.

4. **Overlapping emission regions:** by discovering more sub-structures in sources or observing crowded regions, such as the Galactic Centre, one likely encounters regions, where several source components overlap. Traditionally one fits a model to the dominating emission and subtracts the corresponding photon counts to obtain the second component alone. As source locations and fluxes are just known to a certain extent and the presence of the second source influences the fit of the first one, the obtained results will suffer from systematic errors.

Of those issues, some can be overcome also for the classical analysis approach. Issue 1 can be solved by re-weighting the Monte-Carlo events used for the effective area determination according to the expected source morphology. Issue 2 and 3 are related to the background determination. Their severity depends on the instrument's FoV and the pointing scheme. By adopting a different background determination method, such as the template background (Berge et al., 2007), one may resolve the issues at the cost of the uncertainties depending on the background model assumption. Finally issue 4 can never be overcome in the aperture photometry framework.

Besides those disadvantages the aperture photometry approach has certain advantages over the spatial likelihood method described in the following sections, among those are:

Model independence: the downside that the aperture photometry cannot tell the contributions from different sources apart, comes with the advantages that the results are model independent. It is thus less prone to errors in cases where the morphology of a source is unknown or cannot be derived using other wavelengths; given that none of the issues from above applies.

Short observation times: short observation times can result in noisy structures in the source and background region, which may spoil the fit of a 2D model to this data

set. The aperture photometry approach neglects structures within the extraction region and thus can operate with far less events than the likelihood approach. It just needs to have sufficient photons for the Wilks theorem to be valid. In case the number of counts falls below the limit, one can either calibrated the test statistics using Monte-Carlo simulations or use Bayesian statistics instead e.g. as in (Knoetig, 2014).

Aperture photometry thus remains a model-independent method for cross-checking the results of the likelihood analysis. In cases of variable and isolated point sources, such as AGNs, it may even be the more appropriate method. Still the issues listed are serious for mainly Galactic source and thus require the development of an alternative analysis method.

4.3. The *Fermi*-LAT data analysis

Due to its large field of view of 2.46 sr and its large point spread function at lower energies, the *Fermi*-LAT can apply the aperture photometry method in very few cases (e.g. for isolated points sources outside the Galactic plane). For sources inside the Galactic plane, overlapping sources are always unavoidable. Thus the standard *Fermi*-LAT analysis employs an approach based on the concept of the EGRET analysis as outlined in Mattox et al. (1996). Instead of just computing the likelihood function in the aperture region, it uses the likelihood in the entire FoV: a model $M\left(E, u, t; \alpha\right)$ with the parameters α is defined in terms of differential flux per sky area. By convolving the prediction of the physical model S with the instrument responses of the detector, one obtains the predicted integral counts C^{mod} of a certain arrival direction and energy:

$$C^{\mathrm{mod}}\left(E', u', t\right) = \iiint M\left(E, u, t; \alpha\right) \mathcal{A}_{\mathrm{eff}}\left(E, u\right) \times \mathcal{P}\left(u' | E, u\right) \; \mathcal{D}\left(E' | E, u\right) \; \mathrm{d}E \, \mathrm{d}\Omega \, \mathrm{d}t \tag{4.16}$$

The variables E and u denote the true energy and true direction respectively, while E' and u' are the measured ones. The instrument response function entering in the prediction are the effective area $\mathcal{A}_{\mathrm{eff}}$, the point spread function $\mathcal{P}$, and the energy dispersion $\mathcal{D}$, which were introduce in section 3.3.1.

Binning *Fermi*-LAT events in a 2D histogram in celestial coordinates, so-called skymaps, one can follow the likelihood approach outlined in section 4.1.1 since the counts in the LAT skymaps follow a Poisson distribution. The model is fitted to the data minimising

$$\ln(\mathcal{L}) = \sum_{ij} n_{ij} \ln\left(C_{ij}^{\mathrm{mod}}\right) - \sum_{ij} C_{ij}^{\mathrm{mod}} \,, \tag{4.17}$$

where the last term of equation 4.3 is model independent and can be omitted. To test the existence of sources or features, the LAT analysis use the likelihood ratio test (equation 4.5). The test statistics (TS) is defined as

$$TS = 2\left(\ln\left(\mathcal{L}(f_1)\right) - \ln\left(\mathcal{L}(f_0)\right)\right) . \tag{4.18}$$

Mattox et al. (1996) found that if the test statistics is used for testing the existence of a source, Θ_0 is on the edge of Θ and thus the requirements for the Wilks theorem are not fulfilled (Protassov et al., 2002). Instead TS is distributed as $1/2(\chi_0^2 + \chi_1^2)$ as derived by Chernoff (1954), where χ_0^2 corresponds to a $\delta(0)$ distribution. Hence, for $TS > 0$ the distribution follows $\chi_1^2/2$. Mattox et al. (1996) qualitatively explained it via a reduction of the statistical fluctuations to $1/2$ since the parameters of the additional source cannot be negative. If TS is used for testing model parameters such as the extension of a source, however, TS still follows a χ^2-distribution.

Beside the presented binned likelihood analysis, the Fermi Science Tools can also perform an unbinned likelihood analysis. The unbinned case uses the location of each photon and hence is more accurate, but also computationally more demanding. At the highest energies the number of photons per bin decreases and together with a fine grid binning the binned approach approximates the unbinned one. As the *Fermi*-LAT analysis used in this thesis focuses on the $>$GeV only and employs a binning smaller than the LAT PSF, the binned likelihood approach is used.

4.4. SkyPrism - the novel spatial likelihood analysis for MAGIC

The *Fermi*-LAT data analysis provided the concept for the development of the SkyPrism software suite applying this technique to data of the MAGIC telescopes: by applying the known IRFs to a 2D user-defined model of the emission, the programs can generate a model of the emission as it would be measured by the telescopes. As sketched in figure 4.3, together with a background model, this "realistic" model is fitted to the data sky map to obtain the flux parameter agreeing best with the data. Further binning the events in energy allows for obtaining SEDs.

This way the limitations of the standard approach outlined in section 4.2 can be overcome: the photons in the entire FoV are used to determine the flux, overlapping sources are fitted together, arbitrary source models can be supplied, and the 2D skymaps do not require a radial symmetric IRFs. The latter is crucial for the MAGIC telescopes as due to its configuration with just two telescopes no radially symmetric detector response can be assumed.

Such a likelihood approach is also considered for the analysis of the forthcoming

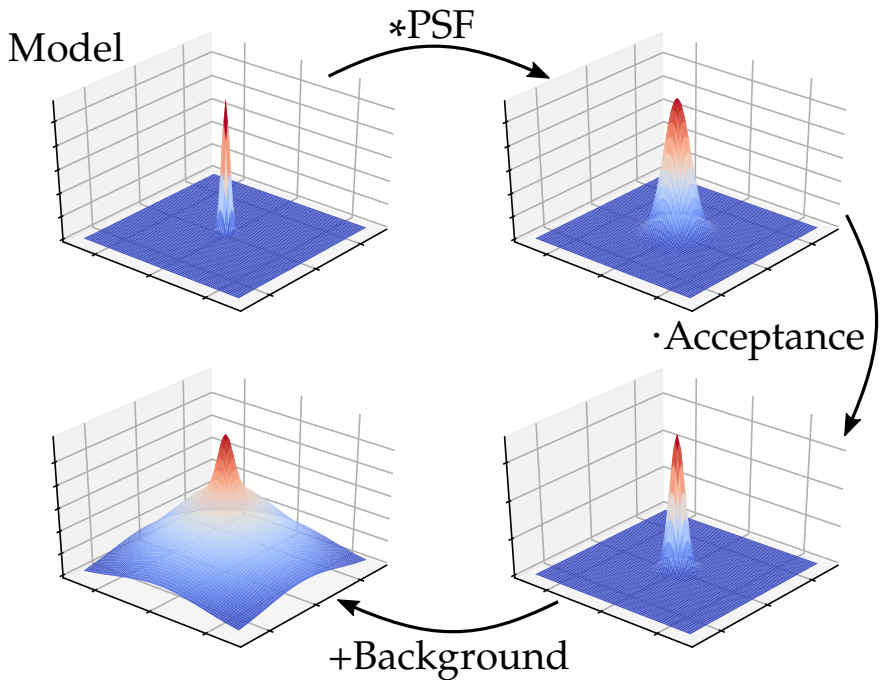

Figure 4.3.: Sketch illustrating the concept of the likelihood analysis technique

CTA in software packages like CTools (Knödlseder et al., 2016) or Gammapy[i] (Deil et al., 2017). Those packages differ from the work presented here in the way the IRFs are generated and require a parametrised background model or radially symmetric IRFs.

SkyPrism builds on MARS as it uses data, which are reduced using MARS up to the highest data level containing the results of the RF classifier, the energy estimation, and the disp stereo reconstruction. The events are read from the MARS events list which are in ROOT format. Thus for compatibility and efficiency, the programs generating the skymaps and IRFs are written in C++. The programs performing the likelihood fit instead are implemented in Python[ii].

4.4.1. Generation of the skymaps and instrument response functions

Sky map or On map

Skymaps, also called On maps, are 2D histograms in celestial coordinates containing all events passing the selection criteria. For those maps, SkyPrism uses the equatorial coordinate systems in the epoch of the supplied MAGIC data (currently J2000). If the data are also binned in energy, a skymap for each energy bin is generated. The cuts can be the event size or the hadronness. The first cut ensures that sufficiently large and thus well reconstructed events are used, while the latter controls the number of

[i] https://github.com/gammapy/gammapy
[ii] `https://www.python.org/`

background events. To create accurate models that can be fitted to the On Maps by SkyPrism, the IRFs and background map are generated using the same event selection.

Pointing history and sampling of events for computing the IRFs

The development of an air shower and thus the performance of the telescope depends on the pointing direction in the horizontal coordinate system (Azimuth/Zenith). In order to compute accurate background maps and IRFs, the telescope pointings are binned into Az/Zd histogram weighted with the time spent in the corresponding direction. These time weights are based on reports of the pointing direction that are written to the data at a rate of $9\,\mathrm{min}^{-1}$. Accordingly, the accuracy of the weights is limited to a few seconds, which is still sufficient. Since the depth of the atmosphere increase roughly $\propto \cos(Zd)$ and the performance parameters scale accordingly, the Zd is binned in terms of cos(Zd). The size of the pointing bins is left free to the user and is always a compromise between accuracy (smaller bins preferred) and event statistics (larger bins preferred).

The IRF estimation of an IACTs is dominantly based on Monte-Carlo simulations. To consider the changing telescope performance with time, the MAGIC Collaboration generates dedicated MC sets for so-called "analysis periods", over which the technical performance of the telescope is stable. To be applicable for any source analysis, these Monte-Carlo events are uniformly distributed over the observational sky. Out of this event set, only events, whose simulated pointing direction is located close to a populated pointing history bin, are used to generate the IRFs. The size of the acceptance box around the pointing bin centres can be chosen freely and by default agrees with the pointing history bins. As for the pointing history, the size balances the statistical uncertainty (depending on the event number) and the systematic uncertainties (events close to source track). This sampling method is used for the PSF and effective area. The background map generation instead requires sampling from measured events, which is explained in section 4.4.1.

The final IRFs are computed summing up the IRFs of all pointing bins weighted with the observation time. However, in order to sum them up properly, one needs to first bring all maps in the same celestial coordinate system.

Transformation between coordinate systems

While the instrument response depends on the horizontal coordinate system and the MC events are selected in the same, the skymaps in SkyPrism are in Equatorial coordinates since the sources and background emission rather depend on the skyfield. Except at the poles, the celestial equator is tilted against the horizon and one needs to transform the coordinates between the two coordinate systems. The level of mis-

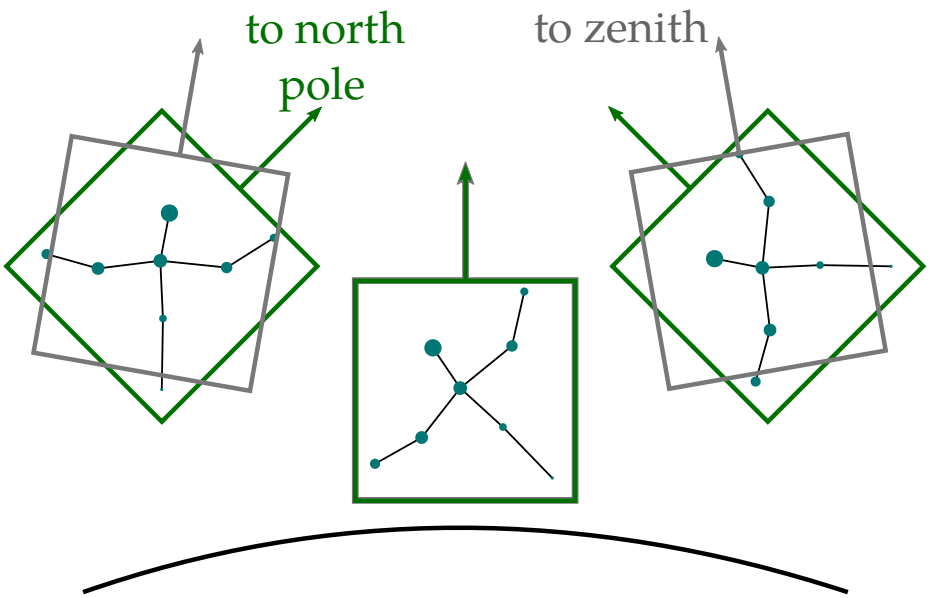

Figure 4.4.: Difference between the orientation of the horizontal and equatorial coordinates due to the misplacement of the geographical and the celestial north pole.

alignment depends on the geographic latitude of the observer ϕ. Figure 4.4 illustrates that the transformation changes with the position of the source and thus the rotation is performed for each bin of the pointing direction histogram.

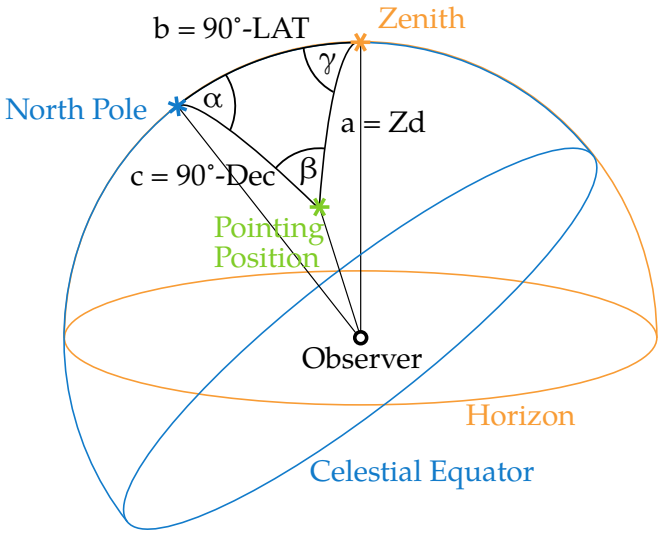

Figure 4.5.: Different Coordinate Systems. This figure is part of Vovk et al. (2018).

For usual observations, the horizontal and equatorial coordinates for the centre of the MAGIC camera are stored together with the data, so the time dependence of the transformation can be factored out. The transformation of the sampled IRFs from horizontal to equatorial coordinates is a rotation by an angle β. It can be computed using the so called navigational triangle shown in figure 4.5, which is formed by

the pointing position, the celestial north pole, and the zenith. As the azimuth γ, ϕ ($b = 90^\circ - \phi$, and the Zenith distance of the pointing a are given β can be calculated via:

$$c = \arccos\left(\cos\left(a\right)\ \cos\left(b\right) + \sin\left(a\right)\ \cos\left(b\right)\ \cos\left(\gamma\right)\right) \tag{4.19}$$

$$\beta' = \arcsin\left(\sin\left(b\right)\ \sin\left(\gamma\right)\ /\ \sin\left(c\right)\right) \tag{4.20}$$

$$\beta = \begin{cases} \beta' & \text{if } \cos\left(a\right)\cos\left(c\right) \leq \cos\left(b\right) \\ \pi - \beta' & \text{else} \end{cases} . \tag{4.21}$$

The rotated image is finally centred onto the known equatorial position of the centre of the pointing direction.

Background map

The likelihood analysis relies on accurate skymaps of the background shape throughout the FoV since it will become a component of the model. If the shape is not accurate it may spoil the fit and lead to a mismatch not just in one place but possibly anywhere across the map. In general the distribution is expected to resemble the camera acceptance to an isotropic γ-ray flux. For long exposures, however, the background skymap deviates from the γ-ray Monte-Carlo based exposure map. This discrepancies between data and simulations might be due to camera inhomogeneities in the data, which can be caused by dead pixels, stars in the FoV, imperfect flat-fielding of the camera, or a class of hadronic events surviving the cuts, but still having an acceptance distribution different to the one of γ-rays.

As a result, the background needs to be computed from measurements. SkyPrism contains three different versions to reconstruct a background exposure model from wobble-mode observations. Two of these alternatives are re-implementations of skymap generation techniques used in MARS (called wobble and blind map; Moralejo et al., 2009). The third method (exclusion map) is a refinement of the concept regarding generalisation and flexibility. All three methods follow the same basic scheme:

1. The events passing the selection criteria are grouped by wobble pointings and binned in horizontal coordinates. The binning of the background pointing history can deviate from the pointing history used for the other IRFs.

2. A 2D histogram binned in camera coordinates is filled for each wobble and pointing history bin.

3. For each pointing history bin, the program constructs one camera exposure model out of camera histograms of the different wobble pointings.

4. The background model in celestial coordinates is populated by random sampling from the corresponding camera exposure models and by applying the

correct coordinate rotations and observation time weights along the pointing track.

The methods vary in the way the camera exposures for each wobble pointing are combined into a single, supposedly source-free background camera exposure model (step 3). The available options illustrated in figure 4.6 are:

- **Wobble map:** the single camera exposures are divided into halves, such that the nominal source position (centre of the wobble setup) is contained in one half of the skymap. The the separating line between the halves is the normal to line through the source position and the camera centre. The combined background camera exposure model is obtained by normalising and summing the source-free halves. This method can only be applied if the γ-ray emission is confined in one side and does not extend beyond the wobble offset.

- **Blind map:** the single camera exposures are normalised by the exposure times. From these, the combined background camera exposure is obtained by taking the median value in each pixel. The median automatically suppresses large count contribution from a potential source. Strong sources will inevitably lead to an upward-bias of the background model in the corresponding regions, causing a systematic flux underestimation for these objects. On the contrary if only two wobbles are used, the blind map by construction underestimates the background. Since the background map in SkyPrism is fitted to the data, the latter, global bias, can be ignored in contrast to the first, local one. This method has the advantage that no prior knowledge about the position of sources inside the FoV is necessary.

  The implementation in SkyPrism deviates from the blind map mode in MARS, where the values in each bin of a wobble pair are compared and always the lower value is chosen. The downward bias is compensated for by a correction factor.

- **Exclusion map:** this method follows the same path as the blind map, but the user can specify regions containing known or expected sources, which can have circular or line shape. These regions are excluded from the computation of the median. Excluding too large regions must be avoided, as this leads to camera bins without background estimates.

Point spread function

The point spread function (PSF) can be estimated using the reconstructed and original arrival direction (as reconstructed by a perfect instrument) of MC events. The events are sampled according to page 82. For each event, the vector between the reconstructed

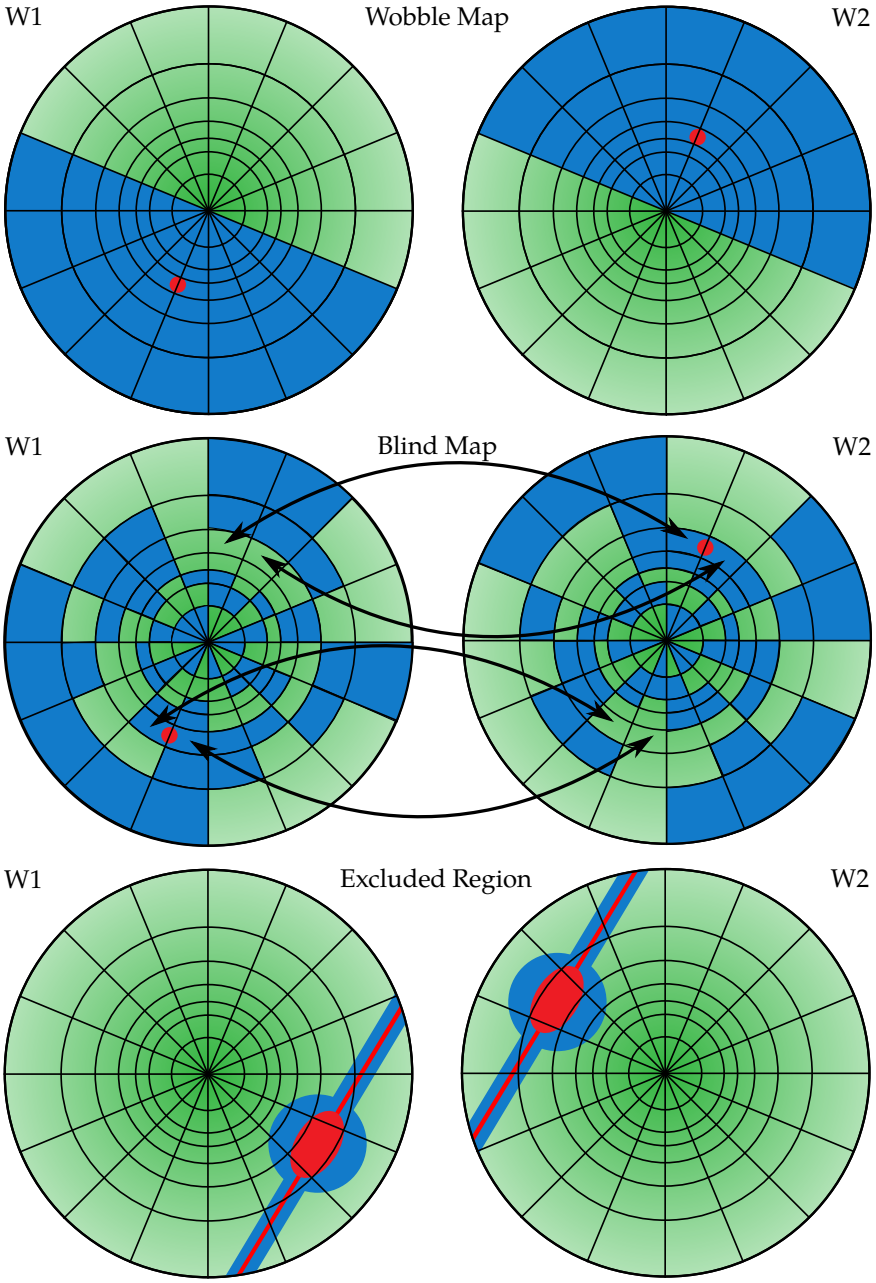

Figure 4.6.: Illustration of the different methods for the construction of a background camera exposure model from wobble observations (here one wobble pair). The source position and extension is shown as red point, ellipse, or stripe. The blue shading marks bins excluded from the background map reconstruction. This figure is part of Vovk et al. (2018).

and original arrival direction in camera coordinates is computed. This vector is finally rotated into the equatorial coordinate system according to section 4.4.1 and positioned at the centre of the corresponding pointing history bin. The sum of all events reflects the shape of a point source observed along the track of the target.

Since the number of MC events is limited, the simulated shape is noisy and is better modelled by a smooth, analytical function. As section 3.5.6 showed either a 2D double Gaussian or a 2D King function are viable options. Because of the lower number of free parameters, SkyPrism use the King function:

$$K(r, \sigma, \gamma) = \frac{1}{2\pi\sigma^2}\left(1 - \frac{1}{\gamma}\right)\left(1 + \frac{r^2}{2\sigma^2\gamma}\right)^{-\gamma}, \tag{4.22}$$

where σ sets the angular scale of the resulting profile and γ determines the weight of the tails. To allow for an asymmetry of the MAGIC PSF, the distance variable r is defined as:

$$\begin{aligned} x_r &= x_{\alpha\beta}\cos(\phi) - y_{\alpha\beta}\sin(\phi) \\ y_r &= x_{\alpha\beta}\sin(\phi) + y_{\alpha\beta}\cos(\phi) \\ r &= \sqrt{x_r^2 + (\epsilon y_r)^2}, \end{aligned} \tag{4.23}$$

where ϕ is a positional angle and ϵ is the asymmetry parameter, which accounts for the non-symmetry of the MAGIC system as well as the influence of the Earth's magnetic field. The King function is fitted during the conversion of the ROOT output to the intermediate FITS[iii] (Wells et al., 1981) format using the Python implementation of the Minuit minimiser (James & Roos, 1975), `iminuit`[iv]. Finally the obtained King function is evaluated on a sufficiently large grid around the camera centre.

Exposure map

Besides its energy dependence, the exposure is not homogeneous across the FoV. The limited extension of air showers and the size of MAGIC trigger area (see page 51) lead to a drop of the camera acceptance towards its outer regions, resulting in a non-uniform camera response to γ-ray events at different distances from the centre. Both effects are included in the MAGIC MC simulations.

As for the PSF, the MCs for a specified observation are sampled as outline on page 82. However, the pointing history of the data is not filled with only time weights, but with the effective observation time T_{eff} for each pointing bin. It is computed using the arrival time of the events in the corresponding bin, excluding gaps of more than 2 s, and correcting for the dead time of the trigger as described in section 4.2.3.

For the sampled events, the program computes the difference between the simulated pointing direction for the telescope and the arrival direction of the event, then

[iii] https://fits.gsfc.nasa.gov/fits_documentation.html
[iv] http://iminuit.readthedocs.io/en/latest/

transforms this vector to the equatorial coordinate system (see page 82), and adds it to the equatorial coordinates of the pointing bin. Each event is additionally re-weighted according to an assumed source spectrum with the weights $w(E) = F(E)/M(E)$, where $F(E)$ is the source spectrum and $M(E)$ is the energy spectrum used for the MC generation (usually a power law with index -1.6). To not spoil the count statistics $w(E)$ is corrected by $M(\bar{E})/F(\bar{E})$ where $\bar{E}$ is the geometrical mean energy of the corresponding energy bin. Thus, the re-weighting just affects the energy distribution inside the bin, but less the count statistics.

Due to the limited size of the MC sample, the statistical noise in the obtained maps can exceed the tolerance level of $\sim 5\,\%$ required for the accuracy of subsequent source analysis. To overcome this noise, we fit the efficiency map with a modified Gaussian function:

$$\begin{aligned} x_r &= x_{ij}\cos(\phi) - y_{ij}\sin(\phi)\,, \\ y_r &= x_{ij}\sin(\phi) + y_{ij}\cos(\phi)\,, \\ \vec{r} &= (s_1 x_r, s_2 y_r)\,, \\ l_x^2 &= [r - \arctan(r)]_x^2/(2\sigma_x^2)\,, \\ l_y^2 &= [r - \arctan(r)]_y^2/(2\sigma_y^2)\,, \\ \varepsilon_{ij}^{\mathrm{Det}} &= A \times \exp\Big\{(-(l_x^2 + l_y^2))\Big\}\,. \end{aligned} \tag{4.24}$$

This parametrisation reproduces the change of the MAGIC acceptance throughout the FoV for a wide range of energies, encompassing those that are usually selected for data analysis. To perform the fit, we assumed that the number of simulated n_{ij} and detected k_{ij} events in each camera pixel (ij) follows the binomial distribution

$$P_{ij}\left(k_{ij}|n_{ij}, \varepsilon_{ij}^{\mathrm{Det}}\right) = \binom{n_{ij}}{k_{ij}} \left(\varepsilon_{ij}^{\mathrm{Det}}\right)^{k_{ij}} \left(1 - \varepsilon_{ij}^{\mathrm{Det}}\right)^{n_{ij}-k_{ij}}\,. \tag{4.25}$$

Given the re-weighting with the assumed spectrum, this assumption is strictly not correct, but due to the above mentioned correction the deviation is sufficiently small. The best-fit is obtained by minimising the log-likelihood function

$$\ln(\mathcal{L}) = \sum_{ij} k_{ij} \ln\left(\varepsilon_{ij}^{\mathrm{Det}}\right) + \sum_{ij} (n_{ij} - k_{ij}) \ln\left(1 - \varepsilon_{ij}^{\mathrm{Det}}\right)\,. \tag{4.26}$$

The term $\sum_{ij} \ln \binom{n_{ij}}{k_{ij}}$ can be dropped as it does not depend on the function of interest $\varepsilon_{ij}^{\mathrm{Det}}$. The minimiser used is Minuit2[v] provided by ROOT estimating the parameters of the modified Gaussian model and their uncertainties.

Using equation 3.11, the efficiency models can be converted to collection area maps and by multiplication with the effective time T_{eff} to exposure models. In case of several bins this procedure is applied to each bin separately.

[v] `https://root.cern.ch/guides/minuit2-manual`

The fit of the efficiency model comes with uncertainties, which can be propagated to the flux extraction and spectral fitting. Therefore the program simulates a certain number of random representations (usually 100) of the model parameters ($A, \phi, s_1, s_1, \sigma_x$, and σ_y). The parameters sets are drawn from a multivariate Gaussian distribution with the best fit values as the mean and combined with the covariance matrix from the fit. The efficiency model of each random representation is converted to an exposure model and stored in an output file. It can later be supplied to the spectral fitting routines of SkyPrism.

Energy dispersion

The energy estimation algorithm in MARS can only reconstruct the energy of an event to a certain accuracy (see page 62). An event whose energy falls into a true energy bin k may thus be incorrectly classified into a reconstructed energy bin l. This transfer of events between the energy bins can be described by the 2D energy migration or dispersion matrix $\mathcal{D}_{kl}$:

$$C_{\text{obs}}\left(E'_l\right) = \sum_k \mathcal{D}_{kl}\left(E'|E\right) C_{\text{real}}\left(E_k\right) , \tag{4.27}$$

where $C_{\text{obs}}(E'_l)$ is the measured number of event counts and $C_{\text{real}}\left(E_k\right)$ the count distribution as emitted by the source. For convenience, the migration matrix is normalised along the reconstructed energy axis E'

$$\sum_l \mathcal{D}_{kl}\left(E'|E\right) = 1 , \tag{4.28}$$

which is equivalent to assuming that an event with true energy E will be with 100% probability contained in the E'_l set.

The energy matrix for a given observation is generated from sampled MC events and weighted in the same way as the PSF construction. For the PSF and exposure program, the user can switch between generating the IRFs in E or E'. By default, SkyPrism uses a wider energy range in true energy than in reconstructed energy, which is set by the user. This accounts for the possible spill-over of the events from energy bins outside the analysed energy range to those used in the analysis. By extending the energy range in E down to $1/3\, E'_{\text{min}}$ and up to $3 \times E'_{\text{max}}$[vi], we ensure that the lowest and highest true energy bins outside the considered range do not contribute more than 10% to the flux in the E' range. Furthermore, the number of bins in E is increased compared to E' to allow for an accurate flux reconstruction when changing the spectral parameters during the maximal likelihood fit and to account for possible sharp spectral features such as cut-offs or bumps. By default, the binning in the true energy is chosen to approximately match the energy resolution of the MAGIC telescopes, which is about 15-20% (Aleksić et al., 2016).

[vi] with $E'_{\text{min}} = \inf(E'_l)$ and $E'_{\text{max}} = \sup(E'_l)$

Conversion to FITS format and quick analysis

The previous programs save the obtain skymaps and models in the ROOT format. For a better interaction with the fitting procedure and to make these outputs usable in the astrophysics community, SkyPrism converts these to the **F**lexible **I**mage **T**ransport **S**ystem format[vii] (Wells et al., 1981). At this stage the PSF is fitted by a King function, while the fitting of the exposure map already happens in the exposure generation program.

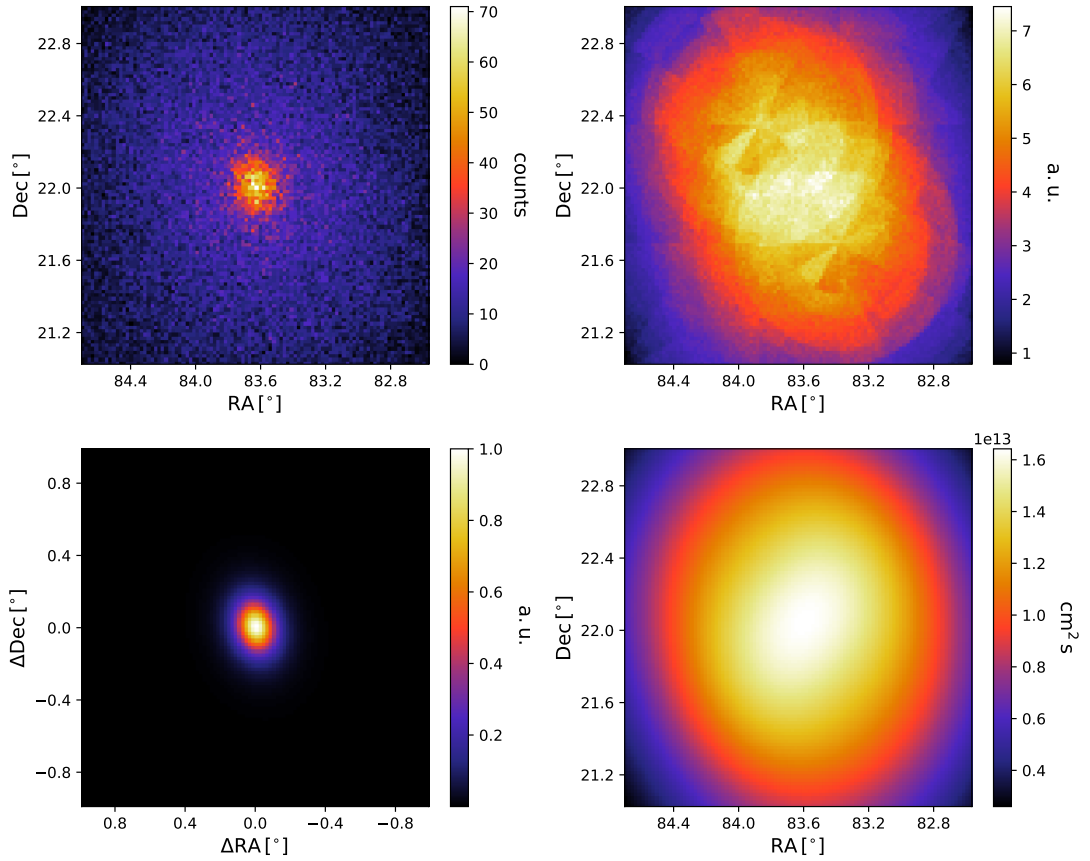

Figure 4.7.: On Map (upper left), background map (upper right), PSF (lower left), and exposure map (lower right) generated by the SkyPrism tools for a low Zd Crab observation. In the background map one can see the two wobble pointing positions used as well as the binning in camera coordinates.

The On map, background map, PSF, and exposure map for a Crab observation are shown in figure 4.7. The On map is in counts and the exposure is in cm^2 s. The PSF is normalised to the maximal value and the background map is in arbitrary counts due to the background reconstruction method in combination with the random sampling. The background level is obtained via the likelihood fitting. Hence, the fitting routines just require the PSF and background map to have the correct shape.

[vii] https://fits.gsfc.nasa.gov/fits_documentation.html

To check the outcome of the simulation and extraction tools, SkyPrism can generate simplified skymaps without the likelihood fitting. These are an excess map, a test statistic (TS) map, and a relative flux map. They allow assessing the possible outcome and serve as a robust cross-check for the likelihood results. For all three maps, the On and background maps are smoothed with a kernel of approximately the size of the PSF. The background model is scaled to match the On sky map in terms of the median, excluding the exclusion regions if this background option is selected, and subtracted from the latter giving the excess map. The relative flux map divides the excess by the scaled background. The TS is constructed by sampling 500 times from the non-smoothed background model, using Poissonian random numbers in each pixel. The obtained random representations are smoothed in the same way as the map. Due to the smoothing, the residuals of the background-subtracted simulations very closely follow a Gaussian distribution around zero in each pixel. The TS is thus defined as the local deviation in units of the Gaussian σ. A similar procedure is used in MARS to generate skymaps (Zanin et al., 2013). The TS values constructed this way are approximately significances in terms of a Gaussian σ. Still they provide a quick and robust estimate for the significance of a point source in the corresponding skymap bin.

Stacking of skymaps

As described in section 3.5.5 the data sample might be split according to weather and Moon conditions, but also due to periods of different hardware performance each requiring corresponding MC samples. In such a case, the On map, background map, and IRFs are generated for each data set separately. The resulting On $\mathcal{C}_i$, background $\mathcal{B}_i$, and exposure maps $\mathcal{E}_i$ indirectly, the exposure map even directly, consider the observation time differences between the samples and thus can be added:

$$\mathcal{E} = \sum_{i=0}^{n} \mathcal{E}_i \qquad \mathcal{C} = \sum_{i=0}^{n} \mathcal{C}_i \qquad \mathcal{B} = \sum_{i=0}^{n} \mathcal{B}_i \,. \tag{4.29}$$

The PSF and Migration matrix do not contain such weights, so their mean weighted with the exposures are used:

$$\mathcal{P} = \frac{\sum_{i=0}^{n} \mathcal{E}_i \mathcal{P}_i}{\sum_{i=0}^{n} \mathcal{E}_i} \qquad \mathcal{D} = \frac{\sum_{i=0}^{n} \mathcal{E}_i \mathcal{D}_i}{\sum_{i=0}^{n} \mathcal{E}_i} \,. \tag{4.30}$$

4.4.2. The likelihood fitting procedure

The extraction of the information of the observed sources, such as the flux and the extension, is performed by a set of Python routines, which can be accessed from a

user script. In this way, the fit and analysis procedure can be adapted to the user's needs. The fitting procedure combines background, PSF, energy migration matrix and exposure information obtained in the previous steps to provide the maximum likelihood estimate of the fluxes of the sources specified by the user.

As displayed in figure 4.7, the IRFs (e.g. exposure and PSF) are represented as 2D images for each of the energy bins where the analysis takes place; they are prepared by the tools described above and loaded at the moment of fitting. The source images are prepared during runtime based on the information given in the "source model":

- for point sources, the image contains one filled skymap bin at the specified source position;
- for extended sources, the image is taken either from a predefined FITS file or a 2D array defined by the user inside the analysis script.

The source maps are further interpolated to exactly match the pixel grid of the sky, background, and exposure maps. In each energy bin, the best-fit estimate of the source fluxes is obtained by maximising the Poissonian likelihood (see formula 4.1 and 4.3) of the measured number of counts $C^{\mathrm{obs}}_{\alpha\beta}$ given the source model $\mathcal{S}^{p}_{ij}$ (p denotes the source number in the model) and background $\mathcal{B}_{\alpha\beta}$:

$$C^{\mathrm{mod}}_{\alpha\beta} = \sum_{p} \left[\left(\mathcal{S}^{p}_{ij} \times \mathcal{E}_{ij} \right) \otimes \mathcal{P}^{ij}_{\alpha\beta} \right] + \mathcal{B}_{\alpha\beta} \tag{4.31}$$

$$\mathcal{L} = \prod_{\alpha\beta} e^{-C^{\mathrm{mod}}_{\alpha\beta}} \frac{{C^{\mathrm{mod}}_{\alpha\beta}}^{C^{\mathrm{obs}}_{\alpha\beta}}}{C^{\mathrm{obs}}_{\alpha\beta}!} \,. \tag{4.32}$$

$\mathcal{E}_{ij}$ is the exposure maps and $\mathcal{P}^{ij}_{\alpha\beta}$ the PSF model, mapping an (i, j) pixel to (α, β). Computationally the program minimises the negative log-likelihood $-\ln(\mathcal{L})$ using `iminuit`[viii]. Following the Wilks theorem the program computes the uncertainties on the obtained fluxes as deviations of the log-likelihood from its best value (formula 4.6) by $-2 * \Delta \log \mathcal{L} = \chi^2_1(\alpha)$ ($k = 1$ as there is only one parameter of interest: flux). α is the desired confidence quantile.

Additionally, we have also implemented a Markov chain Monte Carlo (MCMC) sampling procedure, based on the `emcee`[ix] (Foreman-Mackey et al., 2013) library, which allows a more accurate computation of non-symmetric error bars in case of strong correlations between the fit parameters (e.g. if overlapping extended sources are specified in the model).

In addition to the fit of individual source fluxes, the implemented procedure also allows for the source positions to be fitted. For this, the supplied source models $\mathcal{S}^{p}_{ij}$ are

[viii] http://iminuit.readthedocs.io/en/latest/
[ix] http://dfm.io/emcee/current/

shifted with respect to the originally specified position; the amounts of the shifts are optimised with the rest of the parameters during the fit. Hence, the procedure cannot adopt the source shape at a certain position. However, more sophisticated source position / extension scans can be easily implemented in the user analysis script by altering the source model and repeating the fit of the already loaded data.

When using the likelihood approach to test the existence of a source, similarly to the *Fermi* analysis (see section 4.3), the test statistics ($TS = -2\,\Delta \log \mathcal{L}$) of the true null hypothesis does not follow a χ^2_1. The test shown in figure 4.8 is based on $\sim 10^5$ trials on simulated empty skymaps. The skymaps are simulated using an isotropic model and simulating events along the track of an empty low Zd skyfield.

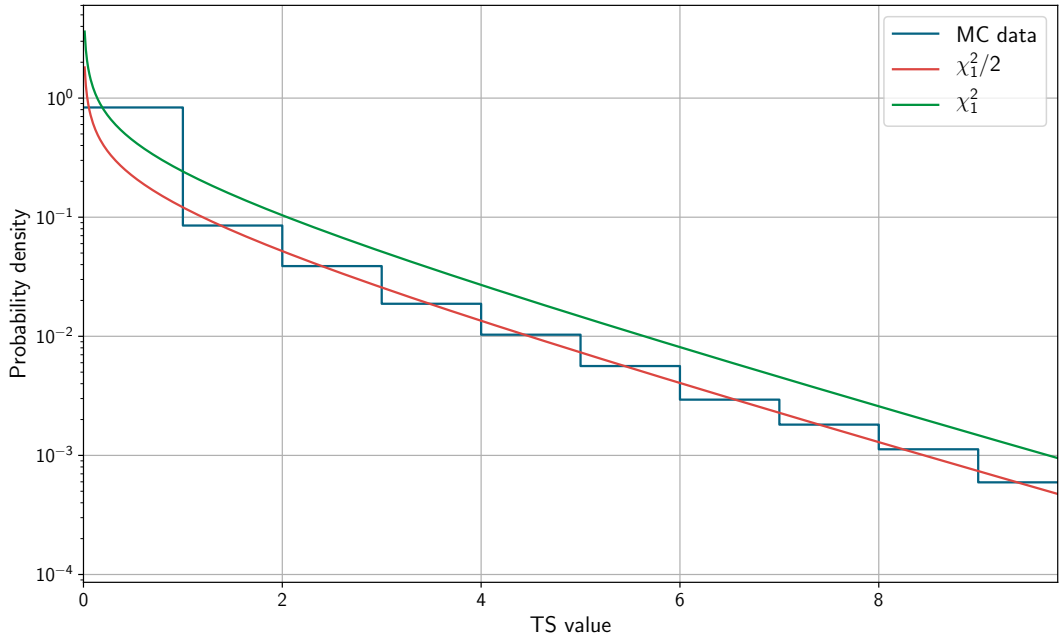

Figure 4.8.: Distribution of the test statistics values obtained for $\sim 10^5$ trials of a point source on mock simulated skymaps.

The obtained test statistic distribution is compare against a $\chi^2_1(\alpha)$ and $\chi^2_1(\alpha)/2$ distribution. As in the case of the *Fermi*-LAT analysis, the distribution for the null hypothesis and for $TS > 0$ seems to be best described by a $\chi^2_1(\alpha)/2$ function. Hence, the significance of a source in terms of a Gaussian σ can easily be estimated by $\sqrt{TS}$.

Likelihood fitting considering the energy migration

The previous procedure, even when using energy bins and fitting spectra, is using estimated event energies only. Thus, the obtained spectra still include the energy dispersion. Therefore the SkyPrism Python library can also fit in the true energy space via a forward-folding procedure.

In this case, the assumed source spectrum (which is part of the model component) is integrated in all true energy bins E_k, multiplied with the exposure, and convolved with the PSF corresponding to the E_k. Through a multiplication with the energy migration matrix, the predicted counts of each model component in the reconstructed energy bin E'_l are obtained. The sum of all components together with the background image (which is always constructed as a function of the estimated energy E' as it directly comes from the data) leads to the model counts in E':

$$C^{\mathrm{mod}}_{\alpha\beta}(E'_l) = \sum_{kp} \mathcal{D}_{kl} \left[\left(\mathcal{S}^{p}_{ij}(E_k) \times \mathcal{E}_{ij}(E_k) \right) \otimes \mathcal{P}^{ij}_{\alpha\beta}(E_k) \right] + \mathcal{B}_{\alpha\beta}(E'_l)\,. \tag{4.33}$$

The likelihood function in this case is defined as a product of all E' bins in formula 4.32, which is then optimised via the model parameters using the same routines as described in section 4.4.2.

In contrast to the fits in the estimated energy space (formula 4.31), the reconstruction of the flux points in the true energy space is not a well-defined procedure. It requires assumptions of the source spectral shape between the points (or, equivalently, inside the energy bins, defined in the true energy space).

In SkyPrism, such differential flux points are interpreted as the nodes of the source spectral model. The inter-node energies in the $\log E - \log dN/dE$ space are linearly interpolated. This is equivalent to a broken power law with multiple energy breaks at the position of the data points. The energies of the desired data points (nodes) can be chosen freely. The output of this fit can be used for instance to assess the validity of the chosen source spectral model. However, the resulting data points (along with their uncertainties) may be strongly correlated and cannot be used as independent measurements e.g. for performing a typical χ^2-fit.

4.4.3. Validation on MAGIC data

To ensure that the SkyPrism tools and routines work as expected, this section presents a series of tests for every part of the package. The tests compare the tool outputs based on the standard MAGIC MC simulations, which include the low-level data reductions presented in section 3.5.5, against (a) real data and (b) results of analyses with MARS.

Background map

Since the normalisation of the background is obtained during the maximum likelihood fit, the background model only needs to match the real background distribution in shape. A possible mismatch can be tested by comparing the model with

- an isotropic background, obtained through a simplified simulation of a typical MAGIC observation;
- the skymap for an observation of an empty region of sky.

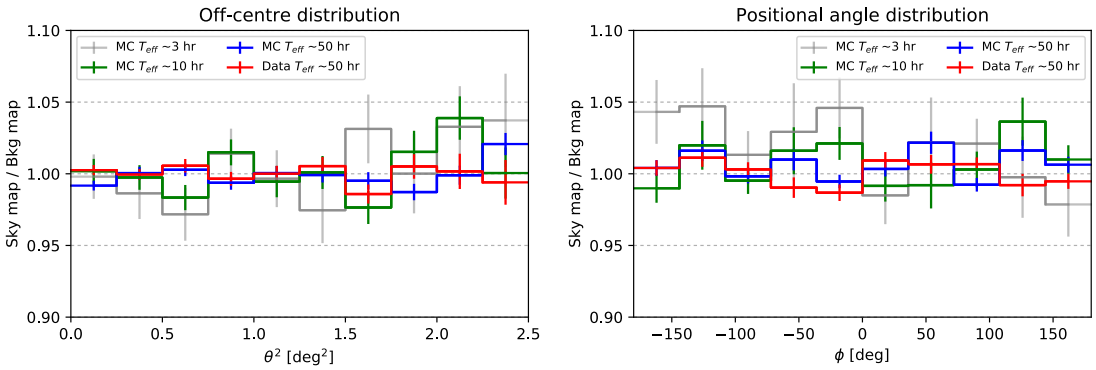

Figure 4.9.: Comparison of a simulated sky map with no source and a background profile, reconstructed from it with SkyPrism. We also show a similar profile, obtained from the real empty field data with the BlindMap method of the SkyPrism analysis. *Left*: Off-centre distribution. *Right*: Positional angle distribution; the zero-point is arbitrarily set to a horizontal direction. This figure is part of Vovk et al. (2018).

The simulation has the advantage of eliminating possible small variations of the real instrument performance, providing a consistency check of the procedure itself, whereas the comparison with real data demonstrates the overall performance with all the imperfections included.

For the comparison with the simulated events, a various number of events isotropically across the FoV are simulated along the track of low zenith angle observations (Zd $< 35°$) with MAGIC. The number of simulated events matches what is usually recorded using typical analysis criteria in the energy range above 100 GeV with exposure times of 3 to 30 hr. These events were supplied to the blind map procedure of SkyPrism, with no modifications to the reconstruction settings. In the absence of a source, the blind map is expected to provide the most accurate reconstruction.

The comparison of the simulated event distribution with the reconstructed background is displayed in figure Figure 4.9. The left panel shows the radial distribution of the simulated events (Sky map) with respect to the reconstructed background (Bkg map) as a function of the offset from the pointing centre. The performance of the reconstruction method degrades towards the edges of the field of view, where the acceptance of the camera and thereby the number of events drops. Still, spurious variations, resulting from the SkyPrism methods, do not exceed $\sim 5\%$ even for short exposures ($\sim$ 10 h). For longer exposures of $>$ 10 hours, variations are in general less than 2-3% in the 3.5 deg wide FoV. Similar conclusions can be drawn from the right panel, which depicts the reconstructed background variations as a function of the polar angle with respect to the observation pointing centre indicating that the any non-radial symmetry of the acceptance is correctly reproduced.

Additionally, the different background methods of SkyPrism can be compared to the On sky map of an empty sky region observed for 50 hr in standard wobble mode. The

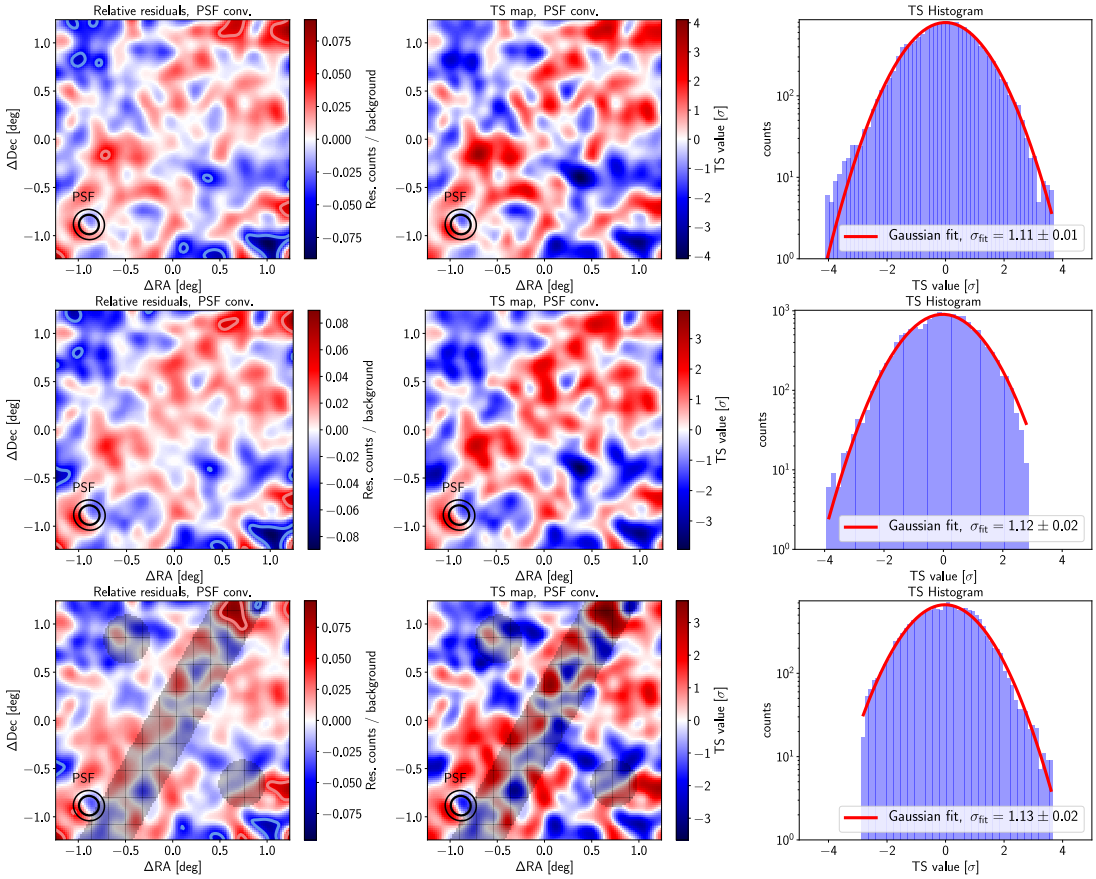

Figure 4.10.: Background methods tested with an empty sky region at Zd $< 35°$. Top to bottom: Wobble map, blind map, and excluded region map. For the excluded region map, the ignored regions (a stripe and two circles) are shaded. The PSF after convolution with a smoothing kernel is depicted in terms of 39% and 68% containment contours. *Left:* Ratio of the residuals (skymap-reconstructed background) to the skymap. The blue and red contours indicate $\pm 5\%$ relative flux boundary. *Centre:* Test statistic maps computed for the residual counts in the left panels. *Right:* Distribution of the test statistic values (blue histogram) compared to the expected normal distribution (red curve). This figure is part of Vovk et al. (2018).

maps are compared using the relative flux and TS map described in section 4.4.1. The results of this test are shown in figure 4.10. All three background estimation methods show a similar performance.

The distribution of the TS values matches the normal distribution well enough to not lead to detections of spurious sources in the image. This can be seen from the fitted σ_{map} values, given in each TS histogram plot of Fig. 4.10. These values are approximately 1.1 ± 0.02, indicating a slight excess in addition to the statistical fluctuations, which are supposed to be about 1. This excess likely comes from a shape discrepancy between the background model and the observed empty field. Assuming that the statistical error σ_{stat} and systematic uncertainty σ_{sys} of the model are both normally distributed, the contribution from the systematic component can be quantified as $\sigma_{\text{sys}} = \sqrt{\sigma_{\text{map}}^2 - \sigma_{\text{stat}}^2}$. This makes $\sigma_{\text{sys}} \approx 0.46$ in units of standard deviation of the simulated background maps, which is $\approx$ 1.8% of the background flux. It suggests that the systematic uncertainty of the SkyPrism background maps is $\sim 1\%$, which is comparable to the quoted systematics of the MAGIC telescopes (Aleksić et al., 2016).

It should be noted that the statistical uncertainty of the constructed background model depends significantly on the event selection criteria. For relaxed cuts and a wide energy range, similar to those used here, the relative statistical background uncertainty would scale with the observation time as $\sim 2\% \sqrt{50\,\text{h}/t_{\text{obs}}}$.

Point spread function

As mentioned in section 4.4.1, the MAGIC PSF in general is not circularly symmetric. This instrumental effect is covered by the MAGIC MCs, but not considered in the standard analysis, where just a circular source region is used (see section 4.2). Usually the source region is chosen to contain a significant fraction ($\gtrsim 75\%$) of the signal, so the positional angle dependence of the PSF has a minor impact on the reconstructed source fluxes in most of the applications of the standard MAGIC analysis chain.

For a 2D image analysis, as performed by SkyPrism, this effect cannot be neglected. Particularly towards large zenith angles the PSF has a non-circular shape and even for low Zd observation like in figure 4.7 the deformations are noticeable. Using a circular PSF could result in noticeable residuals and consequently a bias of the fit, especially in crowded regions. To ensure that the effect is properly reconstructed by SkyPrism, we performed a 2D fit of the reconstructed PSF profiles with the King function (see section 4.4.1). The shape parameters of the fit results can be compared against real data of a point source.

This comparison is performed using recent MAGIC observation of Mrk 421 at low and medium zenith angles in the energy range from 100 GeV to 10 TeV. The MC event selection (described in section 4.4.1) results in a limited number of MC events in the subsample towards the edges of the energy range. Therefore the highest (lowest) energy bin for the low (medium) zenith range analysis is dropped to avoid issues

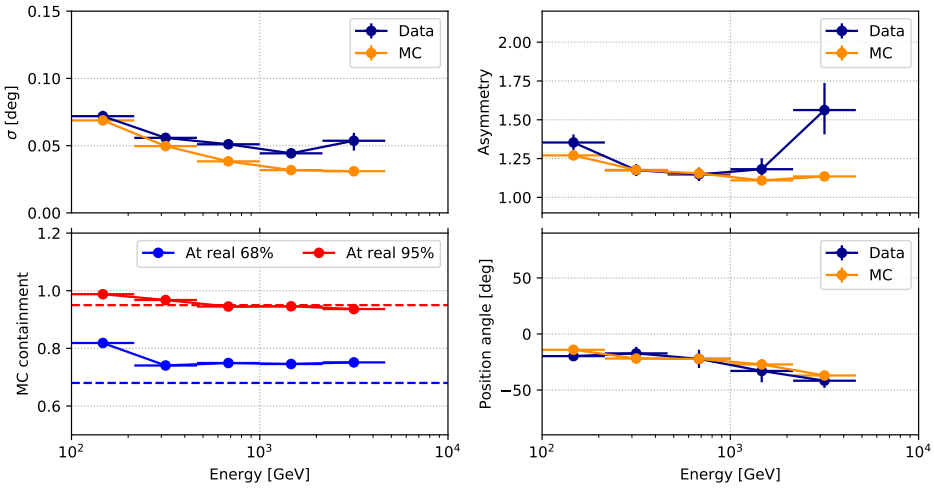

Figure 4.11.: Comparison of the MC PSF to the real data in the $0^\circ - 35^\circ$ zenith angle range, performed in terms of the King function fit. *Top left*: σ parameter of the King function, which defines the spacial scale. *Top right*: Asymmetry ϵ of the fitted profile. *Bottom left*: MC event containment, computed at the radial distance corresponding to the 68% (95%) data containment radius. *Bottom right*: Positional angle ϕ of the non-symmetric PSF extension. This figure is part of Vovk et al. (2018).

related to the low statistics limit.

Figure 4.11 and 4.12 show the comparisons of the King function fit results to the low and medium zenith angle data sample as well as to the corresponding MC PSF profile, computed with SkyPrism. It is evident that the MC based PSF is sharper than the real source profile; the relative event containment difference is $\sim$ 10%, estimated at the angular distance, where the measured event containment is 68%. At larger distances, corresponding to 95% containment of the real data, the MC data mismatch is reduced to $\lesssim$ 5%. This is comparable to the results obtained in Aleksić et al. (2016).

The excessive peakedness of the core of the MAGIC MC PSF has been shown earlier on page 61. In practice, an additional systematic random component of $\sim 0.02^\circ$ should be added in order to compensate for the difference of MC to the data (Aleksić et al., 2016). Adding a 0.02° smearing to the MC PSF results in $\lesssim$ 5% residuals in the 2D data-to-model comparison plots, shown in figure 4.13, throughout the entire PSF extension.

Certain small differences between the MC estimated PSF and real data, apparent in the right panels in Figs. 4.11 and 4.12, play a second-order role when the MAGIC mispointing is considered. We have checked that the largest deviation in asymmetry for the $0^\circ - 35^\circ$ zenith angle (Fig. 4.11) range comes from the low number of counts in the source image in the energy bin 2.1 - 4.6 TeV. At larger zenith angles in Fig. 4.12, the difference between the MC and real PSF asymmetries in the 215 - 464 GeV bin appears significant because only very few MC events survive the selection cuts, which results in a significant underestimation of the corresponding error bars.

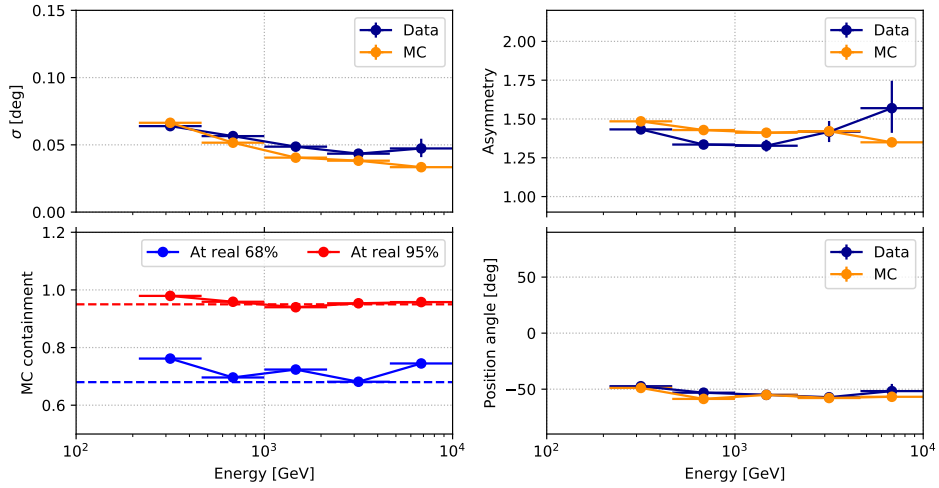

Figure 4.12.: Comparison of the MC PSF to the real data in the $35° - 50°$ zenith angle range, performed in terms of the King function fit. The panels are the same as in Fig. 4.11. This figure is part of Vovk et al. (2018).

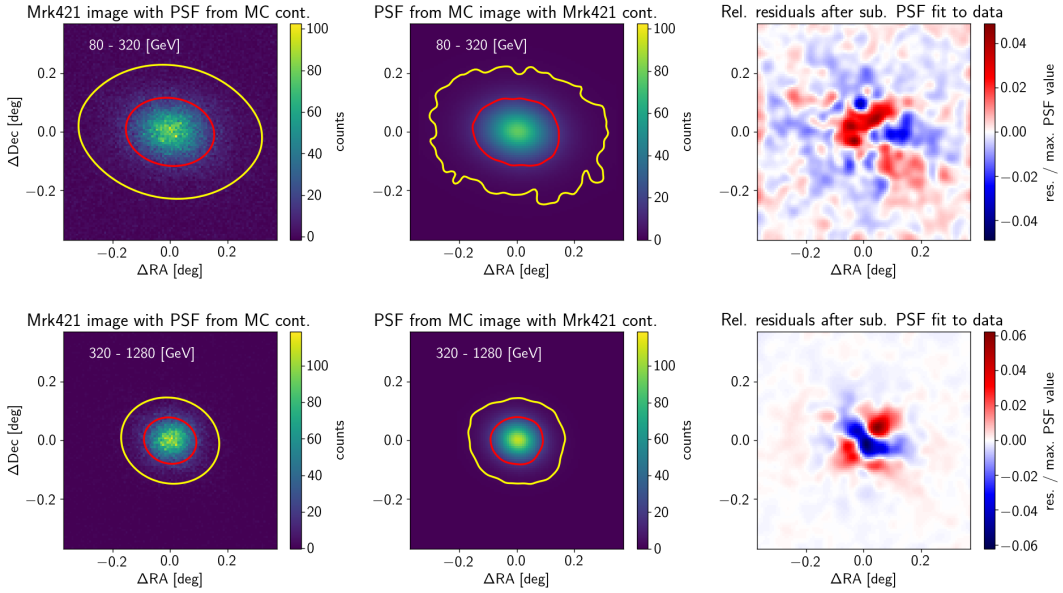

Figure 4.13.: PSF model validation on Mrk421 data taken at zenith angles $< 30°$ in two energy ranges: 80 GeV to 320 GeV (top group) and 320 GeV to 1280 GeV (bottom group). First column: source images with the 68% and 95% level contours of the corresponding PSF model; second column: PSF model with the 68% and 95% containment contours of the sky map. Right column: residuals after subtracting the normalized PSF model from the sky image. This figure is part of Vovk et al. (2018).

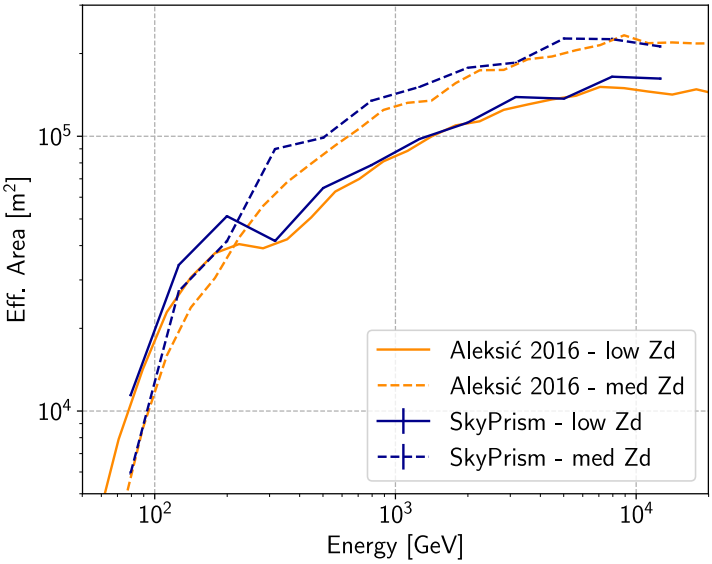

Figure 4.14.: Effective area vs. energy as estimated with the SkyPrism package compared to the standard MAGIC analysis from Aleksić et al. (2016). This figure is part of Vovk et al. (2018).

Overall, the comparison above demonstrates a reasonable agreement between the MC PSF model, computed with the presented software, and real data.

Exposure map

As described in section 3.5.6, the effective area primarily depends on the energy. For a point source, SkyPrism should reproduce the same energy dependence of the effective area as displayed in figure 3.21. Since those results were obtained with the aperture photometry approach, this approach needs to be reproduced: an circular aperture is cut out if the effective area map and the effective area inside is averaged by weighting each bin according to the PSF distribution. In this way, one obtains the effective area curve for a point source inside a certain area. The size and the data set used were the same as in Aleksić et al. (2016).

Figure 4.14 shows the comparison of the SkyPrism result for low (Zd $<$ 30°) and medium (30° $<$ Zd $<$ 45°) zenith range with those from figure 3.21. The curves obtained with both methods agree for all energies within 20%. The discrepancy may well result from the difference in the approaches as they can just be made compatible to a certain extent. Furthermore, the SkyPrism analysis uses MC events distributed over the whole camera, whereas the analysis from Aleksić et al. (2016) uses the simulation of a point source at an offset of 0.4°.

As the exposure program should further compute the effective area correctly across the entire FoV, it needs to properly reproduce the telescope off-axis performance. Aleksić et al. (2016) measured the rate from the Crab Nebula depending on the offset pointing distance from the source to determine the off-axis acceptance. The measured rate and the effective area off-axis dependence differ only by one factor, determined by the integral spectrum of the source above a given energy. Since this factor is a constant (for steady sources such as the Crab Nebula), the measured rate and the effective area

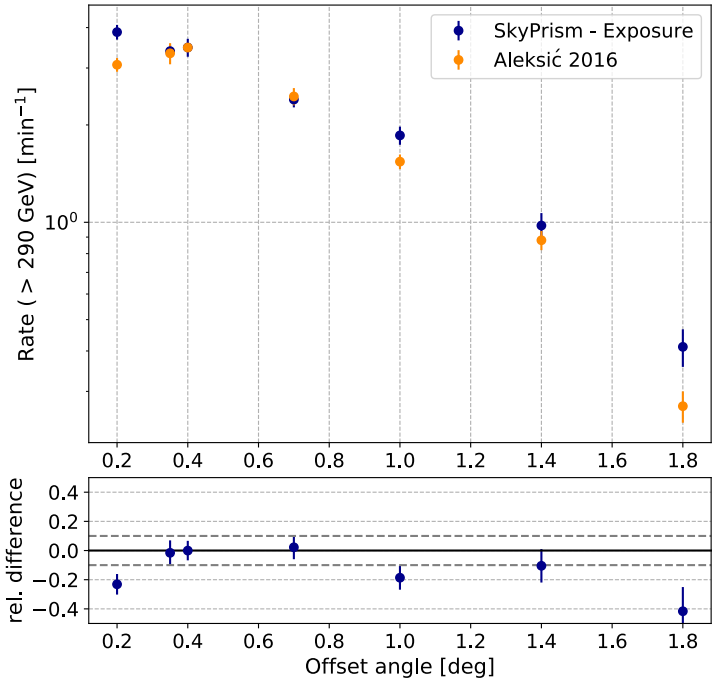

Figure 4.15.: Crab Nebula count rate as a function of the off-axis angle. Orange points correspond to Aleksić et al. (2016), and the blue points denote the estimates from the SkyPrism exposure model, obtained for the same data and selection cuts. The bottom panel shows the relative difference between the two data sets at each offset angle. This figure is part of Vovk et al. (2018).

have the same off-axis angle dependency.

We computed the effective area for the off-axis data sets of the rate measurement. The effective area was extracted for each off-axis angle separately in the same way as for the energy/effective area comparison. By multiplying the effective area at each offset with the integral spectrum extracted with SkyPrism at 0.4° offset one obtains the expected rate. Figure 4.15 shows that the effective area estimates agree with the measurements in nearly all bins within the error bars, and the relative difference is less than 20% except for 1.8° offset. The MAGIC MC simulation include events up to 1.5° offset, hence the data point at 1.8° is based on the extrapolation from the fit to the exposure model, and thereby only approximately correct.

Considering the differences in the approaches of SkyPrism and the standard MARS analysis, as well as the limited FoV in the MC simulations, the estimations and measurements of both procedures agree. Hence, the SkyPrism package is able to correctly compute the effective area across the MAGIC FoV.

Stability of IRFs across FoV

In contrast to the exposure and background map the PSF and migration matrix are are not generated for each position in the FoV individually. Instead all MC events accepted for the IRF computation are used to create one single response used over the entire FoV. Since the FoV and the trigger area is limited, the PSF and migration matrix may change across the FoV as the exposure does. Hence, it is important to check how much the PSF and migration matrix depend on the position in the camera, mainly the distance from the camera centre. Using one averaged PSF and migration matrix may

otherwise lead to a bias when applied to sources observed at a certain distance from the camera centre.

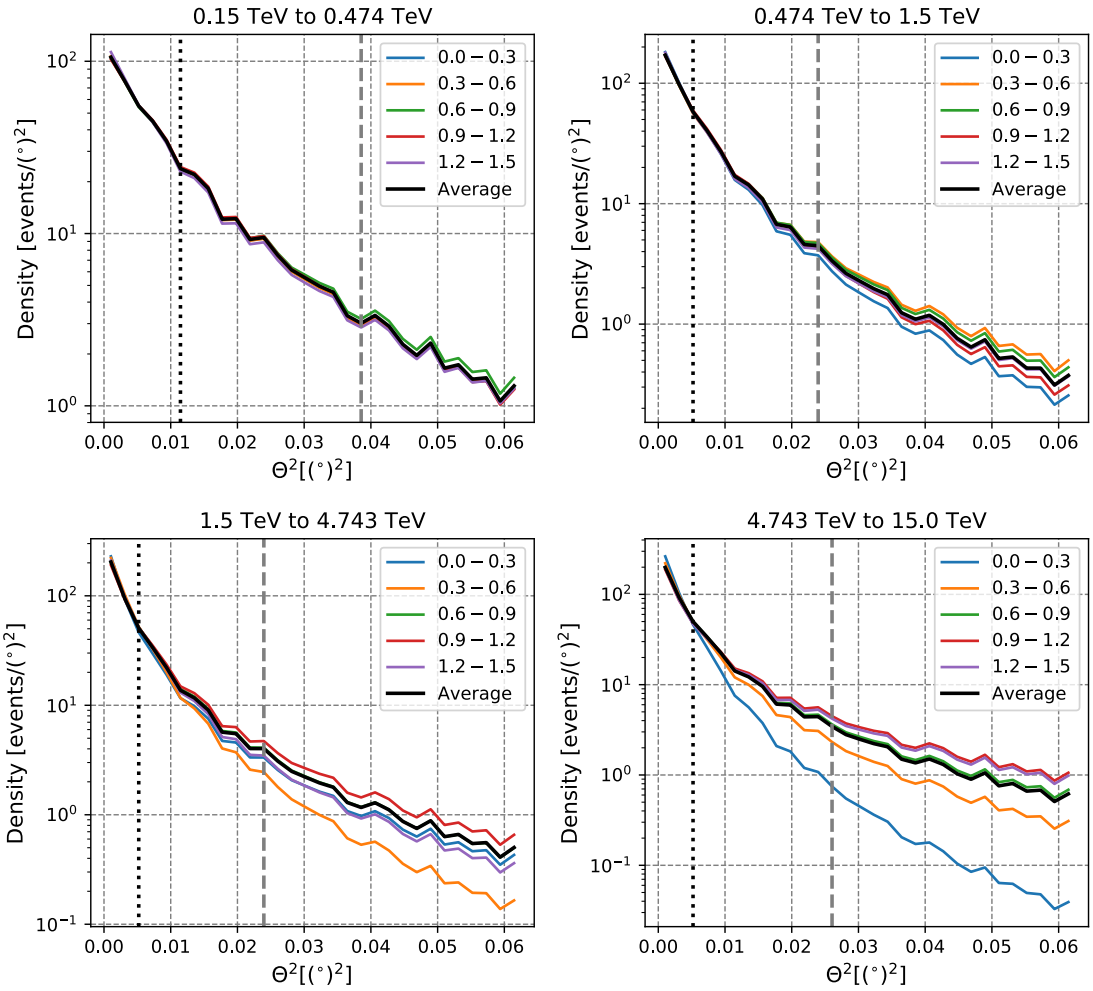

Figure 4.16.: θ^2 profile of fitted Point spread function based on MC events from different camera offsets in the energy range between 150 GeV and 15 TeV binned in two bins per decade. The black graph uses all MC events and agrees with the PSF used in SkyPrism. The dotted (dashed) line indicates the 68 % (95 %) containment radius of the averaged PSF.

Figure 4.16 shows the PSF depending on the camera offset for several energy ranges. Each PSF is based only on MC events from the corresponding camera offset range, fitted with the King function (see 85), and evaluated on a fine grid. The PSFs are compared in terms of their θ^2 profile. The breaks of the lines are a result of the binning of the grid. The black line shows the PSF based on the MC events of the entire FoV as it is used by default in the SkyPrism analysis. At the lowest energies the PSF agree well inside the 68% and 95% containment radius of the default PSF indicated by the dotted and dashed grey lines respectively. However, already at 474 GeV to 1.5 TeV differences in the tail of the PSF become visible. Only at the highest energies the PSF

starts deviating inside the 95% containment radius for the PSF of the region close to the camera centre, which seems much sharper than at other offset ranges. The arrival direction for the shower is usually different from the place in the camera where the shower image is located. Showers with a reconstructed arrival direction at the centre of the camera predominately correspond to shower images at 0.3° to 0.6° camera offset. Thus even showers at the highest energies are more likely to be completely contained in the camera resulting in a better reconstruction of the arrival direction. Since the PSF inside the 68% containment radius agrees and, due to the wobble mode, sources are rarely observed at the camera centre only, the deviation from the average PSF is not expected to affect the analysis even at the highest energies. Nonetheless, for On/Off observation the deviation should be considered.

The migration matrices generated with MC at certain camera offset are displayed in figure 4.17 in terms of their relative difference to the average migration matrix based on the MC from the whole FoV. At energies $< 1\,\mathrm{TeV}$ and along the diagonal the relative differences are smallest, while off-diagonal they can reach values up to $\pm 100\%$. In general the migration matrix at the outer camera regions seem to agree better with the average migration matrix than the one from the inner regions.

Since most of the events fall into bins along the diagonal (see containment contours in figure 4.17), it is difficult to judge the influence of the off-diagonal entries where the deviations from the average migration matrix are largest. To test the effects onto the spectrum, the migration matrices are multiplied with an Crab Nebula spectrum in event counts. The Crab Nebula spectrum from Aleksić et al. (2016) is multiplied with an effective area for the Crab Nebula position, which is extracted in the same way as for the test of the effective area. Figure 4.18 shows the relative difference between the count spectra modified with the different migration matrices and the count spectrum based on the average matrix. As for the matrices the count spectra show little differences $< 1\,\mathrm{TeV}$ and even for higher energies the deviation from the average spectrum are $< 10\%$, except for the innermost part of the camera. The higher the energy of a shower the farther the centre of gravity is offset from their constructed arrival direction in the camera. High energetic showers with a reconstructed arrival direction towards the centre of the camera thus on average belong to a camera image towards the edge of the camera where they are likely prone to leaking out of the camera.

The same effect can be seen in figure 4.19 comparing the SED reconstructed with the migration matrices at different camera offsets. Using the average migration matrix the reference spectrum is transformed into a count spectrum, which is then fitted with a forward folded spectrum based on the migration matrices at the different camera offsets. This way one can assess the effect of the migration matrix on the obtained spectra.

The black line in figure 4.19 indicates the reference SED from Aleksić et al. (2016)

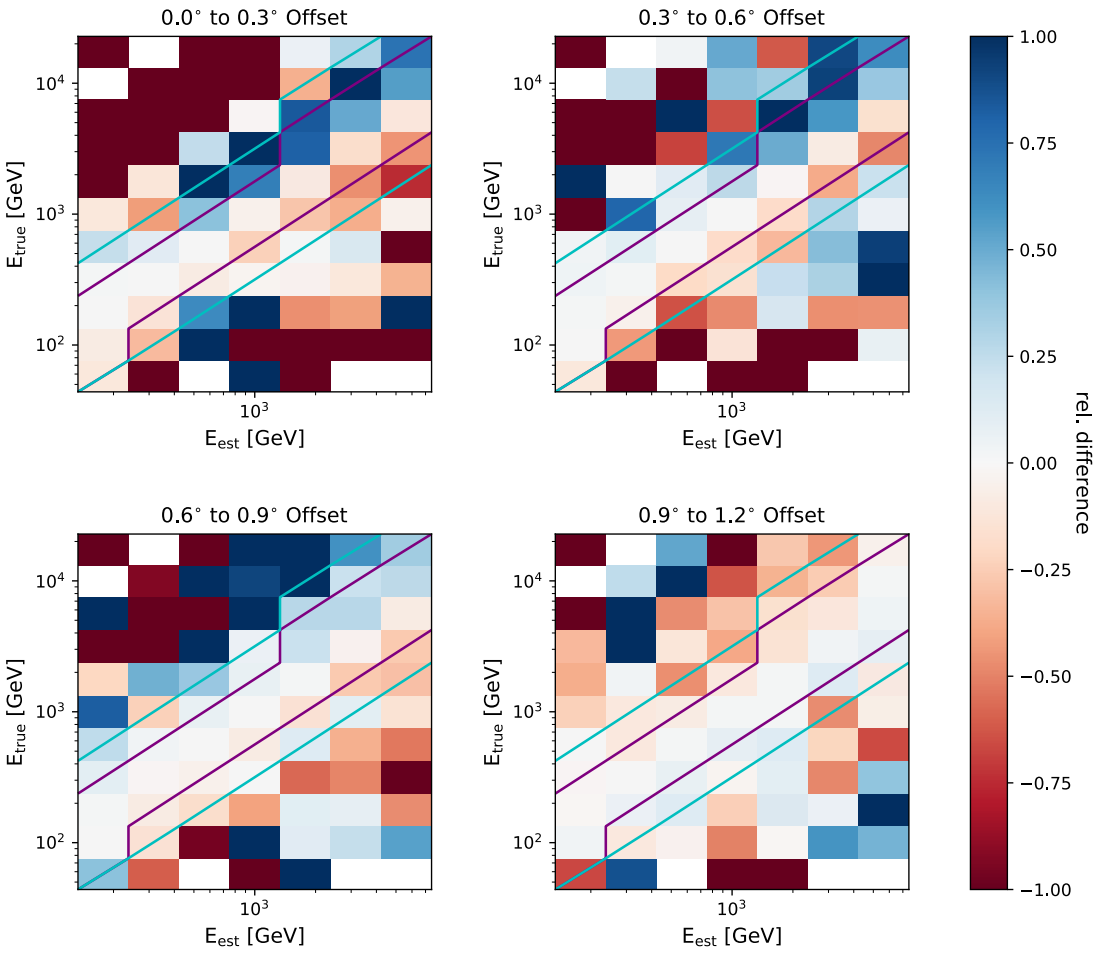

Figure 4.17.: Relative difference of the migration matrix at different camera offsets and the migration matrix with MC events of the entire FoV.

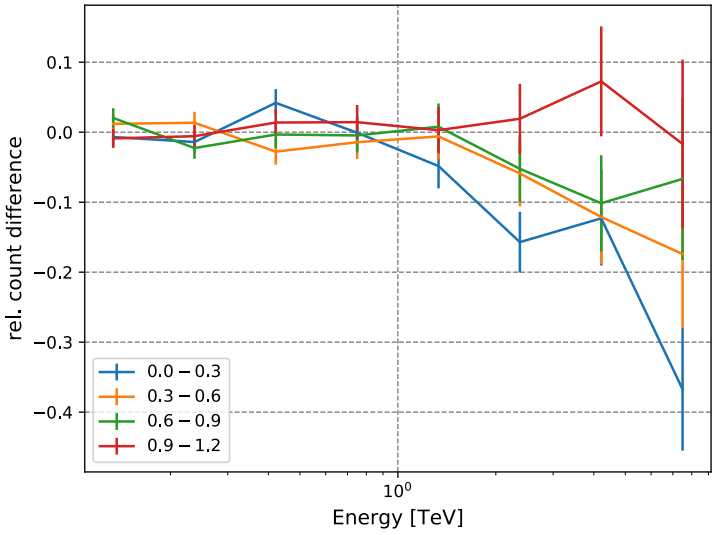

Figure 4.18.: Relative difference of an Crab SED (from Aleksić et al. (2016)) in terms of events counts generated from a Crab reference spectrum, an exposure, and migration matrices obtained with MC events from different camera offsets with the one obtained using the MC events of the entire FoV.

and the grey area 1 σ confidence region of the statistical uncertainties. The SEDs reconstructed with migration matrices from the outer camera regions agree within the statistical uncertainties with the reference spectrum. Also, the matrix for 0.3° to 0.6° camera offset agrees with the reference spectrum considering additional systematic uncertainties ignored in the butterfly region. Again the energy dispersion matrix from the camera centre leads to a reconstructed SED deviating significantly beyond 1 TeV. For On/Off observations of strong sources, instead of an averaged migration matrix one should use a matrix based on MC events from the camera centre only. For the usual wobble mode observations a source is rarely placed at the camera centre. Even in case the source extends towards the camera centre in one pointing position, the alternating wobble scheme places it farther off-axis in the corresponding wobble partner. For the usual observation strategy an averaged energy dispersion matrix does not cause any issues for the reconstruction of a source SED situated a different location of the skymap.

Source flux estimation using the likelihood fit

Finally, the overall performance of the SkyPrism package and its image fitting routines can be tested by reproducing the spectrum of a well-measured source. Its γ-ray brightness and the fact that the source is well studied make the Crab Nebula a prime candidate for performance studies of IACTs. This test is based on the same data set of the Crab Nebula observations at low ($0° - 30°$) zenith angle as used in Aleksić et al. (2016). The setup for the fit includes the PSF, γ-ray exposure, and background model, estimated with SkyPrism, and employs the MAGIC data in the energy range from 60 GeV to 10 TeV. The fitted model consists of a point source at the Crab Nebula position and the isotropic background.

The resulting spectrum, presented in figure 4.20, does not show any significant

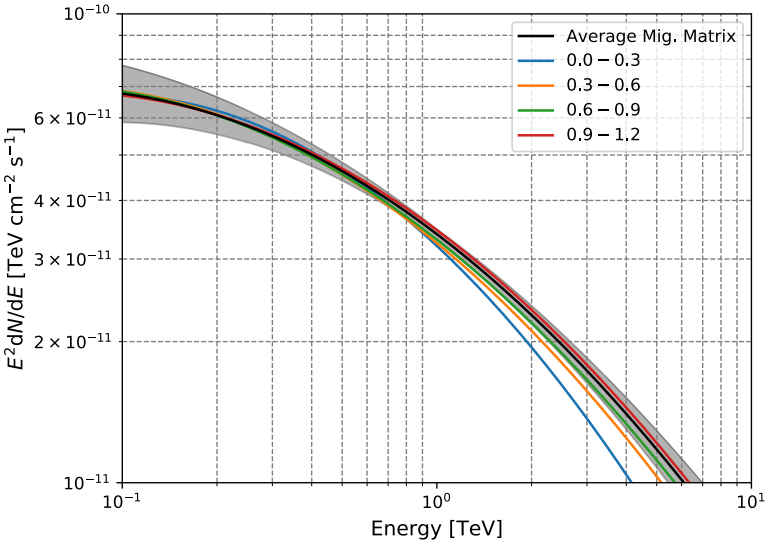

Figure 4.19.: Crab SED obtained using migration matrices generated with MC at different camera offsets. A reference Crab SED is converted to a count spectrum using an exposure and migration matrix based on MC across the whole FoV. The count spectrum is fitted with a forward folded fit using the migration matrices at the different camera offsets. The black line is the Crab reference spectrum from Aleksić et al. (2016) and the grey band the $1\,\sigma$ statistical uncertainty band.

deviations from the reference spectrum from Aleksić et al. (2016). Over the entire energy range the relative flux difference $\Delta F/F$ is $\lesssim 10\%$, which is within the combined uncertainties of both spectra. The stronger curvature of the reconstructed spectrum may likely be caused by using the instrument responses averaged over the entire FoV as explained in the previous section.

To confirm the accurate reconstruction of the off-axis performance was demonstrated in section 4.4.3, the Crab Nebula spectrum is reconstructed from data taken at different offsets (0.2°, 0.7°, 1.0° and 1.4°). The spectra (see appendix) show the same level of agreement with the reference spectrum, although the amount of data is insufficient to obtain statistical uncertainties of $\lesssim 10\%$ over the entire energy range.

4.5. Summary and outlook

Based on the analysis used by *Fermi*-LAT this chapter introduced the SkyPrism package, which adopts this approach for data from the MAGIC telescopes. Particularly, the package accurately estimates the instrument response function based on MC events across the entire FoV. As the tests have demonstrated SkyPrism reaches the same level of precision as the standard MAGIC analysis, MARS (discrepancy $\lesssim 10\%$ in terms of the reconstructed source flux). In addition, SkyPrism allows analysing extended

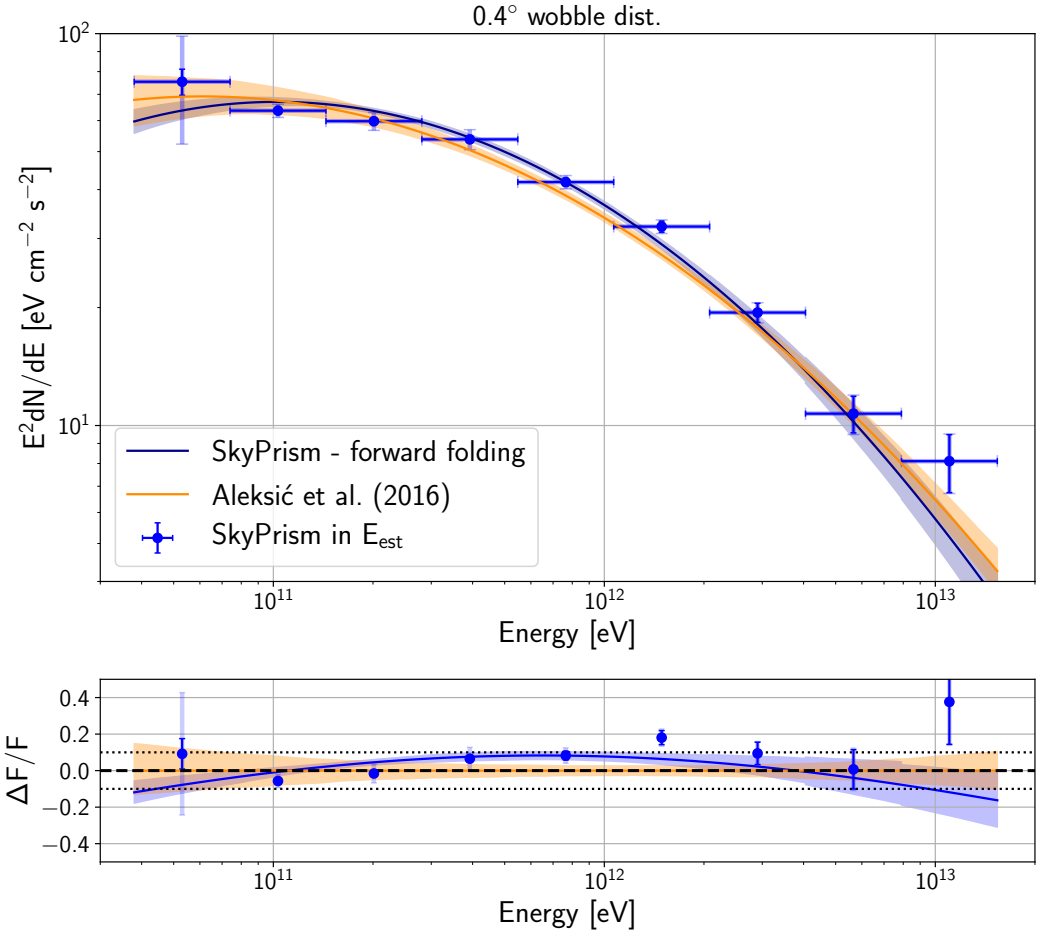

Figure 4.20.: SED of the Crab Nebula obtained by processing the data set used by Aleksić et al. (2016) with the full SkyPrism tool chain. The spectral fit is obtained via the forward folding procedure, whereas the data points are the results of the individual fits in each E_{est} bin. The dark blue error bars of the data points are the statistical error, and the light blue error bars indicate the uncertainties from the exposure model. The obtained results are also compared to the Crab Nebula SED from the same publication in terms of the relative flux difference (ΔF/F.). This figure is part of Vovk et al. (2018).

sources of arbitrary morphology in a convenient way.

Because of its wider applicability compared to the traditional aperture photometry approach, the same technique is considered as the standard analysis approach of the upcoming Cherenkov Telescope Array (CTA) in software packages such as ctools (Knödlseder et al., 2016) and γ-py (Deil et al., 2017). Currently these packages lack dedicated tools for generating the IRFs or assume a radially symmetric detector response, which is not accurate in case of the MAGIC telescopes and might not be for CTA depending on the telescope configuration. Although the structure of SkyPrism is different from CTools (Knödlseder et al., 2016) and Gammapy (Deil et al., 2017), its parts can be further optimised for the data analysis of different IACTs. Hence, parts of SkyPrism may add to the current ongoing developments for the CTA analysis pipeline.

The main limitation for the SkyPrism at the current stage is the necessity to still observe parts of the sky without any sources. Even the "exclusion region" method of SkyPrism requires the source to have a smaller diameter than twice the Wobble offset. Larger sources require On-Off observations involving the issues of increased systematic differences between On and Off data. An alternative approach is the so-called template background method (Rowell, 2003). If the morphological connection between background maps of hadron-like background events and γ-like background events is known, the background map at low hadronness values can be determined from the (source-free) On source event map at high hadronness values. Alternatively, the background could be simulated from CR Monte-Carlo simulated events and a background map constructed in a way similar to the exposure map in SkyPrism. Moreover, it is worth considering to even extend SkyPrism to a 4D analysis by not cutting in the "hadronness" parameter space, but instead adding it as an additional dimension.

Due to their limited resolution, for the current generation of IACTs the main focus was on pointed observations of mildly extended objects. Due to the continuous improvement of the γ-ray telescopes and the extended coverage of the sky, the importance of image analysis techniques in γ-telescopes rises. Such are the denoising (Schmitt et al., 2012) and deconvolution of skymaps (e.g. Heinz et al., 2012) or techniques for identifying source regions (Göring et al., 2013, e.g. Minkowski functionals) reducing the need for user supplied model assumptions (for an overview of various techniques see e.g. Starck, Jean-Luc and Murtagh, Fionn, 2006). An interesting approach combining the aforementioned aspects based on a Bayesian approach is the D3PO algorithm (Denoising, deconvolving, and decomposing photon observations, Selig & Enßlin, 2015). Selig et al. (2015) successfully applied this technique to *Fermi*-LAT data providing new insights in the dominant emission mechanism in different parts of the Milky Way. Such efforts will be even more important for surveys of large sky areas considered as part of the key science program for the CTA (Cherenkov Telescope Array Consortium et al., 2019).

Bibliography

Akaike, H. 1974, IEEE Transactions on Automatic Control, 19, 716

Albert, J. et al. 2007, Nuclear Instruments and Methods in Physics Research A, 583, 494

Aleksić, J. et al. 2016, Astroparticle Physics, 72, 76

Berge, D., Funk, S., & Hinton, J. 2007, Astronomy and Astrophysics, 466, 1219

Cherenkov Telescope Array Consortium et al. 2019, Science with the Cherenkov Telescope Array (World Scientific Publishing Co. Pte. Ltd.)

Chernoff, H. 1954, The Annals of Mathematical Statistics, 25, 573

Deil, C. et al. 2017, in International Cosmic Ray Conference, Vol. 301, Proc. of the 35th International Cosmic Ray Conference, Busan, South Korea, 766, 1709.01751

Fomin, V. P., Stepanian, A. A., Lamb, R. C., Lewis, D. A., Punch, M., & Weekes, T. C. 1994, Astroparticle Physics, 2, 137

Foreman-Mackey, D., Hogg, D. W., Lang, D., & Goodman, J. 2013, Publications of the Astronomical Society of the Pacific, 125, 306

Göring, D., Klatt, M. A., Stegmann, C., & Mecke, K. 2013, Astronomy and Astrophysics, 555, A38, 1304.3732

Heinz, S., Jung, I., & Stegmann, C. 2012, Astroparticle Physics, 36, 146

James, F., & Roos, M. 1975, Computer Physics Communications, 10, 343

Knödlseder, J. et al. 2016, Astronomy and Astrophysics, 593, A1

Knoetig, M. L. 2014, The Astrophysical Journal, 790, 106

Lafferty, G. D., & Wyatt, T. R. 1995, Nuclear Instruments and Methods in Physics Research A, 355, 541

Li, T.-P., & Ma, Y.-Q. 1983, The Astrophysical Journal, 272, 317

Mattox, J. R. et al. 1996, The Astrophysical Journal, 461, 396

Moralejo, A. et al. 2009, in Proc. of the 31st International Cosmic Ray Conference, Lodz, Poland, Vol. 1, 2693–2696, arXiv: 0907.0943

Neyman, J., & Pearson, E. S. 1933, Philosophical Transactions of the Royal Society of London Series A, 231, 289

Protassov, R., van Dyk, D. A., Connors, A., Kashyap, V. L., & Siemiginowska, A. 2002, The Astrophysical Journal, 571, 545

Rolke, W. A., López, A. M., & Conrad, J. 2005, Nuclear Instruments and Methods in Physics Research A, 551, 493

Rowell, G. P. 2003, Astronomy and Astrophysics, 410, 389

Schmitt, J., Starck, J. L., Casandjian, J. M., Fadili, J., & Grenier, I. 2012, Astronomy and Astrophysics, 546, A114

Selig, M., & Enßlin, T. A. 2015, Astronomy and Astrophysics, 574, A74

Selig, M., Vacca, V., Oppermann, N., & Enßlin, T. A. 2015, Astronomy and Astrophysics, 581, A126

Starck, Jean-Luc and Murtagh, Fionn. 2006, Astronomical Image and Data Analysis (Springer, Berlin, Heidelberg)

Vovk, I., Strzys, M., & Fruck, C. 2018, Astronomy and Astrophysics, 619, A7

Wells, D. C., Greisen, E. W., & Harten, R. H. 1981, Astronomy and Astrophysics Supplement, 44, 363

Wilks, S. S. 1938, The Annals of Mathematical Statistics, 9, 60

Wittek, W. 2002, Determination of the effective Observation time, MAGIC-TDAS 02-02, Max-Planck-Institut für Physik, Munich, Germany

Zanin, R., Carmona, E., Sitarek, J., Colin, P., & Frantzen, K. 2013, in Proc. of the 33rd International Cosmic Ray Conference, Rio de Janeiro, Brasil, Vol. 4, 2937–2940

Chapter 5.

New gamma-ray light shed on the gamma-Cygni supernova remnant

Note: the observational results of this chapter were carried out within the MAGIC collaboration with main contributions from myself, Shu Masuda, Ievgen Vovk, and David Green. The theoretical model was mainly developed by Giovanni Morlino and Silvia Celli. I led the project as principal investigator and main analyser of the MAGIC and *Fermi*-LAT data.

5.1. The gamma-Cygni SNR

The γ-Cygni supenova remnant, G 78.2+2.1, is a mixed-morphology SNR (section 2.2) in the Cygnus-X region, a massive star formation region, close to the γ-star of the Cygnus Constellation, Sadr. The Cygnus region is an astrophysical rich environment hosting various objects such as a giant molecular-cloud complex, OB associations, bright and dark nebulae, pulsars and supernova remnants. This provides a primary laboratory for understanding the life-cycle of the interstellar matter.

In the 70s the shell of the supernova remnant G 78.2+2.1 was identified. A detection of γ-ray emission from the vicinity of γ-Cygni by the *COS-B* satellite even makes the γ-Cygni region one of the first γ-ray sources detected (Pollock, 1985). Since then it has been studied by several experiments at various wavelength, still the origin of the very high energy emission remains unclear and the source is classified as unidentified in the TeVCat source list (Wakely & Horan, 2007)[i]. After an overview of the current multi-wavelength view of the SNR, this chapter describes how the observations performed with the MAGIC telescopes together with analysed data from *Fermi*-LAT improve the understanding of the processes leading to the high-energetic gamma-ray emission from this supernova remnant.

As the γ-Cygni can also refer to the star Sadr, the SNR is usually explicitly called γ-Cygni SNR or the catalogue name G 78.2+2.1 is used. For brevity and to avoid confusions in the following γ-Cygni refers to the supernova remnant while the star is

[i] `http://tevcat.uchicago.edu/`

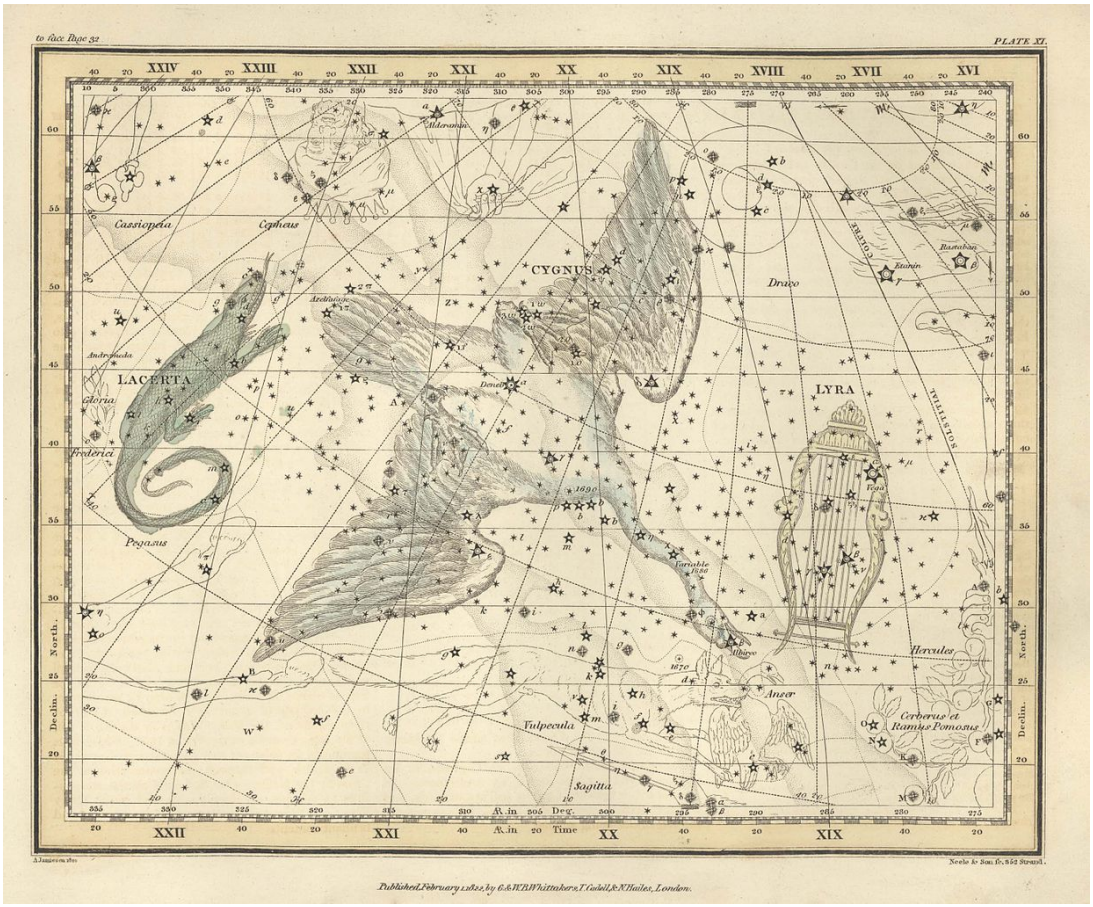

Figure 5.1.: Plate 11 from Alexander Jamieson's Celestial Atlas showing an illustration of the Cygnus region and neighbouring constellations. The γ-Cygni star, Sadr, is located at about the chest of the Cygnus.

called by its IAU star name, Sadr. Relative positions will be referred to by the cardinal directions. North is defined as the direction of increasing declination and east as the direction of increasing right ascension.

5.2. The current multi-wavelength image

5.2.1. The radio shell

In the radio band the γ-Cygni SNR, also known as G 78.2+2.1, exhibits a distinctively roundish shell structure. It is centred at RA(J2000)=20^{h} 21^{m} 14^{s}, Dec.(2000)=40°26′ and has a diameter of about $\sim 1°$. The object has a flux of 320 Jy at 1 GHz making it one of the brightest SNR in the Green's catalogue (Green, 2014). However, the emission is not evenly distributed over the shell, but is brighter towards two opposing regions in the south-east and north-west of the shell and dimmer along the north-east south-west axis. Figure 5.2 displays the radio emission of the source at 408 MHz as observed by

the Canadian Galactic Plane Survey (CGPS, Taylor et al., 2003).

Zhang et al. (1997) and Ladouceur & Pineault (2008) found that the spectral index varies across the shell between ~ 0.8 and $\lesssim 0.4$. The former computed an average spectral index of $0.54 \pm 0.02_{\text{stat}}$, whereas the latter disentangled the thermal and non-thermal component resulting in a softer average index of $0.75 \pm 0.03_{\text{stat}}$. The non-thermal emission more or less agrees with the total intensity structure of the SNR except for the emission from outside the shell in the north-west. In the following, to indicate the radio shell this work uses the 400 K contours of the 408 MHz observation by the CGPS. At this brightness level the contours agrees best with published extension values and non-thermal morphology.

The softest index is found in the bright south-eastern part, while the spectrum is harder in the south-west and north-west ($\sim$0.55). This could indicate that the shock wave at the different parts of the shell is in different stages of evolution as harder spectra suggest stronger magnetic fields and thereby the confinement of higher energetic CRs.

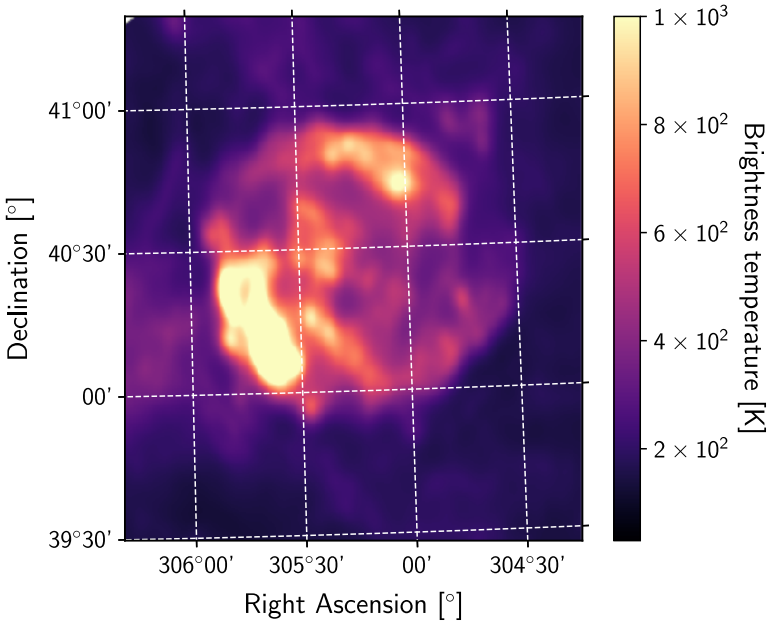

Figure 5.2.: 408 MHz radio image of the γ-Cygni supernova remnant taken by the Canadian Galactic Plane Survey.

Furthermore, radio observations can be used to estimate the distance to the object either by using the absorption lines against the continuum radio emission, association with other objects with known distance, or the relation between the surface brightness to diameter relation (Σ-D) (Dubner & Giacani, 2015, and references therein). The latter assumes that there is a universal dependency between both quantities for Sedov phase SNRs. Indeed when applying to different SNR, they seem to follow the prediction, but there is no physical explanation for it. In general estimates based on absorption lines (e.g. HI) are more robust.

Based on Σ-D relations Higgs et al. (1977) estimated the distance to γ-Cygni to be (1.8 ± 0.5) kpc and Lozinskaya et al. (2000) obtained (1.7 ± 0.5) kpc. Landecker et al.

(1980) and Leahy et al. (2013) inferred the determined from HI velocity measurements to be (1.5 ± 0.4) kpc and 1.7 kpc to 2.6 kpc respectively. Uchiyama et al. (2002) inferred a distance of 1.5 kpc by associating the SNR with the Wolf-Rayet binary V444 Cyg.

Radio observations further suggest that the SNR is surrounded by a HI shell, even though the extent of the shell is different for Gosachinskij (2001) and Ladouceur & Pineault (2008). Gosachinskij (2001) reports a shell of $2\overset{\circ}{.}0 - 2\overset{\circ}{.}8 \times 2\overset{\circ}{.}5 - 3\overset{\circ}{.}5$ diameter centred at about the SNR, while Ladouceur & Pineault (2008) observed structures in emission bordering the SNR shell. However, the association of the HI structures with the SNR is uncertain. Gosachinskij (2001) noted that the HI structures are not necessarily at the same distance and Leahy et al. (2013) claimed that the features found by Ladouceur & Pineault (2008) are not due to emission but absorption in layers situated in front of the SNR. If the features are related to the SNR, they could be the remnant of a cavity blown by the wind of the progenitor's stellar wind or the supernova explosion, of which the former scenario is more plausible (Lozinskaya et al., 2000).

5.2.2. CO properties

Observations of CO lines did not reveal any interaction of the SNR with molecular material (Higgs et al., 1983a) except for a hint at the south-eastern part (Fukui & Tatematsu, 1988). The search for maser emission led to a negative result (Frail et al., 1996). Even though there is no hint for an interaction of the SNR with the interstellar medium in the north, nearby emission is present in the CO skymaps (figure 5.3).

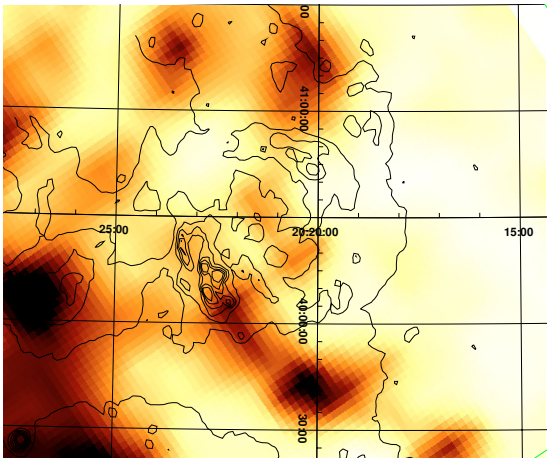

Figure 5.3.: The total molecular CO emission in the field of γ-Cygni with contours of the radio emission at 1400 MHz. The CO data (from Leung & Thaddeus (1992)) were interpolated to produce a smoother image. Figure from Mavromatakis (2003).

5.2.3. Optical properties

So far, no optical counterpart of the γ-Cygni SNR has been detected. Its location in the Cygnus region hosting HII regions, clouds, and nebulae impairs the search for optical emission. Mavromatakis (2003) searched for optical emission lines in the [NII], [SII], and [OIII]. The author found patchy emission in all three filters towards the south,

south-east, and north-west of the SNR. For the south-east region (around (RA, Dec; J2000) = ($20^h\ 22^m\ 53^s$, $40°26'21''$)), he further found hints for shock heated gas using long-slit spectroscopy based on which he estimated a shock speed of $90\,\mathrm{km\,s^{-1}}$ and a pre-shock density of $20\,\mathrm{cm^{-3}}$. Assuming that the SNR evolves into a low density medium of $\sim 0.3\,\mathrm{cm^{-3}}$ with high density interstellar clouds, the author computes an initial shock velocity of $\sim 750\,\mathrm{km\,s^{-1}}$.

Based on his observations Mavromatakis (2003) further inferred that most of the hot dust visible in infrared images and most of the X-ray absorbing matter lies in the foreground of the SNR. This foreground matter possibly obscures most of the optical emission.

5.2.4. X-ray properties

Due to its extent of about 1° in diameter, exceeding the FoV of most of the X-ray instruments, in the X-ray band the entire SNR was only covered by the *ROSAT* satellite so far. Parts of the SNR were also observed by the *Einstein*, *ASCA*, *XMM-Newton*, and *Chandra* telescope.

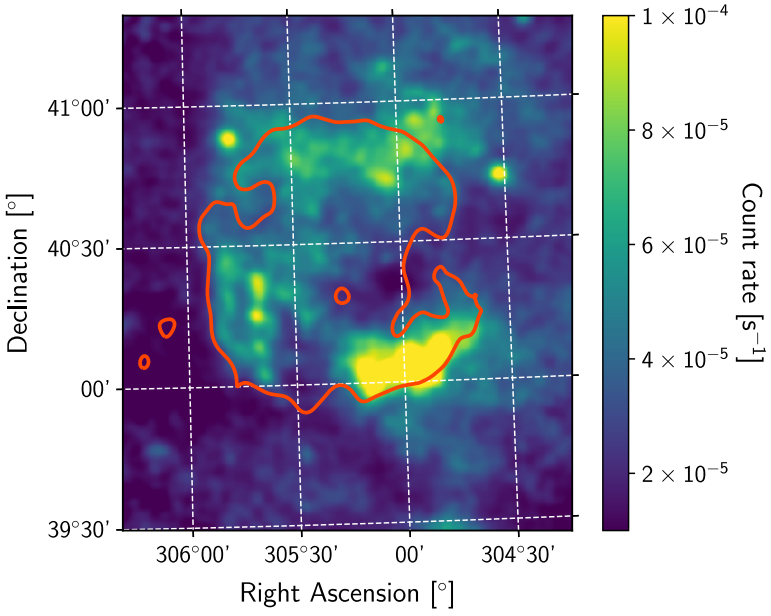

Figure 5.4.: X-ray emission between 0.9 keV–2.4 keV from the γ-Cygni SNR observed by the ROSAT PSPC. The count image is divided by the exposure and smoothed with a Gaussian ($\sigma = 45''$). The orange contour marks the 400 K level of the radio image from figure 5.2.

The field around the γ-Cygni SNR shows extended, patchy emission over and partially extending beyond the radio shell. Figure 5.4 shows the X-ray emission detected by the position sensitive proportional counter (PSPC) on board of *ROSAT* in the energy range from 0.9 keV to 2.4 keV. The image is a combination of pointed PSPC-B observations and PSPC-C survey observations from the ROSAT all sky survey (RASS). The data were obtained from the ROSAT X-ray all-sky survey server at the Max Planck Institute for extraterrestrial physics (MPE)[ii]. The count image is divided by the expo-

[ii] `http://www.xray.mpe.mpg.de/cgi-bin/rosat/rosat-survey`

sure map. The regions that are brightest in radio are also bright in X-ray. However, the region that shows by far the brightest X-ray emission is the radio dim south-west of the shell. Towards the north of the shell the X-ray emission extends beyond the radio shell.

Most of the X-ray emission is of thermal origin as expected for a Sedov-phase SNR. Even in case of efficient acceleration, the thermal emission outshines the non-thermal one below 5 keV (Castro et al., 2011). This dominance makes it hard to derive important quantities such as the magnetic field strength at the shock. At higher energies no structures corresponding to the SNR shell were found. Using observations with the ASCA telescope in the energy range 4 keV to 7 keV Uchiyama et al. (2002) found three hard X-ray clumps in the northern part of the shell, of which two (C1 and C3) were identified by Leahy et al. (2013) to be of extragalactic origin. Leahy et al. (2013) further found that the X-ray emission north of the SNR comes from a closer distance and which could be associated with the stellar wind of the B3 start V1685 Cyg.

Based on formula 2.10 the temperature of the downstream gas measured by the X-ray observations can be used to determine the shock speed. Using the data from various X-ray missions the following authors estimated the shock speed for different parts of the SNR: analysing *Einstein* data Higgs et al. (1983b) found a shock speed of$\sim$ 1100 km s^{-1} for radio-bright region in the south-east, Lozinskaya et al. (2000) estimated (1-1.5)$\times 10^3$ km s^{-1} based on *ROSAT* data and by averaging over a region about the radio shell, based on *ASCA* observations Uchiyama et al. (2002) computed a speed of 800^{+50}_{-60} km s^{-1} for brightest in X-ray region in the south-west, and with *Chandra* data Leahy et al. (2013) determined 860^{+240}_{-160} km s^{-1} for the north-west region.

Analysing the data from *XMM Newton* (Hui et al., 2015) found that the plasma spectrum of the SNR can be best described with a non-equilibrium ionisation (NEI) state. The authors concluded that the plasma at the centre of the SNR has been shock-heated $\sim$ 1900 yr ago, though they stress that the model is rather simple. Since this is much shorter than the lifetime of the SNR, it suggests that the reverse shock returned to the centre of the SNR.

Bykov et al. (2004) reported an hard X-ray clump at the north-west of the SNR detected in the 25 keV to 40 keV range with ISGRI detector on board of the *Integral* satellite. The source, IGR J2018.7+4041, was later associated with an AGN (Krivonos et al., 2012) and will not be considered in this work.

5.2.5. Previous gamma-ray observations

γ-ray emission from the direction of the γ-Cygni SNR was first detected by the COS-B satellite (Lamb, 1978; Pollock, 1985) and later confirmed by *EGRET*(Gaisser et al., 1998; Casandjian & Grenier, 2008).

The *Fermi*-LAT collaboration later found that the γ-ray emission detected by the previous missions does not come from the supernova remnant but the pulsar PSR J2021-

+4026 (Abdo et al., 2010). However, when observing the region at energies well above the cut-off energy of the pulsed spectrum ($\gtrsim$ 10 GeV), the *Fermi*-LAT also found diffuse emission all over the SNR shell (Lande et al., 2012). The authors modelled the source with a radial disk and reported an extension $0.^{\circ}63 \pm 0.^{\circ}05_{\mathrm{stat}} \pm 0.^{\circ}04_{\mathrm{sys}}$. A later analysis by (Ackermann et al., 2017) using the Pass8 reconstruction and 6 years of data found a smaller extension of $0.^{\circ}58 \pm 0.^{\circ}01_{\mathrm{stat}} \pm 0.^{\circ}02_{\mathrm{sys}}$. The spectrum of the source reported by these authors was a power law with a normalisation of $(13.22 \pm 0.81_{\mathrm{stat}} \pm 0.29_{\mathrm{sys}}) \times 10^{-10}\,\mathrm{cm}^{-2}\,\mathrm{s}^{-1}$ above 10 GeV and a spectral index of $2.15 \pm 0.07_{\mathrm{stat}} \pm 0.02_{\mathrm{sys}}$.

The SNR is embeded in the Cygnus Cocoon a region bright in γ-rays.

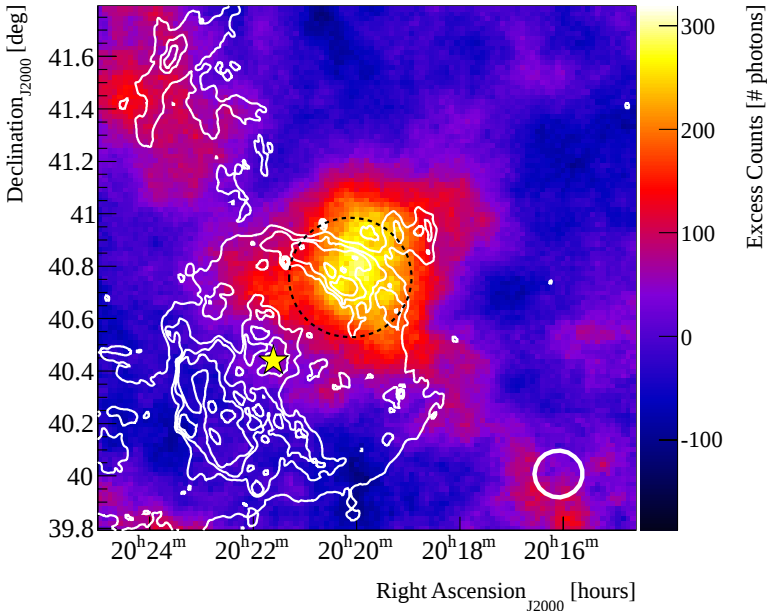

Figure 5.5.: Excess count map of the γ-ray emission from the γ-Cygni SNR measured by VERITAS and its fitted extension (dashed black circle). The yellow star marks the position of the PSR J2021+4026 and the white contours show brightness levels between 23.6 K and 100 K of the 1420 MHz CGPS observations. The white circle shows the size of the VERITAS PSF. Figure adapted from Aliu et al. (2013).

At TeV the SNR was observed by the VERITAS IACT array during a survey of the Cygnus region and follow up dedicated pointed observations. VERITAS observed the remnant for 21.6 h and found patchy extended emission towards the north-west of the SNR (Aliu et al., 2013). Figure 5.5 shows the excess count map observed with VERITAS. The authors modelled the emission with a Gaussian and extracted RA(J2000)=$20^h\ 20^m\ 4.8^s$, Dec.(2000)=$40^{\circ}45'36''$ as its centre and an extension of $0.^{\circ}23 \pm 0.^{\circ}03_{\mathrm{stat}}{}^{+0.^{\circ}04}_{-0.^{\circ}02}$. The positional uncertainties were stated as $\pm 0.^{\circ}03_{\mathrm{stat}} \pm 0.^{\circ}018_{\mathrm{sys}}$. From the a region of $0.^{\circ}23$ around the centre Aliu et al. (2013) extracted a power-law spectrum above 320 GeV with a flux normalisation of N_0=$(1.5 \pm 0.2_{\mathrm{stat}} \pm 0.4_{\mathrm{sys}}) \times 10^{-12}\,\mathrm{TeV}^{-1}\,\mathrm{cm}^{-2}\,\mathrm{s}^{-1}$ and a spectral index of Γ=$2.37 \pm 0.14_{\mathrm{stat}} \pm 0.20_{\mathrm{sys}}$.

The source contained in the 2nd HAWC Observatory γ-ray catalogue (2HWC J2020+403, Abeysekara et al., 2017). The emission was found to be point like (disk extension $< 0.^\circ5$). The authors report a flux level of $(18.5 \pm 2.6_{\text{stat}}) \times 10^{-15}\,\text{TeV}^{-1}\,\text{cm}^{-2}\,\text{s}^{-1}$ at 7 TeV and a spectral index of -2.95 $\pm$ 0.10$_{\text{stat}}$.

5.2.6. PSR J2021+4026

The SNR hosts the pulsar (PSR) J2021+4026. Observation by *AGILE* (Chen et al., 2011) and *Fermi*-LAT (Allafort et al., 2013) found that the γ-ray flux has exhibited abrupt changes making it the only known γ-ray variable pulsar. It has a spin-down power of $\dot{E}_{SD} \sim 10^{35}\,\text{erg}\,\text{s}^{-1}$ and a characteristic age of $\tau_C \sim 77\,\text{kyr}$ (Abdo et al., 2009). The spectrum measured by *Fermi*-LAT can be described by a power-law with exponential cut-off of the form

$$\frac{\mathrm{d}N}{\mathrm{d}E} = K \left(\frac{E}{E_0}\right)^{-\Gamma} \exp\left(\left(\frac{E_c}{E_0}\right)^b - \left(\frac{E}{E_c}\right)^b\right) \tag{5.1}$$

with a normalisation $K = (3.87 \pm 0.03_{\text{stat}}) \times 10^{-10}\,\text{MeV}^{-1}\,\text{cm}^{-2}\,\text{s}^{-1}$, a pivot energy $E_0 = 0.655\,\text{GeV}$, a power-law index $\Gamma = 1.57 \pm 0.01_{\text{stat}}$, a cut-off energy $E_c = (2.37 \pm 0.06_{\text{stat}})\,\text{GeV}$, and a exponential index $b = 1.0$ according to Acero et al. (2015). Due to the high flux level the pulsar dominates the emission in at lower GeV energies, but quickly falls off beyond the cut-off and the γ-Cygni SNR gets visible at energies $E > 10\,\text{GeV}$.

The PSR has no detected counterpart in radio (Becker et al., 2004; Trepl et al., 2010). In X-rays the discovery of an X-ray counterpart (2XMM J202131.0+40264) $\sim 0.^\circ1$ away from the SNR centre was claimed by Trepl et al. (2010) and Weisskopf et al. (2011) and later reinforced by the detection of a pulsed signal agreeing with the γ-ray frequency Lin et al. (2013). The spectrum consists of two components, a thermal pulsed spectrum originating from the hot polar cap of a neutron star and a off-phase non-thermal spectrum from a pulsar wind nebula surrounding it (Hui et al., 2015). The latter results from a bow shock (10′ diameter) due to the pulsar's supersonic velocity. Based on the HI absorption, the authors further associate the PSR with the supernova remnant.

5.2.7. Summary of the MWL properties

Table 5.1 summarises the properties of the γ-Cygni SNR from the given references going to be used in the subsequent analysis. In addition to the aforementioned characteristics, it lists the age, the density inside the shell, and the explosion energy. The age is inferred from the size of the radio shell together with the shock speed or particle density assuming a Sedov-Taylor model (see e.g. formula 2.5). Based on these measurements, in the following we will assume a distance of 1.7 kpc, and an age of 7000 yr, an explosion energy of 10^{51} erg, and a shock speed of $10^3\,\text{km}\,\text{s}^{-1}$. For the centre of the SNR radio shell we will use ($\alpha = 305.^\circ3$, $\delta = 40.^\circ43$; J2000). As the ejecta

Table 5.1.: Physical parameters of the γ-Cygni SNR based on various measurements.

Characteristic	value used in this work	value range	References
Radius [°]	0.53	0.51 - 0.56	(1), (4), (9)
Distance [kpc]	1.7	1.5 - 2.6	(1), (2), (6), (7), (10)
Age [kyr]	7	4 - 13	(1), (6), (7), (10)
shock speed [km/s]	1000	600 - 1500	(1). (3), (6), (7), (10)
density in shell [$1/\mathrm{cm}^3$]	0.2	0.14 - 0.32	(5), (6), (10)
explosion energy [10^{51} erg]	1	0.8 - 1.1	(8), (10)

References. (1) Higgs et al. (1977) ; (2) Landecker et al. (1980) ; (3) Higgs et al. (1983b) ; (4) Wendker et al. (1991) ; (5) Saken et al. (1992) ; (6) Lozinskaya et al. (2000) ; (7) Uchiyama et al. (2002) ; (8) Mavromatakis (2003) ; (9) Kothes et al. (2006) ; (10) Leahy et al. (2013)

mass is unknown, but the SNR likely resulted from a core-collapse supernova of an OB star, in the following a canonical value of $M_{ej} = 5\,\mathrm{M}_\odot$ for type II supernovae will be used (Chevalier, 1977). It is important to note that the ranges given in table 5.1 just consider the optimal values from the listed publications excluding the uncertainties. The uncertainty ranges of all measurements are similar and thus the average values are still an accurate representations. The parameters are further correlated due to their connection via the Sedov-Taylor model. Combining all estimates considering their statistical uncertainties, systematic uncertainties of each instrument and method, and their correlation is beyond the scope of this work. Accordingly, when using the extreme values from table 5.1 in our estimations later on, the resulting ranges are rather suggestive than accurate uncertainty intervals.

Overall the observed properties make the γ-Cygni SNR a prime example for a Sedov-Taylor phase SNR and for studying a possible escape of CRs. The discrepancy between the morphology at GeV energies observed by *Fermi*-LAT and the concentrated emission at TeV energies reported by VERITAS indeed suggests an ongoing, energy dependent process (see morphology described above or compare figure 25 from Lande et al. (2012) and figure 1 from Aliu et al. (2013)). We report on the observation of γ-Cygni with the MAGIC telescopes and combine them with an analysis of *Fermi*-LAT data to explore the discrepancy in GeV to TeV regime in greater detail.

5.3. Observations and data analysis

5.3.1. The MAGIC observation campaign and data analysis

The observation for this work were performed over two periods between May 2015 and November 2015 and between April 2017 and September 2017. The total dead-time corrected observation time after quality cuts was 45 h for the former and 50 h for the latter period. The data cover a Zenith range from 10° to 55°. The observations used two pointing positions in wobble mode with an distance of 0.°6 and wobble angles of

45° and 225° around the VERITAS source location (RA; Dec)$_{J2000}$ = (305.°0167; +40.°76). The pointing directions were chosen to have the same angular distance to the bright γ-Cygni star (Sadr) to avoid a systematic mismatch between both pointings.

The MAGIC data were analysed using the MARS analysis pipeline outlined in section 3.5.5. During observations the transparency of the atmosphere was controlled with the LIDAR system (see section 3.5.4). This analysis only includes data with an atmospheric transmission of $> 80\,\%$ of the optimal transparency. The data from 2017 also contain dim and moderate moon data. The data set was split according to the DC level: up to a level of 2 µA the data are equivalent to dark NSB level and between 2 µA to 4 µA were classified as dim. Data with higher Moon level were not considered in this analysis. To keep the surviving pedestal fraction below 10%, the cleaning levels were $Q_c = 6$ and $Q_b = 3.5$ for dark conditions and $Q_c = 7$ and $Q_b = 4.5$ for the dim Moon data (see section 3.5.5). After quality cuts, the total dead-time corrected observation time summed up to 85 h.

Effect of the γ-star, Sadr

The γ-Cygni star, Sadr, is a variable star of spectral-type F8 Ib (yellow to white; ∼6 kK) with a visible brightness of 2.2 mag (Hoffleit & Jaschek, 1991). It has a distance to the Earth of ∼0.5 kpc and thus is in the foreground of the γ-Cygni and not associated with the latter. The starlight increases the number of photoelectrons (ph.e.) in the pixels close to the position of Sadr in the camera. If the DC level exceeds 47 µA, the corresponding pixel will be switched off automatically, what applies to $\sim 2-3$ pixel closest to the position of Sadr. In the 12 neighbouring pixels the higher currents leads to higher light content. Regarding the trigger rate, the higher light yield is compensated by a dynamic, pixelwise adjustment of the discriminator thresholds. To further reduce the effect of the star the position of Sadr was kept outside the trigger region (up to 1.17° from the camera centre). As mentioned above the pointings were also chosen to be equally affected by the star light and to avoid differences in the source and background control regions.

Still artefacts from these features survived the analysis procedure at images sizes of $S < 150$ ph.e.. At those energies one can clearly see an excess of events at the stars position and a deficit around. At higher energies the contribution from the star light gets smaller compared to the shower's light and the shower images are larger, so affected pixels affect the fitted ellipse less. Additionally, the distance between the arrival direction of the shower and the centre of gravity of the shower image in the camera plane increases with energies. Accordingly, towards higher energies the arrival directions of showers affected by the starlight get spread over a wider area of the reconstructed skymap and do not create distinct features in the skymaps.

We thus limited the MAGIC data to image size $S > 150$ ph.e. implying an energy

threshold of 250 GeV. This limit was well above the energy threshold resulting from the general observational conditions (Moon conditions or zenith range).

The high level data analysis

We analysed the high level data with the SkyPrism spatial likelihood analysis package (see chapter 4.4). We used the "exclusion map" method for generating the background map excluding a circular region of $0.^{\circ}56$ around the radio centre ($\alpha = 305.^{\circ}3$, $\delta = 40.^{\circ}43$; J2000) and around the VERITAS centre ($\alpha = 305.^{\circ}02$, $\delta = 40.^{\circ}76$; J2000). The considered MAGIC region of interest (RoI) had a size of $2.^{\circ}5 \times 2.^{\circ}5$ with a pixel size of $0.^{\circ}02 \times 0.^{\circ}02$. The MAGIC angular resolution, characterised by the point spread function (PSF), for this study was estimated to be $0.^{\circ}08$ (68% containment radius) at $E > 250$ GeV. As the bins were smaller than the PSF, the spatial pixels are highly correlated, what was considered by the likelihood analysis. The size of Gaussian smoothing kernel agreed with the size of the PSF.

For MAGIC Aleksić et al. (2016) studied the systematic uncertainties on the spectral parameters (flux normalisation, spectral index, and energy scale) resulting from the telescope performance[iii] for low and medium Zenith angles (see section 3.5.7). Since the observations for this work were performed at the same elevations, we scaled those uncertainties with the signal-to-background ratio of each source component as described in Aleksić et al. (2016). Furthermore, the authors investigated the systematic uncertainty on the source position, which we considered for the localisation of MAGIC J2019+408. However, Aleksić et al. (2016) only examined point sources or slightly extended sources. Hence, we additionally studied the uncertainties arising from the imperfect knowledge of our 2D background and exposure shape, which are part of our SkyPrism model. To estimate their effect we ran the analysis using 50 random representations of the background model and exposure map. For the former we assumed that the content in each bin of the background acceptance model in camera coordinates follows a Poisson statistics with the original value as the mean value. According to the distribution in each bins we simulate random camera background models and processed in the same way as for the original model following section 4.4.1. For the exposure the random representations are based on the parameter uncertainties of the γ-ray acceptance model fitted to the Monte-Carlo (MC) based acceptance as described in section 4.4.1.

Due to the large energy range, the uncertainties affecting the spectral parameters are less of a concern for the morphological study. Thus, our estimates only include the uncertainties from the background and exposure model together with the effect of a possible underestimation of the MC based PSF model. Figure 3.19, 4.11, and 4.12 show that the MC based PSF might be smaller by $0.^{\circ}02$ compared to the extension of point

[iii] E.g. from instrumental uncertainties, Monte-Carlo data mismatch, and uncertainties from the analysis pipeline

sources. For the spectra we considered the uncertainties from telescope performance and the uncertainties of the background and exposure model. Table 5.3 contains the effect on each spectral parameter and source component for the various uncertainty origins. The uncertainties based on Aleksić et al. (2016) are listed under "instrument" and the background and exposure model uncertainties as "bgr+exposure".

5.3.2. The *Fermi*-LAT data observations and data analysis

This study used data from ~ 9 years of observation between 2008 Oct 27 and 2017 Sep 12 processed with the Pass 8 R2 reconstruction (Atwood et al., 2012) as provided by the Fermi Science Support Center (FSSC). The data were analysed using the Fermi Science Tools (version v11r5p3[iv]) in combination with the Fermipy package (version 0.17.3, Wood et al., 2017). The 'Source' selection cuts and instruments responses (P8R2_SOURCE_V6[v]) were chosen for a balance between precision and photon count statistics. Further, the data were split according to the 4 PSF classes and combined in a joint likelihood function. The zenith angle was limited to 105°, a time filter was applied (DATA_QUAL>0 && LAT_CONFIG==1), and the energy dispersion was considered for all sources except the galactic and extragalactic diffuse emission.

Below ~ 10 GeV the emission from the pulsar (PSR J2021+4026) dominates over the flux from the SNR. To reliably disentangle both components, we limited the energy range of the *Fermi*-LAT data to 5 GeV to 500 GeV. At $E > 5$ GeV the 95 % containment radius of the *Fermi*-LAT PSF is smaller than the radius of the SNR. We chose the region-of-interest (RoI) to be 10 degree $\times$ 10 degree around the radio centre of the SNR with a spatial bin-size of $0.^{\circ}05$ and split the energy range in 18 bins (9/decade).

To model the contribution from background sources (including PSR J2021+4026) in the ROI, we used the FL8Y source list [vi] as a starting point considering sources within 15° from the centre of the analysis. After running the "optimize" procedure of Fermipy, we removed all sources with a test statistic value $TS < 16$ or having no predicted counts. For the Cygnus Cocoon we used the spatial template of the extended source archive V18 provided online by the FSSC. A point source search in the ROI resulted in one significant, positive excess ($> 5\,\sigma$) over the model coinciding with a 2 FHL source (2FHL J2016.2+3713), which we added to our model. The remaining residuals stayed below ($< 5\,\sigma$) across the entire sky map. Sources related to the γ-Cygni SNR system are discussed in section 5.4.3.

For *Fermi*-LAT data we studied the uncertainty of the source localisation by fitting the localisation of all point sources in the RoI and estimating the average off-set from their nominal positions in the FL8Y source list. For the estimation of the source ex-

[iv] https://fermi.gsfc.nasa.gov/ssc/data/analysis/software
[v] https://fermi.gsfc.nasa.gov/ssc/data/Cicerone/Cicerone_Data_Exploration/Data_preparation.html
[vi] `https://fermi.gsfc.nasa.gov/ssc/data/access/lat/fl8y/`

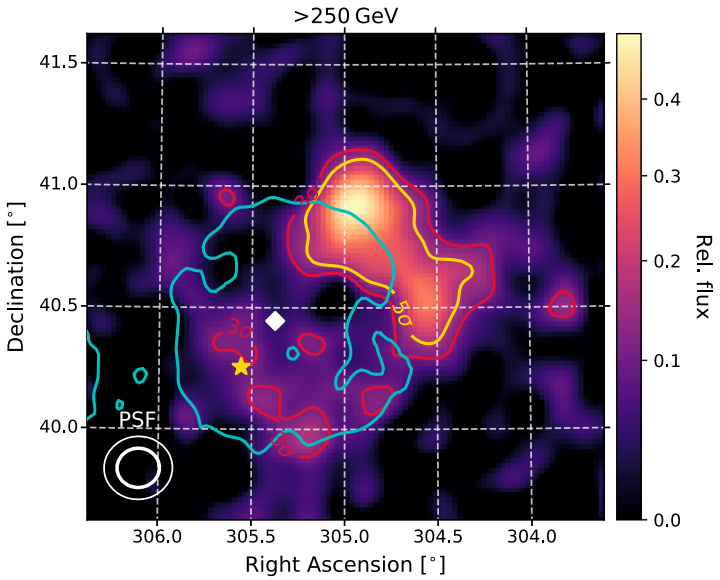

Figure 5.6.: Skymap in units of relative flux (excess over background) of the γ-Cygni region as observed by MAGIC $>$ 200 GeV. Regions exceeding the 3σ (5σ) local, pre-trial TS significance for a point source are indicated by red (yellow) contours. The cyan line is the 400 K contour of the 408 MHz observation by the CGPS. The white diamond shows the position of the PSR J2021+4026, while the yellow star marks the position of Sadr (γ-Cyg star; mag=2.2). The inlay in the lower left corner shows the 39% and 68% containment contours of the MAGIC PSF.

tension we take into account the uncertainty of the PSF and the interstellar emission model (IEM). We evaluated the systematic uncertainty using the P8R2 version of the alternative IEMs from Acero et al. (2016) together with a $\pm$5% scaling of the PSF. The uncertainties of the flux normalisation and spectral index result from the precision of the IEM and the exposure, so we computed it using the alternative IEMs and considering a $\pm$5% uncertainty on the exposure (listed as instrumental uncertainty in table 5.3).[vii]. The instrumental uncertainty on the energy scale is based on Ackermann et al. (2012). The effects onto the spectral parameters are listed in table 5.3.

5.4. Analysis results

5.4.1. MAGIC morphological results

The image of the γ-Cygni SNR measured by the MAGIC telescopes is displayed in figure 5.6 in terms of relative flux. Figure 5.6 also shows the 3 and 5 σ boundaries of the test statistic map (for details how those maps are obtained, see 4.4.1). The cyan lines are the 400 K contours of the 408 MHz observation by the CGPS (Taylor et al.,

[vii] https://fermi.gsfc.nasa.gov/ssc/data/analysis/LAT_caveats.html

2003). The position of the PSR J2021+4026 and Sadr are shown by a white diamond and a yellow star marker respectively.

The emission observed by MAGIC is extended and patchy. The most prominent feature in the map is an extended region along the north-western rim of the radio shell. It seemingly consists of a bright roundish component centred on the rim and an adjunct arc-like appendix extending beyond the radio shell towards the west. The map shows faint emission areas inside the south-east of the radio shell, which, however, are below the detection level for a point source.

Since the roundish emission in the north exhibits a higher surface brightness than the adjunct arc, it seems implausible to account for both with just one source component. The former could be well modelled by a radially symmetric Gaussian with the position and the extension as free parameters. For the latter we used the sector of an annulus centred at the centre of the radio shell with the inner radius, the outer radius, the angular position of the centre (mathematically positive w.r.t. the decreasing RA axis), and the central angle as free parameters.

Since the Gaussian source is better defined, we scanned its position and extension first. The scan resulted in a minimum at (α, δ; J2000)=($304.^{\circ}92 \pm 0.^{\circ}01_{stat}$, $40.^{\circ}84 \pm 0.^{\circ}01_{stat}$) and an extension of $\sigma = 0.^{\circ}12 \pm 0.^{\circ}01_{stat}$. At this position we checked for a possible eccentricity, but the improvement over the radially symmetric Gaussian was not significant. The source was detected with a significance of 17.1 σ. In the following we will refer to this source as MAGIC J2019+408.

Including the Gaussian in the source model, we scanned the parameters of arc. It is detected at a significance of 10.3σ and the best parameters are $0.^{\circ}45 \pm 0.^{\circ}03_{stat}$ for the inner radius, $0.^{\circ}27 \pm 0.^{\circ}03_{stat}$ for extension (outer - inner radius), $5.^{\circ}00 \pm 0.^{\circ}03_{stat}$ for the positional angle, and $36.^{\circ}58 \pm 0.^{\circ}03_{stat}$ for the central angle. A search for point-sources on top of MAGIC J2019+408 and arc did not lead to any significant detection.

5.4.2. Energy dependent morphology

Even though the observations with MAGIC provide a more precise image of the source at hundreds of GeV to TeV than previous observations, its morphology still differs from previously published *Fermi*-LAT skymaps. To study the evolution of the emission over the entire GeV to TeV range, we analysed the data set from the *Fermi*-LAT, which contained 1.5 times the observation time of the latest extended source catalogue (Ackermann et al., 2017). We split the *Fermi*-LAT and MAGIC data into two energy ranges each: 15 GeV to 60 GeV and 60 GeV to 250 GeV for the former and 250 GeV to 500 GeV and 500 GeV to 2.5 TeV for the latter.

The skymaps are shown in figure 5.7. The *Fermi*-LAT maps display the event counts (smoothed with a Gaussian kernel with $\sigma = 0.^{\circ}075$) together with point source TS contours. The count images have the advantage of being free from any model dependency but do not allow the exclusion of sources by including them into the background

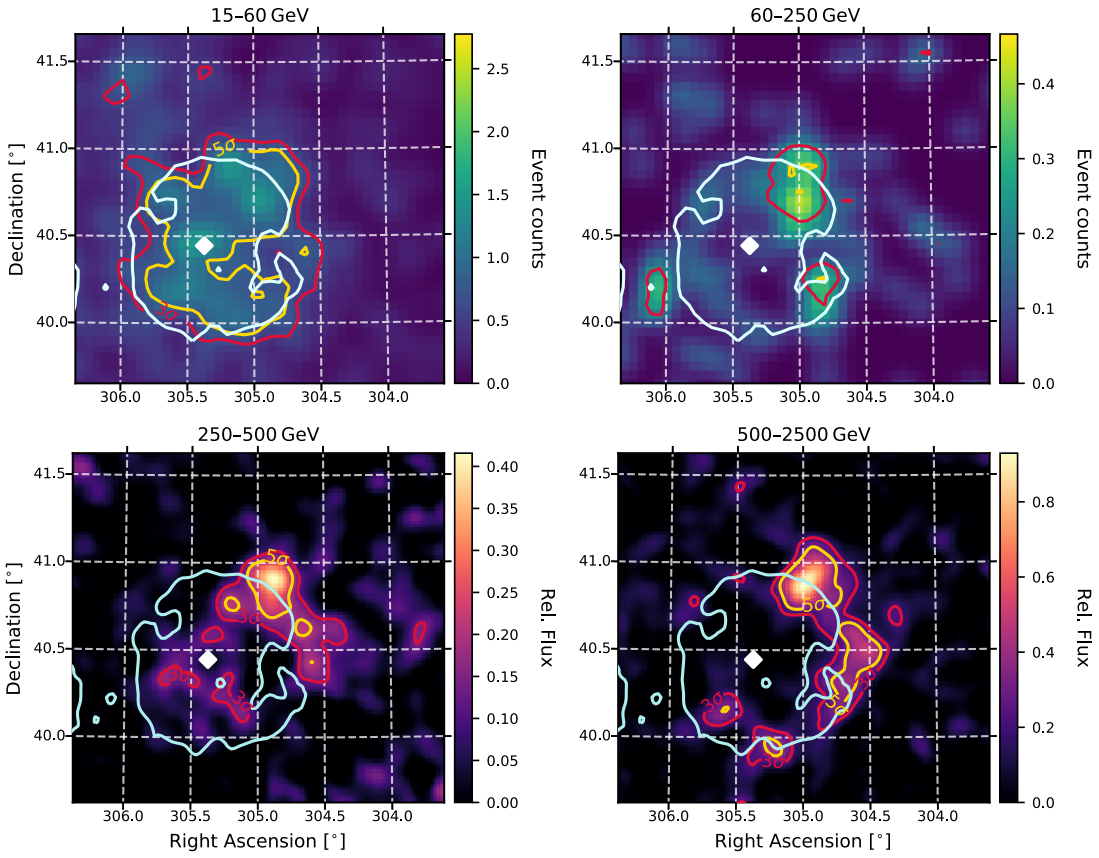

Figure 5.7.: Energy-dependent morphology of the γ-Cygni SNR. **Upper left:** *Fermi*-LAT count map between 15 and 60 GeV with 3 and 5 σ contours of a point source search. The white line is the 400 K contour of the 408 MHz observation by the CGPS. The white diamond identifies the position of PSR 2021+4026. **Upper right:** same as upper left but in the range from 60 and 250 GeV. **Lower left:** relative flux map observed by MAGIC at 250 to 500 GeV together with 3 and 5 σ point source significance contours. The same radio contours as in upper panels are displayed in cyan. **Lower right:** same as lower left but in the energy range from 500 GeV to 2.5 TeV.

model. A lower limit of 15 GeV avoids the pulsar from dominating the image. TS contours are based on a point source search on top of the background source model described in section 5.4.4. The MAGIC skymaps are presented in terms of relative flux together with point source TS contours. In the 15 GeV to 60 GeV range the emission dominantly comes from a region agreeing with the SNR radio shell. The intensity is nearly uniform across the shell and the 3 and 5 σ local significance contours seemingly agree with the radio contours. On the contrary at 60 GeV to 250 GeV the shell emission weakened and a slightly extended emission at the north-western rim stands out nearby MAGIC J2019+408. The position, at which MAGIC observed the arc structure, does not show any significant emission.

MAGIC J2019+408 is the main component in the 250 to 500 GeV map measured by MAGIC. Emission at the arc position is starting to get visible but at a lower level compared to MAGIC J2019+408. The inside of the shell shows some faint emission. Finally at 500 GeV to 2.5 TeV, the arc region brightens. The inside of the shell does not show any significant emission, instead, some emission towards the south of the shell gets visible. Since this emission was not significant in the combined MAGIC data set and the TS contours are approximative Gaussian significances, it can only be considered a hint for emission.

5.4.3. *Fermi*-LAT morphological results

To quantify the *Fermi*-LAT results from section 5.4.2, the likelihood analysis presupposes a morphological template. To account for the extended uniform emission well visible in the 15 to 60 GeV skymap, previous analyses of the *Fermi*-LAT data used a radially symmetric disk model. When fitting the *Fermi*-LAT data >5 GeV we used a radial symmetric disk with the position and extension being free parameters and obtained (α, δ; J 2000)=($305.^\circ24 \pm 0.^\circ02_{stat}$, $40.^\circ49 \pm 0.^\circ02_{stat}$) with an radius of $0.^\circ60 \pm 0.^\circ02$. This result is consistent with the disk model reported in the 3 FGL or FL8Y.

As mentioned in section 5.2.5, the estimated size of the disk differs between different *Fermi*-LAT studies (likely due to different energy ranges). However, all models contain parts of the MAGIC J2019+408, which is visible in the *Fermi*-LAT data ($E > 60$ GeV) and MAGIC data and hence might be a distinct object from the disk. If it is not considered as such, photons might be misassigned to the disk pushing the fit towards a larger disk size. Assuming that the disk template is related to the SNR and given the approximate agreement between the TS contours and the radio contours in the 15 GeV to 60 GeV range, we consider it more plausible to base the disk model on the position and extension of the radio shell. The radially symmetric disk model is centred at (α, δ; J 2000)=($305.^\circ30$, $40.^\circ43$) with a radius of $0.^\circ53$. Fitting this model to the *Fermi*-LAT data resulted in remaining residual counts in the north-western region. Figure 5.8 displays the TS map for a point source search on top of the radio disk. The contours suggest the presence of a source of similar morphology to MAGIC J2019+408.

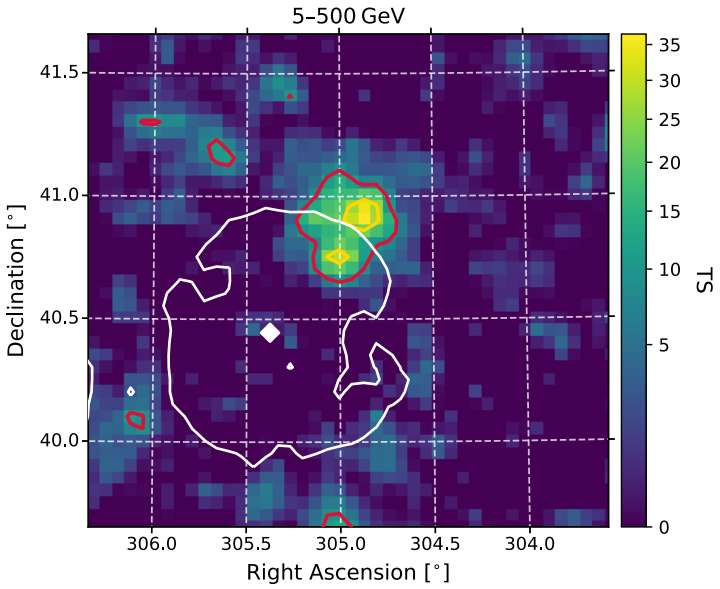

Figure 5.8.: *Fermi*-LAT TS map for a point source search on top of the background sources specified in section 5.4.4 and including the radio-based disk model. Regions exceeding the 3σ (5σ) local, pre-trial TS significance for a point source are indicated by red (yellow) contours. The white line is the 400 K contour of the 408 MHz observation by the CGPS. The white diamond marks the position of PSR J2021+4026.

Table 5.2.: Spatial models used for the MAGIC and *Fermi*-LAT likelihood analysis.

Source name	Spatial model	Centred at		Extension	Positional angle	Central angle
		RA [deg]	Dec [deg]	[deg]	[deg]	[deg]
SNR shell	disk	305.30	40.43	0.53 (radius)	-	-
MAGIC J2019+408	Gaussian	304.93	40.87	0.13 (σ)	-	-
Arc	annular sector	304.30	40.43	0.15 ($r_{\rm out} - r_{\rm shell}$)	7.0	33.0

Assuming a point-source, the source search resulted in the detection at a 6.1σ level at (α, δ; J 2000)=($304.^\circ92 \pm 0.^\circ02_{stat} \pm 0.^\circ02_{sys}$, $40.^\circ87 \pm 0.^\circ02_{stat} \pm 0.^\circ02_{sys}$). Using the Fermipy routines we additionally fitted the extension of the source simultaneously with the position using a radially symmetric Gaussian source model. The best fit is obtained for (α, δ; J 2000)=($304.^\circ97 \pm 0.^\circ03_{stat} \pm 0.^\circ02_{sys}$, $40.^\circ87 \pm 0.^\circ03_{stat} \pm 0.^\circ02_{sys}$) and an extension of $0.^\circ20^{+0.^\circ03}_{-0.^\circ02_{stat}} \pm 0.^\circ01_{sys}$ (68% containment). The extension of the source is significant with a TS value of 28.4. These values agree within errors with the position and extension of the MAGIC-J 2019+408, so we associate the *Fermi*-LAT and MAGIC source.

5.4.4. Common model and source spectra

To extract the spectra in the entire GeV to TeV range, we need to combine the findings in the sections above into a common source model. Particularly, based on the energy

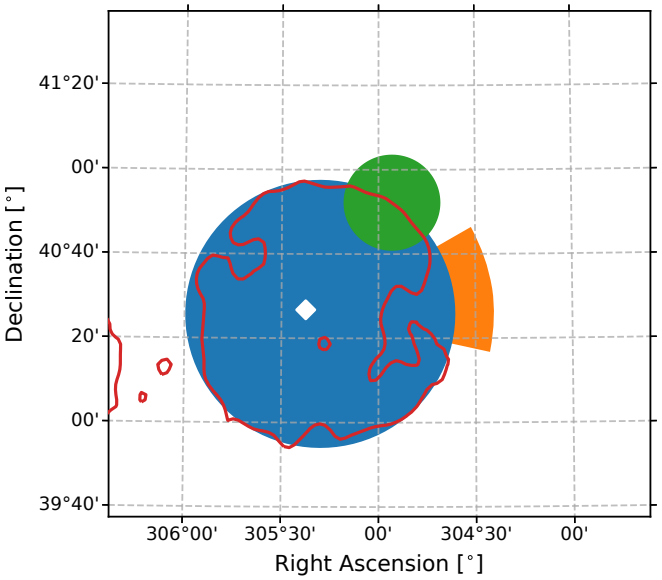

Figure 5.9.: Sketch of the spatial model used in the likelihood of the *Fermi*-LAT and MAGIC data analysis. The blue circle indicates the position and extension of the disk modelling the SNR shell, the green circle marks the position and 68% containment radius of a Gaussian model of MAGIC J2019+408, and the orange annular sector was used for the arc region. The red radio contours and the position of PSR J2021+4026 (white diamond) are shown for reference.

dependent brightness ratio between different parts around the SNR as described in section 5.4.2, in the following we consider the γ-ray emission in the region to consist of three components: the interior of the SNR shell, MAGIC J2019+408, and the arc. The position and parameters of the models for each source are given in table 5.2 and sketched in figure 5.9.

For the emission from the SNR shell, we kept the disk based on radio observation. This disk partially overlaps with MAGIC J2019+408 and the arc region, thus we updated the parameters of the MAGIC analysis including the disk. For MAGIC J2019+408 it resulted in (α, δ; J 2000)=($304.^\circ89 \pm 0.^\circ01_{stat} \pm 0.^\circ04_{sys}$, $40.^\circ88 \pm 0.^\circ01_{stat} \pm 0.^\circ02_{sys}$) and $\sigma = 0.^\circ13 \pm 0.^\circ01_{stat} \pm 0.^\circ02_{sys}$. To model MAGIC J2019+408 consistently for both instruments, we further averaged the MAGIC and *Fermi*-LAT location and extension of the Gaussian weighted with the inverse of their variances (statistical and systematic uncertainties added in quadrature): (α, δ; J 2000)=($304.^\circ93$, $40.^\circ87$) and $\sigma = 0.^\circ13$. For the annular sector template representing the arc we fixed the inner radius at the radius of the shell ($0.^\circ53$ from the SNR centre) and rescanned the other parameters. The best-fit values were $0.^\circ15 \pm 0.^\circ04_{stat}\,^{+0.^\circ27}_{-0.^\circ8\,sys}$ for the extension, $7.^\circ00^{+4.^\circ0}_{-2.^\circ6 stat}\,^{+8.^\circ0}_{-3.^\circ6 sys}$ for the positional angle, and $33.^\circ0 \pm 6.^\circ4_{stat}\,^{+14.^\circ0}_{-13.^\circ0 sys}$ for the central angle. Fitting these sources to the *Fermi*-LAT and MAGIC data results in the detection significances stated in table 5.4.

Table 5.3.: Systematic uncertainties for the spectral analysis of the *Fermi*-LAT and MAGIC data and each source component. The uncertainties are sorted according to their origin from either the IRFs of the detectors or the uncertainties in the shape of the background model and exposure for MAGIC and the IEMs for *Fermi*-LAT.

Source name	MAGIC				
	N_0 [TeV^{-1} cm^{-2} s^{-1}]		Γ		E_0
	Instrument	Bgr + Exposure	Instrument	Bgr + Exposure	Instrument
SNR Shell	1.6×10^{-13}	$\left(^{+3.9}_{-0.7}\right) \times 10^{-13}$	0.21	$^{+0.22}_{-0.13}$	15 %
MAGIC J2019+408	1.2×10^{-13}	$\left(^{+1.3}_{-0.7}\right) \times 10^{-13}$	0.17	$^{+0.13}_{-0.09}$	15 %
Arc	0.5×10^{-13}	$\left(^{+0.8}_{-0.5}\right) \times 10^{-13}$	0.16	$^{+0.15}_{-0.12}$	15 %
	Fermi-LAT				
		IEMs		IEMs	
SNR Shell	1.7×10^{-10}	0.1×10^{-10}	0.01	0.001	5 %
MAGIC J2019+408	$\left(^{+0.6}_{-0.5}\right) \times 10^{-10}$	0.01×10^{-10}	0.01	0.001	5 %

We extract the spectra of the source components from the MAGIC and *Fermi*-LAT data for the spatial components as defined in table 5.2. For the *Fermi*-LAT data we used 9 bins per decade over the range from 5 GeV to 500 GeV and the MAGIC data were binned into 4 bins per decade ranging from 250 GeV to 12.5 TeV. To consider the effect of the energy migration, the Fermi science tools and the SkyPrism analysis adjust an assumed spectral model via a forward folding procedure. As spectral model we used a power law of the form

$$\frac{\mathrm{d}N}{\mathrm{d}E} = N_0 \left(\frac{E}{E_0}\right)^{-\Gamma}, \tag{5.2}$$

with the photon index Γ, the normalization constant N_0, and the scaling energy (or pivot energy) E_0. The best fit results together with their uncertainties are summarised in table 5.4. The contributions to the systematic uncertainties estimated as described in the sections and and listed in table 5.3 are added in quadrature. Since, the spectral models are power-laws, the systematic uncertainty on the energy scale is converted to an uncertainty on the flux normalisation and added to it. We checked for a possible curvature of the spectrum of all sources by fitting a log-parabola spectrum (power-law exponent becomes $\Gamma + \beta \log(E/E_0)$ with the curvature factor β). For none of the components and instruments a significant curvature was detected (improvement over power law based on a likelihood ratio test led to a significance $< 3\sigma$).

Theoretical models do not necessarily follow a power-law and, strictly speaking, thus cannot be compared against the parameters in table 5.4. Therefore we additionally compute data points. For the *Fermi*-LAT data we rebin the 9 bins per decade to 2 bins between 5 – 13.9 GeV, 2 bins between 13.9 – 64.6 GeV, and 2 bins between 64.6 – 500 GeV. Thus, the energy bins are much wider ($\gtrsim 4$ times) than the energy resolution ($\Delta\ E < 5\%$) and, even though the data points are not deconvolved, the correlation

Table 5.4.: Results of the spectral analysis from the *Fermi*-LAT and MAGIC analysis for each source component. All sources were best fit with a power-law function with flux normalisation N_0, spectral index Γ, and scaling energy E_0

Source name	MAGIC			
	N_0 [TeV^{-1} cm^{-2} s^{-1}]	Γ	E_0 [TeV]	Det. Sign. [σ]
SNR Shell	$\left(10.2 \pm 2.6_{\mathrm{stat}}{}^{+6.7}_{-3.5_{\mathrm{sys}}}\right) \times 10^{-13}$	$-2.55 \pm 0.16_{\mathrm{stat}}{}^{+0.30}_{-0.25_{\mathrm{sys}}}$	1.0	6.1
MAGIC J2019+408	$\left(10.0 \pm 0.9_{\mathrm{stat}}{}^{+6.0}_{-3.5_{\mathrm{sys}}}\right) \times 10^{-13}$	$-2.81 \pm 0.10_{\mathrm{stat}}{}^{+0.21}_{-0.19_{\mathrm{sys}}}$	1.0	16.7
Arc	$\left(3.9 \pm 0.7_{\mathrm{stat}}{}^{+2.6}_{-1.5_{\mathrm{sys}}}\right) \times 10^{-13}$	$-3.02 \pm 0.18_{\mathrm{stat}}{}^{+0.22}_{-0.20_{\mathrm{sys}}}$	1.0	10.1
	Fermi-LAT			
SNR Shell	$\left(37.2 \pm 2.5_{\mathrm{stat}}{}^{+4.6}_{-4.0_{\mathrm{sys}}}\right) \times 10^{-10}$	$-2.11 \pm 0.06_{\mathrm{stat}} \pm 0.01_{\mathrm{sys}}$	0.05	23.2
MAGIC J2019+408	$\left(9.8 \pm 1.8_{\mathrm{stat}}{}^{+1.1}_{-1.0_{\mathrm{sys}}}\right) \times 10^{-10}$	$-1.86 \pm 0.13_{\mathrm{stat}} \pm 0.01_{\mathrm{sys}}$	0.05	8.9
Arc	-	-	0.05	0.0

between the points can be considered negligible. Whereas, for the MAGIC data the energy resolution (15 – 20%) is of the same order as the bin width and the correlation between the data points needs to be taken into account. Hence, we used the forward folding technique for data points (see section 4.4.2), in which the differential flux points are interpreted as the breaks of a broken power-law with multiple energy breaks. The arc was not detected in the *Fermi*-LAT data and thus only spectral upper limits could be computed. The upper limits (ULs) of the *Fermi*-LAT data are 95% confidence UL using the semi-Bayesian method of the science tools following Helene (1983) and the MAGIC UL are following the method by Rolke et al. (2005). In section 5.6.1 these data points are compared against a model curve.

5.4.5. Discussion of the observational results

All three source components identified in the *Fermi*-LAT and MAGIC data are significantly extended and, considering the size of the PSF of both instruments, are thus most likely situated within our Galaxy. Regarding the disk, given the agreement of the position and extension of the emission detected by *Fermi*-LAT with the radio shell, a random coincidence seems implausible. As explained above fitting the *Fermi*-LAT data resulted in a slight offset from the radio position and extension, but the fit of the *Fermi*-LAT data might be affected by the presence of MAGIC J2019+408. Hence, a disk model agreeing with the radio shell seems reasonable. Our spectral results are in agreement with previously published results on this source by the *Fermi*-LAT collaboration considering the difference in the area of the disk models.

MAGIC J 2019+408 is present in the MAGIC and *Fermi*-LAT data. Its position is offset with respect to VER J2019+407 ($0.^{\circ}07$ north of the latter) but still compatible ($\sim 2\sigma$ discrepancy considering combined errors). Aliu et al. (2013) did not observe the arc structure and not considering it as a distinct source may explain the different

positions. The fact that the extension of VER J2019+407 is significantly larger and the VERITAS collaboration claimed an asymmetric source when updating their results in Abeysekara et al. (2018) supports this assumption. In the *Fermi*-LAT energy range the spectrum of MAGIC J 2019+408 is slightly harder than the one of the shell, consistent with the findings of Fraija & Araya (2016). The authors analysed *Fermi*-LAT data in a narrower energy range and performed a point-source search on top of the larger disk model from the 3FGL (whereas we used a physically-motivated radio-based model). Accordingly, they obtained a TS map different from ours (figure 5.8), associated the excess emission with VER J2019+407, and extracted the spectrum at the corresponding position. For MAGIC J2019+408 the possibility for an extended source unrelated to the SNR cannot be ruled out. However, X-ray and radio data do not show any hint for a possible Galactic counterpart such as a pulsar powering a wind. Additionally, the spectral agreement with the SNR interior, particularly in the energy range of *Fermi*-LAT, further supports the assumption of a connection with the SNR.

The arc is seen by MAGIC only, though the VERITAS skymaps in Weinstein (2015) and Abeysekara et al. (2018) show hints for an extended emission stretching out towards the west of the SNR. The differences in morphology can be understood as a result of the differences in the observation time ($t_{\mathrm{MAGIC}} \sim 2 \times t_{\mathrm{VERITAS}}$) and different methods for reconstructing the background emission (Exclusion region for MAGIC vs. ring background model for VERITAS), of which the ring background faces issues with extended sources (Berge et al., 2007). The exclusion region method is insensitive to emission regions larger than twice the wobble distance ($1.^{\circ}2$ for our MAGIC data). We can thus not rule out that the arc structure is the residual of a much larger complex such as the Cygnus Cocoon (Ackermann et al., 2011). However, given that the arc traces rim of the SNR and its spectrum agrees with that of MAGIC J2019+408 at TeV energies, the association with the γ-Cygni SNR is very plausible.

The PSF of the HAWC experiment does not allow resolving substructures in the γ-Cygni region making a comparison with the MAGIC results difficult. HAWC determined the centre of the emission in around the SNR close to the centre of the shell (Abeysekara et al., 2017), whereas from the MAGIC high energy skymap one would expect it to be shifted towards the north-west. This suggests additional emission surrounding the SNR likely towards the south of the shell, a region not well covered by the MAGIC observations due to the presence of Sadr. Still the steep spectral index measured by HAWC is in agreement with a softening of the spectrum between the energy range covered by *Fermi*-LAT and MAGIC.

The major uncertainty regarding our spatial model concerns the 3-D orientation of the SNR. The γ-ray emission in the north-west might point towards the Earth and emission situated outside the rim might be mapped onto the SNR shell. The γ-ray data do not allow estimating the distance in the line-of-sight and therefore resolving the ambiguity. Particularly, this may lead to an overestimation of N_0 and an underesti-

mation of Γ for the disk emission. Furthermore, the extension of the arc region might be underestimated. While the impact of the effect is challenging to quantify, we argue that it barely affects the physical implications of our findings.

5.5. Interpretation and modelling

5.5.1. Leptonic vs hadronic?

The radio emission proves the presence of high-energy electrons inside the shell, which can also be the origin of the γ-ray emission via inverse Compton scattering (IC) or bremsstrahlung radiation. Due to the low density of $0.2\,\mathrm{cm}^{-3}$ inside the SNR shell (table 5.1), the former emission will dominate over the latter even when only considering a CMB photon field. The high energy spectrum from the shell of γ-Cygni up to a few hundreds of GeV has a slope of $\sim E^{-2}$. In contrast, the average radio spectral index α_R of 0.48 – 0.75 (Zhang et al., 1997; Gao et al., 2011; Kothes et al., 2006; Ladouceur & Pineault, 2008) implies an electron spectrum between $\mathrm{d}N/\mathrm{d}E \propto E^{-1.96}$ and $\propto E^{-2.5}$ and thereby a harder Inverse Compton (IC) spectrum in γ-rays. Hence, a leptonic scenario requires an additional break in the spectrum in the keV to GeV range to bring both observation into agreement. Such a break can naturally arise from electron cooling. To obtain a synchrotron cooling time shorter than the lifetime of the SNR, the magnetic field inside the SNR needs to be $B \gtrsim 20\,\mu\mathrm{G}$.

If the emission outside the shell originates from IC as well, the morphology of the the arc and MAGIC J2019+408, needs to be explained either by an enhancement of the radiation field in those regions or by a specific guiding magnetic field creating an over-density of electrons compared to other parts around the shell. Observations with the Infrared Astronomical Satellite (IRAS; Saken et al., 1992) indeed suggest a higher IR emission towards MAGIC J2019+408. However, the morphology of MAGIC J2019+408 does not agree with the IR structure and the peak of the former is offset with respect to the centre of the latter by $\sim 0.^\circ 6$. Additionally, the parallaxes of identified IR sources in the vicinity of MAGIC J2019+408 (Gaia Collaboration, 2018) suggest that at least part of the IR emission is farther away than the γ-Cygni system. The absence of non-thermal synchrotron radiation at MAGIC J2019+408 (skymaps in Ladouceur & Pineault (2008)) also renders the magnetic field scenario unlikely. Finally, the arc region is dark in both IR and synchrotron which speaks against an IC scenario as well.

Accordingly, the most likely leptonic scenario for the arc and MAGIC J2019+408 is bremsstrahlung emission. Like a hadronic scenario, it requires a local enhancement of the target gas density and is independent from the constrains above. Nevertheless, in this case the power-law index of the electron spectrum needs to change from $\Gamma \sim -3$ inside shell to $\Gamma \sim -2$ outside. Moreover, in order for the bremsstrahlung to dominate over the pion decay the accelerated electron-to-proton ratio has to be $\gg 10^{-2}$, whereas the study of multi-wavelength emission from several young SNRs

point towards smaller ratios of $\approx 10^{-3}$ or less (see, e.g., Völk et al., 2005; Morlino & Caprioli, 2012). Additionally, theoretical predictions based on particle-in-cell simulations of collisionless shocks hints at values of electron-to-proton ratios of $\lesssim 10^{-2}$ (Park et al., 2015).

In conclusion, even if a leptonic explanation cannot be completely ruled out, its realisation requires extreme conditions. Alternatively, the γ-ray emission can be explained in a hadronic scenario, which is not subject to the aforementioned constrains. Hence, in the following we develop a hadronic model to explain the data and accordingly assume that the bulk of emission is due to hadronic interactions.

5.5.2. Escaping or precursor?

If the emission from the arc region is indeed connected to the SNR, it can be either due to the CR precursor in front of the shock (see section 2.3.4) or produced by particles escaping from the shock. The former interpretation seems unlikely for two different reasons. Firstly, the spectrum from the arc region is softer (at most similar given the uncertainties) than the one detected from the SNR interior. Using the linear theory with a spatially constant diffusion coefficient in the precursor, the spectrum upstream of the shock is given by formula (2.16). If the spectrum at the shock is $f_{sh} \propto p^{-\alpha}$ and the diffusion coefficient is $D_1(p) \propto p^{\beta}$ (in general $\beta > 0$ and $\beta = 1$ for Bohm diffusion), the spatial integrated spectrum upstream is

$$\int_0^{\infty} f_{up}(x,p)\mathrm{d}x \propto p^{-\alpha+\beta}\,. \tag{5.3}$$

Hence, the spectrum from the arc region should be harder than the one inside the remnant unless the diffusion coefficient is constant in momentum, which would be difficult to explain from both observational and theoretical grounds.

The second argument comes from the comparison of the SNR age with the acceleration time. If the arc represents the shock precursor, the thickness of the arc Δ_{arc} corresponds to the diffusion length λ_p of particles with momentum p upstream. Hence, we can estimate the diffusion coefficient at the central energy observed imposing $\lambda_p = \Delta_{arc} \simeq D_1(p)/u_{sh}$. At a distance of 1.7 kpc, the extension of the arc is $\Delta_{arc} \sim 4.5$ pc for central energy of all MAGIC data of ~ 800 GeV, corresponding to parent protons of $\sim$8 TeV, leading to an diffusion coefficient upstream of the shock equal to

$$D_1(8\,TeV) \simeq \lambda_p u_{sh} = 1.4\times 10^{27}\left(\frac{\lambda_p}{4.5\,\mathrm{pc}}\right)\left(\frac{u_{sh}}{10^3\,\mathrm{km\,s^{-1}}}\right)\,\mathrm{cm^2\,s^{-1}}\,. \tag{5.4}$$

Using formula (2.20) for a parallel shock the acceleration time needed to produce particles at 8 TeV can be estimated as

$$t_{acc}(p) = \frac{3}{u_1-u_2}\left(\frac{D_1}{u_1}+\frac{D_2}{u_2}\right) \simeq 8\,\frac{D_1}{u_1^2} \simeq 3.5\times 10^4\,\mathrm{yr}\,, \tag{5.5}$$

which is ~ 5 times the estimated SNR age (D_2 is the diffusion coefficient downstream, u_2 the velocity of the downstream plasma, and u_1 the shock speed). As explained in section 5.4.4 a possible misalignment could lead to an overestimation of the hardness of the spectrum from inside the SNR. Accordingly, the precursor could not be excluded based on the spectral similarity. In that case however, the extension of the arc increases strengthening the argument of the acceleration time. In summary a precursor scenario for the arc region seems improbable and instead it is a region, where particles escaping from γ-Cygni interact with the ISM.

Using the observed extension of the arc a lower limit to the external diffusion coefficient, D_{out}, can be put assuming that particles located in the arc started escaping at the beginning of the ST phase. Considering the typical energy of 8 TeV for CR protons, which produces γ-rays at ~ 800 GeV and reasonable values for the SNR parameters ($n_0 = 0.2$ cm^{-3}, SNR age = 7000 yr, $E_{SN} = 10^{51}$ erg, $M_{ej} = 5 M_{\odot}$, and $d = 1.7$ kpc), the diffusion coefficient can be estimated via the length ($\lambda_{diff} = (4 D_{out} t)^{1/2}$; factor 4 assumes 2 dimensions):

$$D_{out}(8\,TeV) = \frac{\lambda_{diff}^2}{4t} \simeq \frac{(R_{SNR} + \Delta_{arc} - R_{ST})^2}{4\,(t_{SNR} - t_{ST})} \simeq 2.6 \times 10^{27} cm^2\, s^{-1}\,, \qquad (5.6)$$

where $R_{ST} = (M_{ej}/\rho_0)^{1/3}$ and $t_{ST} = E_{SN}^{-1/2} M_{ej}^{5/6} \rho_0^{-1/3}$, while $\Delta_{arc} = 0.^{\circ}15 \simeq 4.5$ pc. The estimated D_{out} is ~ 340 times smaller than the average Galactic diffusion coefficient at 8 TeV as obtained from direct CR measurements, i.e. $D_{Gal} \approx 6\,\beta\, 10^{28} (E/GeV)^{0.3} cm^2\, s^{-1}$ (see e.g. Trotta et al., 2011; Yuan et al., 2017). Note that changing the SNR parameters in the range reported in table 5.1 (always assuming that the estimated extension matches the real one), the ratio D_{Gal}/D_{out} ranges between $\sim$100 and $\sim$550. Note, that the considerations in this section would equally apply to a leptonic scenario with the only difference that the parameters would be tested at a parent particle energy of ~ 2 TeV instead of 8 TeV.

The result obtained in equation (5.6) represents a lower limit for two reasons: 1) we assume that the arc mainly extends orthogonally to the line of sight. If this is not true, Δ_{arc} would be larger than 3 pc, resulting in a larger D_{out}. 2) the arc could represent an over-dense region. If beyond such region the density drops to a lower value, γ-rays could be undetectable even if CR have diffused beyond Δ_{arc}. A more thorough discussion on this point will be done in section 5.6.3.

In the escape scenario, CRs are expected to escape radially symmetrically or, in case of a dominant main magnetic field, to escape mainly along the magnetic field direction. Emission beyond the shell should thus not be solely seen in the direction of the arc. A straightforward explanation is that the arc could have a larger density than the rest of the circumstellar medium. Additionally, a large scale magnetic field oriented in the direction of the arc may cause a larger density of particles escaping into the arc region and can explain why emission is concentrated there. Indeed, the radio emission indicates that the magnetic field is directed along the arc. In fact, the

radio shell is not homogeneous but presents two main lobes in the south-east and north-west, the latter roughly agreeing with the direction of the arc. Because the shock acceleration theory predicts a larger efficiency for the parallel shock configuration (i.e. $\vec{B} \parallel \vec{u}_{sh}$), the two radio lobes could be interpreted as polar caps. In such a situation another bright region can be expected on the opposite side of the SNR with respect to the arc, but again a low target gas density could impede its visibility.

Furthermore, the non-detection of emission on the opposite side of the SNR may partly result from the telescope pointing position chosen to avoid the influence of the bright star Sadr. The opposite site of the SNR is about $\gtrsim 1^\circ$ away from our pointing positions, where the acceptance of the MAGIC telescopes decreases to $\lesssim 1/2$ of the full sensitivity. The hints for emission at the south of the SNR shell visible in figure 5.7 and that HAWC determined the centre of the SNR to agree with the centre of the shell, could be a sign for a counterpart to the arc.

5.5.3. A simplified approach for particle propagation

This section up to section 5.6.1 describes a model for the propagation of accelerated particles inside and outside the SNR in order to properly calculate the γ-ray emission. It closely follows the derivation by Celli et al. (2019b). For simplicity we assume spherical symmetry inside and outside the remnant. The transport equation for accelerated protons in spherical coordinates is

$$\frac{\partial f}{\partial t} + u\frac{\partial f}{\partial r} = \frac{1}{r^2}\frac{\partial}{\partial r}\left[r^2 D \frac{\partial f}{\partial r}\right] + \frac{1}{r^2}\frac{\partial (r^2 u)}{\partial r}\frac{p}{3}\frac{\partial f}{\partial p}\,, \tag{5.7}$$

where u is the advection velocity of the plasma and D the diffusion coefficient. The former is obtained from the SNR evolution. Because γ-Cygni is clearly in the ST phase, we describe its evolution using the ST solution in the case of expansion inside uniform medium with density ρ_0. The shock position R_{sh} and the shock speed as a function of time are given by equation 2.6:

$$R_{sh}(t) = \left(\xi_0 \frac{E_{SN}}{\rho_0}\right)^{1/5} t^{2/5}\,, \tag{5.8}$$

$$u_{sh}(t) = \frac{2}{5}\left(\xi_0 \frac{E_{SN}}{\rho_0}\right)^{1/5} t^{-3/5}\,, \tag{5.9}$$

where $\xi_0 = 2.026$ (for monoatomic gas with specific heat ratio $\gamma = 5/3$). The structure of the gas inside the SNR is described using the linear velocity approximation (Ostriker & McKee, 1988) for the bulk velocity (equation 2.11), so the gas velocity profile for $r < R_{sh}$ is given by

$$u(r,t) = \left(1 - \frac{1}{\sigma}\right)\frac{u_{sh}(t)}{R_{sh}(t)} r\,, \tag{5.10}$$

where σ is the compression factor at the shock. The radial profile of the gas density in the SNR interior (needed to calculate the γ-ray emission) is also given by the ST

solution and can be well approximated by the following polynomial with respect to the self-similar variable $\bar{r} = r/R_{sh}(t)$ (Sedov, 1959),

$$\rho_{in}(\bar{r}) = \sigma\,\rho_0\left(a_1\bar{r}^{\alpha_1} + a_2\bar{r}^{\alpha_2} + a_3\bar{r}^{\alpha_3}\right)\,, \tag{5.11}$$

where ρ_0 the upstream density and the parameters a_k and α_k are obtained from a fitting procedure which gives: $a_1 = 0.353$, $a_2 = 0.204$, $a_3 = 0.443$, $\alpha_1 = 4.536$, $\alpha_2 = 24.18$, and $\alpha_3 = 12.29$ (Celli et al., 2019a).

In the subsequent sections the transport equation (5.7) will be solved using two different approximations, one for particles confined inside the remnant and one for the escaping particles.

5.5.4. CR distribution at the shock

The distribution function of CR at the shock $f_0(p,t)$ follows the description in Ptuskin & Zirakashvili (2005). In this model the distribution function of CR at the shock is given by an analytical formula and thus is not a full non-linear description (see section 2.3.4). However, it takes into account a modification of the particle spectrum by the CR pressure. The acceleration efficiency ξ_{CR}, with which the shock is converting kinetic energy to CR, is assumed to be constant in time. The spectrum is a power law in momentum up to a maximum value $p_{\mathrm{max},0}$ and, in a simplified form, can be written as

$$f_0(p,t) = \frac{3\,\xi_{CR}\,u_{sh}(t)^2\rho_0}{4\pi\,c(m_pc)^4\Lambda(p_{\mathrm{max},0}(t))}\left(\frac{p}{m_pc}\right)^{-\alpha}\Theta\left[p_{\mathrm{max},0}(t) - p\right]\,, \tag{5.12}$$

where m_p is the proton mass, Θ is the Heaviside function while $\Lambda(p_{\mathrm{max},0})$ is the function required to normalize the spectrum such that the CR pressure at the shock is $P_{CR} = \xi_{CR}\,\rho_0 u_{sh}^2$. We keep the power law index α as a free parameter in order to fit the γ-ray data (DSA predicts α to be equal or very close to 4, see section 2.3.2).

The maximum momentum at the shock $p_{\mathrm{max},0}$ is a function of time and its calculation requires a correct description of the evolution of the magnetic turbulence. However, there is currently no comprehensive description considering the magnetic turbulence depends on the self-generation by the same particles, damping effects, and wave cascades altogether. Hence, here we use the general assumption that the maximum momentum increases linearly during the free expansion phase and decreases as a power law during the ST phase:

$$p_{\mathrm{max},0}(t) = \begin{cases} p_M\,(t/t_{ST}) & \text{if } t < t_{ST} \\ p_M\,(t/t_{ST})^{-\delta} & \text{if } t > t_{ST}\,, \end{cases} \tag{5.13}$$

where p_M, the absolute maximum momentum reached at $t = t_{ST}$, and $\delta > 0$ are treated as a free parameter of the model (the same relations are e.g. used in Gabici et al., 2009).

Inverting equation 5.13 gives the *escaping time*, when particles with momentum p cannot be confined any more and start escaping from the remnant,

$$t_{esc}(p) = t_{ST} \left(p/p_M\right)^{-1/\delta} . \tag{5.14}$$

Furthermore, we can define the *escaping radius*, namely the radius of the forward shock when particles with momentum p start escaping, i.e.

$$R_{esc}(p) = R_{sh}\left(t_{esc}(p)\right) . \tag{5.15}$$

The particle distribution evolves in a different way before and after $t_{esc}(p)$, as we discuss below.

5.5.5. Distribution of confined particles

As long as $t < t_{esc}(p)$ particles with momentum p are confined inside the SNR. A reasonable approximation for the distribution of these confined particles f_c can be obtained from equation (5.7) neglecting the diffusion term. This approximation is accurate for $p \ll p_{\max,0}(t)$, but we will show in a moment that in the test-particle case the diffusion inside the SNR does not play an important role. The simplified transport equation is

$$\frac{\partial f_c}{\partial t} + u\frac{\partial f_c}{\partial r} = \frac{1}{r^2}\frac{\partial (r^2 u)}{\partial r}\frac{p}{3}\frac{\partial f_c}{\partial p} \tag{5.16}$$

and the solution can be easily obtained using the method of characteristic, accounting for the plasma speed inside the SNR as approximated by equation (5.10). The solution (see Ptuskin & Zirakashvili, 2005) can be written as

$$f_c(t,r,p) = f_0\left(\left(\frac{R_{sh}(t)}{R_{sh}(t')}\right)^{1-\frac{1}{\sigma}} p, t'(t,r)\right) , \tag{5.17}$$

where $t'(t,r)$ is the time when the plasma layer located at the position r at time t has been shocked, namely

$$t'(t,r) = \left(\rho_0\, \xi_0^{-1} E_{SN}^{-1}\right)^2 r^{10} t^{-3}. \tag{5.18}$$

Using equations (5.12) and (5.8) and neglecting the mild dependence of $\Lambda(p_{\max})$ on t, we simplify equation (5.17) to

$$f_c(t,r,p) = f_0(p,t)\left(\frac{t'}{t}\right)^{\frac{2\alpha(\sigma-1)}{5\sigma}-\frac{6}{5}} \Theta\left[p_{\max}(t,r) - p\right] . \tag{5.19}$$

The maximum momentum of particles $p_{\max}(t,r)$ at position r and time t is equal to the maximum momentum of particles accelerated at time t' and considering adiabatic losses:

$$p_{\max}(t,r) = p_{\max,0}(t')\left(\frac{R_{sh}(t')}{R_{sh}(t)}\right)^{1-\frac{1}{\sigma}} = p_{\max,0}(t)\left(\frac{t'}{t}\right)^{\frac{2}{5}\frac{\sigma-1}{\sigma}-\delta} , \tag{5.20}$$

where the last step uses equation (5.13). Interestingly, assuming test-particle DSA ($\alpha = 3\sigma/(\sigma-1)$, see formula 2.15), the distribution function of confined particles f_c has only a mild dependence on r through the normalisation factor $\Lambda(p_{\max})$. In such a case neglecting diffusion in first approximation is justified because $\partial_r f_c \approx 0$.

5.5.6. Distribution of escaping particles

When $t > t_{esc}(p)$ particles with momentum p cannot be confined any more and start escaping. Typically, this escape is assumed to be instantaneous, meaning that particles with momentum p are immediately located outside the remnant. While this approximation is valid when studying the final CR spectrum released into the Galaxy, it is invalid in the case of γ-Cygni as we aim for describing the early phase of the escape process in a region close to the SNR.

An approximate solution for time $t > t_{esc}(p)$ can be obtained assuming that particles are completely decoupled from the SNR evolution and only diffuse. The evolution is therefore described by equation (5.7) dropping all terms including u:

$$\frac{\partial f_{esc}}{\partial t} = \frac{1}{r^2}\frac{\partial}{\partial r}\left[r^2 D \frac{\partial f_{esc}}{\partial r}\right] . \tag{5.21}$$

This equation needs to be solved with the initial condition: $f_{esc}(t_{esc}(p), r, p) = f_c(t_{esc}(p), r, p) \equiv f_{c0}(r, p)$ for $r < R_{esc}(p)$ and 0 elsewhere. The diffusion coefficient in the medium outside the SNR, D_{out}, is assumed to be spatially constant and shall later be constrained by our observations. Generally, D_{out} differs from the diffusion coefficient inside the SNR, D_{in}. Nonetheless, for simplicity we assume $D_{in} = D_{out}$ (and spatially constant). Such an approximation allows for an analytic solution of equation (5.21) via a Laplace transform (see Celli et al., 2019a, for the full derivation). The final result is

$$\begin{aligned} f_{esc}(t, r, p) = \frac{f_{c0}(p)}{2}\,\Theta\left[t - t_{esc}(p)\right] \times \\ \left\{\frac{R_d}{\sqrt{\pi}\, r}\left(e^{-R_+^2} - e^{-R_-^2}\right) + \mathrm{E}rf\left(R_+\right) + \mathrm{E}rf\left(R_-\right)\right\} , \end{aligned} \tag{5.22}$$

where $R_\pm = \left(R_{esc}(p) \pm r\right)/R_d(p)$, $R_d = \sqrt{4D(p)\left(t - t_{esc}(p)\right)}$, and Erf is the error function. Examples of f_{esc} are plotted in figures 5.10 and 5.11 for different times and different values of the diffusion coefficient. For all plots we assume a strong shock ($\sigma = 4$) and the test particle limit ($\alpha = 4$).

When $D_{in} \neq D_{out}$ the leaking of particles from the remnant changes but the profile of the distribution function outside of the remnant remains essentially the same, being determined mainly by D_{out}.

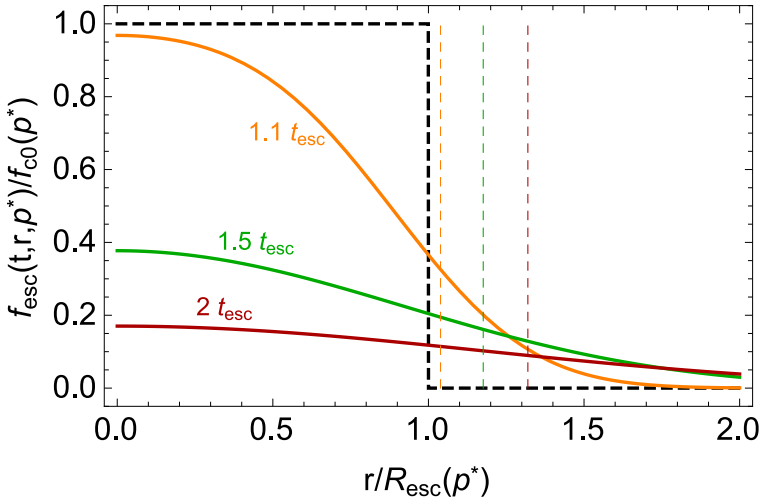

Figure 5.10.: Distribution of escaping particles at one arbitrary fixed momentum, $p^* = 10$ TeV, as a function of the radial coordinate normalised to $R_{esc}(p^*) = 13$ pc. Different lines refer to different times in unit of $t_{esc}(p^*) = 4000$ yr, as labelled, and the vertical dashed lines correspond to the shock position at those times. We assume $D_{out} = D_{Gal}/100$, $\delta = 2.2$ and $p_M = 100$ TeV.

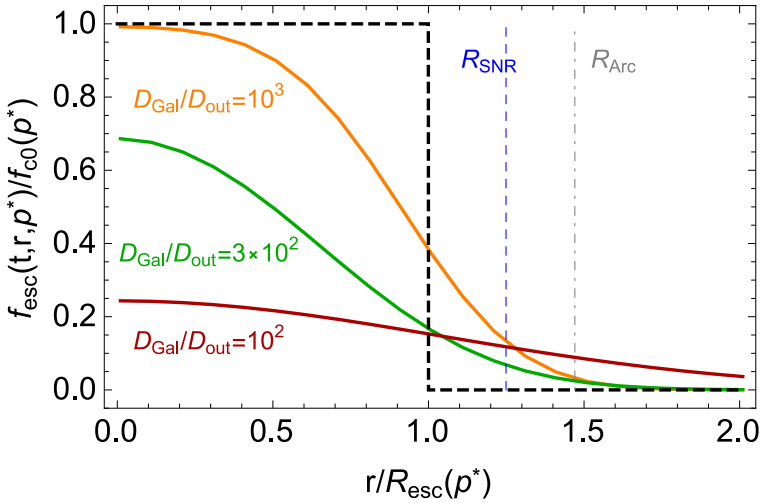

Figure 5.11.: Distribution of escaping particles at $p^* = 10$ TeV$/c$ and $t = t_{SNR}$ as a function of the radial coordinate normalised to $R_{esc}(p^*) = 13$ pc. Different lines refer to different values of the diffusion coefficient, as labelled. The vertical lines correspond to the shock position (dashed) and to the arc external edge (dot-dashed) as observed now. The remaining parameters are the same of figure 5.10.

5.6. gamma-ray spectra

5.6.1. Emission from the SNR interior and arc

Once the particle distribution is known at any position inside and outside the SNR, the calculation of γ-ray emissivity due to hadronic collisions is straightforward. The rate of emitted photons from a given region is

$$\Phi_\gamma(E_\gamma, t) \equiv \frac{\mathrm{d}N_\gamma}{\mathrm{d}E_\gamma\,\mathrm{d}t} = 4\pi c \int \frac{\mathrm{d}\sigma(E_p, E_\gamma)}{\mathrm{d}E_\gamma} J_p(E_p, t)\mathrm{d}E_p\,, \tag{5.23}$$

We parametrise the differential cross section following Kafexhiu et al. (2014). $J_p(E_p, t)$ is the spatially-integrated proton flux as a function of the kinetic energy E_p and observation time t. It is connected to the momentum distribution function as $J_p(E_p)\mathrm{d}E_p = \beta c F_p(p)\mathrm{d}^3p$, where F_p is the proton distribution in momentum convoluted with the target density in the region of interest. In particular we distinguish two regions, the interior of the SNR and the fraction of the external spherical shell which include the arc. The corresponding distributions are

$$F_{p,SNR}(p, t_{SNR}) = \int_0^{R_{SNR}} 4\pi r^2\, n_{in}(r) f_{in}(t_{SNR}, r, p)\,\mathrm{d}r \tag{5.24}$$

$$F_{p,arc}(p, t_{SNR}) = \eta_{arc}\, n_{arc} \int_{R_{SNR}}^{R_{SNR}+\Delta_{arc}} 4\pi r^2\, f_{esc}(t_{SNR}, r, p)\,\mathrm{d}r\,, \tag{5.25}$$

where the particle distribution inside the SNR is $f_{in} = f_c$ for $p < p_{\mathrm{max},0}(t_{SNR})$, while $f_{in} = f_{esc}$ otherwise, with f_c and f_{esc} given by equations (5.19) and (5.22), respectively. The gas distribution inside the remnant is given by equation (5.11), while in the arc we assume a constant density defined by n_{arc}. The additional factor η_{arc} accounts for the spherical shell fraction which includes the arc region.

Figure 5.12 shows the best fit to the observed γ-ray flux for both the SNR interior and the arc region. The parameters used to produce these curves are summarised in table 5.5. Parameters related to the SNR evolution are fixed to the values from table 5.1. All the other parameters are allowed to vary. The corresponding numbers in square brackets show the range of values resulting in curves, which are still in reasonable agreement with the data.

At a first glance, the large number of free parameters (six if we exclude the ones related to the SNR) may suggest a strong degeneracy between them. Nevertheless, we can fix all the values with a reasonable small level of uncertainty because every parameter is connected to a specific feature of the spectrum.

First, the *Fermi*-LAT data from the remnant interior and the radio data fix the slope of the accelerated spectrum below TeV energies to be $\alpha \simeq 4.0$. Secondly, the normalisation of the γ-ray flux fixes the acceleration efficiency to be $\xi_{CR} \simeq 4\%$. In the energy range between 100 and 300 GeV the slope abruptly changes from $\sim E^{-2}$ to $\sim E^{-2.5}$. In our model this turning point defines the maximum energy of particles

Table 5.5.: Values of parameters used to fit the γ-Cygni spectrum shown in figure 5.12. The first block refers to the SNR properties, the second to the acceleration and escaping properties and the last one to the properties of the external medium (density times filling factor and diffusion coefficient). The number in square brackets shows the possible range of values that can still give reasonable fits to the data.

E_{SN}	M_{ej}	t_{SNR}	d	n_0	ξ_{CR}	α	E_{MAX}	δ	$\eta_{arc} n_{arc}$	D_{Gal}/D_{out}
10^{51} erg	$5\,M_\odot$	7 kyr	1.7 kpc	0.2 cm^{-3}	4%	4.0	90 TeV	2.4	0.4 cm^{-3}	18
[see table 5.1]					[3%–7%]	[3.9–4.1]	[20–300]	[2.2–4.0]	[0.3–0.5]	[10–40]

presently accelerated to be $E_{\max}(t_{SNR}) \simeq 1-3$ TeV. Noticeably, such energy is independently constrained by the *Fermi*-LAT upper limits on the flux from the arc region: to be compatible with the MAGIC data, the γ-ray flux from this region needs to have a maximum in the range 100 – 300 GeV. Such a maximum corresponds to γ-rays produced by the lowest energetic particles in the arc, which is very close to the maximum energy of particles accelerated now. Additional information is derived from the shape of the MAGIC spectrum that simultaneously determines E_{MAX} (the maximum energy reached at the beginning of the ST phase), D_{out} and δ. Our model predicts that the shape of the γ-ray emission from the SNR and from the arc should be very similar in the MAGIC band. Considering the uncertainties in the data, this is compatible with observations. Finally, the normalisation of the MAGIC data points of the arc spectrum sets the product of $\eta_{arc} \times n_{arc}$. Because the observed geometry suggests a filling factor $\eta_{arc} \sim$20% (with some uncertainties due to a possible line of sight effect, see section 5.4.5) we also have an estimate of the target density in the arc region which has to be $1-2\,\mathrm{cm}^{-3}$. The targets inside the arc regions could be either the possible cavity wall reported by Ladouceur & Pineault (2008) or smaller clumps like the one found inside the north-west shell by Uchiyama et al. (2002).

We also note that some level of uncertainty is introduced by the parametrisation of the differential cross section used in equation (5.23). We tried all the four models considered in Kafexhiu et al. (2014) (Geant 4.10, Pythia 8.18, SYBILL 2.1 and QGSJET-1) but, for sake of clarity, we only show the results obtained with Pythia because for $E_\gamma > 1$ GeV it gives a γ-ray flux roughly in between the maximum and minimum predictions (obtained with SYBILL and Geant, respectively). At lower energies all the methods give essentially the same result. The uncertainty in the cross section mainly corresponds to a factor ~ 2 difference in the target density of the arc or, equivalently, in the acceleration efficiency. This uncertainty is accounted for in the uncertainty interval shown with square brackets in table 5.5.

5.6.2. Emission from MAGIC J2019+408

MAGIC J2019+408 has been detected both by *Fermi*-LAT and MAGIC. Remarkably the high energy spectrum is very similar to the one detected from the arc region, whereas

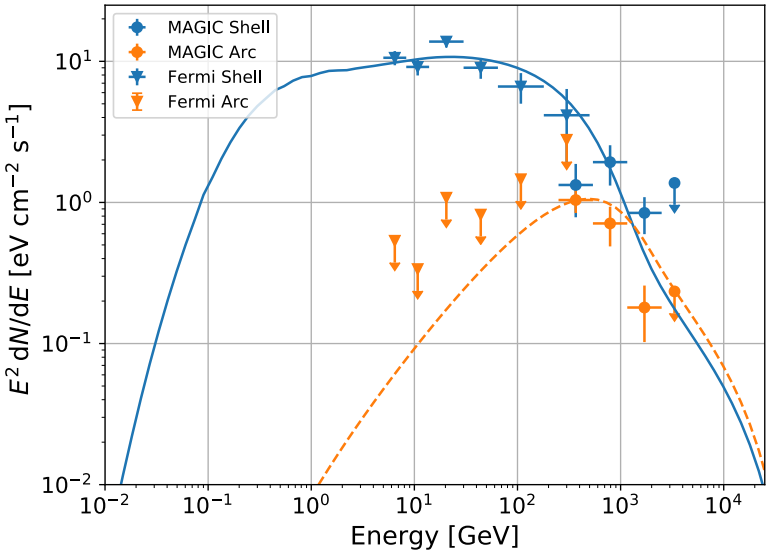

Figure 5.12.: Computed γ-ray flux due to π^0 decay from the SNR interior (solid line) and from the arc region (dashed line) based on our model compared against data points from our *Fermi*-LAT (triangles) and MAGIC (circles) analysis. The colour marks corresponding model and data points: blue for the SNR interior and orange for the arc.

in the *Fermi*-LAT band the slope is slightly harder than the emission from the overall SNR but still compatible with the latter. This finding suggests that at least part of the emission from the hot-spot should come from a region located inside the SNR, where also low energy particles are present.

In the framework of the hadronic model proposed here, MAGIC J2019+408 can be understood as a combination of emission from the remnant interior plus a contribution from escaping particles located outside the SNR. In figure 5.13 we show a possible fit to the data by combining these two components and only adjusting the normalisation via the target density. Remarkably this fit does not require any further tuning of the remaining parameters of the model and we keep the values reported in table 5.5. Considering that the angular extension of MAGIC J2019+408 is $\sim 0.1^\circ$ and assuming a spherical geometry, the shown fit requires a density of $\sim 40\,\mathrm{cm}^{-3}$ both for the internal and the external contributions. Hence, MAGIC J2019+408 could be due to an over-dense cloud partially engulfed by the SNR shock and partially still outside of it. Alternatively, MAGIC J2019+408 could result from two (or more) clouds, spatially separated, one inside and one outside the SNR, but located along the same line of sight. It is worth mentioning that the estimated density of $\sim 40\,\mathrm{cm}^{-3}$ is close to the value of $\sim 20\,\mathrm{cm}^{-3}$ reported by Mavromatakis (2003) but in the East of the SNR. Even though no interaction between the SNR and a cloud has been reported for the north of the SNR, CO observations by Leung & Thaddeus (1992) show the presence of a cloud close to MAGIC J2019+408 (figure 5.3). Considering that the CO might be enveloped in a larger shielding layer, an interaction between the SNR and a cloud

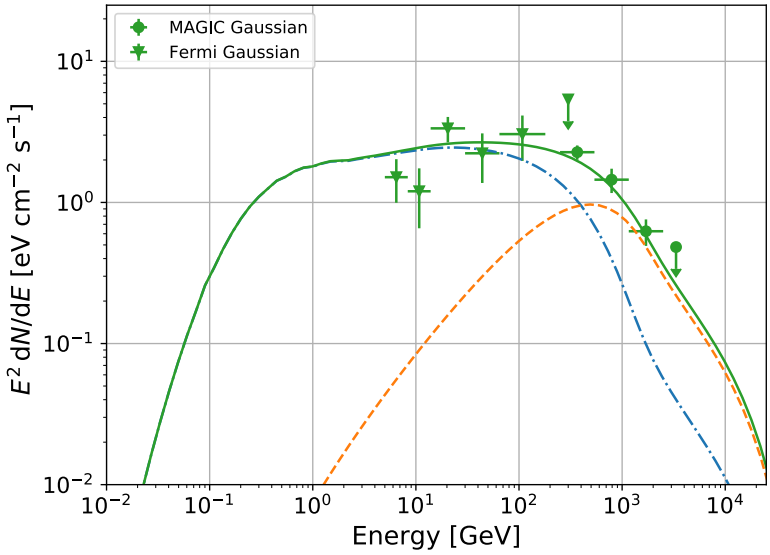

Figure 5.13.: Computed γ-ray flux due to π^0 decay from MAGIC J2019+408 based on our model compared against data points from our *Fermi*-LAT (triangles) and the MAGIC (circles) analysis. The spectrum (solid, green line) is modelled as the sum of emission from the remnant interior (dash-dotted, blue line) and exterior (dashed, orange line).

seems a feasible scenario.

One point to stress is that the presence of a dense cloud engulfed by a shock could result in a harder hadronic spectrum due to magnetic field amplification around the cloud border, which prevents low energy particles from penetrating the cloud. Nevertheless, this mechanism is only relevant when the density contrast between the cloud and the circumstellar medium is $\gtrsim 10^3$ (Celli et al., 2019b). Otherwise, the amplification of the magnetic field around the cloud is not strong enough. The density contrast in our case is below that threshold, hence the spectrum inside the cloud should be very similar to the one inside the SNR.

5.6.3. Discussion of the modelling

Our interpretation of the γ-ray spectra has interesting implications for the shock acceleration theory. First, the slope of accelerated particles is very well constrained to be close to 4, in agreement with the standard prediction of DSA. In addition, we have shown that the maximum energy accelerated at the current SNR age is around a few TeV, while the maximum energy reached at the beginning of the ST phase is at most few hundreds of TeV. Hence γ-Cygni is not a PeVatron during the ST phase, nevertheless we cannot exclude that higher energies could have been reached during the very early stage of its evolution. The fact that the maximum energy now is of the order of TeV immediately provides an estimate of the level of magnetic turbulence

in the shock region. Using equation (5.6) we can estimate the diffusion coefficient upstream of the shock from the maximum energy and the remnant age. In quasi-linear theory, the diffusion coefficient D is expressed as a function of the turbulence level as $D_1(p) = D_{\rm Bohm}/\mathcal{F}(k_{res})$, where $D_{\rm Bohm} = r_L v/3$, r_L being the Larmor radius, and $\mathcal{F} = (\delta B(k_{res})/B_0)^2$ is calculated at the resonant scale $k_{res} = 1/r_L(E_{\rm max})$. Hence $E_{\rm max}(t_{SNR}) = 1$ TeV (obtained from the condition $t_{acc} = t_{SNR}$) inferred from the spectrum implies $\delta B/B_0 \simeq 0.25$ where we assumed $B_0 = 3\mu$G. At a first glance, such a small value for the magnetic turbulence seems at odds with the common assumption that close to strong shocks the Bohm limit is reached. Nevertheless, two different arguments suggest that $\delta B/B_0$ should be smaller than unity as inferred here. First of all, the main mechanism often invoked to excite magnetic turbulence resonating with accelerated particles is the *resonant streaming instability*, which, however, saturates at $\delta B/B_0 \lesssim 1$ (see Blasi, 2013, section 4.2). Higher level of turbulence requires other mechanisms, like the *non-resonant instability* (NRI, Bell, 2004) but such a mechanism is thought to be effective when the shock speed is $\gg 1000$ km/s (Amato & Blasi, 2009). Moreover, the NRI excites small scale modes which, to efficiently scatter high energy particles, requires an inverse cascade up to the larger scales which resonate with such particles. Hence, either the NRI is not efficiently excited or it is excited but the inverse cascade does not occur on the required timescale. CRs can amplify the magnetic field upstream even through another mechanism which takes place when the medium is inhomogeneous (Drury & Downes, 2012). Nevertheless, also such mechanism requires high shock speeds to be effective. The exact condition is $u_{sh} \gg \sqrt{4\pi/\xi_{CR}} v_A (\delta\rho/\rho)^{-1}$, where $\delta\rho$ is the typical level of density fluctuation in the upstream while v_A is the Alfvén speed. Using the parameter values adopted in this work, one easily get the condition $u_{sh} \gg 1000$ km/s. Furthermore, even if the amplification were efficient, the upstream plasma may be partially neutral and the ion-neutral friction could efficiently damp the magnetic turbulence resulting in $\delta B/B_0 \ll 1$ (see, e.g., Nava et al., 2016).

Another important piece of information inferred from the data is the time dependence of the maximum energy. As discussed in Celli et al. (2019b) an approximate way to infer the value of δ is by equating the acceleration time with the age of the remnant. Using equation (5.5) (i.e. $t_{acc}(p) \propto D(p)/u_{sh}^2$) and writing the diffusion coefficient again in terms of the magnetic turbulence ($D = D_{\rm Bohm}\mathcal{F}^{-1}$), we can write $p_{\rm max}(t) \propto \mathcal{F}(t)\, u_{sh}^2(t)\, t$. In the absence of any magnetic field amplification and with a constant turbulence, the time dependence is only determined by the shock speed which is $u_{sh} \propto t^{-3/5}$ in the ST phase, resulting in $p_{\rm max}(t) \propto t^{-1/5}$. On the contrary, our inferred value of $\delta \simeq 2.4$ requires that the magnetic turbulence should decrease in time as $\mathcal{F} \propto t^{-2.2} \propto u_{sh}(t)^{3.7}$. Hence, even accounting for all the uncertainties, a constant value of magnetic turbulence in the shock precursor would be difficult to reconcile with our finding which requires, instead, some level of magnetic amplification and/or damping. Interestingly, $\delta \simeq 2.4$ is in good agreement with the phenomenologi-

cal estimate of $\delta \simeq 2.48$ by Gabici et al. (2009) derived form $p_{max} \propto t^{-\delta}$ and assuming $p_{max}(t$=200 yr)=5 PeV, and $p_{max}(t = 5 \times 10^4$ yr)=1 GeV.

Concerning the propagation of escaping particles, the highest energy points detected by MAGIC clearly require a diffusion coefficient $\sim 10-40$ times smaller than the average Galactic one. This ratio is a factor 2.5 – 55 smaller than the prediction using equation (5.6). However, as already discussed in section 5.5.2, equation (5.6) only provides a lower limit on D_{out} and thus the two estimates can be considered compatible. Our finding that $D_{out} \ll D_{Gal}$ is not surprising given that D_{Gal} (obtained from the measurements of B/C in the local CR spectrum) represents an average over the large volume of the Galactic magnetic halo and could be completely different from the diffusion coefficient in the vicinity of γ-Cygni. A smaller diffusion coefficient could be just due to a stronger turbulence around the SNR which is somehow expected due to the complexity of the Cygnus region which counts several potential sources of turbulence (SNRs and winds from massive stars and clusters). Alternatively, enhanced turbulence could be also naturally produced by the streaming instability of escaping CRs. Such a scenario has been investigated by several authors (Malkov et al., 2013; Nava et al., 2016; D'Angelo et al., 2016) who showed that the diffusion can be easily suppressed by 1 – 3 order of magnitudes up to several parsecs from the SNR. Indeed, the reduced D_{out} of our model compared to D_{Gal} is compatible with the diffusion coefficient derived for the vicinity of other SNRs such as W28 (Hanabata et al., 2014) and W44 (Uchiyama et al., 2012). Distinguishing between these two possibilities (external sources or self-generated turbulence) is not easy but the latter case has the advantage of being more predictive. In fact, if the escaping flux is known, the diffusion coefficient can be calculated without adding any new free parameters. Also note that we assumed for D_{out} the same Kolmogorov scaling inferred for D_{Gal}[viii]. In case of turbulence coming from external sources, the Kolmogorov scaling is indeed expected, while if the turbulence is self-generated, the resulting scaling is usually different. Hence a self-consistent calculation is needed to provide a more detailed answer.

Clearly our model suffers of some limitations, mainly related to the assumptions of spherical geometry and homogeneity of the circumstellar medium. Indeed, the γ-ray map shows a patchy structure suggesting the presence of a clumpy medium. Small dense clumps may significantly modify the hadronic γ-ray spectrum as a result of magnetic field amplification occurring in the shock-cloud interaction which, in turns, modifies the propagation properties of the plasma (Gabici & Aharonian, 2014; Inoue et al., 2012; Celli et al., 2019b). Nevertheless, such an effect is mainly important at high shock speed and for a large density contrast between the clumps and the average circumstellar medium. It has been applied e.g. to the SNR RX J1713 whose shock has a speed $\sim$ 5000 km/s and where the estimated density contrast is above 10^3. In the

[viii] This is true for rigidities $\gtrsim$ 200 GV, while at lower energies the CR spectrum suggests a different scaling (Blasi et al., 2012).

case of γ-Cygni both quantities are much smaller, it is hence probable that such effect plays a minor role.

Another possible issue is related to contribution to the γ-ray spectrum coming from CR-illuminated clouds located along the line of sight and erroneously attributed to the SNR interior. Even if such a scenario remains possible, the CO maps do not show any clear evidence of clouds along the same line of sight of the SNR disc (Leung & Thaddeus, 1992), hence we are inclined to attribute all the emission from the disc region to the SNR interior.

5.7. Summary and outlook

This chapter presented a study of the γ-ray emission around the γ-Cygni SNR over three decades in energy (5 GeV–2.5 TeV) with the *Fermi*-LAT and MAGIC telescopes, which could the existence of 3 distinct emission regions:

- a source coinciding with the radio shell of the SNR and of similar extend,
- a Gaussian shaped source situated in the north-west of the SNR, which we called MAGIC J2019+408,
- and an emission region extending along the rim of the radio shell from the north-west to the west of the shell.

The brightness ratio between the source components is energy dependent with the SNR shell dominating below $\sim$ 60 GeV and the arc only being observed by MAGIC above 250 GeV. The indices for a power-law model for MAGIC J2019+408 and the shell are $\sim$2 in the *Fermi*-LAT energy range and $\sim$2.8 for the three components in the MAGIC energy range (similar within uncertainties). In the absence of alternative counterpart in other wavelengths and based on the morphology and spectra, all three can plausibly be associated with the γ-Cygni SNR. In this case a natural explanation is the escape of high-energetic particles from the shock while the shock is still intact and able to confine less energetic particles or, alternatively, the signature of the shock precursor. However, the latter is incompatible with the observed extension of the arc. The differences between MAGIC J2019+408 and the arc can be understood by the presence of an over-dense cloud partially engulfed by the SNR. An alternative that cannot be ruled out is an association of the emission outside the SNR shell with the larger Cygnus cocoon (Ackermann et al., 2011), though γ-Cygni is also considered to contribute to the cocoon.

This chapter further introduced a theoretical model to interpret the data in the framework of DSA with the inclusion of time-dependent particle escape from the SNR interior. The model assumes that bulk of the particle are proton. While a leptonic origin for the γ-ray emission cannot be ruled out, given the morphologies and spectra

of the source components a hadronic scenario seems more plausible (see chapter 5.5.1). Adjusting the model to the γ-ray emission from all the three regions (the SNR's interior, the arc, and MAGIC J2019+408) it was found that:

- the spectrum of accelerated particles is $\propto p^{-4}$ ($\propto E^{-2}$) and the acceleration efficiency is $\simeq 4\%$.
- the maximum energy of particles at the shock front decreases with time like $\propto t^{-2.4}$. Presently, it is around few TeV while it reached an absolute maximum of ~ 100 TeV at the end of the free-expansion phase. This indicates that the maximum energy does not only depend on the shock dynamics as in formula 2.22.
- the level of magnetic turbulence in the shock region at the present moment is $\delta B/B_0 \lesssim 1$. Based on the previous argument, the level of turbulence has to decrease in time, pointing toward the presence of self-exited magnetic waves from accelerated particles.
- the diffusion coefficient in the region immediately outside the SNR has to be $\sim 10 - 40$ times smaller than the average Galactic one as inferred from the B/C ratio in the local CR spectrum.
- the region around the SNR has to be patchy with extended clouds whose density is between 5 and 200 times larger than the average circumstellar medium.

All these findings agree well with the standard DSA applied to a middle-age SNR produced by a core-collapse explosion, except the quite steep time dependence of the maximum energy: the theory invoking resonant and non-resonant instabilities usually predicts flatter dependences. A way to explain the steep dependence is through some damping mechanism of the magnetic waves. Nevertheless, we stress that the description of the particle escape is not completely understood yet, even when damping processes are neglected.

It is important to mention the limitations of the current model. The description of the particle distribution function at the shock is analytical and thus cannot take into account the interplay between the shock wave, the magnetic waves, and the CRs as described in section 2.3.4. Moreover, the ST model used in the modelling does not consider a possible influence of the circumstellar medium onto the shock dynamics. Hence, it might be worth considering more accurate description of the medium surrounding a core-collapse SNR.

Such an improved modelling certainly should be accompanied by future observations. Improved knowledge about the target material can reduce the uncertainty of our proposed model and determine the contribution from hadrons. Furthermore, it would allow considering the correct environment of the SNR compared to the simple spherical model used in this work.

Given hard X-rays or MeV γ-rays can resolve the SNR shell under the background from the pulsar, they may clarify the remaining uncertainties about a hadronic or leptonic origin by searching for possible bremsstrahlung, a cooling break in the spectrum of the SNR shell, or a pion cut-off. The only full X-ray coverage of the SNR was performed by ROSAT, which could just observe in the band from 0.5 keV to 2.0 keV and thus could not measure the non-thermal X-ray emission. Later X-ray telescopes only partially covered the SNR due to their limited FoV. Therefore, γ-GCygni might be an interesting target for the upcoming eROSITA telescope (Merloni et al., 2012).

The Cygnus region is only visible from the northern hemisphere and thus in the γ-ray band γ-Cygni could be observed with the CTA North. At 1 TeV the sensitivity of CTA North outperforms the one of MAGIC by about a factor of ~ 4.3 (Cherenkov Telescope Array Consortium et al., 2019) and within 9 h a data sample of similar quality to the one presented in this work could be achieved. CTA additionally comes with a slightly improved spatial resolution of a factor ~ 1.25 better than MAGIC, which allows resolving the arc region and the internal region of the SNR in greater details. It may allow testing a possible energy-dependence of the arc and thereby testing the proposed model.

Another general advantage of CTA is its low energy threshold. This will offer the opportunity to study the transition region between confined and non-confined particles in greater detail. It may clarify whether the emission from the arc region has a peak around 100-300 GeV and connect the SNR shell spectrum with the *Fermi*-LAT data points. However, whether CTA can extend the spectrum towards lower energies will depend on its capabilities to deal with the starlight from Sadr. The moderate observation time requirements, but high scientific return, make γ-Cygni a prime target to study the particle escape process from SNRs particularly in the γ-ray band.

Bibliography

Abdo, A. A. et al. 2009, Science, 325, 840

——. 2010, The Astrophysical Journal Supplement Series, 187, 460

Abeysekara, A. U. et al. 2017, The Astrophysical Journal, 843, 40

Abeysekara, A. U. et al. 2018, The Astrophysical Journal, 861, 134

Acero, F. et al. 2015, The Astrophysical Journal Supplement Series, 218, 23

——. 2016, The Astrophysical Journal Supplement Series, 224, 8

Ackermann, M. et al. 2012, The Astrophysical Journal Supplement Series, 203, 4, 1206.1896

Ackermann, M. et al. 2011, Science, 334, 1103

——. 2017, The Astrophysical Journal, 843, 139

Aleksić, J. et al. 2016, Astroparticle Physics, 72, 76

Aliu, E. et al. 2013, The Astrophysical Journal, 770, 93

Allafort, A. et al. 2013, The Astrophysical Journal Letters, 777, L2

Amato, E., & Blasi, P. 2009, Monthly Notices of the Royal Astronomical Society, 392, 1591

Atwood, W. et al. 2012, in 4th International Fermi Symposium Proceedings, Monterey, CA, USA, 8, arXiv:1303.3514

Becker, W. et al. 2004, The Astrophysical Journal, 615, 897

Bell, A. R. 2004, Monthly Notices of the Royal Astronomical Society, 353, 550

Berge, D., Funk, S., & Hinton, J. 2007, Astronomy and Astrophysics, 466, 1219

Blasi, P. 2013, The Astronomy and Astrophysics Review, 21, 70, 1311.7346

Blasi, P., Amato, E., & Serpico, P. D. 2012, Physical Review Letters, 109, 061101

Bykov, A. M. et al. 2004, Astronomy and Astrophysics, 427, L21

Casandjian, J.-M., & Grenier, I. A. 2008, Astronomy and Astrophysics, 489, 849

Castro, D., Slane, P., Patnaude, D. J., & Ellison, D. C. 2011, The Astrophysical Journal, 734, 85

Celli, S., Morlino, G., Gabici, S., & Aharonian, F. A. 2019a, Monthly Notices of the Royal Astronomical Society, 490, 4317, http://oup.prod.sis.lan/mnras/article-pdf/490/3/4317/30437244/stz2897.pdf

——. 2019b, Monthly Notices of the Royal Astronomical Society, 487, 3199, http://oup.prod.sis.lan/mnras/article-pdf/487/3/3199/28840800/stz1425.pdf

Chen, A. W. et al. 2011, Astronomy and Astrophysics, 525, A33

Cherenkov Telescope Array Consortium et al. 2019, Science with the Cherenkov Telescope Array (World Scientific Publishing Co. Pte. Ltd.)

Chevalier, R. A. 1977, Annual Review of Astronomy and Astrophysics, 15, 175

D'Angelo, M., Blasi, P., & Amato, E. 2016, Physical Review D, 94, 083003

Drury, L. O., & Downes, T. P. 2012, Monthly Notices of the Royal Astronomical Society, 427, 2308

Dubner, G., & Giacani, E. 2015, Astronomy and Astrophysics Review, 23, 3

Fraija, N., & Araya, M. 2016, The Astrophysical Journal, 826, 31

Frail, D. A., Goss, W. M., Reynoso, E. M., Giacani, E. B., Green, A. J., & Otrupcek, R. 1996, The Astronomical Journal, 111, 1651

Fukui, Y., & Tatematsu, K. 1988, in International Astronomical Union Colloquium, Vol. 101, 261

Gabici, S., & Aharonian, F. A. 2014, Monthly Notices of the Royal Astronomical Society, 445, L70

Gabici, S., Aharonian, F. A., & Casanova, S. 2009, Monthly Notices of the Royal Astronomical Society, 396, 1629

Gaia Collaboration. 2018, VizieR Online Data Catalog, I/345

Gaisser, T. K., Protheroe, R. J., & Stanev, T. 1998, The Astrophysical Journal, 492, 219

Gao, X. Y., Han, J. L., Reich, W., Reich, P., Sun, X. H., & Xiao, L. 2011, Astronomy and Astrophysics, 529, A159

Gosachinskij, I. V. 2001, Astronomy Letters, 27, 233

Green, D. A. 2014, Bulletin of the Astronomical Society of India, 42, 47

Hanabata, Y. et al. 2014, The Astrophysical Journal, 786, 145

Helene, O. 1983, Nuclear Instruments and Methods in Physics Research, 212, 319

Higgs, L. A., Landecker, T. L., & Roger, R. S. 1977, The Astronomical Journal, 82, 718

——. 1983a, The Astronomical Journal, 88, 97

Higgs, L. A., Landecker, T. L., & Seward, F. D. 1983b, in Supernova Remnants and their X-ray Emission, Vol. 101, 281–286

Hoffleit, D., & Jaschek, C. 1991, The Bright star catalogue, 5th edn. (New Haven, Conn., USA: Yale University Observatory)

Hui, C. Y. et al. 2015, The Astrophysical Journal, 799, 76

Inoue, T., Yamazaki, R., Inutsuka, S.-i., & Fukui, Y. 2012, The Astrophysical Journal, 744, 71

Kafexhiu, E., Aharonian, F., Taylor, A. M., & Vila, G. S. 2014, Physical Review D, 90, 123014

Kothes, R., Fedotov, K., Foster, T. J., & Uyanıker, B. 2006, Astronomy and Astrophysics, 457, 1081

Krivonos, R., Tsygankov, S., Lutovinov, A., Revnivtsev, M., Churazov, E., & Sunyaev, R. 2012, Astronomy and Astrophysics, 545, A27

Ladouceur, Y., & Pineault, S. 2008, Astronomy and Astrophysics, 490, 197

Lamb, R. C. 1978, Nature, 272, 429

Lande, J. et al. 2012, The Astrophysical Journal, 756, 5

Landecker, T. L., Roger, R. S., & Higgs, L. A. 1980, Astronomy and Astrophysics Supplement Series, 39, 133

Leahy, D. A., Green, K., & Ranasinghe, S. 2013, Monthly Notices of the Royal Astronomical Society, 436, 968

Leung, H. O., & Thaddeus, P. 1992, The Astrophysical Journal Supplement Series, 81, 267

Lin, L. C. C. et al. 2013, The Astrophysical Journal Letters, 770, L9

Lozinskaya, T. A., Pravdikova, V. V., & Finoguenov, A. V. 2000, Astronomy Letters, 26, 77

Malkov, M. A., Diamond, P. H., Sagdeev, R. Z., Aharonian, F. A., & Moskalenko, I. V. 2013, The Astrophysical Journal, 768, 73

Mavromatakis, F. 2003, Astronomy and Astrophysics, 408, 237

Merloni, A. et al. 2012, arXiv e-prints, arXiv:1209.3114

Morlino, G., & Caprioli, D. 2012, Astronomy and Astrophysics, 538, A81

Nava, L., Gabici, S., Marcowith, A., Morlino, G., & Ptuskin, V. S. 2016, Monthly Notices of the Royal Astronomical Society, 461, 3552

Ostriker, J. P., & McKee, C. F. 1988, Reviews of Modern Physics, 60, 1

Park, J., Caprioli, D., & Spitkovsky, A. 2015, Physical Review Letters, 114, 085003

Pollock, A. M. T. 1985, Astronomy and Astrophysics, 150, 339

Ptuskin, V. S., & Zirakashvili, V. N. 2005, Astronomy and Astrophysics, 429, 755

Rolke, W. A., López, A. M., & Conrad, J. 2005, Nuclear Instruments and Methods in Physics Research A, 551, 493

Saken, J. M., Fesen, R. A., & Shull, J. M. 1992, The Astrophysical Journal Supplement Series, 81, 715

Sedov, L. I. 1959, Similarity and Dimensional Methods in Mechanics (Academic Press)

Taylor, A. R. et al. 2003, The Astronomical Journal, 125, 3145

Trepl, L., Hui, C. Y., Cheng, K. S., Takata, J., Wang, Y., Liu, Z. Y., & Wang, N. 2010, Monthly Notices of the Royal Astronomical Society, 405, 1339

Trotta, R., Jóhannesson, G., Moskalenko, I. V., Porter, T. A., Ruiz de Austri, R., & Strong, A. W. 2011, The Astrophysical Journal, 729, 106

Uchiyama, Y., Funk, S., Katagiri, H., Katsuta, J., Lemoine-Goumard, M., Tajima, H., Tanaka, T., & Torres, D. F. 2012, The Astrophysical Journal Letters, 749, L35

Uchiyama, Y., Takahashi, T., Aharonian, F. A., & Mattox, J. R. 2002, The Astrophysical Journal, 571, 866

Völk, H. J., Berezhko, E. G., & Ksenofontov, L. T. 2005, Astronomy and Astrophysics, 433, 229

Wakely, S. P., & Horan, D. 2007, in Proc. of the 30th International Cosmic Ray Conference, Merida, Mexico, Vol. 3, 1341–1344

Weinstein, A. 2015, in European Physical Journal Web of Conferences, Vol. 105, European Physical Journal Web of Conferences, 04005

Weisskopf, M. C. et al. 2011, The Astrophysical Journal, 743, 74

Wendker, H. J., Higgs, L. A., & Landecker, T. L. 1991, Astronomy and Astrophysics, 241, 551

Wood, M., Caputo, R., Charles, E., Di Mauro, M., Magill, J., Perkins, J. S., & *Fermi*-LAT Collaboration. 2017, in Proc. of the 35th International Cosmic Ray Conference, Busan, South Korea, Vol. 35, 824

Yuan, Q., Lin, S.-J., Fang, K., & Bi, X.-J. 2017, Physical Review D, 95, 083007

Zhang, X., Zheng, Y., Landecker, T. L., & Higgs, L. A. 1997, Astronomy and Astrophysics, 324, 641

Chapter 6.

Conclusion

In this thesis I introduced a novel spatial likelihood analysis for IACT data, which I developed with two colleagues over the recent years (Vovk et al., 2018). The analysis package, SkyPrism, allows for detailed and statistically accurate morphological studies of extended astrophysical objects with the MAGIC IACTs. Using SkyPrism, observational results on the γ-Cygni supernova remnant (SNR) were carried out, which provide unprecedented constrains on the time dependency of the level of turbulence upstream of the SNR shock and the related cosmic ray (CR) escape.

The SkyPrism package generates a realistic model of a source based on a user-defined spatial model and the instrument response function and finds the optimal parameters by fitting this model to the observed event count maps. It estimates the telescope response (as a function of the FoV and photon energy) based on MC simulations. The estimated response is computed individually for each observation considering the telescope pointing distribution during the corresponding data taking to ensure that it describes the telescope performance accurately.

In addition, this work presented extensive tests of all key ingredients of a data analysis process: the PSF and γ-ray exposure, background model, and fitting procedure. The tests demonstrated an agreement between SkyPrism and the standard MAGIC analysis package, MARS (Zanin et al., 2013), at the level $\lesssim 10\%$ in terms of the reconstructed source flux. Furthermore, they show that the SkyPrism IRFs correctly describe the off-axis dependency, which allows a proper extraction of extended source fluxes across the entire FoV. Furthermore, the program can handle multiple, superimposed sources and combine several data sets covering large sky regions in a convenient way and overcoming the limitations of the "traditional" aperture photometry approach for IACTs.

As outlined in section 4.5, SkyPrism can serve as a starting point for the development of further extensions as well as it may contribute to the software development of the up-coming Cherenkov Telescope Array (CTA).

♢

In the second part of this work, I presented a study on the γ-Cygni supernova remnant with MAGIC based on this technique. Using the SkyPrism packages I could handle the overlapping emission regions of the SNR correctly and provide a consistent analysis of the γ-ray emission in the region with MAGIC and *Fermi*-LAT. Combining the data of both instruments, three main source components were identified: the SNR interior, an extended emission located immediately outside the SNR called the arc, and a Gaussian-shaped extended source, MAGIC J2019+408, in the north-west of the remnant.

The morphologies and spectra suggest an association of all regions with the SNR and thereby the classification of the, so far, unidentified TeV emission as a part SNR system [i]. The emission from all regions can be understood as escape of high-energy particles upstream into the ISM, while the shock is still capable of confining the lower-energetic ones. Due to the extension of the arc beyond the SNR shell a precursor could be ruled out in comparison to the SNR RX J 1713.7-3946, where the extension beyond the X-ray shell is much more narrow (H.E.S.S. Collaboration et al., 2018). This makes γ-Cygni the first SNR, where the escape of CRs from an intact shock is observed. In this framework, MAGIC J2019+408 can be understood as the consequence of an over-dense cloud partially engulfed by the SNR.

A hadronic origin for the source components seemed more likely compared to a leptonic one, even though the latter cannot be completely ruled out. Hence, the escape process was tested in greater detail using a hadronic model in the framework of DSA considering the time-dependent particle escape from the SNR interior. Adjusting the model to the spectra from all three regions, it was found that decrease of the maximum energy of the particles at the shock is steeper than predicted solely by the shock dynamics. Accordingly, the level of turbulence has to decrease with time hinting at self-exited magnetic waves from the particles at the shock. This is further supported by the estimated diffusion coefficient outside the shell, which is found to be lower than the average Galactic one.

This result agrees with the current understanding of NLDSA. As pointed out by Caprioli (2011), understanding the escape process and the time dependence of the maximum energy are among the least explored aspects of NLDSA. Despite its simplicity and thereby certainly shortcomings in correctly describing reality, the presented model provides first estimates based on observation for both aspects. Thus, it would be interesting whether CTA can find agreeing estimates in younger SNRs such as RX J 1713.7-3946.

[i] According to TeVCat: `http://tevcat.uchicago.edu/?mode=1&showsrc=201`

Bibliography

Caprioli, D. 2011, Journal of Cosmology and Astroparticle Physics, 2011, 026, 1103.2624

H.E.S.S. Collaboration et al. 2018, Astronomy and Astrophysics, 612, A6

Vovk, I., Strzys, M., & Fruck, C. 2018, Astronomy and Astrophysics, 619, A7

Zanin, R., Carmona, E., Sitarek, J., Colin, P., & Frantzen, K. 2013, in Proc. of the 33rd International Cosmic Ray Conference, Rio de Janeiro, Brasil, Vol. 4, 2937–2940

Appendix A.

Crab Nebula spectra at different camera offsets

Note: the results of this section have been published in Vovk et al. (2018) (see note at the beginning of chapter 4).

♢

As a demonstration of the performance of the SkyPrism tools for non-standard source positions with respect to the camera centre, this section shows additional SEDs from observations of the Crab Nebula at different offset angles, namely at at $0.^{\circ}2$, $0.^{\circ}7$, $1.^{\circ}0$, and $1.^{\circ}4$. Similarly to the analysis, presented in section 4.4.3, the results are based on the PSF, γ-ray exposure, and background models, constructed with SkyPrism for each of the observations individually. The fitted source model included the Crab Nebula point source and the isotropic background. The obtained spectra are shown in figure A.1. The data sets are comparably small, which increases statistical uncertainties, still the obtained spectra are in agreement with reference Crab Nebula spectrum.

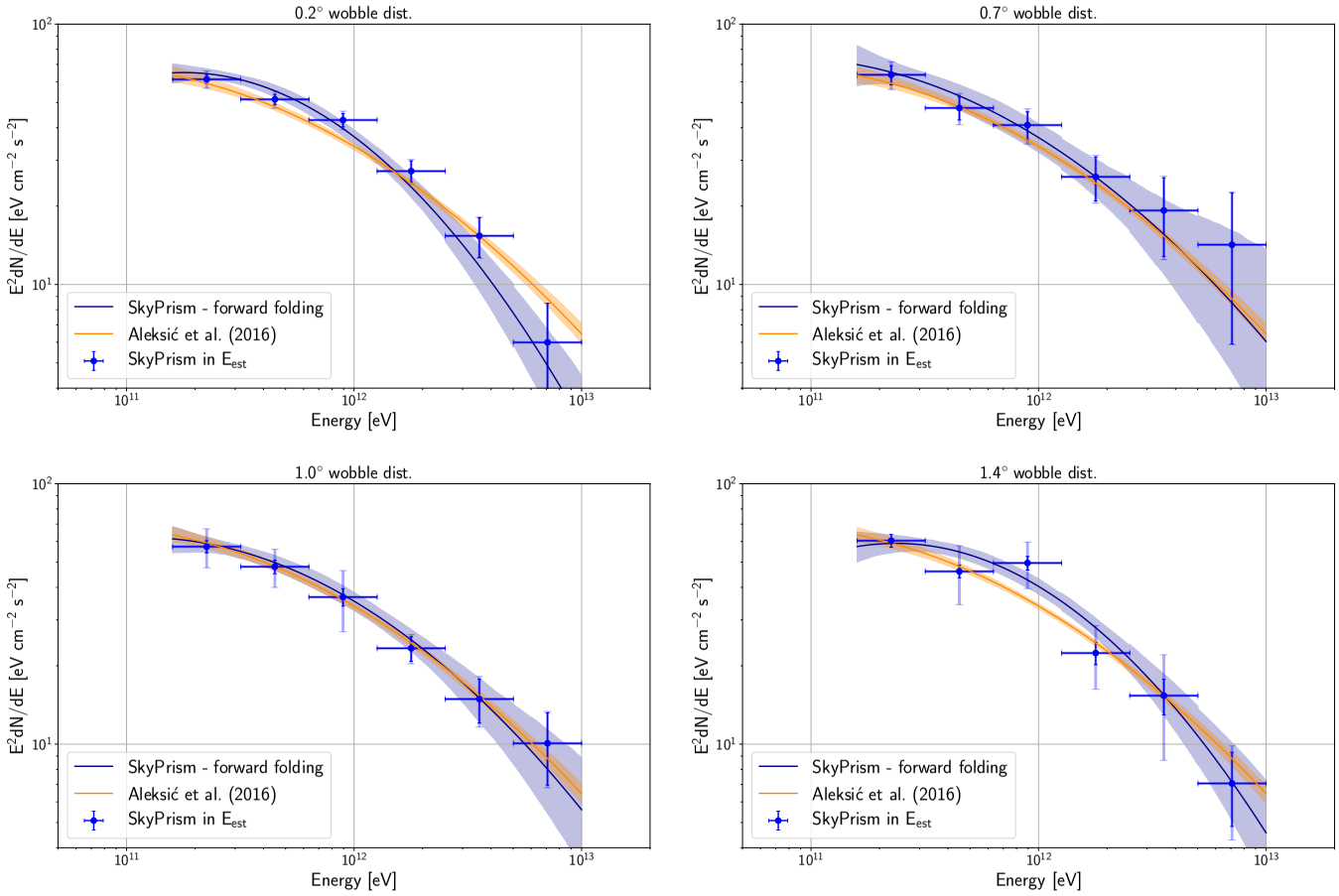

Figure A.1.: SED of the Crab Nebula obtained by processing data with non-standard wobble offsets that has also been used by Aleksić et al. (2016). The solid error bars indicate statistical errors, while the lighter coloured, wider error bars were obtained by also propagating the uncertainties from the constructed exposure model. Because of the short observation times of the data sets, the uncertainties of the fitted exposure map can be larger than the statistical error of the data points. This figure is part of Vovk et al. (2018).

Appendix B.

Cross-check of the analysis chain with Crab Nebula

To check the performance of the analysis chain used to analyse the MAGIC data on γ-Cygni, data from the Crab Nebula are processes with the same settings. This is particularly important as the γ-Cygni contained data taken under moonlight. As described in section 3.5.5 it is possible to assess whether the cleaning level used are too soft based on the number of surviving pedestal events, but not whether they are too constraining. If the cleaning levels remove too many γ-ray events from a source, the reconstructed spectrum will be affected due to a higher energy threshold and a smaller effective area. The reference source used here is the Crab Nebula and the data are selected to agree with the zenith range of the γ-Cygni data. The data are split into the same analysis periods (ST.03.06 latest from 2014 Nov 24 to 2016 Apr 28 and ST.03.07 from 2016 April 29 to 2017 Aug 02) and light conditions and finally stacked in the same way as the γ-Cygni data.

Figure B.1 shows the SEDs obtained for the different data sets as well as the SED of the stacked data set compared to the Crab Nebula reference spectrum from Aleksić et al. (2016). While the single data set have a low event statistics and thus large fluctuations around the reference Crab Nebula spectrum, the stacked spectrum shows a close agreement between reconstructed SED and the reference spectrum.

Bibliography

Aleksić, J. et al. 2016, Astroparticle Physics, 72, 76

Vovk, I., Strzys, M., & Fruck, C. 2018, Astronomy & Astrophysics, 619, A7

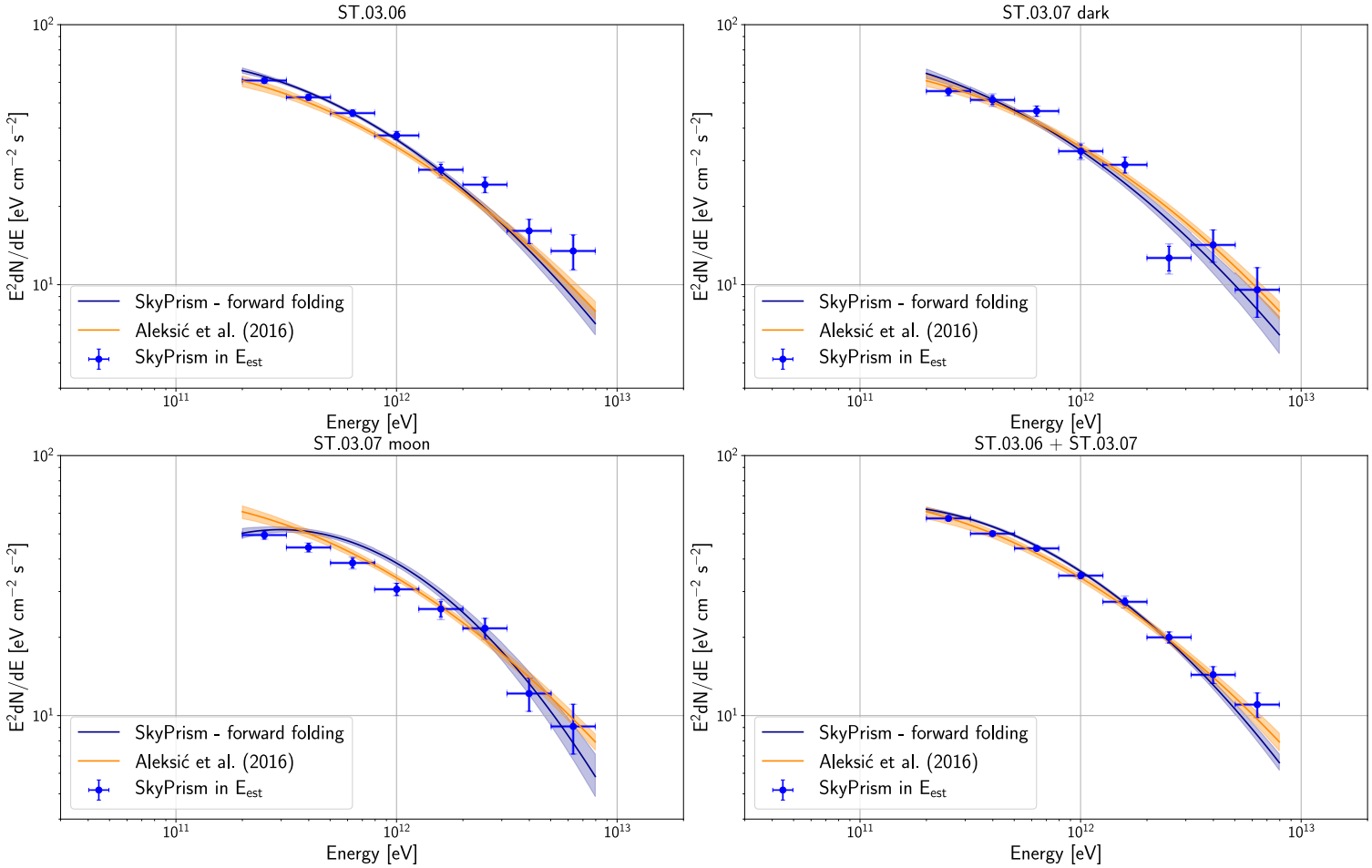

Figure B.1.: SED of the Crab Nebula from different analysis periods and moonlight conditions obtained by processing the data with same analysis chain as the data from γ-Cygni. The Crab data are selected to agree with the γ-Cygni data in terms of analysis period, light conditions, and zenith angle.

Acknowledgements - Danksagungen

"We are like dwarfs sitting on the shoulders of giants. We see more, and things that are more distant, than they did, not because our sight is superior or because we are taller than they, but because they raise us up, and by their great stature add to ours."

— John of Salisbury

First of all, I am deeply grateful to my supervisor Prof. Dr. Masahiro Teshima for giving me the opportunity to carry out this work at the Max-Planck-Institut für Physik. His constant support of my work and guidance became the corner stone of this work!
I wish to show my gratitude to PD Dr. Georg Raffelt for being my Doktorvater at the Ludwig-Maximilian-Universität München. Without his motivating discussions and unconditional help this dissertation would not have been possible.
I consider myself fortunate that I could work with Dr. Ievgen Vovk and Dr. Christian Fruck on the development of the likelihood analysis, which became the major foundation of this thesis. I have greatly benefited from the discussions about all the small details of programming and statistical analysis with you, guys!
My sincere thanks also goes to Dr. Giovanni Morlino, Shu Masuda, and Dr. Ievgen Vovk for the fruitful collaboration on the γ-Cygni SNR. Particularly, thanks to Giovanni Morlino the project lead to a much more significant result for the understanding of SNRs.
A special thanks goes to Dr. David Paneque for sharing his experience about the scientific field and always lending an open ear. His support and advices were absolutely invaluable.
I am indebted to Dr. David Green, Alexander Hahn, Dr. Derek Strom, and Dr. Ievgen Vovk for proofreading parts of this thesis. Furthermore, I would like to thank Alexander Hahn for helping me out with the submission of my thesis while I already left Europe for Japan.
For their supervision at the beginning of my work at MPP I would like to thank Dr. Pierre Colin and Dr. Emiliano Carmona. Especially to you, Pierre, for also being my day-to-day supervisor until your departure from MPP!
A big thanks goes to the MAGIC group at MPP for providing such a friendly and encouraging working atmosphere including countless, stimulating discussions about a huge variety topic over lunch and coffee breaks, barbecue parties, skiing, dinners,

and other activities. Thanks to Jürgen Besenrieder, Francesco Boracci, Giovanni Ceribella, Uta & Pierre Colin, Christian Fruck, Jezabel R. Garcia, David Green, Alexander Hahn, Wojciech Idec, Hanna Kellermann, Julian Krause, Daniel Mazin, Razmik Mirzoyan, Elena Moretti, David Paneque, Juliane van Scherpenberg, Derek Strom, Takeshi Toyama, Ievgen Vovk, and Martin Will. And for always bringing order in the life of this group, a I am very grateful to the secretaries at MPP, Sybille Rodriguez and Diana Werner.
I like to thank for the MAGIC Collaboration, which I experienced to be a great example of a international collaboration. There was always an excellent atmosphere at collaboration meetings — focussed and fruitful at the venue and fun outside. I consider working in such an international environment an honour and an priceless personal gain.
Even the busiest PhD student leaves the institute from time to time and thus I would like to thank my former flatmates in Munich. Danke euch, dass ihr — abgesehen von all den unzähligen Unternehmungen — all die Jahre aus einer WG eine Zuhause gemacht habt!
Even though most of the time I was far away, my friends from school and university were always close in my thoughts and whenever I got home from time to time, it felt as if I'd never been away. Ich kann mich nicht glücklicher schätzen, als euch zu meinen Freunden zu haben!
We, scientists, esteem the great minds of our field for their work and consider them to be the giants, but some giants work in the hidden; they are the ones encouraging us to follow our passion and being there whenever we need them. I am eternally grateful to my parents and my sister for being my giants and making me see far. Danke für eure immerwährende Unterstützung und Liebe!

The author further acknowledge the importance the following software for his work:

- This research has made use of NASA's Astrophysics Data System Bibliographic Services.
- This research made use of Astropy, a community-developed core Python package for Astronomy (Astropy Collaboration, 2018).